Technische Universität München

Physikalische Chemie

Mass Analyzed Threshold Ionization Studies and Quantum-Chemical Calculations of Biologically Relevant Molecules and Hydrogen-Bonded Complexes

Stoyan G. Georgiev

To my beloved ones

Contents

Introduction

The fundamental role of ionized species in many key processes in physics, chemistry and biology has naturally led to the development of various experimental techniques for unveiling their properties. Mass spectrometry is a powerful tool in the study of ions, in particular, molecular ions of organic and biologically relevant species as well as the process of their fragmentation. Such a study is closely related to the ionization methods which in general are very specific for each type of experiment. A variety of ionization techniques has emerged along with the development of mass spectroscopy: electron impact, chemical ionization, fast atom and ion bombardment, plasma desorption, field ionization, etc. Among these, photoionization is known to lead to the most precisely determined excitation conditions. Due to the large amount of energy needed for detaching an electron in a molecule or an atom, however, one-photon ionization is possible only with a VUV (vacuum ultraviolet) light. Some hurdles of the VUV ionization (e.g. special requirements for the beam guiding and focusing optics) are overcome by two- or, in the general case, multiphoton ionization schemes, made possible with the invention and development of the coherent quantum light generators, the lasers. Lasers and especially tunable lasers have revolutionized the field of spectroscopy and many other research and technical disciplines.

To a large extent the numerous achievements in laser spectroscopy were made possible by implementing *liquid* dye lasers. Although facing strong competition by solid-state lasers nowadays, dye lasers are still commonly used in many laboratories due to their broad tuning range (~ 300–1100 nm) that combines the benefits of the conventional light sources with the unique characteristics of the laser radiation. Other characteristics of the liquid dye lasers are the high gain and the high lasing threshold of the laser medium. Ultrashort pulses with duration shorter than 100 fs were generated with a dye laser [1]. Dye lasers can be pumped by flash lamps, excimer lasers, gas lasers or solid-state lasers.

The efficiency of multiphoton ionization is greatly enhanced if real states in a molecule are in resonance with the photon energy [2, 3]. This method known as resonance enhanced multiphoton ionization (REMPI) is characterized by a high species-selectivity due to the resonance conditions in the intermediate state. The use of tunable lasers makes it possible information not only on the masses of the studied species to be obtained, but also information on their electronic, vibrational, or rotational structure.

Thus REMPI renders mass spectrometry a two-dimensional method. In this regard it should be pointed out, however, that the resolution in any form of spectroscopy depends on the linewidths both of the radiation and the sample. Although the extremely narrow

linewidth of lasers lends itself to high-resolution spectroscopic studies, it is therefore important to minimize the collision broadening and Doppler broadening due to the thermal motion of the studied systems, molecules or molecular complexes. The most advantageous and robust method of obtaining Doppler-free experimental conditions is the supersonic jet expansion leading to the formation of molecular beams [4-7] . In such cold molecular beams, the species can be considered as unperturbed by external influences.

Also, the conditions in supersonic beams (reduction of translational and internal degrees of freedom [4, 8]) favor the formation of weakly bound complexes (clusters), held together by noncovalent[1] forces. These complexes survive on a timescale of several microseconds after the adiabatic expansion. Noncovalent interactions are about one to two orders of magnitude weaker than the chemical interactions and were first recognized by J. D. van der Waals [11] in his theoretical studies of real gases in the end of the XIX century. Since that time much knowledge about the driving mechanisms of molecular complex formation has been accumulated as a result of extensive and cooperative studies in physics, biochemistry, and biology. Nowadays, the concept of noncovalent interactions has been extended well beyond the properties of real gases and such interactions are recognized nowadays to play an essential role in the organization of matter on a macroscopic level and many examples can be given here, the most important one being the existence of life itself. A typical manifestation of noncovalent interactions is the hydrogen bonding. This "cohesive force" occurs between a covalently bound hydrogen atom and a hydrogen (or proton) accepting atom or molecular functional group.

A central problem in ion spectroscopy is the production of ions with well defined internal energies. Photoionization, even when utilizing the monochromaticity of laser photons, leads in general to the generation of ions with a broad energy distribution since the photoelectrons carry away an arbitrary amount of kinetic energy. Energy-selected ions are readily produced in threshold ionization techniques, based on the excitation of high-lying long-lived Rydberg states and their subsequent pulsed electric field ionization (PFI). These techniques known as ZEKE (Zero Electron Kinetic Energy)[12], MATI (Mass Analyzed Threshold Ionization)[13, 14] and PFI-PEPICO (PhotoElectron-PhotoIon COincidence) [15, 16] have made possible ion spectroscopic studies with resolution down to 1 meV or less. The detected species in MATI are threshold ions (rather than threshold

---

[1]As in publications by other authors [9, 10], the term "noncovalent" in the present work refers specially to nonchemical bonding and interactions and not to the cases of ionic and metallic bonds.

electrons as in ZEKE) which renders the method mass selective. Thus MATI readily lends itself to the study of processes such as fragmentation of molecules or dissociation of noncovalently bound molecular complexes.

<div align="center">***</div>

The aim of this work is to demonstrate the successful application of the MATI technique to the study of small biological molecular ions and of their noncovalently bonded complexes in their ground electronic state. The influence of hydrogen bonding on the structure, spectroscopic characteristics such as ionization energy, vibrational activity as well as the strength of this bonding in the ionized and neutral complexes have been investigated. The experimental results have been supported by *ab initio* and DFT calculations and serve as evidence for the applicability of the threshold ion spectroscopy combined with mass selectivity as a trustworthy tool for:

1) the study of biologically relevant cations;

2) exploring the nature and properties of the noncovalent bonding in ionized and neutral molecular complexes.

The structure of this work is organized as follows:

- **Chapter I:** *Interatomic and intermolecular interactions.*

- **Chapter II:** *Vibrations in molecules and molecular complexes.*

- **Chapter III:** *Computational chemistry methods*

- **Chapter IV:** *Interaction of molecules and molecular complexes with radiation*

- **Chapter V:** *Mass spectroscopy apparatus*

- **Chapter VI:** *Pulsed field ionization*

- **Chapter VII:** *Experimental setup*

- **Chapter VIII:** *MATI spectroscopy and theoretical studies of 3-methylindole and its 1:1 hydrogen-bonded complexes with water and benzene*

- **Chapter IX:** *MATI spectroscopy and theoretical studies of the conformational structure of 2-phenylethanol*

PART I

Theoretical background

"When I began my physical studies [in Munich in 1874] and sought advice from my venerable teacher Philipp von Jolly... he portrayed to me physics as a highly developed, almost fully matured science... Possibly in one or another nook there would perhaps be a dust particle or a small bubble to be examined and classified, but the system as a whole stood there fairly secured, and theoretical physics approached visibly that degree of perfection which, for example, geometry has had already for centuries."

**from a 1924 lecture by Max Planck
(Sci. Am, Feb 1996 p.10)**

"...the opinion seems to have got abroad, that in a few years all the great physical constants will have been approximately estimated, and that the only occupation that will be left to men of science will be to carry on these measurements to another place of decimals... But we have no right to think thus of the unsearchable riches of creation, or of the untried fertility of those fresh minds into which these riches will be poured."

**James Clerk Maxwell, Inaugural
Lecture as first Cavendish Professor
In Cambridge, 25 October, 1871**

CHAPTER I

Interatomic and intermolecular interactions

The concept that matter is composed of atoms brought forward the need for understanding the nature and the mechanisms of interatomic interactions. Such interactions may lead to the formation of new chemical species (molecules, ions) in the course of chemical reactions. In this case a chemical bond – covalent, ionic or metallic is formed. The products of a chemical reaction may have chemical and physical properties quite different from those of the reactants. Atoms and molecules participate in collision processes, in phenomena induced by external electric or magnetic fields and in light absorption, emission and scattering. In some cases interatomic, inter- and intramolecular interactions may lead to the formation of complexes through noncovalent (nonchemical) bonds. Such interactions are called weak or noncovalent and are of electromagnetic nature. The constituents of the so formed complexes (aggregates, clusters) retain their individual properties to a large degree, determined by the strength of the bonding. The term *intermolecular* often refers to interactions between different functional groups of a molecule [17] as is the case for macromolecules in biological systems.

A consistent description of the interatomic and inter- or intramolecular interactions is possible only on a quantum-mechanical level. This approach is based on the concept that any state of a quantum-mechanical system is completely described by its wavefunction and implies in its non-relativistic variant the task of solving the Schrödinger equation and finding the interatomic (intermolecular) potential surface for this state. The Schrödinger equation can be, however, solved directly only for the hydrogen atom which necessitates the employment of approximation methods, *the variational method* and *the Rayleigh-Schrödinger perturbation theory*, for many-electron atoms. In addition, an adequate quantum-mechanical treatment of the interaction problem for molecules and molecular complexes is greatly simplified by the adoption of the Born-Oppenheimer (BO) approximation as well as by symmetry considerations. Also, when considering the properties of a molecule or a noncovalently bound complex, the overall translational energy of the system is irrelevant and therefore excluded.

The present chapter summarizes the contemporary non-relativistic level of understanding of the various interactions between atoms and molecules leading to the formation of molecules or weakly bound systems.

I.1. Basic concepts and models

I.1.1. Symmetry considerations

In problems concerning molecular structure and spectra as well as noncovalent interactions, the integrals that have to be evaluated have two general forms:

$$\int_V \psi_i^* \hat{H} \psi_j d\boldsymbol{\tau} \equiv \langle \psi_i \mid \hat{H} \mid \psi_j \rangle \quad \text{and} \quad \int_V \psi_i^* \psi_j d\boldsymbol{\tau} \equiv \langle \psi_i \mid \psi_j \rangle \tag{I.1}$$

where the integration is over the whole space and the domain of integration is symmetric with respect to the origin of the coordinate system. The integrals are therefore different from zero only if the corresponding integrands are invariants to the symmetry operations of the point group of a particular molecule or a molecular complex. The Hamiltonian $\hat{H}$ belongs always to the totally symmetric irreducible representation of the point group, which means that the symmetry of the integrands in both cases is determined from the direct product of the wavefunctions ψ_i and ψ_j. The integrals are therefore different from zero only if ψ_i and ψ_j belong to the same irreducible representation of the point group under consideration.

I.1.2. Born-Oppenheimer (BO) approximation

The Born-Oppenheimer approximation [18] often referred to as *adiabatic approximation* plays indispensable role in quantum chemistry. It states that due to the large differrence in the masses of electrons and nuclei the electronic and nuclear motions refer to different time scales and can be separated. This means that the electrons move in the summed Coulomb attractive potential of the *fixed* nuclear framework; also the electrons react instantly to any new rearrangement of this framework. In accord with the Born-Openheimer approximation, the spin-free stationary wavefunction of a *two-atomic* system with N electrons can be factorized in a product of the electronic wavefunction $\varphi(r,R)$ and the nuclear wavefunction $\chi(R)$:

$$\Psi(r,R) = \varphi(r,R)\chi(R) \tag{I.2}$$

where r stands for the set of $3N$ electronic coordinates and R denotes the internuclear distance.

The time-independent Schrödinger equation of the system (electrons + nuclei) includes the terms $\chi \cdot \nabla_R^2 \varphi$ and $2 \nabla_R \varphi \cdot \nabla_R \chi$ that can be neglected according to the BO approximation since the electronic wavefunction $\varphi\,(r, R)$ varies usually very slowly with the nuclear coordinates. This assumption leads to the need of correction in the order of the ratio between the electron and the nuclear masses (10^{-3}), which is quite a small error. This has as a consequence that the task of solving the Schrödinger equation for the composite system of electrons and nuclei becomes a task of solving two separate Schrödinger equations: for the electronic motion with a fixed nuclear framework and for the nuclear motion. The eigenvalues in the former case are a set of solutions $E_m(R)$, where $E_m(R)$ is the energy of the m-th electronic state and depends parametrically on R.

I.1.3. Interatomic and intermolecular potential

The Schrödinger equation for the nuclear motion has the form:

$$-\left[\frac{\hbar^2}{2\mu}\nabla_R^2 + U(R)\right]\chi(R) = E_{total}\chi(R) \qquad \textbf{(I.3)}$$

where μ is the reduced mass of the nuclei and E_{total} is the total energy of the system. The function $U(R)$ is called *interatomic potential* and includes the electronic energy $E_m(R)$ and an additive correction accounting for the electronic-nuclear (vibronic) interaction [19, 20]. The graphical form of $U(R)$ for a particular *bound* electronic state is a potential curve shown in **Fig I.1**. For two interacting molecules such a one-dimensional representation is also possible if the interaction is averaged over all molecular orientations in space. The function $U(R)$ is now called *intermolecular potential* and R is the distance between the centers of masses of molecules. When the molecules are fixed in space, the intermolecular potential $U(R, \vartheta)$ depends on a set of Euler's angles ϑ, which determines the mutual orientation of the molecules.

It is quite important to stress the quantum-mechanical nature of the interaction potential $U(R)$ and its derivation from the Schrödinger equation on the basis of the BO approximation.
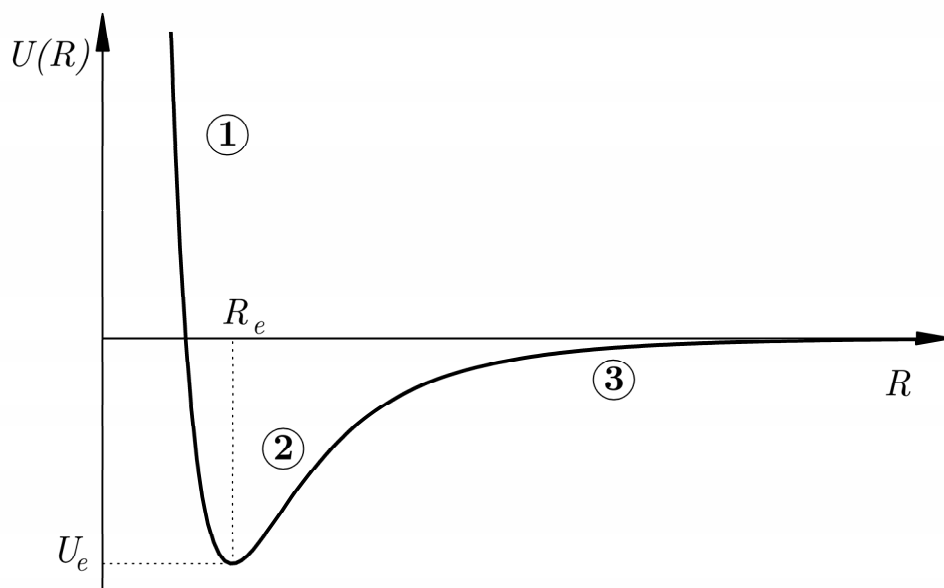
Fig.I.1. The interaction potential *U(R)* plotted against the internuclear distance *R*.
1 – region of repulsive interactions; 2 – potential well; 3 – region of attractive interactions

From a physical viewpoint the potential curve in **Fig.I.1** can be divided into three regions, depending on the behavior of the interaction potential: a region of predominantly repulsive interactions (1), a region of predominantly attractive interactions (3) and a potential minimum (2). The latter is a consequence of the subtle balance between the attractive and the repulsive interactions. The existence of a minimum of the interaction potential represents a bonding (chemical or nonchemical). It provides the stability of a system of interacting atoms or molecules and is hence is of greatest importance in problems concerning the structure and properties of molecules and weakly bound complexes. The depth of the potential well, U_e at the equilibrium position R_e is called **binding energy** and determines the strength of the bonding. It depends upon the system under study and varies widely from several eV to for covalent bonds to 10^{-2}–10^{-3} eV for weakly bound dimers of noble gas atoms. The total energy E_{total} includes terms accounting for the electronic and the nuclear (rotational and vibrational) motion of the studied system. As it was pointed out, the concept of the BO approximation rests on the assumption that the electronic and nuclear motions are separable. Similarly, it is quite often justified to

factorize also the nuclear function χ into two terms accounting for the rotational and vibrational motion. In this case the wavefunction Ψ has the form:

$$\Psi = \varphi \chi_{rot.} \chi_{vibr.} \qquad \textbf{(I.4)}$$

and the total energy is

$$E_{total} = E_{el.} + E_{vibr.} + E_{rot.} \qquad \textbf{(I.5)}$$

Eq. **(I.5)** reflects the fact that the Hamiltonians for each motion commute with one another.

There are several exceptions however, when the separation of the electronic, rotational, and vibrational motions is not adequate and these cases refer to degenerate electronic states as well as interactions of the different types of motions. Also, the validity of the adiabatic approximation is limited for high-energy collisions [21, 22] where the nuclear kinetic operator cannot be neglected.

If m_e and M_p are the electron and proton mass, respectively, the ratio between the different terms in Eq. **(I.5)** is:

$$E_{rot} \approx \sqrt{\frac{m_e}{M_p}} E_{vibr.} \approx \frac{m_e}{M_p} E_{el.}$$

so the electronic energy constitutes the main contribution to the total energy.

I.2. Covalent bonding

The detailed description and explanation of covalent bonding is one of the greatest achievements of quantum mechanics. Two general theoretical approaches have been developed in this regard: the valence-bond (VB) method and the molecular orbital (MO) method. The former considers the bonding as a result of pairing of the valence electrons in the two atoms forming the bond. The strength of the interaction depends on an exchange integral that contains the six coordinates of the two pairing electrons [23]. Originally, the VB method was applied to the H_2 molecule by Heitler and London [24] and was extended by Rumer [25] and Heitler [26]. In contrast to the VB approach, the MO method developed originally by F. Hund, R. Mulliken, J. C. Slater, and Lennard-Jones [27, 28] is based on the association of *one-electron* atomic orbitals (wavefunctions) into linear combinati-

ons (LCAO), called molecular orbitals (MOs) [29], also one-electron functions, which can be delocalized over the whole molecule. The number of the molecular orbitals equals the number of the atomic orbitals, used to form them. This approach can be applied to many-electron molecules with the condition that one should consider linear combinations in which not only *s*-orbitals but also *p*- and other types of atomic orbitals may participate. The electronic configuration of a molecule is built on the basis of the Pauli Exclusion Principle and the Hund's rule of maximal multiplicity. The requirements for the construction of MOs are that the orbitals have similar energies and belong to the same ireducible representation of the molecular point group [30].

I.2.1. Potential surfaces of bound states

In the formalism of the molecular orbitals it can be shown [31] that a covalent bond (and the corresponding *bound* electronic state) is formed as a result of the positive overlap of atomic orbitals. The binding energy is expressed in terms of integrals accounting for the Coulomb interactions of the nuclei and the electrons of the atoms, as well as for the degree to which the atomic orbitals overlap. In case of diatomic molecules the interaction energy can be represented by a potential curve (**Fig.I.1**) which has a minimum at the equilibrium internuclear distance. In the general case of polyatomic molecules the potential energy surface (PES) is $3N - 6$ ($3N - 5$ for linear molecules) dimensional in a $3N - 5$ ($3N - 4$) dimensional space, where N is the number of the nuclei in the molecule. However, for the sake of simplicity such hypersurface is often represented as, similarly for the diatomic molecules, one-dimensional in a cross-section along a given normal coordinate (See Section II.2). Different electronic states have generally energy minima at different internuclear distances. A potential surface may have more than one minimum as is the case of different conformers for example.

Conformers

The discussion about the electronic structure of molecules leads naturally to the question how it is related to the molecular geometry. One point here was discussed above with regard to the symmetry considerations in building the molecular orbitals. On the other hand, the molecular geometry is related to the existence of different conformers. These

are isomers that differ only in the spatial relative positions of the atoms in the molecule[2]. They are called *anti* or *gauche* and may be characterized with different interactions in the molecule. Such interactions between different parts of the molecule (e.g. a side chain and the aromatic ring in a benzene derivative) are of noncovalent character and may be either attractive (with forming of intramolecular weak bonds) or repulsive. A minimum in the electronic potential energy corresponds to each conformer and therefore to different conformers different ground electronic states can be attributed.

I.2.2. Types of molecular orbitals

Molecular orbitals are designated with the Greek symbols σ, π, δ, ….With respect to the bonding character the molecular orbitals are: *bonding* MOs, *anti-bonding* MOs, and *non-bonding* MOs. The first two types result from the positive and negative overlap of atomic orbitals, respectively. In the former case the electron density is concentrated primarily in the volume between the two nuclei. In the latter case the electron density is concentrated around each of the nuclei of the chemical bond. The non-bonding orbitals are atomic orbitals that do not participate in the formation of the covalent bond. The ground electronic state of stable molecules is always characterized by a bonding MO. Excited molecular electronic states correspond to anti-bonding or non-bonding orbitals and their potential surfaces can often have quite shallow potential wells. Such cases should be considered in the processes of dissociation and predissociation.

Common designations that are used extensively when discussing the molecular electronic structure are the acronyms HOMO (Highest Occupied Molecular Orbital) and LUMO (Lowest Unoccupied Molecular Orbital) also referred to as *frontier orbitals*. Molecular orbitals that have the same energy form a *shell*.

Hybridized orbitals

The chemical bonding and geometrical structure in many molecules can be explained with the idea of the so called hybridized atomic orbitals. This is of particular importance in organic chemistry for example, where the ground state electronic configuration of the

---

[2] **The conformation of a molecule is defined by the dihedral angles about all bonds.**

carbon atom can be considered not $2s^2 2p_x^1 2p_y^1 2p_z$ but $2s^1 2p_x^1 2p_y^1 2p_z^1$ instead. Since the s and p orbitals have similar energies, they can combine to form sp^3, sp^2 or sp-hybridized orbitals. The hybridized orbitals form σ-bonds, while the p-orbitals that do not participate in the hybridization form π-bonds. The hybridization leads to a decrease in the electronic energy, despite the fact that an electron is excited from $2s$ to $2p$ orbital [23]. A hybridized orbital is said to have a certain percentage s-character and a certain percentage p-character, which proves to be a useful way of explaining the different electronegativities of the carbon atoms in the different hybridization cases. An orbital with dominating s-character is more electronegative than an orbital with a dominating p-character, since the electron in the first case is attached more strongly to the nucleus.

I.2.3. Conjugated systems

The concept of π-orbitals proves to be very useful in the study of unsaturated hydrocarbons. Here the so called π-*electron approximation* is used, namely the movement of the *delocalized* π-electrons in the fixed effective electrostatic potential of the electrons of the σ-bonds framework. In benzene the six not hybridized $2p_z$ orbitals form an essentially delocalized π-bond. It can be shown with the help of the Hückel molecular-orbital theory [32] that the delocalization of the π-electrons over the whole molecule leads to decrease of the electronic energy and therefore to a stabilization of the ground electronic state (about 150 KJ/mol for benzene [31]). *In the most cases of interest in organic and biochemistry one can consider* π–π* *transitions only, since the energy gap here is much lower than that of* σ–σ* *or* σ–π* *transitions. This model explains the near UV absorption of conjugated systems as well as their fluorescence in the visible electromagnetic range.*

I.3. Noncovalent interactions[3]

Noncovalent interactions are described predominantly by the attractive and repulsive forces that *electric* multipoles exert on one another. Magnetic interactions are generally

---

[3] **A more detailed review of the noncovalent interactions is given for example by I. G. Kaplan [17].**

much weaker than electric multipole interactions and may become substantial at sufficiently large distances only. Depending on the particular system under study the net interaction energy may be a sum of different energy terms accounting for specific multipole-multipole interactions. The individual contributions of these interactions exhibit distinctive distance-dependences and can be estimated by the Rayleigh-Schrödinger perturbation theory or variational methods. The latter are used at short intermolecular distances where the interaction cannot be considered as a small perturbation and also the electron exchange symmetry has to be accounted for.

At a certain balance between the repulsive and attractive contributing terms in the net interaction energy noncovalent interactions may lead to the formation of weakly bound complexes or to structural changes in matter on a microscopic and macroscopic level. From a thermodynamical viewpoint noncovalent interactions may lead to *i*) the formation of a weak (noncovalent) bond on account of *favorable energy* and *ii*) the formation of aggregates on account of *favorable entropy* (as is the case for hydrophobic interactions). The formation of a noncovalently bound system on account of *favorable energy* results in a minimum of the net interaction energy which can be one-dimensionally represented as a potential curve as was already pointed out in *Section I.1.3.*

I.3.1. Types of noncovalent interactions

Noncovalent interactions are, as stated above, interactions generally between electric multipoles. A molecule may possess a permanent multipole moment or such may be induced by neighboring multipoles and external fields through charge redistribution. In this regard, weak inter- and intramolecular interactions fall into the following classes: **electrostatic interactions, induction interactions and dispersion interactions.** The last two types can be united under the common name **polarization interactions.** Also, as in the case of covalent bonding, at short internuclear distances **exchange interaction** plays a substantial role. In addition, at sufficiently large distances ($R >> \hbar c / I$, where I is the first ionization potential) **retardation effects** have to be considered. These account for the finite propagation time of interaction and are important in the coagulation theory of colloid solutions. Retardation effects become noticeable at distances $>>$ 500 bohrs [17].

a) Electrostatic interactions

These are interactions between permanent multipole moments. Multipole moments describe the charge distribution in a molecule. If the two molecules are at distances, sufficiently large so there is no overlap of their charge distributions, the electrostatic potential of each molecule can be expanded into an infinite Taylor series of multipoles. Such an approximation is not completely justified since there is always some degree of overlap due to the quantum mechanical delocalization of the charge. As a consequence the Taylor expansion is convergent only up to a certain multipole moment Q_l^m for any *finite* internuclear distance [17]. The presence or the absence of a particular multipole moment in the multipole expansion is directly related to the molecular symmetry [17]. Molecules are characterized by the first non-vanishing multipole moment in the Taylor expansion of their potential since only this multipole moment does not depend on the choice of the coordinate system. Thus for molecular ions the first non-vanishing moment is the monopole moment (the charge), for polar molecules this is the dipole moment, for neutral molecules with non-spherical charge distribution this is the quadrupole moment, etc.
The electrostatic interactions can be quantitatively treated within the scope of the first-order perturbation theory.

b) Resonance interactions:

Resonance interactions arise between the ground state of one molecule and the excited state of another molecule provided the energy gaps between the ground and the excited state in both molecules are similar. Therefore such interactions are always present when two identical molecules interact. The best examples here are the excimers. Similarly to the case of electrostatic interactions, the resonance interaction energy can be expanded into multipole series for sufficiently large intermolecular distances. In the case of neutral molecules the first term in such expansion is the resonance dipole-dipole interaction.

c) Polarization interactions

Such interactions arise when a molecule induces multipole moments in another molecule (an effect known as polarization) and can be described by second- and higher-order perturbation theory corrections. Correspondingly, molecules in which dipole moments can be

induced are said to be *polarizable.* The polarization interaction energy includes terms accounting for induction interactions and dispersion (London) interactions:

$$E^{(2)}_{pol} = E^{(2)}_{ind} + E^{(2)}_{disp} \tag{I.6}$$

Induction interactions: these are due to interactions between a permanent multipole moment and an induced multipole moment. The induction interaction energy of atoms and molecules in their ground states is always negative (and has therefore attractive contribution to the net interaction energy). For atoms and molecules in excited states the induction interaction can be, however, attractive as well as repulsive.

Dispersion interactions: dispersion (London) interactions are solely responsible for the attraction between uncharged, nonpolar molecules. A theoretical description of these interactions on the basis of quantum mechanics was given by Fritz London [33, 34] in 1930. Their origin can be explained with the following assumptions:

> i)   A non-zero instantaneous dipole (generally multipole) moment exists at any time in molecules even if it equals zero when time-averaged. This time-variable dipole moment results from the charge distribution fluctuations due to the oscillating electrons.

> ii)   The instantaneous dipole moment in a molecule *A* induces a multipole moment in another molecule *B*.

d) Exchange interaction

Unlike the case of covalent bonding, the role of exchange interaction in the intermolecular potential is reversed: for molecules in the ground state with total spin *S*=0 and atoms with *closed* electronic shells (noble gas atoms, alkaline earth atoms) the exchange interaction is always positive (repulsive). Thus the exchange-repulsion interaction sets a minimum distance at which molecules can come close to one another and defines their van *der Waals radii.* When the exchange interaction is taken into account, the standard Rayleigh-Schrödinger perturbation theory loses its validity in a zeroth-order approximation and the Symmetry-Adapted Perturbation theory has to be applied.

e) Hydrophobic interactions

Nonpolar molecules (especially hydrocarbon groups) are reorganized and gather in aqueous solutions due to hydrophobic interactions between the solute and the solvent [35-38]. The hydrophobic effect is entropy-driven and the change of enthalpy is negligible [9, 35, 39]. Hydrophobic interactions contribute to the stabilization of the secondary and tertiary structure of proteins.

I.3.2. Semiempirical potentials

Several models of intermolecular potentials based on theoretical assumptions and considerations of the contributing terms of different types of noncovalent interactions to the net interaction energy have been developed. The analytical expressions of these contributions are found by an approximate solution of the Schrödinger equation in the adiabatic approximation and have parameters that can be experimentally determined. One of the most commonly used models is the Lennard-Jones potential, proposed for the study of the virial coefficients of rare gases [40]:

$$U(R) = \frac{\lambda_n}{R^n} - \frac{\lambda_m}{R^m} \qquad \textbf{(I.7)}$$

often represented in its 6-12 form:

$$U(R) = 4\varepsilon \left[\left(\frac{\sigma}{R} \right)^{12} - \left(\frac{\sigma}{R} \right)^{6} \right] \qquad \textbf{(I.8)}$$

where ε is the depth of the potential depth at $R_e = \sigma 2^{1/6}$ and σ is the value of R at $U(0)$. Mason and Schamp proposed the 12-6-4 potential [41] for including the induction interaction as well as interaction of ions with neutral systems. Buckingham [42] introduced in 1938 a model potential that approximates the repulsive contributions by an exponential function. Other models are for example the Stockmayer potential [43] for predominantly dipole – dipole electrostatic interactions and the Keesom potential [44, 45] that describes the dipole – dipole interactions with small repulsive contributions.

I.3.3. Hydrogen bonding

Hydrogen bonds (H-bonds) are by far among the most important and therefore extensively studied manifestations of noncovalent interactions. The hydrogen bond was first mentioned in 1912 by T.S. Moore and T.F. Winmill [46]. The description of hydrogen bonding in water was given by Latimer and Rodebush in 1920 [47]. The term hydrogen bridge was introduced by Desiraju [48].

The H-bond is a cohesive "force" formed between a hydrogen (in the extreme case: proton) donor X–H and a hydrogen (proton) acceptor Y:

$$X - H \cdots Y$$
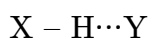
where X and H are covalently bonded. The interaction energy of a hydrogen bond can be represented by the Lennard-Jones 6-12 potential or by [49]:

$$U(R) = \frac{A}{r^{12}} - \frac{B}{r^{10}} \tag{I.9}$$

Other potentials were proposed by Jorgensen, et al. [50] for solvent environments around biomolecules and by Y. Chen, et al.[51] for the design of protein-RNA interactions.

a) Classification

The conventional concept that hydrogen bonding involves only (strongly) electronegative systems X and Y (generally X = O, N, F and Y is an atom with a lone electron pair) has been nowadays radically reviewed and further developed to encompass a variety of interactions in chemistry and biology[48, 52-54]. In the light of the contemporary understanding of hydrogen bonding, the following classification can be made:

a) *"Classical" σ-type hydrogen bonding*: both X and Y are strongly electronegative atoms, usually F, O, N (given in order of decreasing electronegativity). Although the electronegativity of Cl is close to that of N, chlorine atoms are not significantly involved in hydrogen bonding. The reason is that the partial negative charge on a chlorine atom in a covalent bond is more diffuse due to the larger size of Cl and therefore does not attract the hydrogen atom strongly.A few exceptions exist,

for example in the case of metal-bound chlorine that was shown to be a good proton acceptor [55, 56] and in the H_2O ClO radical complex [57].

b)   σ-*type hydrogen bonding involving sulphur*: SH···S, SH···O, OH···S [49].

c)   π-*type hydrogen bonding*: X–H···π, where as in a) X = F, N, O. Here the proton acceptor is a π-electron system (e.g. benzene ring).

d)   *Hydrogen bonding involving the C – H group*: σ-type hydrogen bonding C – H···Y (Y = electronegative atom) or π-type hydrogen bonding C–H···π [58, 59]. Although some indications that hydrogen bonding involving C–H groups exist date back to 1930 [60, 61], the idea was introduced as late as 1960 by Sutor with the C–H···O binding motif [62, 63]. Frequently, however, no H-bond is formed between a CH group and an electron donating system and one speaks of a CH···Y contact [9].

e)   *Dihydrogen bond* [64] involves a positively partially charged H and a partially negatively charged H: XH···HY (which is the situation in systems containing boron or transition metals [65, 66]. A typical example here is the BH_3·NH_3 dimer [67, 68].

f)   *Hydrogen bonds involving transition metals*: X–H···M [49], where X is an electronegative atom (generally a functional group) or carbon.

g)   *Ionic hydrogen bonding (IHB)* [69-72]: involves partial proton transfer from the donor to the acceptor; when a proton interacts with a single water molecule it forms a strong covalent bond with the oxygen to form the hydronium ion H_3O^+ called also Eigen cation [73].

h)   π···H^+···π hydrogen bridges [74].

i)   *Monoelectron dihydrogen bridges* [75, 76]: H···e···H (H_3C·HF complex [76]).

b) Nature of hydrogen bonding

The staggering variety of hydrogen-bond patterns does not lend itself to a general conclusion on the mechanisms and the nature of hydrogen bonding. Although it is accepted [9] that hydrogen bonds are stabilized by several components of the net interaction energy in **Fig.I.1**: electrostatic, induction, and dispersion energy terms [9], the dominant contribution from the various intermolecular interactions depends however on the particular case.

For H-bonds between polar X–H and Y groups as well as for charged systems the main driving force behind bonding is the electrostatic interaction (charge-dipole, dipole-dipole or both). In addition, as empirically calculated by Pauling [77] as early as 1949 and later shown in a series of experiments [78-80] a certain covalent character may be attributed to strong hydrogen bonds. Baker and coworkers analyzed more than 100 000 H-bonds (most of them NH···O) and underlined their partially covalent character [81].
For hydrogen bonds involving aromatic rings as proton acceptors the main contributors to the bonding are induction and dispersion interactions due to the high polarizability of the π-electrons.

Hydrogen bonds involving the C–H group are stabilized mainly from dispersion interactions (as is the case of C–H···O in $CH_4 \cdot H_2O$ complex [82]).

It was shown on the basis of orbital analysis [83] that a small charge transfer (0.01 e^-) from the lone electron pairs of the electron donor (Y) to the C–H antibonding orbitals also contributes to the H-bond. The extent to which this charge transfer affects the bonding depends on the nature of X and Y and is considerable large for H-bonds involving polar groups or charged systems. The charge transfer leads in the case of the so called *proper H-bonds* to an increase of the electron density in the antibonding orbitals of the electron acceptor XH which causes elongation of the X–H bond and a concomitant red shift of the X–H stretching vibration. This red shift **serves as an indication** that an H-bond is formed [9]. However, it was found out that another type of hydrogen bonding with regard to its effect on the covalent X–H bond exists, namely *improper (blue-shifting, antihydrogen) H-bonds* [9, 84-86]. In this case the formation of a hydrogen bond leads to a decrease of the X – H bond length and consequently to a blue-shift of the X–H stretching vibration (as for C–H···O and C–H···F^- in fluoroform·ethylene oxide [87] and C–H···π in chloroform·fluorobenzene complexes [88]). A decrease (or very small increase)

in the σ^* electron density of the X–H bond was observed for improper hydrogen bonds [89-92] in contrast to the case of proper hydrogen bonds. In this regard, another driving mechanism for the occurrence of improper bonds was suggested, namely that Y donates its electron charge to other atoms bonded to X and not to X–H. This charge transfer is accompanied by a geometrical distortion that may lead to X–H bond contraction.

Joseph and Jemmis [93] explain the lengthening/shortening of the X–H distance for proper/improper hydrogen bonds with the competition between two opposite effects: lengthening by attraction between H and Y on the one hand, and shortening due to the electron density gain on X, on the other hand. The net effect depends on the nature of the proton donor X–H and acceptor (Y) and it was pointed out that highly polar donors and strong acceptors form as rule proper hydrogen bonds.

c) Properties of hydrogen bonding:

Hydrogen bonds may differ significantly with respect to their strength, length, and geometry, depending on the nature of X and Y. Also, unlike the case of covalent bonding, the characteristics of hydrogen bonds depend on the environment and the aggregate state of matter.

Bond strength: The strength of an H-bond depends on the nature of the systems X and Y, the bond angle, temperature, pressure [94] and the environment (usually characterized by a local dielectric constant). Hydrogen bonding is typically stronger than other non-covalent interactions but weaker than covalent, ionic and metallic bonds. Depending on the stabilization energy, hydrogen bonds can be classified as: strong ($\Delta E = $ 15–40 kcal/mol), moderate ($\Delta E = $ 4–15 kcal/mol) and weak ($\Delta E < $ 4 kcal/mol) [53]. The stabilization energy for the strongest hydrogen bond F–H$\cdots$F is 155 kJ/mol or $\approx$ 1.6 eV [95]. On the other hand, some of the weakest bonds, C–H$\cdots$O are similar in energy (max. 2 kcal/mol [96]) to van der Waals complexes [54].

Although individual hydrogen bonds can be very weak, hydrogen bonding similarly to other noncovalent interactions manifests **additive** and **cooperative** effects, namely adjacent bonds reinforce each other, especially when polar groups are involved.

Bond length: The length of a H-bond varies usually between 2 and 3 Å and depends on the stabilization energy as well as on temperature and pressure. Two criteria for the formation of a hydrogen bond related to its length are:

- the so-called van der Waals cutoff criterion, stating that the bond length $d(\text{H}\cdots\text{Y})$ is smaller than the sum of the van der Waals radii of H and Y:

$$d(\text{H}\cdots\text{Y}) < r_w(\text{H}) + r_w(\text{Y}) \qquad \textbf{(I.10)}$$

- also, necessary but insufficient condition is imposed on the distance between X and Y:

$$d(\text{XY}) < r_w(\text{X}) + r_w(\text{Y}) \qquad \textbf{(I.11)}$$

The above criteria are, however, not always correct due to factors like the ill-defined van der Waals radii of hydrogen (because of its easily polarizable electron density) or the deviations of the van der Waals surface from sphere for many-atomic ions. It has been pointed out that the second criterion (Eq. **(I.11)**) is in disagreement with the existence of three-center bonds [52].

Bond geometry: Hydrogen bonds show a preference for collinearity, a fact that distinguishes them from van der Waals bonds. However, bond angles up to 90° have been suggested for weak bonds (C–H$\cdots$Y [53]) and down to 130° for O–H$\cdots$Y. Bend geometry is also typical for intramolecular hydrogen bonds. In some cases the proton acceptor shows some angular preference, which can be identified with the position of the electron lone pair (OH$\cdots$O=C for example). The geometry of the H-bond may depend also on the nature of the proton donor. For example, the bond in HCN·HF is linear, while the H_2O·HF and H_2CO·HF have pyramidal and trigonal planar VSEPR[4] symmetry, respectively [97]. In general, strong bonds with electrostatic and covalent character posses a higher directionality than weak bonds stabilized mainly by dispersion interactions [53].

Hydrogen bonds in crystals are rarely linear, because of a sin geometrical factor [98]. The most probable angle is around 165°[99]. Another reason for the nonlinear geometry is the existence of multicenter bonds [100-102].

---

[4] **Valence Shell Electron Pair Repulsion:** R. J. Gillespie, I. Hargittai: *The VSEPR Model of Molecular Geometry*. 8 Aufl., Allyn & Bacon, Boston **1991**, Chem. Soc. Rev., **2005**, 34, p.396.

d) The role of H-bonds in nature

Water: Water is the natural solvent in the living organisms and also plays a key role in their thermoregulation. Its unique macroscopic properties (high boiling point and the fact that water has lower density in solid state than as liquid) are explained with the existence of multiple hydrogen bonds mutually reinforced due to cooperative effects. The boiling point of water for example is higher than its heavier analogue H_2S. This holds true also for other hydrogen-bond forming molecules compared to their no H-bond forming counterparts: NH_3 vs. PH_3 , and HF vs. HCl.

Biological systems: Hydrogen bonds are sufficiently weak to be broken and reformed under the strictly limited conditions (pressure, temperature) in the living organisms. On the other hand, hydrogen bonding can be strong enough to form stable supramolecular aggregates. The role of H-bonding is nowadays unquestionably recognized in DNA and RNA base pairing [103-106], as well as in the protein secondary and tertiary structure [104, 107], in enzyme-substrate complexes, organic supramolecules, and organic nanomaterials [108-111], as well as in crystal engineering [112]. Hydrogen bonds with C–H as a proton donor are generally weak but play an important role in biomolecular structure due to their large number. C–H⋯Y (see Chapter 5 in ref. [49]) bonds are one of the most common intermolecular interactions in organic molecular crystals or those involving organic ligands.

Other systems: Hydrogen bonding is also responsible for the dimer formation in carboxylic acids and hexamer formation in hydrogen fluoride, which occur even in the gas phase, resulting in substantial deviations from the ideal gas law. Ion hydrogen bonds play important roles in ionic crystals and complexes, ion solvation, electrolytes, acid-base chemistry.

CHAPTER II

Vibrations in molecules and molecular complexes

One of the main aspects in the present work concerns the vibrational structure of the first excited electronic state S_1 and the ground cationic state D_0 of molecules and weakly bound complexes. That is why special attention at this point is paid to the theory of molecular vibrations, which is also generally applicable to intermolecular or intramolecular vibrations of noncovalent bonds. In diatomic molecules or noncovalently bound complexes there is only one vibration, namely the stretching totally symmetric vibration of the bond between the two nuclei. In the harmonic oscillator approximation this gives rise to only one frequency corresponding to the excitation of one quantum of this vibration. In contrast, in polyatomic molecules the vibrational motion is much more complex since in this case exist several internuclear distances and even if only harmonic oscillations are considered, this gives rise to much more congested vibrational spectra than in the case of diatomic molecules.

In the present chapter the term "molecules" refers also to noncovalently bonded molecular complexes.

II.1. Harmonic vibrations in diatomic molecules

The electron potential energy that serves as an interatomic or intermolecular potential $U(R)$ in the Schrödinger equation for the nuclei (Eq. **(I.3)**) can be described in the vicinity of the minimum with the potential of a harmonic oscillator:

$$U(x) = \frac{1}{2}k(R - R_e)^2 \equiv \frac{1}{2}kx^2 \qquad \textbf{(II.1)}$$

$$k = \left(\frac{\partial^2 U(x)}{\partial x^2}\right)_0$$

where x is the displacement from the equilibrium position of the nuclei R_e and k is the force constant, characterizing the stiffness of the internuclear bond. Higher derivatives of the potential function of a diatomic molecule with respect to the displacement coordinates are neglected. The solutions of Eq. **(I.3)** with the form of $U(x)$ given by Eq. **(II.1)** correspond to the equidistant energy levels of a quantum harmonic oscillator:

$$E_v = (v + \tfrac{1}{2})\hbar\omega \qquad \textbf{(II.2)}$$

Here $\omega = \sqrt{k / \mu} = 2\pi\nu$, where ν is the vibrational frequency and μ is the effective (also called reduced) mass of the system of the two nuclei. The quantum number v takes any integer values 0, 1, 2 … E_0 is called Zero Point Vibrational Energy[5] (ZPVE) and corresponds to the so called vibrationless level of a given electronic state.

The wavefunction is given by a product of Hermite polynomials $H_v(y)$ and a Gaussian function:

$$\chi_{harm.vibr.} = N_v H_v(y) e^{-\frac{1}{2}(x/\alpha)^2}$$

where N_v is a normalization constant and $\alpha = \left(\hbar^2 / \mu k\right)^{1/4}$.

A more realistic description of the vibrations of a molecule is given by the empirical Morse potential $U(x) = D_e\left[1 - \exp(-\beta x)\right]^2$ that accounts for deviations from the harmonic oscillator approximation. Here β is a measure of the curvature at the bottom of the potential well. The corresponding vibrational energy is

---

[5] **The zero point energy is a common concept in quantum mechanics and has no classical analogue. It refers to the lowest possible energy of a quantum system.**

$$E_v = (v + \tfrac{1}{2})\hbar\omega - \hbar\omega x(v + \tfrac{1}{2})^2 \qquad \textbf{(II.3)}$$

where ωx is a small anharmonic correction. D_e is the dissociation energy measured from the bottom of the potential well. However the true dissociation energy of the molecule is D_0 measured from the zero-point vibrational level (**Fig.II.1**).
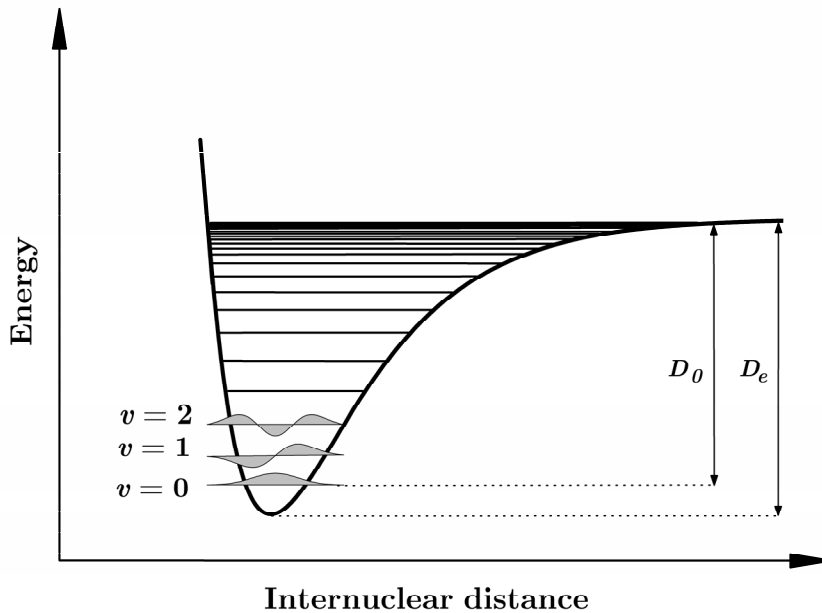
Fig.II.1. Morse potential and the vibrational levels of a diatomic molecule. Also shown is the form of the vibrational wavefunction for $v = 0, 1, 2$.

II.2. Vibrations in polyatomic molecules

II.2.1. Normal modes and coordinates

The seemingly random and complex vibrational motion of a polyatomic molecule can be decomposed into a sum of relatively simple components in the same way in which a Lissajous motion can be represented as a superposition of simple harmonic motions. These components are called normal modes of vibration and each one of them is associated with a certain frequency. The concept of normal modes is strictly valid only in the harmonic oscillator approximation, i.e. for small displacements from the equilibrium. As

shown above for diatomic molecules (Eq.(**II.1**)), such an approximation assumes that the potential energy is a quadratic form of the displacement coordinates (terms containing cubic or higher forms are disregarded). Normal modes correspond to displacements along coordinates called *normal coordinates*. These coordinates allow the diagonalization of the terms of the kinetic energy and potential energy of a system consisting of N particles (e.g. atoms):

$$E_{kinetic} = \frac{1}{2}\sum_{i,j} a_{ij}\dot{q}_i\dot{q}_j \xrightarrow{\;normal\;\;coordinates\;\;Q\;} E_{kinetic} = \frac{1}{2}\sum_i \dot{Q}_i^2$$

$$E_{potent.} = \frac{1}{2}\sum_{ij} k_{ij}q_iq_j \xrightarrow{\;normal\;\;coordinates\;\;Q\;} E_{potent.} \frac{1}{2}\sum_i \lambda_i Q_i^2$$

Here q_i are the generalized coordinates, which are not necessarily Cartesian ones (then the coefficients $a_{ij} \neq 0$ for $i \neq j$), k_{ij} are called generalized force constants, and λ_i are force constants related to the normal coordinates Q_i and the frequencies of the normal vibrations ν_i in the following way: $Q = Q_i{}^0\cos(\lambda_i^{1/2}t + \varphi_i)$, $\lambda_i^{1/2} = \omega_i = 2\pi\nu_i$.

The Hamiltonian of the system is: $\hat{H} = \sum_i \hat{H}_i$, with

$$\hat{H}_i = -\frac{1}{2}\hbar\frac{\partial^2}{\partial Q_i^2} + \frac{1}{2}\lambda_i Q_i^2 \qquad\qquad \textbf{(II.4)}$$

II.2.2. Energy terms and total wavefunction of normal vibrations

The Schrödinger equation for a harmonic oscillator can be applied to each normal mode so the total energy term is given by

$$G(v_1, v_2...) = \sum_i (v_i + \frac{1}{2})\bar{\nu}_i \qquad\qquad \textbf{(II.5)}$$

Here the wavenumber $\bar{\nu}_i = \nu_i / c$ corresponds to the frequency of the i-th vibration [cm^{-1}], excited by v_i quanta ($v_i = 0, 1, 2,...$). The summation is over **all 3N degrees of freedom**, however, those of them corresponding to translation and rotation of the molecule as a whole can be omitted since they have zero frequencies (these motions are also called *non-genuine* vibrations). It is known that for nonlinear molecules there are 6 *non-genuine* degrees of freedom and for linear molecules there are 5 such degrees. Thus the number of the *genuine* vibrations of a molecule consisting of N atoms is $3N - 6$ for nonlinear and $3N - 5$ for linear molecules. An important property of molecular vibrations

is that each normal mode forms a basis for an irreducible representation of the point group of the molecule.

The total vibrational wavefunction of the molecule is a product of the wavefunctions, corresponding to each normal mode i:

$$\chi_{vibr.} \equiv \mid v_1 v_2 v_3 ...\rangle = \prod_i \chi_{v_i}(Q_i) \equiv \prod_i \mid v_i \rangle \qquad \textbf{(II.6)}$$

The ground vibrational state of a molecule is $\mid 0_1 0_2 0_3 ... 0_i \rangle$ and is characterized in the harmonic oscillator approximation by a summed zero-point vibrational energy (ZPVE):

$$E = \sum_i \frac{1}{2} \hbar \omega_i \qquad \textbf{(II.7)}$$

II.2.3. Types of normal vibrations

Normal vibrations can be classified with respect to three criteria:

i) Form of the vibrational motion: depending on how the respective normal coordinates oscillate, there are stretching, bending, and torsional vibrations.

ii) Symmetry: according to their behavior with respect to the symmetry operations of the point group of the molecule the vibrations can be symmetric or antisymmetric. A vibration is considered antisymmetric if it is antisymmetric with respect to at least one symmetry element. The symmetry of the total vibrational wavefunction is determined by the product of the symmetry species of each individual wavefunction: $\prod_i \Gamma^{v_i} \left[\chi_{v_i}(Q_i) \right]$. Since the symmetric vibrations cannot change the species of this product, the symmetry of the total vibrational wavefunction depends solely on the sum $\sum_i v_i$ of the quantum numbers of the antisymmetric vibrations ($\chi_{vibr.}$ is antisymmetric if the sum is odd and symmetric if the sum is even). It can be shown that the wavefunction of the ground vibrational state is totally symmetric under all symmetry operations of the molecular point group [113].

iii) Vibrations can be degenerate or non-degenerate. Vibrations to which correspond closely lying or coinciding energy levels are said to be degenerate. Degeneracy can be necessary or accidental. *Necessary degeneracy* arises from the symmetry of the molecule. A molecule does necessarily have degenerate vibrations only if it has at least one more-

than-two fold symmetry axis. From the properties of the harmonic oscillator eigenfunctions it follows that the zero-point vibration does not introduce degeneracy (the degeneracy is 1 for $v_i = 0$). On the other hand, the degeneracy of a degenerate vibration is increased if this mode is excited by several quanta [114]. A higher degeneracy arises also for a vibrational state that is a result of the excitation of several degenerate vibrations. Such additional degeneracy (associated with the quantum number v) is, however, removed when anharmonicity is taken into consideration. *Accidental degeneracy:* in polyatomic molecules two vibrational levels corresponding to different vibrations (or combination of vibrations) and *belonging to the same symmetry species* may lie energetically close to one another and therefore may mix. Such mixing is known as Fermi resonance and may play significant role in the absorption and emission of a particular molecule.

Similarly to non-degenerate vibrations, degenerate vibrations can be symmetric or antisymmetric with respect to a symmetry element of the molecular point group (for example a centre of inversion). However, in general the wavefunction of a degenerate vibrational level is orthogonally transformed into a linear combination of the eigenfunctions belonging to the same energy level.

The symmetry species of the vibrational wavefunction $\chi_{vibr.}$ can be found from the species of the components $\chi_{v_i}(Q_i)$ for degenerate vibrations in a similar way as for nondegenerate ones with the help of tables like those given by Herzberg [114]. One main difference between degenerate and non-degenerate vibrations is that an angular momentum can be attributed to a singly excited degenerate vibration.

II.2.4. Anharmonicity

For vibrations with large amplitudes an anharmonicity in the vibrational motion arises. In this case cubic and higher terms with respect to the displacement coordinates in the expression for the potential energy should be considered. The symmetry species of the total vibrational wavefunction are determined in the same way as in the harmonic approximation case.

CHAPTER III

Computational chemistry methods

The foundation and development of quantum mechanics and chemistry, in particular, has always gone hand in hand with the search of appropriate theoretical models of the studied systems and interactions. Such models have served as a basis for the implementation and application of a variety of computational methods for calculating and predicting inherent properties of studied species: structure, absolute and relative (interaction energies), electronic charge distributions, dipole and higher multipole moments, vibrational frequencies, etc. Except for the case of the simplest systems H and H_2^+ where analytical solutions are available, quantum chemical calculations are always numerical and rest on certain physical and computational approximations. The Born-Oppenheimer approximation and the neglect of relativistic effects are basically intrinsic for all *ab initio* calculations. On this basis, the wavefunction describing a quantum state and the solution to the Schrödinger equation can be found in two conceptually different approaches: the variational method and the Rayleigh-Schrödinger perturbation theory.

The systems of interest may be either isolated species – molecules and molecular weakly bound complexes or ensembles of such species. Three main tasks in the application of computational chemistry methods can be pointed out: *i) to assist the understanding and interpretation of experimental data, such as spectroscopic results (position and origin of peaks); ii) to serve as a basis for laboratory synthesis; iii) to predict the existence of new molecular species or to explore reaction pathways.*
Ab initio methods are typically computationally expensive, especially when dealing with large-size systems. High levels of calculations performed by the employment of more sophisticated methods with the use of large basis sets require for such systems substantial amount of time and computer resources.

The experimental results presented in this work are supported with *ab initio* and Density Functional Theory (DFT) computational estimations of the energies, frequencies, and the geometries of the studied systems. The aim of the present chapter therefore is to give a concise review of some popular computational techniques widely used in the study on isolated species (molecules or noncovalently bound molecular complexes).

III.1. *Ab initio* methods

III.1.1. Basis sets

Basis sets should be chosen in such a way that they accomplish two, often opposite requirements:

-   The basis set functions should correctly represent the electron density distributions on the individual atoms in a molecule, i.e. their choice has to be consistent from physical and chemical viewpoint. For example the functions should have large amplitudes in those regions where the electron wavefunction amplitude is also large.
-   The form of the basis functions should permit a computationally feasible evaluation of the various integrals appearing in an *ab initio* calculation.

Also, because of inaccuracy stemming from the incompleteness of the basis sets used in the computational programs, generally employing larger sets improves the accuracy of the calculations.

The simplest and closest to chemical intuition choice for a basis set is when a molecular orbital is represented as a linear combination of atomic orbitals, AOs (1s, 2s, 2p,...), in the LCAO-MO approach. The atomic orbitals can be quite good approximated with Slater functions (also called Slater-type orbitals, STOs):

$$\psi_{nlm}^{\mathrm{STO}}(r,\theta,\varphi) \propto r^{n-1}\exp(-\zeta r)Y_l^m(\theta,\varphi) \ ,$$

where $Y_l^m(\theta,\varphi)$ are called spherical harmonics and the parameter zeta ζ varies with the chemical nature of the atom and the atomic orbital. Such functions properly describe the radial shape of the atomic wavefunctions. However, due to the exponential factor calculations employing basis sets consisting of STOs are computationally challenging. A way to overcome this problem is to replace the $\exp(-r)$ dependence of the STOs with the $\exp(-r^2)$ dependence of Gaussian functions (Gaussian type orbitals, GTOs):

$$\psi_{nlm}^{\mathrm{GTO}}(r,\theta,\varphi,\alpha) \propto r^{n-1}\exp(-\alpha r^2)Y_l^m(\theta,\varphi)$$

On the other hand, as Gaussian functions do not have proper radial shape in the vicinity of the nucleus, a compromise between the two types of orbitals is made in the following way. A STO is represented by a *contracted* Gaussian function that is a linear combination of *primitive* Gaussian functions g_i:

$$\psi_j^{\mathrm{GTO}} = \sum_{i=1}^{M} d_{ij} g_i(r, \theta, \varphi, \alpha_i) \qquad \textbf{(III.1)}$$

where d_{ij} are called contraction coefficents and M is the number of the primitive Gaussians that approximate the GTO. Each molecular orbital then is represented as a linear combination of n contracted GTOs:

$$\psi_i^{\mathrm{MO}} = \sum_{j=1}^{n} c_{ij} \psi_j^{\mathrm{GTO}} = \sum_{j=1}^{n} c_{ij} \sum_{i=1}^{M} d_{ij} g_i(r, \theta, \varphi, \alpha_i) \qquad \textbf{(III.2)}$$

As the number of the primitive Gaussians is increased, the radial behavior of the GTO is better approximated. The exponents and the coefficients for the contracted functions are optimized in a variational procedure using a test set of atoms and molecules.

The described scheme is known as a *single-zeta* or *minimal* basis set since one STO corresponds to each AO. A further improvement of the basis set is its *decontraction* in which each atomic orbital is represented by two or more STOs, each one of these being represented by a suitable linear combination of Gaussian primitives. This allows for a more accurate description of the electron density for an atom within a molecule. Such sets are known as *double-zeta* basis sets (each AO is represented by two STOs basis functions, differing in their zeta values, *triple-zeta* basis sets (each AO is represented by three GTOs) and so on. Multiple-zeta basis sets are usually used only for calculations on valence orbitals, since these can be significantly influenced by chemical bonding and a more flexible basis set is needed for their adequate representation. On the other hand, inner-shell orbitals are generally approximated by single-zeta basis sets. The result from the different mathematical treatment of the inner-shell and valence-shell orbitals is what is called a *split-valence* basis set.

Drawbacks of finite basis sets

The true (exact) molecular wavefunction is a linear combination of an infinite basis set, however the basis sets employed in *ab initio* calculations are always finite. This leads to the so called **basis set truncation error** in the calculation that depends on the par-

ticular choice of the basis set for the system under study. For the HF (SCF) procedure (Section *III.1.2.*) this error is the difference between the HF limit and the energy, calculated with the chosen basis set for a particular HF SCF calculation. Truncation errors can be reduced with the use of large basis sets, although this usually increases the complexity of the calculations and therefore the time needed for their accomplishment.

Another source of inaccuracy may be the **basis set superposition error (BSSE)**. It arises when performing *ab initio* calculations on a weakly bound molecular complex $A \cdot B$ and its separated constituents A and B. BSSE leads to a non-physical lowering of the energy of the dissociated complex compared to that of the separated partners A and B. The reason for the BSSE is again that the basis functions do not form an infinite set and as a consequence there are more basis functions available for the calculation of the complex than for either of the monomers. This can be overcome with an approach called **counterpoise (CP) correction**. It uses the additional employment of the basis functions for the B partner (called in this case sometimes *ghost functions*) in the calculation of A partner.

III.1.2. Hartree-Fock (self-consistent field, SCF) method

The task of solving the Schrödinger equation is simplest when a complete neglect of the electron correlation is employed. In this case the N-electron wavefunction of a given state is represented as a product of N one-electron wavefunctions (orbitals) called Hartree-product: $\Psi_{HP} = \psi_1 \psi_2 \psi_3 ... \psi_N$. The total many-electron Hamiltonian is a sum of N non-interacting individual one-electron Hamiltonians; the total electronic energy is a sum of the individual energies associated with each orbital: $E = \varepsilon_1 + \varepsilon_2 + \varepsilon_3 + ... \varepsilon_N$. However, the non-interacting Hamiltonian and the Hartree-product wavefunction are quite poor approximations, because they do not account for any electron correlation. A better approach is to account for the electron spin and the antisymmetry of the electronic wavefunction, introducing the so called Slater determinant which has the following compact form:

$$\Psi_{SD} = (N!)^{-\frac{1}{2}} \det \left| \phi_1 \phi_2 \phi_3 ... \phi_N \right| \equiv (N!)^{-\frac{1}{2}} | \phi_1 \phi_2 \phi_3 ... \phi_N \rangle \qquad \textbf{(III.3)}$$

The individual one-electron wavefunctions ϕ_i are called spin-orbitals and each is a product of the corresponding orbital wavefunction ψ_i and spin function (the latter is designnated as α or β). The main concept of the Hartree-Fock (HF) method is to find a wave-

function Ψ_{HF} in the form of a single Slater determinant (Eq. **(III.3)**), which when acted upon with $\hat{H}$, gives the needed energy of the system E_{HF}. Three formalisms are developed within the SCF procedure: restricted close-shell HF (all orbitals are doubly occupied i.e. all spins are paired), restricted open-shell HF (only close-shell orbitals are doubly occupied), and unrestricted HF (electrons are not constrained to doubly occupy orbitals). Here only a discussion of the restricted HF (RHF) method follows. The principal assumption of the HF technique is that each electron "senses" all other electrons not as individuals but as average field acting upon it. The determinant consists of N one-electron **occupied** spatial orbitals that are calculated by expanding them over a basis set $\{\chi_1, \chi_2, \cdots \chi_n\}$[6]:

$$\psi_i = \sum_{j=1}^{n} c_{ij}\chi_j \qquad \textbf{(III.4)}$$

The task is to find the expansion coefficients c_{ij}, which can be done by solving a set of equations known as Roothaan equations $\mathbf{Fc} = \mathbf{S\varepsilon}$ that have a non-trivial solution only if:

$$\det\left|\mathbf{F} - \varepsilon_a\mathbf{S}\right| = 0 \qquad \textbf{(III.5)}$$

Here $\mathbf{F}$ is the so called Fock matrix composed of one-electron Fock operators and $\mathbf{S}$ is a matrix composed of overlap integrals: $S_{\mu\nu} = \langle\chi_\mu \mid \chi_\nu\rangle$, ε_a is the energy of the a occupied orbital. The explicit form of $F_{\mu\nu}$ includes two-electron integrals and the so called **density matrix** defined as

$$P_{\lambda\sigma} = 2\sum_{i}^{occupied} c_{\lambda i}c_{\sigma i} \qquad \textbf{(III.6)}$$

The density matrix describes the degree to which each basis function χ_j contributes to the total (many-electron) wavefunction and also determines how energetically important the Coulomb and exchange integrals are [115]. Equation **(III.5)** is solved in a numerical iteration procedure for finding the variational coefficients $c_{\lambda i}$ and $c_{\sigma i}$ (that is the density matrix $P_{\lambda\sigma}$) and subsequently ψ_i. The iteration starts with a choice of molecular geometry and a set of guess coefficients and continues until the output density matrix is sufficiently similar to the input one[7] and the molecular geometry is optimized (if required). The variational nature of the HF method implies that the calculated energy is an upper

---

[6] **An approach suggested by C.C.J. Roothaan and G.G. Hall in 1951**

[7] **When machine accuracy is obtained and within the mathematical and physical approximations**

bound to the true one. If *an infinite basis set* is used, the best (that is the lowest) value that can be obtained with the HF approach (neglect of the electron correlation) is called *Hartree-Fock* limit. The difference between the calculated energy when the HF limit is reached and the "true" energy E defines the **correlation energy**:

$$E_{corr} = E - E_{\text{HF limit}} \qquad\qquad \textbf{(III.7)}$$

The main drawback of the HF method is the neglect of electron correlation (except for exchange effects). This leads to large inaccuracies when modeling processes involving a change in the number of paired electrons or the nature of chemical bonds. Certain exceptions do exist when the incompleteness of the basis set compensates for the neglect of electron correlation as is often the case with the polarized double-zeta basis sets [115].

III.1.3. Correlated ab initio methods

Various post-HF methods have been developed to account for the electron correlation and to recover as much as possible of the correlation energy (apart from that included in the HF method due to the electron exchange). The principal idea of such techniques is to modify Ψ_{HF} in such a way, that the energy E_{HF} is minimized. Electron correlation is accounted for by introducing additional determinants describing single, double and higher excitations to virtual (unoccupied) spinorbitals from the N occupied spinorbitals.

a) Configuration interaction (CI) *ab initio* methods

Configuration interaction is present in all many-electron systems and consists of contributions from higher excited electronic configurations to the wavefunction of a lower electronic state. In CI *ab initio* calculations the electronic wavefunction of a state a is represented as a linear combination of many-electron determinants:

$$\Psi_a = \sum_{I=0} C_{Ia} \Phi_I \qquad\qquad \textbf{(III.8)}$$

where Φ_0 is usually the HF wavefunction for the ground state, Φ_1 represents all singly excited (with respect to Φ_0) determinants, Φ_2 – all doubly excited determinants and so on. An I-excited determinant Φ_I called also *configuration state function* (CFS) is

formed from Φ_0 with the replacement of I occupied spinorbitals with virtual (unoccupied, vacant) spin-orbitals. It is often the case that the HF wavefunction dominates in the expansion **(III.8)**. The electron correlation is thus considered to be described by a sum of small individual contributions from several excited determinants to the wavefunction rather by a single large contribution from one excited determinant. Correlated methods then are based on using the HF wavefunction as reference (*single reference*). However, Ψ may also have a *multireference* character, i.e. several other determinants in addition to Φ_0 may have significant individual contributions (i.e. the coefficients C_{Ia} are large). In this case a multireference function should be used. The coefficients in **(III.8)** can be found by solving the secular equation $\det\left|H_{ij} - ES_{ij}\right| = 0$ for the energy E. Here $H_{ij} = \langle \Phi_i \mid \hat{H} \mid \Phi_j \rangle$ and $S_{ij} = \langle \Phi_i \mid \Phi_j \rangle$. CI is a variational method, i.e. the found energy is an **upper bound** to the true value. The following CI methods have been developed: **Full CI and Limited CI methods** (*CI-singles (CIS), CI-doubles (CID), CI-singles-doubles (CISD)), Multiconfiguration SCF (MSCF)* and *Multireference CI (MRCI))*.

b) Møller - Plesset (MP) perturbation theory

Møller and Plesset (1934) [116] suggested a method for including the electron correlation using the Rayleigh-Schrödinger perturbation theory. The true many-electron Hamiltonian of a system is represented as $\hat{H} = \hat{H}^{(0)} + \lambda\hat{V}$, where $\hat{H}^{(0)}$ is the sum of the one-electron Fock operators and the perturbation $\hat{V}$ is chosen in such a way that it corrects for the double counting of elelctron-elelectron repulsion terms when the energy of the system is calculated by acting with $\hat{H}^{(0)}$ on Ψ_{HF}. As the reference function here is one determinant, namely Ψ_{HF} (that is $\Psi^{(0)} = \Psi_{\mathrm{HF}}$) this model is also known similarly to the CI method as single reference. Another possibility (not described here) is to use a MCSCF wavefunction (multireference). The general form of the theory is MPn, where n is the order at which the expansion of $\Psi = \sum_{k=0} \lambda^k \Psi^{(k)}$ and $E = \sum_{k=0} \lambda^k E^{(k)}$ is truncated.

It can be shown [113, 115] that MP1 level of calculations does not provide corrections beyond the HF approach. At MP2 level, the energy is:

$$E_{\mathrm{MP2}} = E^{(0)} + E^{(1)} + E^{(2)} \tag{III.9}$$

The chief drawback of MPn is that it is not a variational method; i.e. the calculated energy is not an upper bound to the true one. The method overestimates the energy

(instead of underestimating it), but it may happen that this inaccuracy is partly compensated for by the introduced underestimation by the finite basis sets. The MPn approach can yield correct results only when the perturbation $\hat{V}$ is small.

c) Coupled cluster method

The main concept of this approach is that the full CI electronic wavefunction can be written in the form (in the case of single reference):

$$\Psi = e^{\hat{T}}\Psi_{\text{HF}} \tag{III.10}$$

where the operator with the introduction of the cluster operator $\hat{T} = \sum_{k=1}^{N}\hat{T}_k$, where N is the number of electrons. Each operator $\hat{T}_k$ generates all determinants containing k excitations. Usually the summation is truncated after the second term, thus only singly and doubly excitation operators are considered:

$$\hat{T}_1 = \sum_{i}^{\text{occ.}}\sum_{a}^{\text{virt.}} t_i^a \Psi_i^a, \quad \hat{T}_2 = \sum_{i<j}^{\text{occ.}}\sum_{a<b}^{\text{virt.}} t_{ij}^{ab}\Psi_{ij}^{ab} \tag{III.11}$$

where i and j count all occupied orbitals; a and b – all virtual ones. If the exponential function is expanded in Taylor series, it can be seen that the electronic wavefunction contains terms associated with multiple excitations. This stems from the appearance of products of cluster operators in the expansion of Ψ. The exponential form of Ψ in Eq. **(III.10)** thus ensures size-consistency through the algebraic generation of triple, quadruple, and higher excitations. The task is to find the coefficients in Eq. **(III.11)** and then to determine the energy within the particular truncation level of calculation. Some of the most widely used CC methods are:

CCD (doubles) – only $\hat{T}_2$ is considered in the expansion **(III.10)**.
CCSD (singles and doubles) – only $\hat{T}_1$ and $\hat{T}_2$ are included. *CCSDT* – a computationally costly method, that employs $\hat{T}_1, \hat{T}_2$, and $\hat{T}_3$ operators. Here triple excitations appear uniquely, not as products of $\hat{T}_1$ and $\hat{T}_2$.
CCSD(T) – an approach which similarly to CCSD includes only operators associated with single and double excitations but additionally estimates the influence of triple excitations by the means of perturbation theory.

III.2. Density Functional Theory (DFT)

The Density functional theory is an alternative to the *ab initio* calculations based on the Hartree-Fock method as described above. The principles of the method were firmly established with the emergence of the two Hohenberg-Kohn theorems [117]. The first theorem states that the ground-state energy E_0, the wavefunction and all molecular properties are uniquely determined by electron probability density that depends on only three (instead of $3N$ for the N electrons) spatial coordinates: $\rho\,(x, y, z)$. According to the second theorem the energy can be expressed as a functional $E\big[\rho(x, y, z)\big]$ that is minimized by the ground-state electron density ρ_0. This means that for any "trial" probability density ρ_{tr} the following relation for the ground-state energy holds:

$$E_0 = E_0\Big[\rho_0(x, y, z)\Big] \leq E_{tr}\Big[\rho_{tr}(x, y, z)\Big] \tag{III.12}$$

The task of the DFT method is to calculate the ground-state electron density in a variational manner. It should be kept in mind that such calculations are only valid for electron densities for which the associated Schrödinger equation yields an antisymmetric wavefunction. Such electron densities are called *v*-representable [118]. The Hohenberg-Kohn theorems however tell nothing about the form of the functional; it is only proved that such a functional exists. Kohn and Sham [119] derived a set of one-electron equations from which theoretically the electron probability density could be obtained.

DFT is a reliable and relatively inexpensive method in terms of computational cost. It is extensively used in calculations on large molecular systems. Some modifications of DFT known as hybrid methods use the electron exchange described in the HF theory. The resulting hybrid exchange-correlation functional is then a linear combination of the HF exchange functional and other correlation density functionals (e.g. E_c^{LDA}, the local density approximation functional [120]). Several functional have been proposed for performing DFT calculations and one of the most widely used hybrid functionals is B3LYP [121].
Although suitable for molecular systems, most functionals however fail to describe properly intermolecular interactions, in particular dispersion and charge transfer excitations. A great progress in this regard has been made with the introduction of the M05, M05−2X, M06, and M06-2X Exchange-Correlation Functionals [122-124].

III.3. Geometry optimization

Ab initio and DFT calculations are often accompanied by optimization of the molecular geometry. Such procedures are of great importance for structural chemistry and are based on the calculation of the derivatives of the potential energy with the respect to the nuclear coordinates. The equilibrium molecular geometry can be found numerically by finding the potential energy at several geometries and exploring the change in energy as each coordinate is varied. For the simplest case of diatomic molecules this means that one has to find the minimum of the function $E(R)$ where R is the internuclear distance. In the general case of polyatomic molecules the problem is aggravated by the multidimensional form of the potential energy surface (PES). In such cases calculating the energy derivatives *analytically* with respect to all nuclear coordinates by the implementation of **gradient methods** is more accurate and computationally less expensive. Analytical first and second energy derivatives are available for various *ab initio* levels of calculation. The equilibrium structure is determined by the condition that the derivatives of the energy with respect to each nuclear coordinate are zero (within some accuracy criteria set beforehand). The nature of the extremum (whether it is a minimum, maximum, or a first-order saddle point) is determined by constructing the so called **Hessian matrix** and finding its eigenvalues. The Hessian matrix consists of the second derivatives of the energy with respect to the nuclear coordinates. A minimum of the PES corresponds to all eigenvalues being positive. In addition one may be interested to find not only the local minima corresponding to different conformers, but also the global minimum that corresponds to the most stable conformer. This is not a trivial task and algorithms for global optimization are yet to be developed.

Energy derivatives are calculated by finding the derivatives of the coefficients and the functions in the basis set expansion with respect to the nuclear coordinates. For the coefficients such a task can be accomplished by solving the *coupled perturbed Hartree-Fock equations* (CPHF) for single-reference methods or the *coupled perturbed MCSCF equations* for multireference methods. On the other hand, the derivatives of Gaussian-type orbitals used as basis functions are again GTOs. In addition, symmetry considerations can significantly alleviate the problem of calculating the derivatives of the basis functions (more precisely of the four-index integrals appearing in the secular equations).

CHAPTER IV

Interaction of molecules and molecular complexes with radiation

The interaction of atoms, molecules and molecular complexes with electromagnetic radiation gives rise to a variety of processes and can aid the study of molecular structure and geometry as well as macroscopic properties such as permittivities, refractive indices, lasing, and optical activity. When excited to higher energy levels, molecules relax to their ground electronic states in two ways – via radiative and nonradiative transitions. The former include absorption, emission, elastic (Rayleigh) scattering, and inelastic (Raman) scattering, while the latter refer to processes like vibrational relaxation, internal conversion, and intersystem crossing. Inelastic scattering arises from the induction of electric dipole moment in molecules by the electro-magnetic field (polarizability of the molecule). The spectra due to such transitions feature the so called Stokes and anti-Stokes components of the scattered light, with frequencies lower and higher than that of the incident light, respectively (in addition to the Rayleigh or elastic component). Also, excited molecules or noncovalently bound molecular and atomic complexes can under certain conditions undergo processes like dissociation, predissociation, or autoionization.

In contrast to atomic spectra which arise only from electronic transitions, the spectra of molecules[8] are additionally complicated and essentially enriched in terms of information and structure due to the molecular rotational and vibrational motion. The resulting spectra fall in different energy regions of the electromagnetic radiation ranging from microwave to ultraviolet. Additional complexity arises from the simultaneous stimulations of rotational and vibrational modes in combination with electronic excitations. Accordingly, a transition is defined as rotational – vibrational – electronic (rovibronic).
The information derived from various molecular spectra aids the study of important characteristics of molecules. Rotational spectra aid the study of moments of inertia, shapes, and bond lengths (both intra– and intermolecular), while vibrational spectra provide information about the strength and stiffness of a molecular bond.

---

[8] As in Chapter II the terms „molecules" and "molecular" here refer both to chemical species and to complexes, formed by noncovalent interactions.

IV.1. Electric dipole transitions

IV.1.1. Transition dipole moment and resonance condition

The interaction of molecules with electromagnetic radiation can be in most cases described by interaction of their electric dipole moment μ with the electric component of the incident radiation $\mathbf{E}$ (this assumption is often referred to as *electric dipole approximation*). In the semiclassical theory of matter-radiation interactions, radiation is treated as an electromagnetic wave. If the interaction is sufficiently weak, it can be introduced as a perturbation to the unperturbed molecular Hamiltonian $\hat{H}^0$:

$$\hat{H} = \hat{H}^{(0)} + \hat{H}^{(1)} = \hat{H}^{(0)} - \mu.\mathbf{E}_0 \cos \omega t \qquad \textbf{(IV.1)}$$

where ω is the frequency of the oscillating electric field. The nature of transitions implies that $\hat{H}$ must satisfy the time-dependent Schrödinger equation:

$$\hat{H}\Psi = i\hbar \frac{\partial \Psi}{\partial t} \qquad \textbf{(IV.2)}$$

Here $\hat{H}$ is the Hamiltonian of the joined system molecule – electromagnetic field. If we assume that the perturbation couples a lower state n and an upper state m in the molecule, the wavefunction in Eq. **(IV.2)** can be written in the form $\Psi(t) = c_n(t)\Psi_n(t) + c_m(t)\Psi_m(t)$. The coefficient $c_m(t)$ is given by the expression:

$$c_m(t) \propto \ -\frac{i}{\hbar} \int_0^t e^{i\omega_{mn}} \mu_{nm} dt \qquad \textbf{(IV.3)}$$

where $\mu_{mn} = \langle \Psi_m^{(0)} \,|\, \mu \,|\, \Psi_n^{(0)} \rangle$ is the *transition dipole moment* between states n and m and $\omega_{mn} = (E_m - E_n)/\hbar$ is the frequency of the transition. Here E_m and E_n are the energies of state m and n, respectively. The population of the upper state m is given by:

$$c_m^*(t)c_m(t) \propto \frac{\sin^2\left[\left(E_m - E_n - \hbar\omega\right)t\,/\,2\hbar\right]}{\left(E_m - E_n - \hbar\omega\right)^2} \qquad \textbf{(IV.4)}$$

which defines the resonance *condition* for an allowed transition:

$$E_m - E_n = \hbar\omega \qquad \textbf{(IV.5)}$$

Electric dipole transitions are not the only types of transitions that may occur. Perturbations arising from the effect of the magnetic component of the electromagnetic field can induce magnetic dipole transitions. Such transitions are typically 10^5 times weaker than the allowed electric dipole transitions and obey different selection rules. Another type of transition is an electric quadrupole transition in which the spatial variation of the electric field interacts with the electric quadrupole moment operator. Such transitions are 10^8 times weaker than electric dipole transitions. The small intensity of magnetic dipole and electric quadrupole transitions stems from the fact that both depend on the variation of the electromagnetic wave over the extent of the atom or molecule. As these diameters are often smaller than typical wavelengths of radiation, this variation is usually very small and the intensity is correspondingly weak.

IV.1.2. Allowed radiative transitions

As in atoms, the absorption and emission of radiation in molecules obey given selection rules. Although even the spectra of diatomic molecules are much more complex than the atomic spectra, some general considerations can be outlined.

Unlike atoms, for molecules one should take into account the symmetry properties of a molecule or a chromophore to find out whether a transition is allowed or not (considerations aided by the group theory). Also, unlike the case for atoms, the constraints on a transition arising from the definition of μ_{mn} for molecules (in particular polyatomic molecules) can become less rigorous if vibronic or rotational-electronic interactions come into play. Allowed radiational transitions are said are said to couple to the electromagnetic field.

The necessary conditions for an allowed electric dipole transition can be generalized in the following way:

- A transition is allowed if the *resonance condition* **(IV.5)** is met.
- The molecule must posses a nonzero transition dipole moment. For vibrational transitions this quantity must also change during the change of the internuclear distance.
- Pure vibrational transitions within the harmonic oscillator approximation are allowed only if the quantum number for the *i*-th vibration changes by 1:

$v''_i - v'_i \equiv \Delta v_i = \pm 1$. This condition follows from the vibration-al wavefunctions [113].

–   The integrand $\Psi_m^{(0)*}\mathbf{\mu}\Psi_n^{(0)}$ for a non-zero μ_{mn} must be invariant to the symmetry operations of the molecular point group. The selection rules must be expressed in terms of the point group of the whole molecule (in small molecules) or the localized group of atoms (chromophore) in large molecules. It has to be however kept in mind that quite often a molecule has different symmetry in the initial electronic and the excited electronic state which eases the symmetry restrictions on a transition. In this case only the common elements of symmetry must be accounted for and the product $\Psi_m^{(0)*}\mathbf{\mu}\Psi_n^{(0)}$ should be examined under the smaller restrictions, imposed by the lower symmetry. A forbidden transition may also acquire intensity because of the departure from the assumed pointed group symmetry as a result of the presence of substituents. For vibrational transitions a normal mode must belong to the same symmetry species as at least one of the components of the electric dipole moment.

–   For small spin-orbit interactions the electronic wavefunction can be factorized in a pure orbital and pure spin part (the latter is totally symmetric to any symmetry operations carried on the molecule). In this case only states of the same multiplicity can be combined, that is $\Delta S = 0$.

IV.2. Interactions

The allowed or forbidden character of the radiational transitions in molecules is often valid only within the model of a simplified molecular Hamiltonian. This simplification neglects various interactions between states, motions (rotational, vibrational, and electronic) as well as higher terms in the Taylor expansion of potential energy (as is the case for example for the harmonic oscillator approximation). There are generally two types of interactions between states to be considered: *i)* mixing of states belonging to a particular motion and *ii)* coupling between states belonging to different motions. Both can contribute to an additional complexity in the molecular spectra and depending on their strength may be or may be not neglected as perturbations in the Hamiltonian. These interactions may remove the degeneracy of energy states and may also lead to breakdown cases of the BO approximation.

Interactions between different motions include: *vibrational-rotational* interaction (centrifugal distortion, coriolis interaction); *electronic-rotational* interaction, that may lead to the so called Λ-doubling (for states with angular momentum $\boldsymbol{\Lambda} \neq 0$) in diatomic and linear molecules; *vibrational-electronic (vibronic)* interaction, and *rotational-vibrational-electronic (rovibronic)* interaction.

As interactions of states belonging to the same motion two general types can be pointed out: *i) vibrational-vibrational mixing* known as Fermi resonance and *ii) mixing of electronic states.* In the former case vibrational levels that have similar energies (i.e. are accidentally degenerate) and are of the *same symmetry species* mutually repel each other, which leads to the removal of the degeneracy. Similarly, closely lying electronic states can also mix (*ii*) but the symmetry condition is strictly necessary only for diatomic molecules. In polyatomic molecules such mixing can be brought about on account of vibronic interaction even for electronic states belonging to *different symmetry species*. Such mixings are the vibronic analogues of Fermi resonances and it is now the vibronic species that must be the same $\Gamma(1^{\text{st}}$ el. state$) \times \Gamma($vibration$) = \Gamma(2^{\text{nd}}$ el. state$)$. The mixed electronic states assume mutual properties and this plays an important role in forbidden transitions.

Mixing of states with similar energies and the same symmetry species is essential in the processes like predissociation and autoionization. In this case it is the interaction between the discrete states and the continuum moiety of ionic or dissociative states that is to be accounted for. The processes of predissociation and autoionization are more common for polyatomic than for diatomic molecules because of the greater number of continuous ranges in such molecules.

Anharmonicity

Symmetry arguments alone do not rule out transitions for which $\Delta v_i > 1$. Such transitions can arise on account of anharmonicity terms either in the potential energy (mechanical anharmonicity) or in the dipole moment (electrical anharmonicity). The anharmonicity leads to appearance of additional bands in the infrared spectra of molecules due to overtones and combination bands (summation bands or difference bands).

***

A forbidden transition may acquire intensity also in the cases of *magnetic dipole* and *electric quadrupole* transitions, *strong spin-orbital* interactions (breaking of the $\Delta S = 0$

rule) and therefore states of different multiplicity can combine (e.g. giving rise to singlet-triplet transitions), *rotational-electronic* interactions, and *enforced dipole* transitions. In the latter case forbidden electronic transitions can gain intensity in the presence of external electric fields [125].

IV.3. Vibronic transitions

The complexity of the spectra of polyatomic molecules is partly due to the fact that many electronic transitions forbidden by symmetry considerations may be *vibronically allowed*. The description of simultaneous electronic and vibrational transitions is based on the Franck-Condon principle: *Due to the large difference in the masses of the electrons and the nuclei, an electron transition occurs instantaneously compared to the nuclear vibrational motion.* The Franck-Condon principle defines therefore vertical transitions (**Fig.IV.1**) which occur at a stationary nuclear framework. At a negligible difference between the molecular geometries between the two electronic states, the Franck Condon principle correctly predicts that the $S_1 \leftarrow S_0, 0_0^0$ transition[9] has substantial intensity due to the largely enhanced overlap of the wavefunctions of the zero-point vibrational levels in both electronic states (large Franck-Condon factors). However, as can be seen from **Fig. IV.1** for a prominent change in the equilibrium positions of the nuclei upon electronic excitation, the Franck Condon principle may favor a better overlap for wavefunctions referring to different vibrational motions.

The selection rules for vibronic transitions in a molecule-fixed coordinate system (rotations are not considered) are derived from the constraint that

$$\mu_{(ev)mn} = \langle \Psi_{(ev)m} \mid \mu \mid \Psi_{(ev)n} \rangle \neq 0 \qquad \textbf{(IV.6)}$$
$$\Psi_{(ev)} = \varphi \chi_{vibr}$$

Here $\Psi_{(ev)m}$ and $\Psi_{(ev)n}$ are the wavefunctions characterizing the **vibronic** states m and n, involved in the transition. The above condition means that $\Gamma \Psi_{(ev)m} \times \Gamma \Psi_{(ev)n} \subset \Gamma \mu_{(ev)mn}$ for

---

[9] **In general the statement refers to a transition for which no change in the vibrational motion occurs. In the text it is assumed that a vibronic transition starts at the vibrationless level of the lower electronic state, which is usually but not always the case in molecular spectroscopy.**

at least one component of the transition moment. If the wavefunctions can be factorized in accord with the BO approximation the necessary condition for a non-zero vibronic transition moment **(IV.6)** is fulfilled if separately $\langle \varphi_m \,|\, \mu \,|\, \varphi_n \rangle \neq 0$ and $\langle \chi_m \,|\, \chi_n \rangle \neq 0$. The latter statement means that the product of the symmetry species of the vibrational functions of the two electronic states must be totally symmetric.
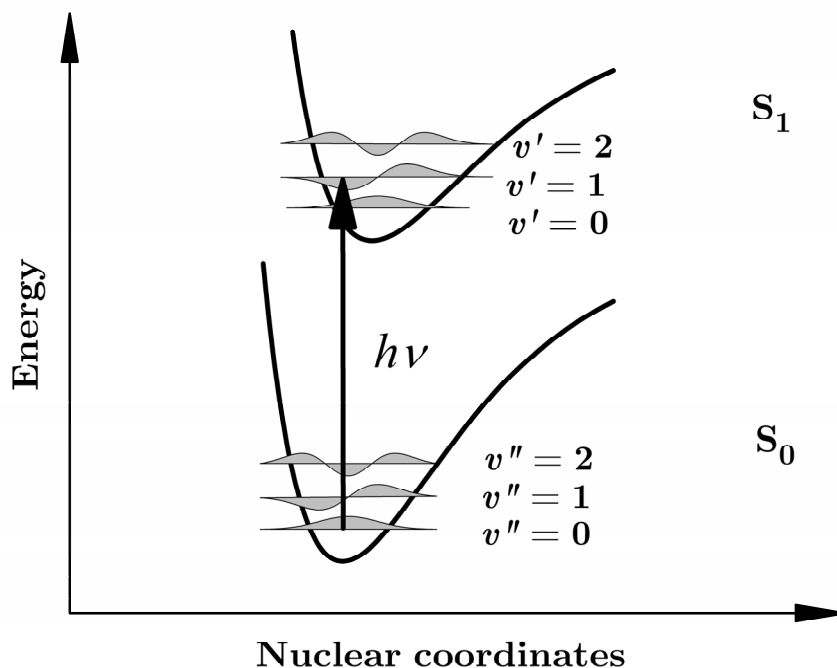
Fig.IV.1. A vertical transition occurring in accord with the Franck-Condon principle between the respective vibrational levels of two electronic states.

The product $\langle \chi_m \,|\, \chi_n \rangle$ is known as a Franck-Condon factor and mathematically describes the overlap of the wave-functions of the respective vibrational levels participating in the vibronic transition.

Even if the BO-approximation breaks down and a representation $\Psi_{(ev)} = \varphi \chi_{vibr}$ is not valid, the symmetry species of the Ψ_{ev} can be still derived from the product $\Psi_e \Psi_v$. The imposed symmetry restraints lead to the following conclusions:

    i)   If an electronic transition is allowed, then it is allowed for all totally symmetric vibrational levels.

ii)   If an electronically transition is forbidden, it can be allowed for particular antisymmetric or degenerate vibrational levels. This is valid not only for forbidden transitions but also for forbidden components of an allowed electronic transition. The above statement shows a main difference between polyatomic and diatomic molecules where there is only one vibration, the totally symmetric stretching mode.

iii)   For degenerate electronic states (e.g. Π states in linear molecules or E states in non-linear molecules) if the vibronic interaction is strong one must consider the Renner-Teller (linear molecules) and the Jahn-Teller (non-linear molecules) effects and it may turn out that transitions to some vibronic members of the splittings are symmetry allowed.

<div align="center">***</div>

Chromophores

The spectra of large polyatomic molecules may often be interpreted not in terms of the whole molecule but of small groups of atoms within the molecule. Such groups are called chromophores and they are characterized by rovibronic transitions typical for a given chromophore. Some examples for chromophores are the carbonyl and the nitro groups as well as larger species like benzene in many organic compounds and indole (e.g. in proteins as the building block of the amino acid *tryptophan*). Chromophores may experience perturbations by other groups, e.g. substituents that can alter their spectroscopic properties through inductive or mesomeric effects.

Bibliography to Part I

1.   For a review, see e.g. D.L. Andrews, *Lasers in Chemistry*. 1997, Berlin: Springer.

2.   G. Petty, C. Tai, and F.W. Dalby, Phys. Rev. Lett., 1975. **34**: p. 1207.

3.   P.M. Johnson and C.E. Otis, Ann. Rev. Phys. Chem., 1981. **32**: p. 139.

4.   G. Scoles, *Atomic and molecular beam methods*. 1988, New York: Oxford University Press.

5.   H.J. Neusser and R. Sussmann, *Structure of weakly bound complexes from electronic spectra*. Jet spectroscopy and molecular dynamics, ed. J.M. Hollas and D. Phillips. 1994, London: Chapman and Hall.

6.   R.E. Smalley, L. Wharton, D.H. Levy, and D.W. Chandler, J. Mol. Spectrosc., 1977. **66**: p. 375.

7.   N.F. Ramsey, *Molecular Beams*. International Series of Monographs on Physics, ed. R.J. Elliot, et al. 1985, New York: Oxford University Press.

8.   D.H. Levy, Ann. Rev. Phys. Chem., 1980. **31**: p. 197.

9.   K. Müller-Dethlefs and P. Hobza, Chem. Rev., 2000. **100**: p. 143.

10.   J. Cerny and P. Hobza, Phys. Chem. Chem. Phys., 2007. **9**: p. 5291.

11.   J.D. van der Waals, *Doctoral Dissertation*. 1873, Leiden.

12.   K. Müller-Dethlefs, M. Sander, and E.W. Schlag, Chem. Phys. Lett., 1984. **112**: p. 291.

13.   L. Zhu and P.M. Johnson, J. Chem. Phys., 1991. **94**(8): p. 5769.

14.   H. Krause and H.J. Neusser, J. Chem. Phys., 1992. **97**(8): p. 5923.

15.   K.M. Weitzel, M. Malow, G.K. Jarvis, T. Baer, Y. Song, and C.Y. Ng, J. Chem. Phys., 1999. **111**: p. 8267.

16.   G.K. Jarvis, K.M. Weitzel, M. Malow, T. Baer, Y. Song, and C.Y. Ng, Rev. Sci. Instr., 1999. **70**: p. 3892.

17.   I.G. Kaplan, *Intermolecular Interactions: Physical Picture, Computational Methods and Model Potentials*. 2006 John Wiley & Sons Inc.

18.   M. Born and R. Oppenheimer, Ann. Physik, 1927. **84**: p. 457.

19.   M. Born, Nachr. Acad. Wiss. Math. Nat. , 1951. **Kl. 1**

20.   M. Born and K. Huang, *Dynamical Theory of Crystal Lattice*. 1956, London: Oxford University Press.

21.   N.F. Mott and H.S.W. Massey, *The Theory of Atomic Collisions*. 1965, Oxford Clarendon Press.

22.   J.B. Hasted, *Physics of Atomic Collisions*. 1964, London Butterworths.

23.   G. Herzberg, *Molecular spectra and molecular structure, III. Electronic spectra and electronic structure of polyatomic molecules*. Vol. III. 1991, Malabar: Krieger Publishing Company. p. 555.

24.   W. Heitler and F. London, Z. Physik, 1927. **44**: p. 455.

25.   W. Heitler and G. Rumer, Z. Physik, 1931. **68**: p. 12.

26.   W. Heitler, Phys. Rev. , 1931. **38**: p. 243.

27.   J.E. Lennard-Jones, Trans.Faraday Soc. , 1929. **25**: p. 668.

28.   C. Coulson, A. , *Valence*. 1952, Oxford Clarendon Press.

29.   R. Mulliken, *Spectroscopy, Molecular Orbitals, and Chemical Bonding* , Nobel Lecture, 1966.

30.   I. Hargittai and M. Hargittai, *Symmetry through the Eyes of a Chemist*. 1987, New York: VCH Publishers, Inc.

31.   D.A. McQuarrie and J.D. Simon, *Physical Chemistry: A Molecular Approach*. 2005, New Delhi: Vinod Vasishtha for Viva Books Private Limited.

32.   E. Hückel, Zeitschrift für Physik, 70, 204, (1931); 72, 310, (1931); 76, 628 (1932); 83, 632, (1933).

33.   R. Eisenschitz and F. London, Z. Physik, 1930. **60**: p. 491.

34.   F. London, Z. Phys., 1930. **63**: p. 245.

35.   W. Kauzmann, Adv. Prot. Chem., 1959. **14**: p. 1-63.

36.   G. Nèmethy and H.A. Scheraga, J. Phys. Chem., 1962. **66**: p. 1773.

37.   D.L. Beveridge, G. Ravishanker, and M. Mezei, *Structure and Dynamics: Nucleic Acids and Proteins*, ed. E. Clementi and R.H. Sarma. 1983, New York: Adenine Press.

38.   P. Backx and S. Goldman, Chemical Physics Letters, 1985. **113**(6): p. 578.

39.   D. Chandler, Nature, 2005. **437**: p. 640.

40.   J.E. Lennard-Jones, Proc. Roy. Soc., 1924. **A106**: p. 463.

41.   E.A. Mason and J. Homer W. Schamp, Annals of Physics, 1958. **4** (3): p. 233.

42.   R.A. Buckingham, Proc. Roy. Soc., 1938. **A168**: p. 378.

43.   W.H. Stockmayer, J. Chem. Phys., 1941. **9**: p. 398.

44.   W.N. Keesom, Comm. Phys. Lab. Leiden, , 1912. **Suppl. 246**(Section 6).

45.   J.O. Hirschfelder, C.F. Curtiss, and R.B. Bird, 1954.

46.   T.S. Moore and T.F. Winmill, J. Chem. Soc. , 1912 **101**: p. 1635.

47.   W.M. Latimer and W.H. Rodebush, J. Am. Chem. Soc., 1920. **42**: p. 1419.

48.   G.R. Desiraju, Accounts of Chemical Research, 2002. **35**(7): p. 565.

49.   S.J. Grabowski, ed. *Hydrogen bonding - new insights (Challenges and Advances in Computational Chemistry and Physics) 1 edition*. 2006, Springer.

50.   W.L. Jorgensen, J. Chandrasekhar, J.D. Madura, R.W. Impey, and M.L. Klein, The Journal of Chemical Physics, 1983. **79**(2): p. 926.

51.   Y. Chen, T. Kortemme, T. Robertson, D. Baker, and G. Varani, Nucl. Acids Res., 2004. **32**(17): p. 5147.

52.   G.A. Jeffrey and W. Saenger, *Hydrogen Bonding in Biological Structures*. 1991, Berlin: Springer.

53.   T. Steiner, Angewandte Chemie International Edition, 2002. **41**(1): p. 48.

54.   G.A. Jeffrey, *An Introduction to Hydrogen Bond*. 1997, New York: Oxford University Press. 320.

55.   G. Aullón, D. Bellamy, A.G. Orpen, L. Brammer, and E.A. Bruton, Chemical Communications, 1998: p. 653.

56.   G.P.A. Yap, A.L. Rheingold, P. Das, and R.H. Crabtree, Inorganic Chemistry, 1995. **34**(13): p. 3474.

57. H. Fu, Z. Zhou, and X. Zhou, Chemical Physics Letters, 2003. **382**(3-4): p. 466-474

58. T. Steiner and G.R. Desiraju, Chem. Commun., 1998: p. 891.

59. S. Djafari, H.-D. Barth, K. Buchhold, and B. Brutschy, J. Chem. Phys., 1997. **107**(24): p. 10573.

60. S. Glasstone, Trans. Faraday Soc., 1937. **33**: p. 200.

61. J.F. Dippy, Chem. Rev., 1939. **25**: p. 151.

62. D.J. Sutor, Nature, 1962. **195**: p. 68.

63. D.J. Sutor, Journal of the Chemical Society 1963: p. 1105.

64. T. Richardson, S. de Gala, R.H. Crabtree, and P.E.M. Siegbahn, Journal of the American Chemical Society, 1995. **117**(51): p. 12875.

65. J. Lee Jr., C., P. Eduardo, A. Rheingold, L., and R. Crabtree, H., J. Am. Chem. Soc., 1994. **116**(24): p. 11014.

66. R. Custelcean and J.E. Jackson, Chemical Reviews, 2001. **101**(7): p. 1963.

67. P.L.A. Popelier, The Journal of Physical Chemistry A, 1998. **102**(10): p. 1873.

68. Y. Meng, Z. Zhou, C. Duan, B. Wang, and Q. Zhong, Journal of Molecular Structure: THEOCHEM, 2005. **713**(1-3): p. 135.

69. D. Payer, A. Comisso, A. Dmitriev, T. Strunskus, N. Lin, C. Wöll, A. DeVita, J. V. Barth, and K. Kern, Chemistry - A European Journal, 2007. **13**: p. 3900.

70. Y.-L. Zhao, M. Meot-Ner, and C. Gonzalez, The Journal of Physical Chemistry A, 2009. **113**(12): p. 2967.

71. S.Y. Hana and H.B. Ohb, Chemical Physics Letters, 2006. **432**(1-3): p. 269.

72. M. Meot-Ner Chemical Reviews, 2005. **105**(1): p. 213.

73. M. Eigen, Angewandte Chemie International Edition in English, 1964. **3**(1): p. 1.

74. S.J. Grabowski, W.A. Sokalski, and J. Leszczynski, The Journal of Physical Chemistry A, 2004. **108**(10): p. 1806.

75. T. Tsurusawa and S. Iwata, The Journal of Chemical Physics, 2000. **112**(13): p. 5705.

76. B.-Q. Wang, Z.-R. Li, X.-Y.H. Di Wu, R.-J. Li, and C.-C. Sun, Chemical Physics Letters, 2003. **375**(1-2): p. 91.

77. L. Pauling, *The Nature of the Chemical Bond*. 1960, Ithaca, New York: Cornell University Press.

78. A.J. Dingley and S. Grzesiek, J. Am. Chem. Soc., 1998. **120**: p. 8293.

79. N.S. Golubev, I.G. Shenderovich, S.N. Smirnov, G.S. Denisov, and H.-H. Limbach, Chem. Eur. J., 1999. **5**: p. 492.

80. E.D. Isaacs, A. Shukla, P.M. Platzman, D.R. Hamann, B. Barbiellini, and C.A. Tulk, Physical Review Letters, 1999. **82**(3): p. 600.

81. T.K. A. V. Morozov, K. Tsemekhman, and D. Baker, Proc. Natl. Acad. Sci. USA 2004. **101** p. 6946.

82. J.J. Novoa, Tarron,B.,Whangbo,M.-W.andWilliams,J., J.Chem.Phys., 1991. **95**: p. 5179.

83. A. Reed, E., L. Curtiss, A., and F. Weinhold, Chem. Rev., 1988. **88**: p. 899.

84. G.T. Trudeau, J.M. Dumas, P. Dupuis, M. Guerin, and C. Sandorfy, Top. Curr. Chem 1980. **93**: p. 91.

85. P. Hobza, V. Špirko, H.L. Selzle, and E.W. Schlag, J. Phys. Chem. A, 1998. **102**(15): p. 2501.

86. P. Hobza and Z. Havlas, Chem. Rev., 2000. **100**: p. 4253.

87. P. Hobza and Z. Havlas, Chemical Physics Letters, 1999. **303**(3-4): p. 447.

88. P. Hobza, V. Spirko, Z. Havlas, K. Buchhold, B. Reimann, H.-D. Barth, and B. Brutschy, Chem. Phys. Lett., 1999. **299**(2): p. 180.

89. B.J. van der Veken, W.A. Herrebout, R. Szostak, D.N. Shchepkin, Z. Havlas, and P. Hobza, Journal of the American Chemical Society, 2001. **123**(49): p. 12290.

90. P. Hobza and Z. Havlas, Theoretical Chemistry Accounts, 2002. **108**(6): p. 325.

91. P. Hobza, Phys. Chem. Chem. Phys. , 2001. **3**: p. 2555.

92. W. Zierkiewicz, D. Michalska, Z. Havlas, and P. Hobza, Chem. Phys. Chem., 2002. **3**(6): p. 511.

93. J. Joseph and E.D. Jemmis, Journal of the American Chemical Society, 2007. **129**(15): p. 4620.

94. R.C. Dougherty, The Journal of Chemical Physics, 1998. **109**(17): p. 7372.

95. J. Emsley, Chem. Soc. Rev., 1980. **9**: p. 91.

96. T. Steiner, Chemical Communications, 1997: p. 727.

97. A.C. Legon and D.J. Millen, Chem. Soc. Rev, 1987. **16**: p. 467.

98. J. Kroon, J.A. Kanters, J.G.C.M. van Duijneveldt-van De Rijdt, F.B. van Duijneveldt, and J.A. Vliegenthart, Journal of Molecular Structure, 1975. **24**(1): p. 109.

99. G.A. Jeffrey and W. Saenger, *Hydrogen Bonding in Biological Structures* 1991, Berlin: Springer, p.20.

100. R. Taylor, O. Kennard, and W. Versichel, Journal of the American Chemical Society, 1984. **106**(1): p. 244.

101. G.A. Jeffrey and H. Maluszynska, International Journal of Biological Macromolecules, 1982. **4**(3): p. 173.

102. G.A. Jeffrey, H. Maluszynska, and J. Mitra, International Journal of Biological Macromolecules, 1985. **7**(6): p. 336.

103. W. Saenger, *Principles of Nucleic Acid Structure*. 1984: Springer-Verlag. 556.

104. G.E. Schulz and R.H. Schirmer, *Principles of protein structure*. 1979, New York: Springer-Verlag. 314

105. L. Pauling, R.B. Corey, and H.R. Branson, Proc. nat. Acad. Sci. USA, 1951. **37**: p. 205.

106. J.D. Watson and F.H.C. Crick, Nature, 1953. **171**: p. 737.

107. A.L. Lehninger, D.L. Nelson, and M.M. Cox, *Principles of Biochemistry, 3rd ed.* 2000, New York: Worth Publishing.

108. K.S. Kim, P. Tarakeshwar, and J.Y. Lee, Chem. Rev., 2000. **100**: p. 4145.

109. S.K. Burley and G.A. Petsko, Science 1985. **229**: p. 23.

110. E.A. Meyer, R.K. Castellano, and F. Diederich, Angew. Chem., Int. , 2003. **42** p. 1210

111. B.H. Hong, J.Y. Lee, C.-W. Lee, J.C. Kim, S.C. Bae, and K.S. Kim, J. Am. Chem. Soc., 2001. **123**: p. 10748.

112. G.R. Desiraju and T. Steiner, *The Weak Hydrogen Bond in Structural Chemistry and Biology*. 1999, New York: Oxford University Press. 480.

113. P.W. Atkins and R.S. Friedman, *Molecular Quanum Mechanics*. First Indian ed. 2004, New Delhi: Oxford University Press, p.345.

114. G. Herzberg, *Molecular Spectra and Molecular Structure, II. Infrared and Raman Spectra of Polyatomic Molecules*. Vol. II. 1991, Malabar: Krieger.

115. C.J. Cramer, *Essentials of Computational Chemistry: Theories and Models*. 2002, New York: John Wiley & Sons, LTD.

116. C. Møller and M.S. Plesset, Phys. Rev., 1934. **40**: p. 618.

117. P. Hohenberg and W. Kohn, Phys. Rev., 1964. **136**(3B): p. 864.

118. R.M. Dreizler and E.K.U. Gross, *Density Functional Theory*. 1990, Berlin: Springer-Verlag.

119. W. Kohn and L.J. Sham, Chem. Rev., 1965. **140**(4A): p. 1133.

120. S.H. Vosko, L. Wilk, and M. Nusair, Can. J. Phys., 1980. **58**(8): p. 1200.

121. C. Lee, W. Yang, and R.G. Parr, Phys. Rev. B, 1988. **37**(2): p. 785.

122. Y. Zhao, N.E. Schultz, and D.G. Truhlar, J. Chem. Phys., 2005. **123**: p. 161103.

123. Y. Zhao, N.E. Schultz, and D.G. Truhlar, Journal of Chemical Theory and Computation, 2006. **2**(2): p. 364.

124. Y. Zhao and D.G. Truhlar, Accounts of Chemical Research, 2008. **41**(2): p. 157.

125. G. Herzberg, *Molecular Spectra and Molecular Structure. Vol. 1. Spectra of Diatomic Molecules. (Reprint ed.w/correction)* 1989, Malabar, Florida: Krieger Publishing Company.

PART II

Mass spectroscopy of
threshold ions

CHAPTER V

Mass spectroscopy apparatus

Mass spectroscopy is an assembly of experimental mass spectrometry techniques that provide data on the spectroscopic properties of the studied species, including their ionization energies and (or) dissociation thresholds. Mass spectrometry employs the ionization of atoms, molecules, and molecular complexes in the gas phase and their subsequent quantitative analysis based on the different mass-to-charge (m/z) ratios of the various species. This allows obtaining chemical and structural information about different constituents in compounds as well as about fragmentation processes.

The present chapter addresses the experimental tools of mass spectroscopy that are relevant to the ionization techniques employed in this work.

V.1. Virtues of lasers as light sources in spectroscopy

As spectroscopic tools, lasers are particularly valuable due to the unique properties of the generated light:

- *Small beam divergence:* This allows for the focusing of the beam on an area comparable to the laser wavelength. Also, the collimated laser beam makes it possible to use long path lengths through samples for increasing the sensitivity of the spectroscopic measurements.

- *Monochromaticity:*   The narrow spectral linewidth of the radiation lends itself to high-resolution spectroscopic studies. It should be kept in mind, however, that such experiments are dependent on the linewidths both of the laser and the atoms or molecules. In addition to the factors determining these linewidths in conventional spectroscopy such as natural line-broadening, collision broadening and Doppler broadening, two other effects have to be considered in laser spectroscopy: the time-of-flight broadening and the saturation broadening have to be considered.

- *Attainable high intensity of the laser light:* The high output intensity of the radiation I_{laser} as well as the possibility for tight focusing facilitate such experiments as multiphoton ionization ($I_{laser} \sim 10^6$ W/cm^2) or fragmentation ($I_{laser} \sim 10^8$ W/cm^2).

In mass spectrometry in particular, laser light excitation and ionization is a preferred method due to the defined time (~ 10 ns) and place (100 μm) of the production of ionized or excited species. This makes appropriate the use of a time-of-flight spectrometer.

V.2. Time-of-flight mass spectrometry

V.2.1. Principle of operation and overall performance

In a time-of-flight (TOF) mass spectrometer the separation of ions is achieved on the basis that ionized species with different m/z ratios obtain different velocities at identical

aceleration conditions and therefore are discriminated on account of their different flight times.
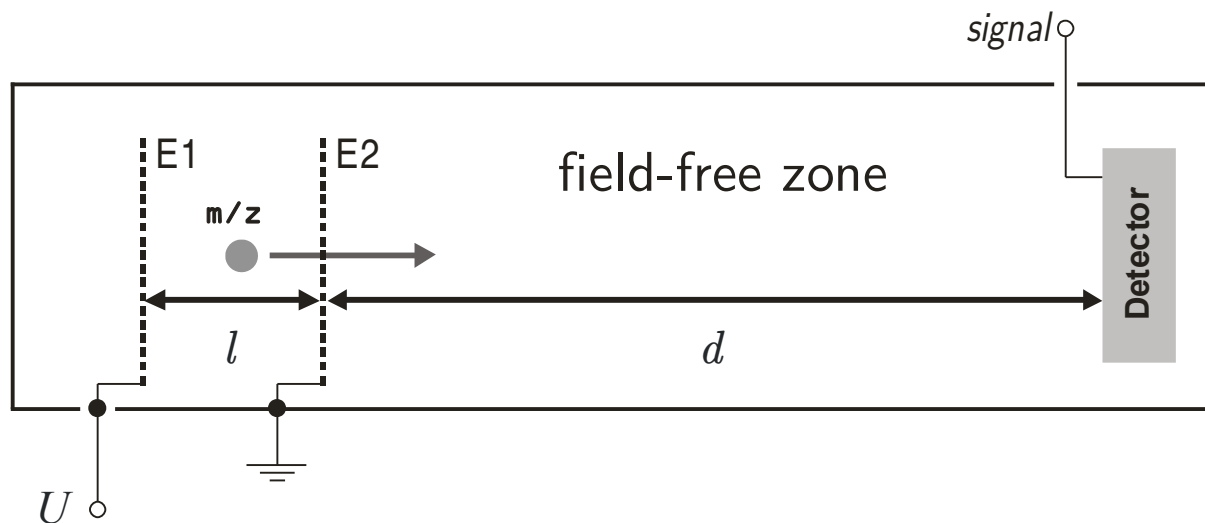

Fig.V.1. A scheme of the basic components of a (linear) TOF spectrometer with a single acceleration stage. An ion with a mass *m* and a charge *z.e* is accelerated by the potential difference *U* between two electrodes E1 and E2 separated at a distance *l.* The flight time of the ion in a field-free (drift) zone with a length *d* is determined according to Eq.**(V.2)**.

The acceleration and the trajectories of the ions are determined by a system of electrodes building the ion optics of the spectrometer. For single charged ions (i.e. $z = 1$) the flight times are proportional to the ion masses.

A schematic drawing of a TOF spectrometer is shown in **Fig.V.1**. The kinetic energy of an ion with charge *ze* (*e* is the elementary charge) and mass *m* accelerated in an electric field with a potential difference *U* is given by:

$$E_{kin} = zeU = \frac{1}{2}mv^2 \tag{V.1}$$

Here *v* is the velocity of the ion at the end of the acceleration region *l*. The flight time of the ion traveling the distance *d* is

$$t = d \,/\, v = d\sqrt{1\,/\,2eU}\,\sqrt{m\,/\,z} = k\sqrt{m\,/\,z} \tag{V.2}$$

where the parameter *k* depends on the length of the drift zone (region) *d* as well as the strength of the applied electric field.

TOF mass spectrometers are usable with a wide variety of ion sources and inlet systems. Having only electric and no magnetic fields, their construction, maintenance and calibration are generally rather simplified and straightforward in contrast to other spectrometers. Other major advantages of a TOF spectrometer are:

- high transmission, i.e. up to 50% of the produced ions reach the detector, which leads to high signal sensitivity;

- mass detection with no theoretical upper limit: all ions can be made to proceed from the source to detector;

- ions of all masses are simultaneously detected (in contrast to magnet sector- or quadrupole spectrometers);

- the complete mass spectrum can be recorded within just several µs and for every ionization pulse. This allows for monitoring possible changes in the ion signal when the ionizing conditions change (e.g. the intensity of the laser light) either due to the goals of the particular experiment or unpredictably.

Resolving power

The resolving power of a time-of-flight spectrometer, i.e. is its ability to distinguish between a mass m and a mass $m + \Delta m$ is given by the standard formula for a general type of mass spectrometer

$$R = \frac{m}{\Delta m} \tag{V.3}$$

or, according to Wiley and MacLaren [1] by:

$$R = \frac{dt}{\Delta t} \tag{V.4}$$

Here Δt is the FWHM[1] of the arrival time corresponding to an ion with mass m and dt is the time difference between the arrival times of an ion with mass m and an ion with

---

[1] **Full Width at Half Maximum**

mass $m + 1$. Despite their simple construction and easy-to-handle operation, TOF spectrometers suffer from two general issues with respect to their resolving power:

- The time difference dt is proportional to $\sqrt{m/z} - \sqrt{(m+1)/z}$ so it becomes progressively smaller as m increases. This problem is inherent to the principle of time-of-flight mass discrimination and sets restrictions on the resolving power of the TOF spectrometer for large masses.

- Another resolution limiting factor is the increase of Δt due to kinetic energy spread of ions with the same m/z ratios. For identically charged species this means that ions with the same mass reach the detector at different times. The reasons for this technically arising discrepancy are spatial inhomogeneities of the electric field, unequal kinetic energies (energy resolution problem) of the molecules prior to ionization due to a thermal distribution, and the different initial positions of the produced ions (space resolution problem).

For a TOF spectrometer with a single acceleration stage (**Fig. V.1.**) the resolution is limited to $R{\sim}50$. A second acceleration stage can increase the resolution up to $R{\sim}300$ [1]. Such a configuration (not shown here, but discussed in detail in Section VII.2) is in addition more flexible and easier to adjust.

Reflectron

The resolution of a mass spectrum can be greatly improved with the implementation of a reflectron [2, 3] though often at expense of sensitivity (due to ion losses by collision and dispersion from the main beam especially for ions of large mass). The implementation of a reflectron in multiphoton ionization spectroscopy was demonstrated by Boesl et al. [4].Various configurations are possible but in general the reflectron may enhance the resolving power of a TOF spectrometer in two ways:

- *by increasing dt:* since the flight distance is extended (the time difference in the arrival times of two ions with different masses is proportional to the flight distance);

- *by decreasing Δt.*   The reflectron can be operated in two configurations of the reflecting potential: hard and soft reflection. In the **hard reflection** mode the reflectron acts simply as an ion mirror with no compensation of the velocity mismatch (correspondingly decreasing of Δt). The **soft reflection** is achieved through a linearly increasing potential so the high-energy ions penetrate the reflectron deeper than the low-energy ions. This allows for the compensation in the flight times of ions with the same mass but different kinetic energies (thus reducing Δt) if an appropriate reflecting voltage as well as field configuration are used. In this way a mass resolution of 10 000 has been achieved [5, 6]. The principle of reducing the velocity distribution in a linear reflectron TOF (ReTOF) spectrometer is shown on **Fig.V.2**.

V.2.2. Linear ReTOF mass spectrometer

Most of the reflectron time-of-flight spectrometers are designed in such a way that the ions are reflected at a certain angle towards the detector. This has as a consequence that ions with various kinetic energies travel on slightly different trajectories since they penetrate the reflector to a different extent. This discrepancy is even more prominent in the case of dissociating clusters and leads to an offset between the reflected beams of the parent ions and daughter ions. The detection of the signal with identical efficiency both for the clusters and the fragments by a detector of a finite size can thus be strongly hampered. Additionally, the intensities of both cluster and fragment signals depend strongly on the alignment of the ion optics. These issues can be overcome with the implementation of a linear ReTOF spectrometer, in which the ion transmission is independent from the different ion kinetic energies.

Another application of the linear ReTOF spectrometer is a kinetic energy analysis for the study of dissociation processes as demonstrated by Krause and Neusser [7].
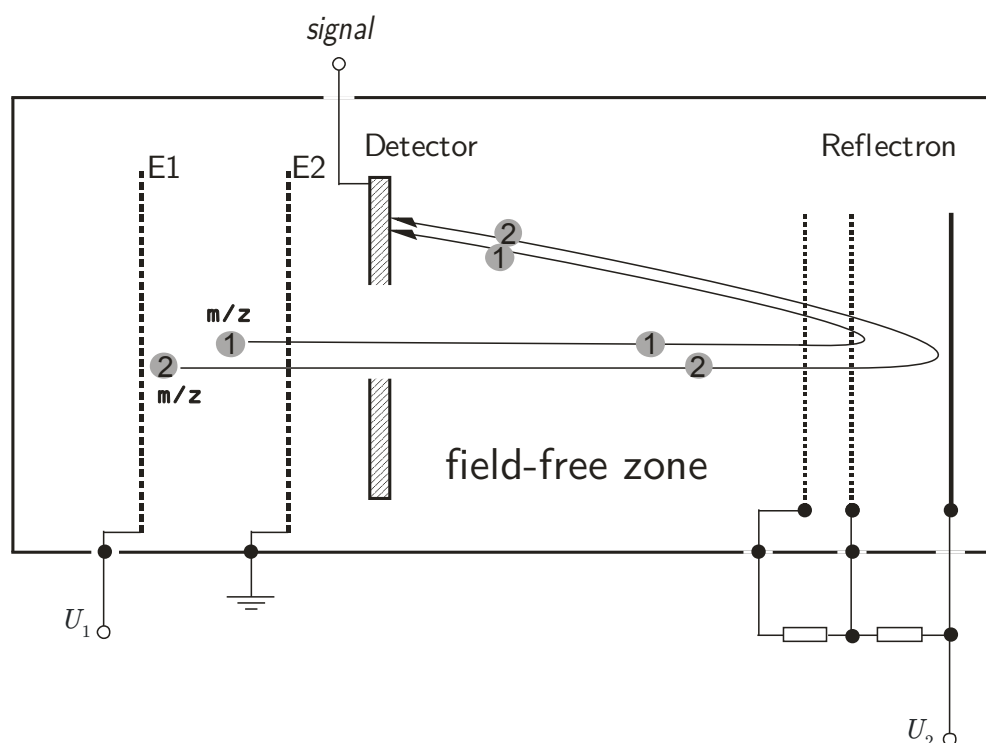
Fig.V.2. Principle of operation of a linear ReTOF spectrometer in soft reflecting mode. Ions of the same m/z ratio with different initial positions travel different distances in the acceleration region between the two electrodes E1 and E2. Ion 2 "starts" behind ion 1 and therefore gains a higher kinetic energy. Consequently however, it penetrates deeper in the reflectron region and is reflected with a certain delay in comparison to ion 1. At a proper ratio of the voltages applied to the electrodes of the reflectron, the difference in the flight times of the two ions is compensated for after the reflection. Both ions arrive simultaneously at the detector.

V.3. Noncovalently bound complexes (clusters) in cold molecular beams

V.3.1. Principles of supersonic jet expansion

The adiabatic supersonic jet technique was introduced by Kantrowitz and Grey in 1951 [8] and is used for producing cold beams of collision-free atoms, molecules and consequently weakly bound clusters and even unstable species as free radicals. The method has been used in a variety of experiments such as low-temperature kinetics, photochemical

dynamics and molecular spectroscopy [9, 10]. Some works devoted on the principles of the supersonic jet technique and cluster formation are worth mentioning here [10-14].

The adiabatic jet is achieved by expanding the gas of interest from a reservoir at high stagnation pressure P_0 and temperature T_0 through a continuous or pulsed nozzle into a chamber (vacuum chamber) kept at significantly lower background pressure P_b. In this process the thermal kinetic energy of the studied species in the source is partly transferred into kinetic energy of the jet which leads to a narrower velocity distribution and cooling. Since the energy redistribution takes place at the orifice where the collision probability is very high, the following condition for the so called *Knudsen number* must be met for an efficient cooling and consequently cluster formation:

$$K = \frac{\lambda_d}{d} << 1 \qquad (V.5)$$

Here λ_d is the mean collision-free flight length of the molecules prior to expansion and d is the diameter of the orifice opening. The value of λ_d can be reduced by mixing of the probe molecules with carrier gas (Ar, Ne, or He). It should be pointed out that the cross section for elastic collisions is larger than that for collision-induced rotational transitions, which in turn is larger than that for collision-induced vibrational transitions. This means that the translational cooling (monokinetization) is more effective than the rotational and vibrational cooling [11]:

$$T_{transl} < T_{rot} < T_{vibr} \qquad (V.6)$$

During its propagation the supersonic jet pushes the gas in the vacuum chamber (as a consequence of the nonzero background pressure). This results in the formation of standing shock waves that enclose the jet (**Fig.V.3**): *i) a symmetric shock wave* around the jet called barrel shock; *ii) a disc shape shock wave* downstream the jet called *Mach disc*. The disc originates from the intersection of the compression waves and characterizes a zone where the initial pressure is re-established.

The presence of shock waves sets limitations on the jet propagation and the length of *the zone of silence*, where the supersonic jet conditions are optimal: low density, pressure, temperature and absence of velocity gradients. The zone of silence is characterized by a
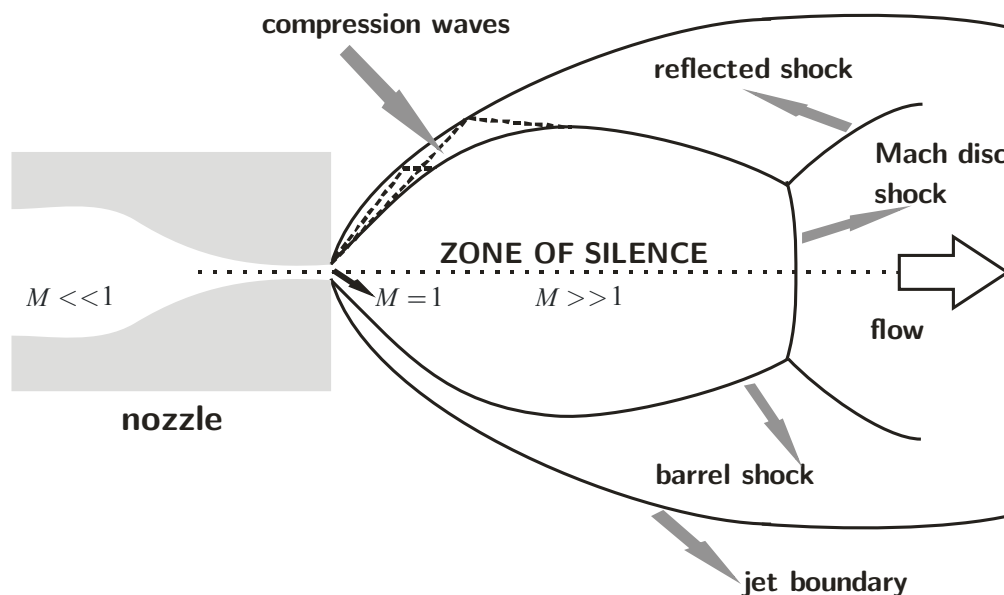
Fig.V.3. Formation of standing waves during a supersonic jet expansion as a consequence of the presence of residual gas in the vacuum chamber. Also shown is the Mach number at various stages of the jet propagation inside and outside the nozzle [12, 13].

Mach number[2] $M >> 1$. The higher the ratio between the stagnation pressure P_0 and P_b, the farther is the Mach disc from the nozzle.

The location of the Mach disc is given by:

$$X_m = 0.67d\sqrt{P_0 / P_b} \qquad\qquad \textbf{(V.7)}$$

Therefore, to be on the safe side especially at relatively high pressures P_b, the measurements should always be taken at close distances from the nozzle.

The Mach number in the vicinity of the jet axis increases proportionally with the distance X from the nozzle ($M \propto (X/d)^{\gamma-1}$) [14], where $\gamma = C_P / C_V$ is the heat capacity ratio of the gas. Depending on the pressure ratios, the flow downstream of the Mach disc can re-expand. However, for very long distances from the nozzle, M approaches a finite

---

[2] **The Mach number is defined as the ratio of the mean flow velocity V at a given point to the speed of sound at that point.**

terminal value since the jet gets weaker and the hydrodynamic stability of the flow is violated.

V.3.2. Formation of noncovalently bound complexes

The production of weakly bound complexes (clusters) and their detailed spectroscopic study are efficiently achieved in cold molecular beams formed by supersonic jet expansion [11, 15-23]. Other methods for complex formation are for example: gas aggregation [24], laser ablation [25], laser-induced pyrolisis [26] and cluster aggregation [27].

The distribution of complexes sizes and structures in a supersonic jet may be influenced not only by the energetics but also by the kinetics of cluster formation. The internal degrees of freedom of the clusters have temperatures $T_{rot} \sim 5$ K, $T_{vibr} \sim 50$ K $-$ 100 K which are very different from those in solution. The investigated species in a supersonically expanded jet have small relative velocities; hence the collision rates are greatly reduced, which favors the formation of noncovalent complexes.

The noncovalent bonding is usually strongly environment-dependent (the weaker or "softer" the bonding the stronger this dependence may be). Cold gas-phase molecular clusters make possible the study of the properties of the lowest energy configuration(s) for the solute-(solvent)$_n$ aggregate in unsurpassed detail and clarity. The spectroscopy of this complex then directly probes the environmentally unperturbed noncovalent bond by determining its structure, bond strength, the effects of the bond on the internal modes of the solute and the solvent.

CHAPTER VI

Pulsed field ionization

State-selected ions play important role in the study of various chemical reactions, dissociation processes, as well as in the vibrational and high-resolution ion spectroscopy [28]. The concept of producing ions with well defined internal energies E_{ion}^{int} is similar to the state selection in case of neutral species as with the resonance enhanced multiphoton ionization technique. However, the task of preparing energy-selected ions is more complicated even when monochromatic ionizing sources are used since generally the detached electron carries away an unknown amount of energy $E_{kin}(e^-)$ upon photoionization.

The present chapter gives a concise description of the concept of pulsed field ionization (PFI), employed for producing ions with well defined internal energies (threshold ions). In particular, the method combining mass selectivity with the virtues of PFI detection, the mass analyzed threshold ionization, is discussed in more detail (Section VI.3), because this is the ionization technique employed for the experimental studies in the present work.

VI.1. Rydberg states

Rydberg states are electronic excited states in which the electron occupies relatively large orbitals. The principal number n (and possibly the orbital number l, resp. m) of such states is higher than that of a valence (valence-shell) state. The distinction between low-lying Rydberg states and valence states is often not rigidly defined due to effects like mixing and rydbergization [29]. Rydberg states have been extensively studied [29-41] and can be excited by means of electron impact, charge exchange, collisional optical excitation but the best selectivity in terms of energy can be achieved with photoexcitation [42].

The stability of the Rydberg states in molecules depends on whether the electron is excited from a bonding, anti-bonding, or non-bonding orbital. As n takes successive integer values Rydberg states form series for a given l. These series converge in case of molecules to a given rovibrational state of the ion [43, 44] as depicted in **Fig.VI.1**. The energy of each member of such a Rydberg series is given by:

$$E_{nlm} = \text{IP} - R_\mu / (n - \delta_l)^2 \qquad \textbf{(VI.1)}$$

where IP is the limit of the series, R_μ is the mass-corrected Rydberg constant for a given molecule or molecular cluster and δ_l is a correction called quantum defect[3]. It accounts for the electron-core interaction and therefore for deviations from the hydrogen-atom like potential model. The value of δ_l is relatively large for Rydberg orbitals with low n and l, also called *penetrating orbitals* and decreases with increasing n and/or l (*non-penetrating orbitals*). For $n > 10$ δ_l becomes more or less constant and for sufficiently high orbitals $\delta_l \approx 0$. The members of a series and the continuum of states above the series limit in molecules or many-electron atoms form a channel.

The average radius of a Rydberg orbit $r_n \sim n^2$ is in the order of several hundred Å for $n \gg 20$. The electron in such a large orbit is very weakly bound to the ionic core and has therefore large cross sections for collisions with ions and neutrals as well as it is easily perturbed by external electric and magnetic fields.

---

[3] **The m dependence of the energy manifest itself at strong electric fields [44].**
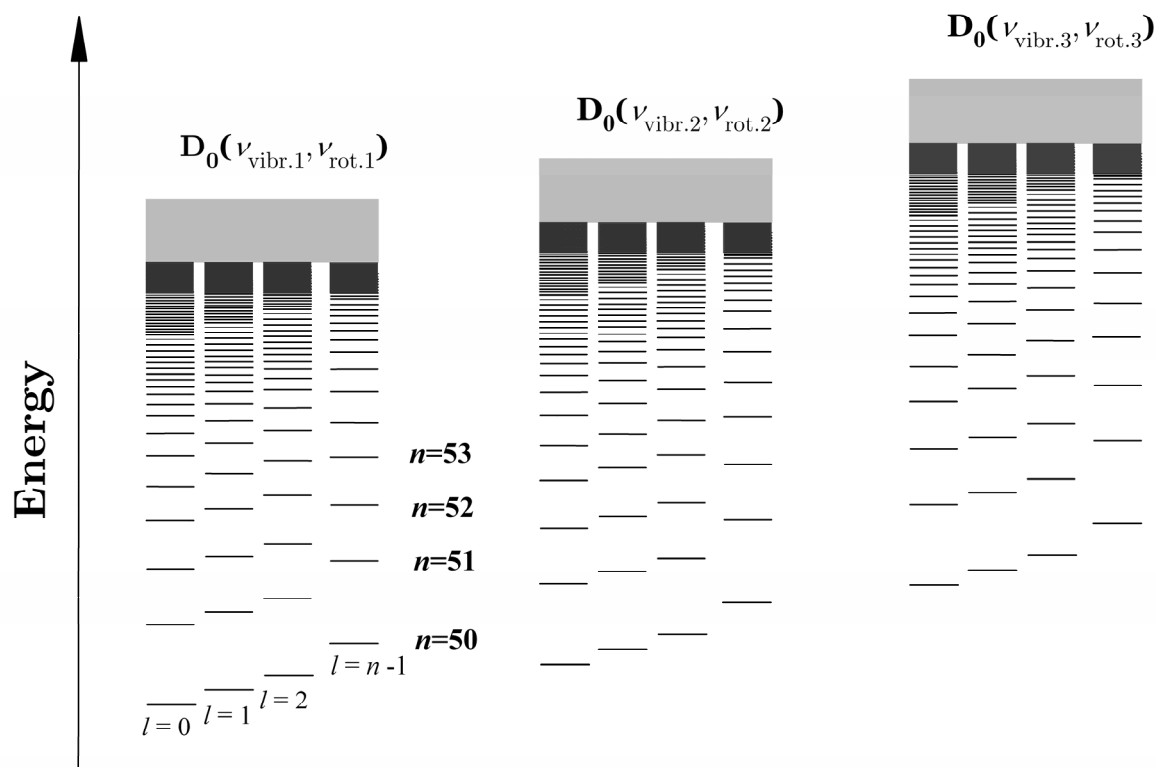
Fig.VI.1. Molecular Rydberg states forming series that converge to different rovibrational states of the ion.

Interactions between different channels may lead to energy shifts of bound states or to electronic and spin-orbit autoionization[4]. Some properties of Rydberg states and their n-dependence are given in **Table VI.1**.

Low-lying Rydberg states. Rydberg molecular states with low n and l quantum numbers ($n = 50 - 70$) play the major role in vibrational predissociation and rotational or vibrational autoionization [45, 46], because of their strong interaction with the molecular ion core. Both predissociation and autoionization for such states have rates k in the order $\sim 10^{10}n^{-3} - 10^{12} n^{-3}$ [47] and therefore occur on a shorter timescale than the radiative decay ($k \sim 10^8 n^{-3}$).

---

[4] In molecules processes like predissociation and vibrational or rotational autoionization as well as predissociation are additionally possible.

Property	n dependence	$n = 10$	$n = 100$	$n = 1000$
Mean radius	$a_0 n^2$	53 Å	0.53 μm	53 μm
Binding energy	Rn^{-2}	1100 cm^{-1}	11 cm^{-1}	0.1 cm^{-1}
Spacing between adjacent levels	$2Rn^{-3}$	200 cm^{-1}	0.2 cm^{-1}	2×10^{-4} cm^{-1}
Polarizability [MHz cm^2/V^2]	$\propto n^7$	0.2	0.2×10^7	0.2×10^{14}
Threshold ionization field [V/cm]	$\propto n^{-4}$	33 000	3.3	3.3×10^{-4}

Table VI.1. Properties of Rydberg states [48] a_0 and R are the Bohr radius and the Rydberg constant, respectively.

High-lying Rydberg states. High Rydberg states in the range of $n >> 100$ are located within several cm^{-1} below the ionization threshold of the investigated system. Deviations from the $1/r$ - Coulomb potential and higher order (multipole) couplings of the positive charged core to the Rydberg electron for such states can be neglected and the series limits denote the energetic position of the rovibrational eigenstates of the molecular ion core with a high precision of a few cm^{-1}.

Rydberg states with high n and especially l numbers have been suggested to have extremely long lifetimes [49] because of their non-penetrating character. Experimentally, the long lifetimes of high-lying Rydberg states were first observed by Reiser et al.[43]. These lifetimes are in the μs-range, thus exceeding those predicted by the n^3 scaling law, deduced for Rydberg states with low orbital angular momentum[5]. On the other hand, high n optically accessible "bright" Rydberg states, although selectively populated, have low l-numbers because of the $\Delta l = \pm 1$ selection rule for optical transitions and therefore would have short lifetimes. However, it is already well accepted that the lifetimes of such states are enhanced by a factor of n due to l-mixing with the "dark" states (also called *Stark manifold*), possessing high angular momentum in the presence of residual electric stray fields or external electric fields [43, 49-52]. Such mixing results from the Stark effect and in a first approximation occurs if the Stark splitting of the long-lived "dark" states becomes comparable to their field-free energetic separation from the short-lived Rydberg sta-

---

[5]**According to the n^3 scaling law Rydberg states in the range 100-200 are expected to decay on a nanosecond scale [44].**

tes with the same number n but different quantum defect. For an applied external field this energetic separation is smaller for higher n while the Stark splitting becomes larger. It was shown by Bixon and Jortner [53] that the lowest n in a Rydberg series for which such mixing can occur is related to the electric field strength F in the following way:

$$F = \frac{\overline{F} \cdot 3.4 \cdot 10^9 \delta_l}{n^5} \qquad \textbf{(VI.2)}$$

where the dimensionless parameter $\overline{F}$ is in the range between 0.5 and 3.0. Very high Rydberg states ($n > 100$) are above the so called Inglis-Teller limit which means that the mixing is complete even for states with different quantum numbers n and sets limitations on Eq.(**VI.1**). Here some important works, devoted to the discrimination of high Rydberg states are therefore worth mentioning. Vrakking and Lee [52, 54] were able to resolve states up to $n = 122$ for the NO molecule. Neuhauser and Neusser reported the first results on rotationally resolved Rydberg states with $n > 100$ of a polyatomic molecule (benzene) by using sub-Doppler double resonance excitation [34]. Siglow and Neusser resolved individual Rydberg states of van der Waals clusters of benzene with argon and neon in the region $45 < n < 110$ [39].

The lifetime of high lying Rydberg states can be additionally increased by another factor of n due to m mixing [44, 55, 56] caused by collisional effects and inhomogeneous fields originnating from surrounding ions [57].

VI.2. Concepts of PFI spectroscopy

The fact that high-lying Rydberg states mark the position of the respective ionic rovibrational state or the adiabatic ionization energy AIE in a molecule and a molecular complex with an accuracy within a few cm^{-1} has found wide application for the production of ions with well defined internal energies (threshold ions) in delayed pulsed field ionization (PFI) techniques. These states belong to the so called *"magic region"* and have lifetimes long enough to survive the time delay of several μs between the excitation and ionization needed in such experiments.
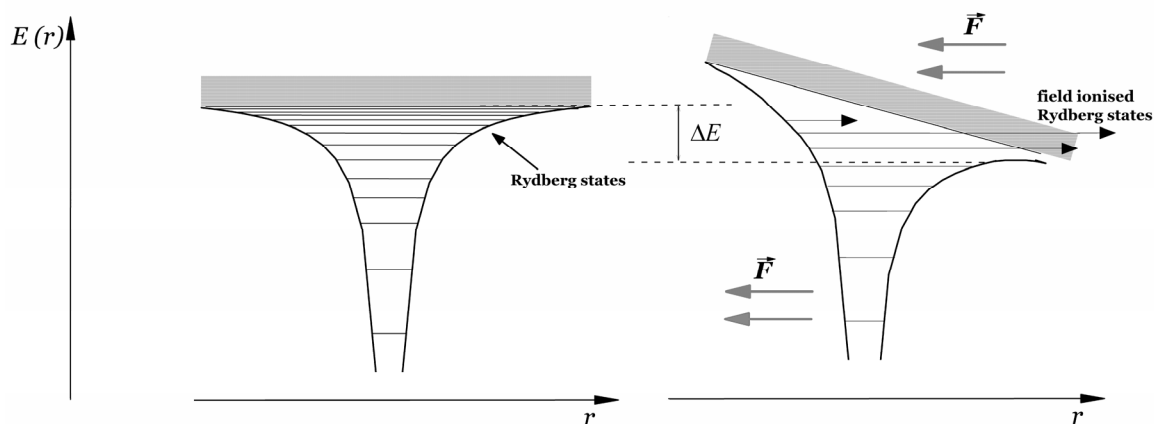
Fig.VI.2. Field ionization of high lying Rydberg states. *Left*: Rydberg states and potential well in a field-free environment. *Right*: An applied electric field F distorts the Coulomb potential and shifts the ionization threshold is shifted in the presence of electric field by ΔE.

The spectroscopic methods, based on pulsed field ionization are PFI-PEPICO, PFI-ZEKE (Zero Electron Kinetic Energy), and MATI (Mass Analyzed Threshold ionization).

As a first step in a PFI experiment the high Rydberg states are populated either by synchrotron radiation excitation or laser excitation along with directly produced (prompt) ions and electrons. The species originating from direct photoionization are discriminated from the Rydberg molecules by different approaches, depending on the particular PFI technique. As a next step the Rydberg states are ionized by pulsed field (> 100 V) after a delay of several μs. This time delay is essential in the experiment because:

i)   the neutral Rydberg states and the photoions (photoelectrons) can be sufficiently spatially discriminated and

ii)   the short-lived Rydberg states decay prior to the field ionization. This accounts for the observation that the bandwidths in PFI experiments are generally no larger than $5 - 10$ cm^{-1} [58].

It has been suggested that the Rydberg states of interest in PFI experiments are ionized *diabatically* in contrast to the penetrating Rydberg states for which *adiabatic* ionization is predominant [44]. In addition, the delayed PFI of molecular Rydberg states occurs for much lower n values than predicted for atoms due to process called forced autoionization. The latter is due to a channel interaction between a low n Rydberg state and a *pseudo-*

continuum of long-lived high Rydberg states [44, 59, 60]. It was also shown that the field ionization efficiency reaches unity for the Rydberg states lying within 10 cm^{-1} from the respective ionization threshold [61].

The threshold ions produced by the pulsed field ionization have well defined internal energies $E_{ion}^{int} \approx E_{neutral}^{int} + \hbar\omega - \text{AIE}$[6]. This is opposite to the case of direct photoionization since the photon energy is deposited in a neutral molecule or an atom and not distributed *arbitrarily* between a photoion and a photoelectron. One has however to take account on the lowering of the ionization thresholds due to presence of electric field (**Fig.VI.2** and Eq. (**VI.3**)). The field-induced shift has been assessed to be

$$\Delta E = a\sqrt{F\left[V / cm\right]} \; \left[\text{cm}^{-1}\right] \tag{VI.3}$$

where the parameter a depends on the rising time of the ionizing electric field pulse and has values $3.2 \leq a \leq 6.1$ [49, 62]. The increase of the rising time improves the resolution, obtainable in a PFI experiment as was shown in a series of works [58, 63, 64]. Also, an adequate combination of several ionizing pulses can be used to increase the resolution in ZEKE and MATI as will be discussed in *Section VI.3.6.*

The signal in a PFI experiment is obtained either by collecting the threshold electrons (ZEKE) or the threshold ions (MATI) or both (PFI-PEPICO) accelerated towards the detector by the ionizing field, e.g. in a TOF spectrometer.

VI.3. Mass Analyzed Threshold Ionization

VI.3.1 Basic principles

The PFI method of threshold ions detection was introduced by Zhu and Johnson [65] back in 1991. The separation of the threshold ions and the promptly produced photoions in a linear TOF spectrometer was achieved by a special configuration of electric fields so that the two types of ions arrived at different times at the detector. Krause and Neusser

---

[6] **AIE is the adiabatic ionization energy.**

demonstrated shortly after that threshold ions and directly ionized species can be discriminated in a linear reflectron TOF spectrometer with kinetic energy analysis [7, 66]. A reflecting electric field was also utilized for vibrational spectroscopy of fluorobenzene·Ar cluster in a cylindrical ion trap [67].

The photoexcitation in MATI is similar to that in ZEKE technique: the laser excitation of molecular Rydberg states can be realized in a two-color REMPI scheme or in a VUV one-color scheme. In the former case, the first laser has a frequency matching a (ro)vibronic band of the $S_1 \leftarrow S_0$ transition in a molecule or a cluster while the second laser frequency is scanned across the ionization thresholds of the (ro)vibrational levels in the ground cationic electron state above the AIE (**Fig.VI.3a**). The described scheme makes it possible to record the spectra via different (ro)vibrational levels of the S_1 state. Due to the Franck-Condon principle these intermediate states play the role of a "filter" for the final state thus increasing the resolution of the signal and the species selectivity of the excitation which lends itself to the studies of different clusters. An additional advantage is that conclusions on effects due to intra- and intermolecular interactions can be drawn.

One-color excitation makes use of vacuum UV radiation that excites the studied molecules or clusters directly from their ground state to high Rydberg states. This method has the advantage of bypassing the S_1 state which may not be accessible with the frequency of the first laser or may be dissociative. The disadvantages of this type of excitation are the complicated production of VUV radiation and that not all spectral ranges are easily accessible. Another issue of the direct excitation from S_0 to Rydberg states in a given molecule or molecular cluster is that the thermal distribution of the ground neutral state is transferred to the ion.

Recording the total ion current produced by the prompt ions while scanning the second laser frequency leads to a photoionization efficiency curve with steps at the individual lowest thresholds (**Fig.VI.3b**). By applying a weak electric field ($\sim 0.5 - 1$ V/cm) the Rydberg molecules or clusters can be spatially separated by the prompt ions, produced by direct photoionization. As a result of the delayed pulsed field ionization of the Rydberg states as a next step, sharp peaks located on the steps are observed at the individual thresholds (**Fig.VI.3c**).
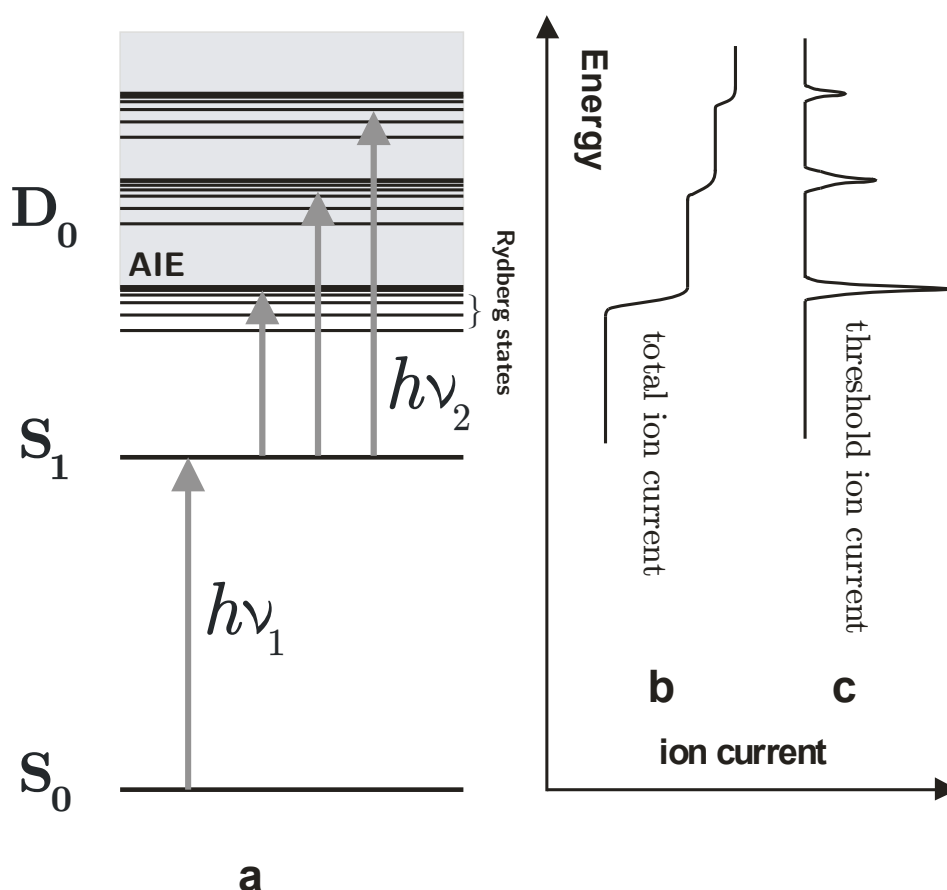
Fig.VI.3. A two-color excitation scheme in a MATI experiment: (a) total ion current curve with steps at the individual thresholds (b), and a threshold ion current profile (c).

VI.3.2. Advantages and disadvantages of the mass analyzed threshold ionization. Effect of the separation field on the resolution in a MATI experiment.

Both MATI and ZEKE can provide valuable information on the adiabatic ionization energies of molecules and molecular complexes. The study on the vibrational structure of the cations is, however, usually restricted to the ground electronic state. The reason for this is that the need of very high photon excitation energies and the generally short lifetimes make the PFI techniques not well suited for studies of excited states of the ionic core.

The most important feature of MATI is its mass selectivity since ions and not electrons are detected. This can be utilized for studying spectra of different compounds in a gas

mixture or fragmentation processes in molecules or weakly bound complexes. Also, the shielding with μ-metal needed when electrons are detected (ZEKE) is obsolete in the case of ion detection due to the larger masses of ions compared to electrons. However, one has to take into account that in the case of MATI the separation (discrimination) field destroys (ionizes) some of the highest lying and most populated Rydberg states (Eq. **(VI.3)** leading to a somewhat lower resolution and lower signal intensity in case of MATI compared to ZEKE.

VI.3.3. MATI of monomers

A number of recent works demonstrated the applicability of the mass analyzed threshold ionization technique for the study of organic and biomolecules. Unterberg et al. [68] reported results from MATI experiment and theoretical calculations of 3- and 4-aminophenol, Xie et al. [69] also reported MATI spectra on 3-aminophenol (*m*-aminophenol) for the two isomers with values for the AIEs that are in agreement with those found by Unterberg et al. Several works demonstrated the application of MATI to indole derivatives. Lin et al. [70] presented results on MATI spectroscopy of 7-azaindole (7AI) via 4 intermediate vibrational levels of S_1. MATI spectra of 5-methylindole (5MI) were also reported [71]. A study of the indazole cation with the MATI technique was conveyed by Su et al. [72]. MATI experiments in a VUV excitation scheme were presented by several groups [73-75]. The one-photon mass analyzed threshold ionization was implemented as an experimental technique for determining the ionization energy and the vibrational structure of the ground cationic state for several other molecular systems, known as aliphatic halides [76-79].

VI.3.4. MATI of weakly bound complexes

The mass and energy selectivity of the PFI production and detection of threshold ions can be used for studying the dissociation of van der Waals [7, 35, 66, 80, 81] and hydrogen bonded complexes [80, 82, 83]. The MATI technique refers to investigating the spectroscopic properties of the cation, yet as shown in Eq.**(VI.4)** and **Fig.VI.4** this PFI method offers a relatively easy and straightforward way for determining the binding energy of the neutral cluster through the simultaneous observation at the mass channels of the fragment and the cluster as discussed below.

Firstly, the AIEs of the complex (cluster) $A \cdot B$ and the bare molecule (monomer) A are found experimentally. Generally the ionization of the cluster refers only to the species A and there is no electron transfer between A and B due to the large difference in their ionization potentials. If excited to sufficiently high vibrational levels in its ground electronic state the cation of the cluster dissociates which is observed as a switching from the signal in the parent $(A \cdot B)^+$ mass channel to a signal in the fragment (daughter) A^+ mass channel (**Fig.VI.4a**). This allows in principle the experimental determination of the binding energy E_0 of a complex in its ground cationic state D_0 as a difference between the appearance energy (AE) and the AIE of the cluster (**Fig.VI.4.b** and Eq. **(VI.4)a**).
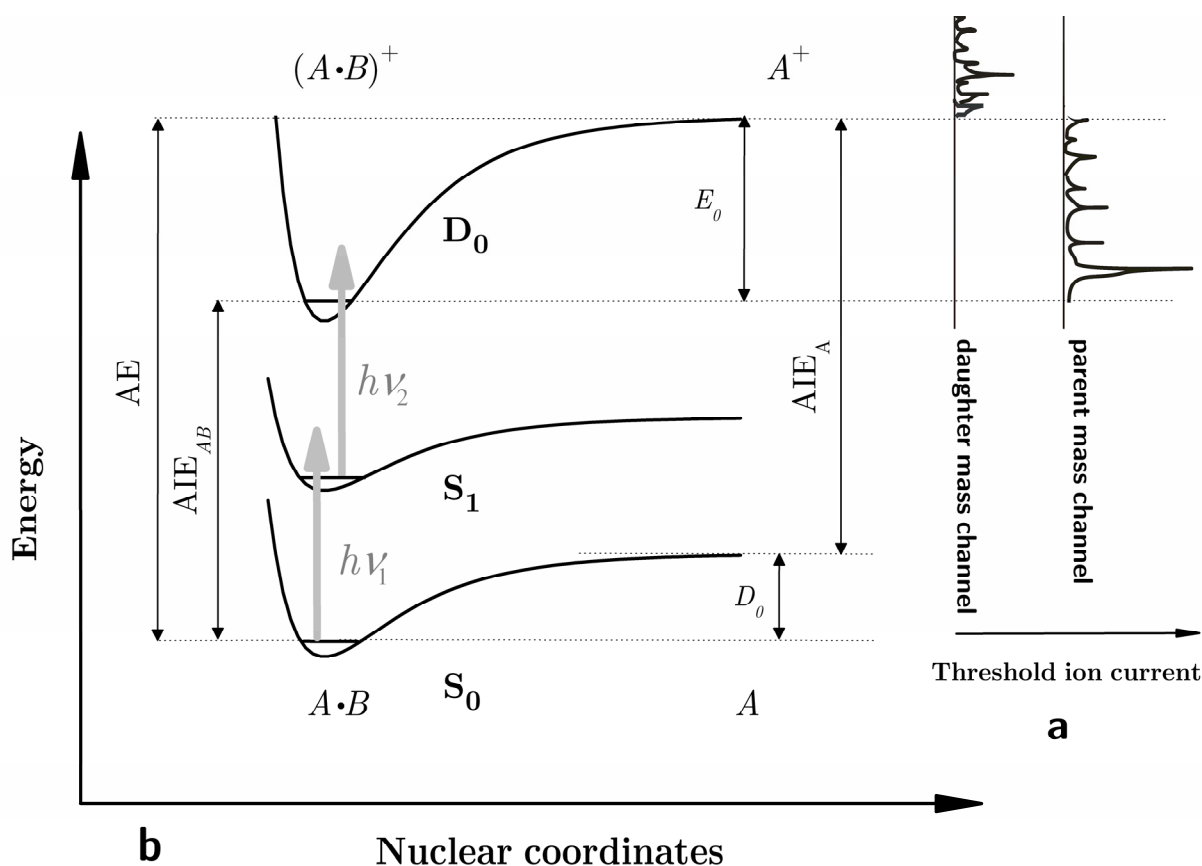

Fig.VI.4. *a)* A "switch" of the threshold ion signal from the parent to the fragment (daughter) mass channel is observed when the scanned laser frequency goes beyond the dissociation threshold of the complex. *b)* Energy diagram of the two-color excitation (ionization) scheme in a threshold ionization technique.

$$\textbf{a)} \quad E_0 = \text{AE} - \text{AIE}_A$$
$$\textbf{b)} \quad D_0 = \text{AE} - \text{AIE}_{A \cdot B} \qquad \textbf{(VI.4)}$$

However, the appearance energy depends on the ionization field as was shown for van der Waals complexes for the first time by Grebner et al. [35]. This field dependence shifts the onset of the daughter signal to somewhat lower energy (≈ 50 cm^{-1} for indole·Ar at field strength 1000 V/cm [80]) than the observed fall-off of the parent signal. An explanation for the observed shift is the field-induced Rydberg-core coupling of high n members of Rydberg series converging to vibrational ionic states below the field-free dissociation threshold of a cluster and low n members of Rydberg series converging to vibrational ionic states above this threshold (**Fig.VI.5**). It has been shown that the field-free appearance energy that has to be used in Eq. **(VI.4)** agrees with the energy at *the observed breakdown in the parent ion signal* [35].
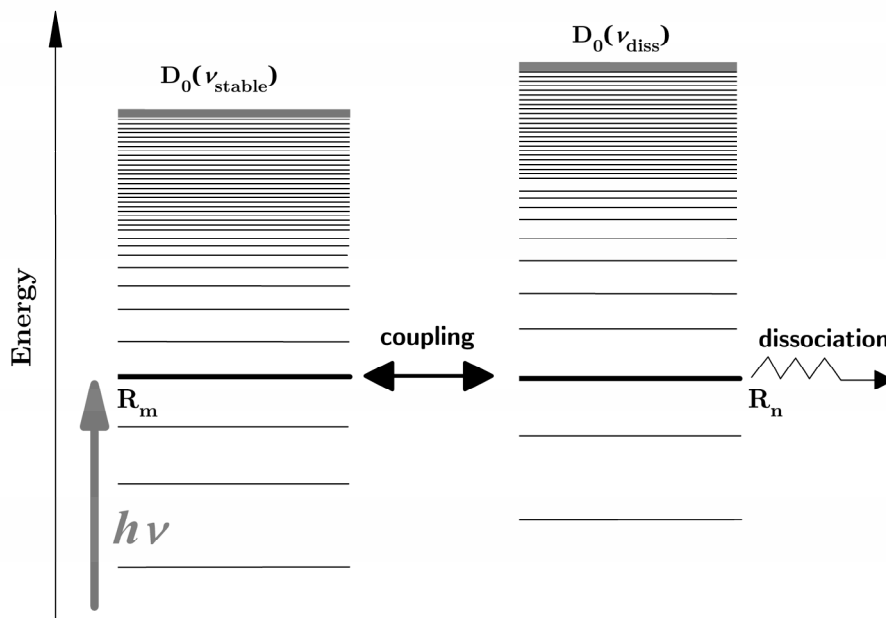

Fig.VI.5. Field-induced coupling of Rydberg states. The photoexcited Rydberg state R_m in a series converging to a stable vibrational ionic state is coupled to a Rydberg state R_n belonging to a series converging to a dissociative vibrational ionic state.

The binding energy D_0 of the complex can be calculated from Eq. **(VI.4)b** on the basis of the experimentally found values for AIE$_A$, AIE$_{A·B}$, and E_0.

VI.3.5. Factors determining the applicability of MATI for dissociation studies of complexes

At this point it is relevant to mention that, as was experimentally shown [7, 66], the high Rydberg states excited in the complex have lifetimes long enough to survive its dissociation and the Rydberg electron stays attached to the fragment. This finding is in good agreement with the predictions of the ion core model [84, 85] and gives a positive answer to the question whether a PFI leads to threshold daughter ions in the first place in contrast to the method of "breakdown graphs" [86-89]. MATI is therefore well suited as a method for studying the dissociation dynamics of clusters not only because of its mass selectivity but also on account of the sufficient stability of the high Rydberg orbits. The following scheme (**Fig.VI.6**) can be thus given as an illustration of the successive steps in a PFI experiment on a dissociating cluster:
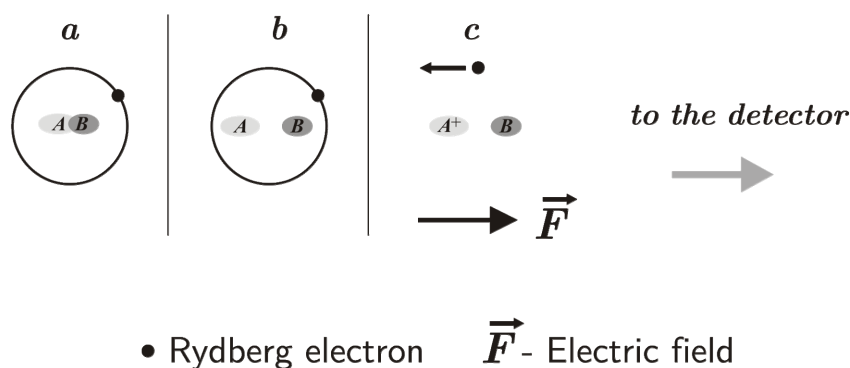

Fig. VI.6. Detection of cluster dissociation in a PFI experiment. *a)* Excitation of a Rydberg electron in a cluster *A·B* → *b)* dissociation of the cluster → *c)* pulsed field ionization and acceleration of the threshold daughter ions *A⁺* to the detector

Also, an important prerequisite for the unambiguous determination of E_0 and therefore D_0 is the sufficient density of intra- or intermolecular vibrational levels in the vicinity of the dissociation threshold of the cation so the parent signal – daughter signal switching be clearly pronounced. As already previously demonstrated [80, 82] (and also in the experimental section of the present work) this condition is readily fulfilled for the cations of

hydrogen bonded clusters since the dissociation occurs at internal ion energies in the order of several thousands cm^{-1} where the density of the vibrational modes in the spectrum is high enough.

VI.3.6. Improving the resolution in MATI and ZEKE

As discussed in Section VI.2 the shape and the duration of the electric field pulse needed for field ionization or discrimination affects the population of the high lying Rydberg states, the ionization thresholds and the resolution in a PFI experiment. A simple approach for increasing the resolution would be the decrease of the ionization field magnitude. However, this method is of little practical use since a resolution of 0.5 cm^{-1} could be achieved at field strengths less than 16 mV/cm. Such a weak field would ionize only Rydberg states with $n \geq 470$ which are difficult to be utilized unless special efforts are invested in minimizing stray fields and gas densities etc. [44].

Two other approaches for increasing the resolution in ZEKE have been suggested [44, 90]:

- *a single multi-stepped pulse* [63]. An electron time-of-flight spectrum is generated with the application of a multistep staircase-like electric field pulse with peaks at each step. The method also provides the exact determination of the ionization energy under field-free conditions [64]. Using this approach FWHM of 0.2 cm^{-1} was obtained for ZEKE of benzene [63].

- *a combination of successive electric pulses with different duration and polarity* [44, 61, 91, 92]. Müller-Dethlefs and co-workers demonstrated that the resolution of ZEKE can be increased by using a two-pulse sequence [91]. This method called *Fractional Stark State Selective Electric Field Ionization (FSSI)* uses a weak positive prepulse followed by a strong negative probe (extraction) pulse. The achieved high resolution is explained with the following arguments: The prepulse acts in a similar way to the separation field in MATI and discriminates the neutrals from the photoelectrons that may lead to a high energy tail on a ZEKE band [93]. This field ionizes the highest lying (also called "red") Rydberg states, while the lower lying "blue" states survive. The second pulse which extracts the ZEKE electrons has an opposite polarity which leads to *Stark-state inversion* and ionization of the original "blue" states. The FSSI method was applied also for MATI of phenol·Ar complex with the use of a third electric pulse for the separation of the high-reso-

lution MATI ions from the remaining Rydberg states. These states contribute to the low resolution MATI signal after ionization by the strong field of 290 V/cm into the ReTOF analyzer. A FWHM of 3 cm^{-1} was reported which is similar to that in the ZEKE spectrum and twice smaller than the obtained in the low-resolution MATI spectrum [94].

Merkt and co-workers used a combination of pulsed electric field sequences and multistep pulses to achieve a very high resolution of 0.06 cm^{-1} for the ZEKE spectroscopy of N_2 and Ar [95]. Goode, Le Claire, and Johnson [96] showed that, depending on the pulse duration and magnitude of the separation electric field as well as on different pulse sequences, the highest n of the Rydberg states that mainly contribute to the threshold ion signal at the AIE in their experiment is ≈ 180. A similar study by Boogaarts et al. [97] gave values of n in the much lower region $105 - 165$ with the use of static bias field. These results are in line with the conclusion that it is preferable to use as weak as possible *pulsed* discrimination (separation) field in a PFI experiment [44, 98, 99] in order to achieve smaller red shifts of the ionization thresholds and better spectral resolution.

$$***$$

At the end of this chapter it is relevant to mention threshold ionization techniques that employ the excitation scheme of MATI and ZEKE to high-lying Rydberg states although, however, they are not based on pulsed field ionization. These methods are: photoinduced Rydberg ionization (PIRI) spectroscopy [96], infrared PIRI (IR/PIRI) spectroscopy [100], IR-photodissociation (IRPRD) spectroscopy [101], and autoionization detected infrared (ADIR) spectroscopy[102].

Bibliography to Part II

1. W.C. Wiley and I.H. McLaren, Rev. Sci. Instr., 1955. **26**: p. 1150.
2. B.A. Mamyrin, V.I. Karataev, D.V. Shmikk, and V.A. Zagulin, Sov. Phys. JETP, 1973. **37**: p. 45.
3. B.A. Mamyrin and D.V. Shmikk, Sov. Phys. JETP, 1979. **49**: p. 762.
4. U. Boesl, H.J. Neusser, R. Weinkauf, and E.W. Schlag, J. Phys. Chem., 1982. **86**: p. 4857.
5. T. Bergmann, T.P. Martin, and H. Schaber, Rev. Sci. Instrum., 1989. **60**: p. 792.
6. K. Walter, U. Boesl, and E.W. Schlag, Int. J. Mass Spectrom. Ion Proc., 1986. **71**: p. 309.
7. H. Krause and H.J. Neusser, J. Chem. Phys., 1992. **97**(8): p. 5923.
8. A. Kantrowitz and J. Grey, Review of Scientific Instruments, 1951. **22**(5): p. 328.
9. P.P. Wegener, ed. *Molecular Beam and Low Density Gasdynamics*. 1974, Marcel Deker: New York.
10. R.B. Bernstein, *Chemical Dynamics via Molecular beam and Laser Techniques*. The Hinshelwood Lectures. 1982, Oxford, New York: Clarendon Press, Oxford University Press
11. H.J. Foth and W. Demtröder, Phys. Bl., 1987. **43**: p. 7.
12. G. Scoles, *Atomic and molecular beam methods*. 1988, New York: Oxford University Press.
13. H. Pauly, *Atom, Molecule, and Cluster Beams I: Basic Theory, Production and Detection of Thermal Energy Beams* Springer Series on ATOMIC, OPTICAL, AND PLASMA PHYSICS. 2000, Berlin: Springer-Verlag.
14. D.H. Levy, Ann. Rev. Phys. Chem., 1980. **31**: p. 197.
15. D.H. Levy, in *Quantum Dynamics of Molecules*, R.G. Wodley, Editor. 1980, Plenum Press: New York.
16. D.H. Levy, Science, 1981. **214**: p. 263.
17. A.W. Castleman Jr and R.G. Keesee, Chem. Rev., 1986. **86**: p. 589.
18. T.D. Märk, Int. J. Mass Spectrom. Ion Proc., 1987. **79**: p. 1.
19. E.W. Becker, K. Bier, and W. Henkes, Z. Physik, 1956. **146**: p. 333.
20. R.L. Whetten and M.Y. Hahn, in *Atomic and Molecular Cluster*, E.R. Bernstein, Editor. 1990, Elsevier: Amsterdam.
21. M. Kappes and S. Leutwyler, in *Atomic and Molecular Beam Methods*, G. Scoles, Editor. 1988, Vol.1, Oxford University Press: New York.
22. D.R. Miller, in *Atomic and Molecular Beam Methods*, G. Scoles, Editor. 1988, Vol.1, Oxford University Press: New York.
23. J.B. Anderson, in *Molecular Beams in Low Density Gas Dynamics*, P.P. Wegener, Editor. 1974, Dekker: New York.
24. K. Sattler, Jpn. J. Appl. Phys., 1993. **32**: p. 1428.

25. T.G. Dietz, M.A. Duncan, D.E. Powers, and R.E. Smalley, J. Chem. Phys., 1981. **74**: p. 6511.

26. M. Ehbrecht, M. Faerber, F. Rohmund, V.V. Smirnov, O. Stelmakh, and F. Huisken, Chemical Physics Letters, 1993. **214**(1): p. 34.

27. M. Rutzen, S. Kakar, C. Rienecker, R.v. Pietrowski, and T. Möller, Z. Physik D, 1996. **38**: p. 89.

28. R.G. Neuhauser, K. Siglow, and H.J. Neusser, J. Chem. Phys., 1997. **106**(3): p. 896-907.

29. R.S. Mulliken, Accounts of Chemical Research, 1976. **9**(1): p. 7-12.

30. J.C. Person, R.L. Watkins, and D.L. Howard, J. Phys. B: At. Mol. Phys., 1976. **9**(10): p. 1811-1822

31. E. Rabani and R.D. Levine, J. Chem. Phys., 1996. **104**: p. 1937.

32. M.J.J. Vrakking and Y.T. Lee, Phys. Rev. A, 1995. **51**(2): p. 894.

33. A. Wójcik, R. Parzyn-acuteski, and A. Grudka, Physical Review A, 1997. **55**(3): p. 2144.

34. R. Neuhauser and H.J. Neusser, Chem. Phys. Lett., 1996. **253**: p. 151.

35. T.L. Grebner, P.v. Unold, and H.J. Neusser, J. Phys. Chem. A, 1997. **101**: p. 158.

36. J.D. Corless and C.R. Stroud Jr, Phys. Rev. Lett., 1997. **79**: p. 637.

37. E. Reinhold and W. Ubachs, Molecular Physics, 2005. **103**(10): p. 1329.

38. K. Siglow and H.J. Neusser, J. Chem. Phys., 2000. **112**: p. 647.

39. K. Siglow and H.J. Neusser, Faraday Discuss., 2000. **115**: p. 245.

40. K. Siglow and H.J. Neusser, J. Electron Spectrosc. Relat. Phenom., 2000. **112**(1-3): p. 199.

41. M. Sobczyk and J. Simons, J. Phys. Chem. B, 2006. **110**: p. 7519.

42. T.F. Gallagher, *Rydberg Atoms*. Cambridge Monographs on Atomic, Molecular and Chemical Physics. 1994, Cambridge: Cambridge University Press.

43. G. Reiser, W. Habenicht, K. Müller-Dethlefs, and E.W. Schlag, Chem. Phys. Lett., 1988. **152**: p. 119.

44. F. Merkt, Annual Review of Physical Chemistry, 1997. **48**: p. 675.

45. H. Lefebvre-Brion and R.W. Field, *Perturbations in the Spectra of Diatomic Molecules*. 1986: Academic Press.

46. G. Herzberg, *Molecular Spectra and Molecular Structure. Vol. 1. Spectra of Diatomic Molecules. (Reprint ed.w/correction)* 1989, Malabar, Florida: Krieger Publishing Company.

47. R.S. Berry, Rec. Chem. Prog., 1970. **31**: p. 9.

48. R. Signorell and F. Merkt, *Artifacts in PFI-ZEKE Photoelectron Spectroscopy*, in *The Role of Rydberg States in Spectroscopy and Photochemistry, Low and High Rydberg States*, C. Sándorfy, Editor. 1999, Kluwer Academic Publishers: New York. p. 479.

49. W.A. Chupka, J. Chem. Phys., 1993. **98**(6): p. 4520.

50. W.A. Chupka, J. Chem. Phys., 1993. **99**: p. 5800.

51.   J. Jortner and M. Bixon, Ber. Bunsenges. Phys. Chem., 1995. **99**: p. 296.

52.   M.J.J. Vrakking and Y.T. Lee, J. Chem. Phys., 1995. **102**: p. 8818.

53.   M. Bixon and J. Jortner, J. Phys. Chem., 1995. **99**: p. 7466.

54.   M.J.J. Vrakking and Y.T. Lee, Phys. Rev. A, 1994. **51**: p. R894.

55.   F. Merkt, J. Chem. Phys., 1994. **100**: p. 2623.

56.   F. Merkt and R.N. Zare, J. Chem. Phys., 1994. **101**: p. 3495.

57.   M.J.J. Vrakking, I. Fischer, D.M. Villeneuve, and A. Stolow, J. Chem. Phys., 1995. **103**: p. 4538.

58.   K. Müller-Dethlefs and E.W. Schlag, Angewandte Chemie International Edition, 1998. **37**(10): p. 1346.

59.   F. Merkt and T.P. Softley, The Journal of Chemical Physics, 1992. **96**(6): p. 4149-4156.

60.   F. Merkt and T.P. Softley, Phys. Rev. A, 1992. **46**: p. 302.

61.   F. Merkt, R.J. Rednall, S.R. Mackenzie, and T.P. Softley, Phys. Rev. Lett., 1996. **76**: p. 3526.

62.   F. Merkt, H. Xu, and R.N. Zare, J. Chem. Phys, 1996. **104**: p. 950.

63.   I. Fischer, R. Lindner, and K. Müller-Dethlefs, J. Chem. Soc. Faraday Trans., 1994. **90**: p. 2425.

64.   R. Lindner, H.J. Dietrich, and K. Müller-Dethlefs, Chem. Phys. Lett., 1994. **228**: p. 417.

65.   L. Zhu and P.M. Johnson, J. Chem. Phys., 1991. **94**(8): p. 5769.

66.   H. Krause and H.J. Neusser, J. Photochem. Photobiol. A, 1994. **80**: p. 73.

67.   T.L. Grebner and H.J. Neusser, Int. J. Mass Spectrom. Ion Proc., 1996. **159**: p. 137.

68.   C. Unterberg, A. Gerlach, A. Jansen, and M. Gerhards, Chemical Physics, 2004. **304**(3): p. 237.

69.   Y. Xie, H. Su, and W.B. Tzeng, Chem. Phys. Lett., 2004. **394**(1-3): p. 182.

70.   J.L. Lin and W.B. Tzeng, Chem. Phys. Lett., 2003. **380**: p. 503.

71.   J.L. Lin, S. Zhang, and W.B. Tzeng, J. Chem. Phys., 2004. **120**(11): p. 5057.

72.   H. Su, M. Pradhan, and W.B. Tzeng, Chem. Phys. Lett., 2005. **411**(1-3): p. 86.

73.   C.H. Kwon, H.L. Kim, and M.S. Kim, J. Chem. Phys., 2003. **119**: p. 215.

74.   E.W. Schlag, S. Schneider, and S.F. Fischer, Annual Review of Physical Chemistry, 1971. **22**(1): p. 465.

75.   C.H. Kwon, H.L. Kim, and M.S. Kim, J. Chem. Phys., 2003. **118**: p. 6327.

76.   Y.J. Bae, M. Lee, and M.S. Kim, J. Chem. Phys., 2005. **123**(4): p. 044306.

77.   S. Choi, K.W. Choi, S.K. Kim, S. Chung, and S. Lee, J. Phys. Chem. A, 2006. **110**(49): p. 13183.

78.   M. Lee and M.S. Kim, J. Phys. Chem. A, 2006. **110**(30): p. 9377.

79.   Y.J. Bae and M.S. Kim, International Journal of Mass Spectrometry, 2007. **267**(1-3): p. 89.

80.   J.E. Braun, T. Mehnert, and H.J. Neusser, Int. J. Mass. Spectrom., 2000. **203**: p. 1.

81.   H. Krause and H.J. Neusser, J. Chem. Phys., 1993. **99**: p. 6278.

82. J.E. Braun, T.L. Grebner, and H.J. Neusser, J. Phys. Chem. A, 1998. **102**: p. 3273.

83. S.R. Haines, C.E.H. Dessent, and K. Müller-Dethlefs, J. Chem. Phys., 1999. **111**: p. 1947.

84. K.C. Smyth, J.A. Schiavone, and R.S. Freund, The Journal of Chemical Physics, 1973. **59**(10): p. 5225.

85. R.S. Freund, *High-Rydberg molecules*, in *Rydberg states of atoms and molecules*, R.F. Stebbings and F.B. Dunning, Editors. 1983, Cambridge University Press: Cambridge.

86. B. Ernstberger, H. Krause, A. Kiermeier, and H.J. Neusser, J. Chem. Phys., 1990. **92**: p. 5285.

87. N. Ohmichi, Y. Malinovich, J.P. Ziesel, and C. Lifshitz, J. Phys. Chem., 1989. **93**: p. 2491.

88. H.J. Neusser and H. Krause, Int. J. Mass Spectrom. Ion Proc., 1994. **131**: p. 211.

89. H. Krause, B. Ernstberger, and H.J. Neusser, Chem. Phys. Lett., 1991. **184**: p. 411.

90. M.C.R. Cockett, Chem. Soc. Rev., 2005. **34**: p. 935.

91. H.J. Dietrich, K. MüllerDethlefs, and L.Y. Baranov, Phys.Rev.Lett., 1996. **76**: p. 3530.

92. H. Palm and F. Merkt, Chemical Physics Letters, 1997. **270**(1-2): p. Chemical Physics Letters 1.

93. M.C.R. Cockett, M. Takahashi, K. Okuyama, and K. Kimura, Chemical Physics Letters, 1991. **187**(3): p. 250.

94. C.E.H. Dessent, S.R. Haines, and K. Müller-Dethlefs, Chem. Phys. Lett., 1999. **315**: p. 103.

95. U. Hollenstein, R. Seiler, H. Schmutz, M. Andrist, and F. Merkt, J.Chem.Phys., 2001. **115**: p. 5461.

96. J.G. Goode, J.E. LeClaire, and P.M. Johnson, Int. J. Mass. Spec. Ion Processes, 1996. **159**: p. 49.

97. M.G.H. Boogaarts, I. Holleman, R.T. Jongma, D.H. Parker, and G. Meijer, J. Chem. Phys., 1996. **104**: p. 4357.

98. F. Merkt, S.R. Mackenzie, and T.P. Softley, J. Chem. Phys., 1993. **99**: p. 4213.

99. H.J. Dietrich, R. Lindner, and K. Müller-Dethlefs, J. Chem. Phys., 1994. **101**: p. 3399.

100. M. Gerhards, M. Schiwek, C. Unterberg, and K. Kleinermanns, Chem. Phys. Lett., 1998. **297**: p. 515.

101. A. Fujii, T. Sawamura, S. Tanabe, T. Ebata, and N. Mikami, Chem. Phys. Lett., 1994. **225**: p. 104.

102. A. Fujii, A. Iwasaki, T. Ebata, and N. Mikami, J. Phys. Chem. A, 1997. **101**: p. 5963.

PART III

Studies of biologically relevant molecules and hydrogen-bonded complexes

CHAPTER VII

Experimental setup

The accomplishment of threshold ion spectroscopy experiments in our lab has been made possible with the use of an adequately built experimental setup. The original apparatus [1-3] was modified in terms of software upgrades and hardware implementations to respond to the contemporary goals of studying relative large molecular species and their hydrogen bonded complexes as well as achieving better control over the experimental conditions and more flexible and easy-to-handle data acquisition.

The experimental setup employed for the purposes of threshold ion mass spectroscopy in the present work consists of three main components:

- light sources (two dye lasers pumped by an excimer laser);
- an inlet system coupled to a linear ReTOF mass spectrometer;
- an electronic control block
- a signal averaging stage
- a data acquisition and processing block.

The different components of the apparatus are described in detail in the following sections.

VII.1. Lasers

VII.1.1. Excimer laser

The excimer laser ("EMG 1003i", Lambda Physik), operates in a pulse regime with a XeCl mixture as laser medium at wavelength of 308 nm. The width of the pulse is about 17 ns (FWHM) and the repetition rate is typically 10 Hz. The output of the laser is about 200 mJ and is sufficient to pump synchronously the two dye lasers, employed in the experiment.

VII.1.2. Dye lasers

The dye lasers ("LPD 3000" and "FL 3002", Lambda Physik) operate in a pulse regime and use pump driven dye circulators (Radiant dyes) with quartz cells. Both lasers are equipped with a light amplifying stage in addition to the oscillator compartment (resonator) and thus each one can be used either as an excitation laser or as an ionization laser. The lasers can be scanned over the fluorescence spectrum of the particular dye in use through a stepping motor driven grating in the resonator. The lasers operate usually in the visible wavelength region and therefore each one uses a second harmonic generation (SHG) crystal for supplying UV light pulses. The used SHG crystals are:

BBO-1	β-barium borate type 1 phase matching, θ=52°, φ =90°, 440 − 630 nm
BBO-2	β-barium borate type 1 phase matching, $\theta = 78°$, φ =90°, 410 − 442 nm
KDP	Potassium Dihydrogen Phosphate type 1 phase matching, $\theta = 76°$, φ =45°, 540 − 690 nm

The stepping motors of the grating and the SHG crystal in each dye laser can be synchronously run either internally (by applying an input TTL pulse to trigger the internal counter) or externally (by a computer through a GPIB interface).

In some cases it was more adequate to use the first harmonic frequency of UV dye instead of the SHG output from a dye lasing in the visible part of the spectrum. The most commonly used dyes in our experimental setup are listed in **Table VII.1**:

dye	solvent	tuning range, nm	λ_{max}, nm	efficiency, %
QUI	DI	364 –404	390	12
PBBO	PC	386 – 430	399	8
RDC 360-Neu	MeOH	338 – 365	355	18
Stilbene 3	Me/PC	409 – 460	428	12
Coumarin 153	MeOH	520 – 602	544	16
Rhodamine 6G	MeOH	570 – 610	580	16
DCM	PC	605 – 698	640	15

Table VII.1. Typical dyes used as active lasing media in "LPD 3000" and "FL 3002" in the experiments on threshold ions in the present work.

VII.2. Reflectron TOF spectrometer and inlet system

The linear ReTOF mass spectrometer has been originally designed by Krause [1] on the basis of Mamyrin's and Della Negra's fundamental works [2-4] and has later sustained some modifications regarding its construction. A schematic view of the apparatus (inlet system and the linear ReTOF spectrometer) in its present form is given in **Fig.VII.1**.

The housing comprises as a main chamber a cylindrical stainless steel tube (length: 150 cm, diameter: 20 cm) with a coupled to it cubic forechamber (length: 33 cm) accommodating the pulsed nozzle body. The main chamber is kept under high vacuum ($10^{-8} - 10^{-9}$ mbar) through the implementation of a cylindrical turbomolecular pump P2 at the bottom of the housing (TPU 520, Pfeiffer Balzers 520 l/s) while the vacuum in the forechamber sustained by another cylindrical turbomolecular pump P1 (TPU330 Pfeiffer Balzers 330 l/s) pump is considerably lower (10^{-3} mbar).

VII.2.1. Linear ReTOF spectrometer

Our linear ReTOF spectrometer consists of four functionally distinguishable subsections and components: ion optics, drift region, reflectron and ion detector.

Fig.VII.1. A schematic view of the apparatus (inlet system and the linear ReTOF mass spectrometer). Also shown is the jet direction inside the spectrometer.

Ion Optics

The ion optics consists of three graphite coated metal discs (plates) each with a central opening. The discs form two zones (Z1 and Z2) with length distances of 3 cm and 2 cm, respectively. The supersonic jet entering the first zone is accessible to the excitation (ionization) laser beam(s) through built-in circular windows.

Depending on the particular experiment, voltages of different magnitudes, duration, and polarity as well as time delays with respect to the triggering of the excimer laser are applied on each of the plates.

Drift region

This is the field-free region in the TOF spectrometer. The construction of our main vacuum chamber allows for a variation in the length of the drift region (see **Reflectron**).

Reflectron

The reflectron consists of a series of equidistantly placed metal blends held by Teflon rings, which also provide their electrical insulation [1]. This construction ensures a homogenous field in the reflectron and is similar to that suggested by Weinkauf [2]. A voltage of $1.8 - 2$ kV is applied at a potential divider connected to the metal blends which builds up a linearly increasing reflecting potential (soft reflection). The potential divider consists of a series of resistances (1 MΩ each). The field is confined within the reflectron by two fine Copper meshes with a transmission of 90%. The reflectron is positioned on mechanically adjustable rails (length: 1.05 m) that enable its movement and therefore a variation in the length of the drift region (between 1 m and 2 m). Such a construction allows for a more flexible use of the reflectron depending on whether a high mass resolution (at larger drift region lengths) as in the case of cluster studies or enhanced transmission (at shorter drift region lengths) is needed.

Ion detector

The ion detector is mechanically connected to the ion optics in a homemade construction and consists of two microchannel plates (Photonis Long-Life^{TM}) in a Chevron assembly with central holes (**Table VII.2**). The gain of this configuration at 2.2 kV is $\sim 10^7$.

Type:	Thickness of each plate, mm	Min. quality diameter, mm	Outside diameter, mm	Central hole diameter, mm	Channel diameter, μm
S40-10-D60-CH-SET	0,61	40	50.4	6.4	10

Table VII.2. Mechanical characteristics of the microchannel plates used in a Chevron assembly as an ion detector

VII.2.2. Inlet system

The inlet system consists of a nozzle (initially homemade, replaced by General pulse valve: Series 9) mounted on a homemade body connected to a carrier gas container and to a small reservoir of solvent molecules vapors outside the forechamber. The reservoir is needed in experiments on weakly bound complexes. The solvent has to have relatively high vapor pressure and therefore volatile solvents such as water, benzene, methanol, etc. are typically used. The solvent vapor pressure can be increased if needed by heating the reservoir in a boiling water bath.

The carrier gas is usually Ar since it favors the collisional cooling due to its large atomic mass. The carrier gas and the solvent molecules vapors are introduced as a mixture in the nozzle, where they mix additionally with the vapors of the investigated sample. The necessary vapor pressure of a few mbar of the studied species is achieved by heating a small container filled with the sample and mounted near the nozzle valve. The heating is realized and controlled by a "Minco CT15" temperature controller.

In the case of the homemade nozzle [3] water cooling was needed for temperatures above 100°C and the operation temperature of the nozzle was limited to 150°C. These problems were overcome with the implementation of a modified General Valve nozzle, operating without additional cooling up to 150°C – 160°C.

Skimmer

The homogenized gas mixture of the sample vapors, the carrier gas (Ar or Ne at 2 – 3 bar) and optionally of the solvent vapors (~ 25 mbar) is seeded by the nozzle valve through a conical skimmer into the high-vacuum chamber where it is introduced in the form of a supersonically expanded cold molecular beam and interacts with the laser beam(s) in zone Z1 of the ion optics. The use of a skimmer leads to a selection of the central part of the molecular beam (along its axis) with a cross-section of ~ 2 mm only, while the rest of the molecules are cut off and pumped out from the forechamber. This has the following consequences:

-   The light-matter interaction that takes place in the first zone of the ion optics (Z1, **Fig.VII.1**) is thus limited to a very small region comparable to the lasers beam profile.

- Species in a skimmed molecular beam have very low velocities in a (anti) parallel direction of the laser beams (perpendicular to the jet propagation direction), which greatly reduces the Doppler broadening.

- The pressure in the main chamber is kept low ($10^{-7} – 10^{-6}$ mbar) even at a long opening times of the nozzle. This on one hand impedes the formation of extra spatial charges that might affect the signal and on the other hand prevents the electronic components (ion optics, ion detector, reflectron) operating at high voltage from damage. Also, the concentration of particles in the molecular jet is reduced which favors their collision-free propagation.

VII.3. Electronic block

Master trigger: generates a starting TTL pulse sequence (typically 10 Hz, in some cases up to 25 Hz). Each pulse triggers the nozzle and the delay generator at moment t_0.

Delay generator: DG535 (four channel digital delay/pulse generator) sets a time delay between the opening of the nozzle valve and the triggering of the excimer laser.

Digital oscilloscope: Oscilloscope LeCroy 9350A for visualizing the threshold ion signal as well as for aiding the positioning of the gates and adjusting their widths.

Gated boxcar analog integrator: integrates the signal from the MCPs between a start time point $\tau_0 + \tau_a$ and an end time point $\tau_0 + \tau_b$. Both τ_a and τ_b can be varied uniformly or independently so the integrated time domain can be modified in terms of delay with respect to τ_0 and width. Two boxcar integrators have been employed in experiments on complexes for collecting the MCP signal simultaneously at two time (mass) channels, the parent and the fragment channel.

Analog-digital (ADC) and digital-analog (DAC) converters: a series of TTL channels that set the communication between the PC and the experimental apparatus and electronics.

PC, Software: The software is developed under LabView and has the following functions:

- scanning of the dye lasers (i.e. the control of the stepping motors for the gratings and for the SHG crystals);
- calibration of the SHG crystals;
- data acquisition (DAQ) and processing of the signals from the gated boxcar integrators.

The software program sets a start and an end point for the scan, a scanning step and tuning parameters of DAQ. The program also offers a graphical representation of the spectra at two (or more) mass channels. Each point on the spectral curves is a *software average* from 1 (no averaging) to typically 10 or 30 measurement cycles.

VII.4. Experimental sequence

An overall view of the experimental setup and the connections (electrical or optical) between its different components is represented in **Fig. VII.2**. The following steps describe one measurement cycle.

1. The master trigger generates a starting TTL pulse sequence (typically 10 Hz, in some cases up to 25 Hz). Each pulse sets a measurement cycle by triggering the nozzle and the delay generator at moment t_0.

2. The delay generator sends a triggering signal to the excimer laser at a moment $t_0 + t$, where t is set typically in the $700 - 900$ µs range.

3. The excimer laser pumps the two dye lasers and feedbacks the electronic block by triggering a photodiode. Both dye lasers generate usually in the visible region of the spectrum so each laser is equipped with a SHG crystal. The two dye lasers beams are steered by a system of guiding optics into the first zone Z1 of the linear ReTOF mass spectrometer where they target the supersonically expanded molecular beam.
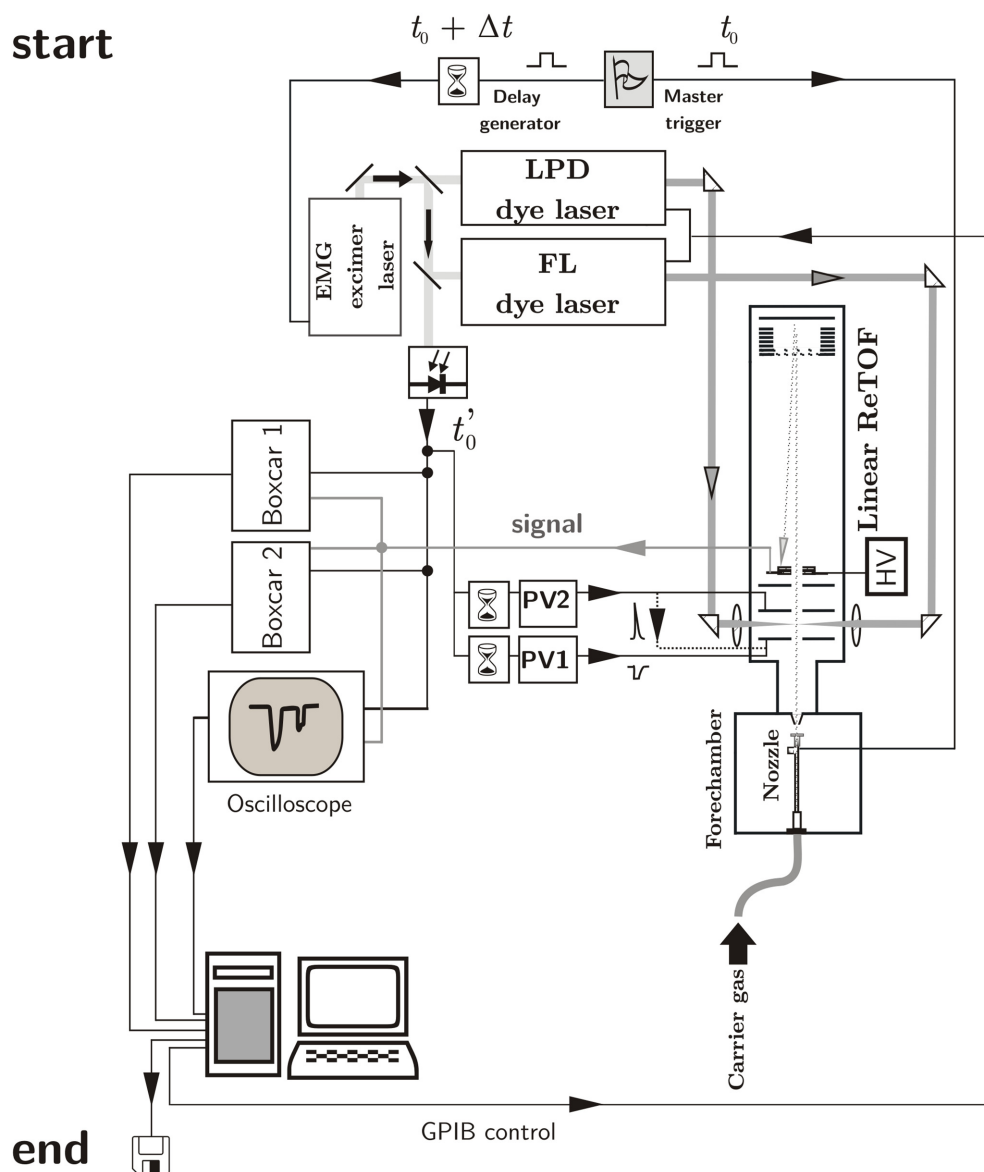
Fig.VII.2. An overall schematic view of the experimental setup employed for REMPI and MATI studies in the present work. Also shown is the optical and electrical control between the different components in one measurement cycle. For more details see text.

4. The feedback from the photodiode has the following function: it sets a zero time moment t'_0 for triggering of the boxcar integrators and the pulsed voltage supplies (PV1 and PV2 on **Fig.VII.2**). The measurement cycle splits here in two different schemes of applying voltages to the ion optics of the ReTOF spectrometer, depending on the particular experiment, REMPI or MATI.

5. REMPI (See **Fig.VIII.3a**)

   The laser(s) ionize the neutral species at t'_0. The so produced photoions are acelerated by the applied voltage (+1000 V) from the pulser PV2 towards the reflectron.

6. MATI (See **Fig.VII.3b**)

   A negative voltage of 1 V is applied from PV1 at time $t'_0 + 100$ ns on the first plate in Z1 of the TOF spectrometer. This is the separation electric field that discriminates spatially the photoions from the Rydberg species. The value of 1 V is not universal, but may be altered depending on the experimental conditions. At $t'_0 + \delta t$ [μs] (usually $\delta t \sim 20$ μs) the Rydberg species that have survived the ionization caused by the separation voltage and the time delay are pulsed field ionized in Z2 and subsequently accelerated towards the reflectron by applying a positive voltage on the second plate of the ion optics from PV2.

7. The photoions (in REMPI) or the threshold ions (in MATI) are accelerated towards the reflectron and after their reflection are collected by the MCP detector. In both cases the signal is transmitted to the oscilloscope and the gated boxcar integrator(s) where it is selected and discriminated according to the position of the electric gate(s). The output from the boxcar integrators is digitized and then processed in a PC.

In REMPI the strength of the signal depends on the concentration of the ionized species and together with the mass-resolution also on the focusing and the intensities of the laser beam(s). A relatively strong dependence of the signal strength on the opening time of the nozzle was also observed (for both types of nozzles) in the experiments in our lab. The optimal working pressure was found to be about 2 to 3 times higher than the zero value (at closed nozzle). In addition in MATI one has to solve the problem of finding the opti-
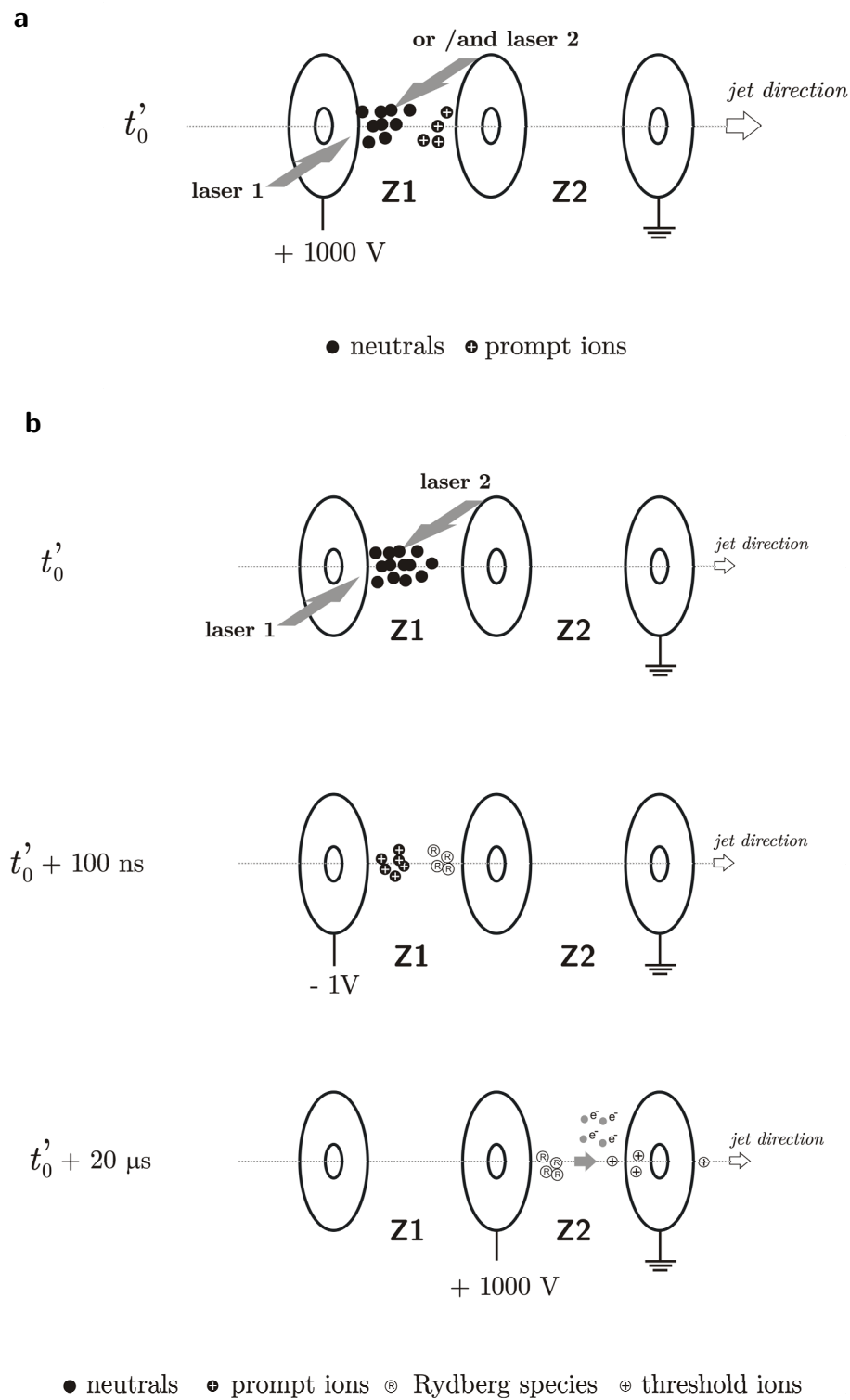
Fig.VII.3. Excitation and ionization sequences in REMPI (a) and MATI (b) experiments. For details see text.

mal combination of the following experimental parameters in order to obtain a maximal prompt ions-free and well mass-resolved threshold ion signal (at fixed position of the reflectron):

separation voltage strength – prompt ions signal strength – MCPs voltage – time delay δt.

Also, the signal from the ion detector in case of MATI is much weaker than the prompt ion signal (in REMPI) and therefore is usually electrically amplified.

In both cases the mass-resolution and the strength of the signal at a certain gate position depend on the reflecting voltage (at fixed reflectron position).

In studies of weakly bound complexes, both the REMPI and the MATI signal were found to depend slightly on the distance between the nozzle and the skimmer.

CHAPTER VIII

MATI spectroscopy and theoretical studies of 3-methylindole and its 1:1 hydrogen-bonded complexes with water and benzene

This chapter focuses on the two-photon REMPI (R2PI) and, in particular, on the mass analyzed threshold ionization study of 3-methylindole (3MI) [4] and two complexes, $3MI \cdot H_2O$ [4] and $3MI \cdot C_6H_6$ [5], which represent prototypes of hydrogen bonding in biological systems. The experimental findings confirm the N-H$\cdots$O bonding in $3MI \cdot H_2O$ and strongly suggest a NH$\cdots\pi$ type hydrogen bonding for the $3MI \cdot C_6H_6$ complex. The measured ionization energies and, for the latter two systems, the ionic dissociation thresholds E_0, are used for calculating the binding energies D_0 in the ground neutral state of the respective complexes.

Furthermore, the experimental results on the studied systems are compared with those on their unsubstituted analogues (indole, indole·H_2O, and indole·C_6H_6) in order to elucidate the effect of methyl group substitution at position 3 in the indole ring on the excitation and ionization energy as well as on the hydrogen-bond strength.

The threshold ionization studies of 3MI, $3MI \cdot H_2O$, and $3MI \cdot C_6H_6$ systems are supported and complemented by quantum chemical calculations. The latter are implemented also for elucidating the role of methylation, ionization and complex formation regarding the geometrical changes in the indole ring.

All calculations were performed with the GAUSSIAN 03 suite of programs [118].

VIII.1. Introduction

3-methylindole, (4-Methyl-2,3-benzopyrrole) is a metabolite product of tryptophan, one of the essential amino acids in the human diet and a biochemical precursor for serotonin (a neurotransmitter) and melatonin (a neurohormone). 3MI is used in the synthesis of dyes, pigments, as well as in pharmaceutics.

Similarly to indole, 3MI has a bicyclic structure that consists of a phenyl ring fused to a pyrrole ring (**Fig.VIII.1**) with the hydrogen at C3 site (position) being substituted by a methyl group. As in indole and pyrrole, the lone electron pair at nitrogen is not readily available to acids but is part of the aromatic system which renders 3MI a *weak* base in contrast to other amines.
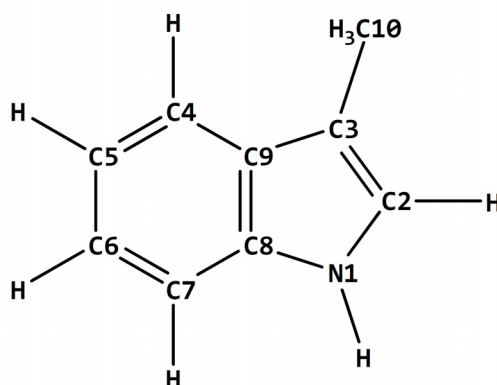
Fig.VIII.1. Structure of 3-methylindole. Also shown is the carbon and nitrogen nuclei numbering.

It is generally known that the effect of any substituent on the chemical and spectroscopic properties of a molecular system depends on two main factors: the nature of the substituent and the site of substitution. The C3 position in indole is of great importance in chemical synthesis [6, 7] since it is the preferred binding site in alkylation [8] and particularly electrophilic substitution reactions [7] (and references therein), [9]. The alkylation synthesis of 3MI from indole has been demonstrated in some recent works [10, 11]. On the other hand, C3 is the site where the alanyl side chain is attached to the chromophore (indole) in tryptophan. Therefore 3MI seems to be an appropriate system for investigating how the spectroscopic properties of indole are affected by alkyl substitution at C3

site, and accordingly how appropriate indole is as a spectroscopic model for tryptophan. Also, hydrogen-bonded complexes of indole with various solvents serve as prototypes for noncovalent interactions that involve large biomolecules and are often under the influence of various substituent groups. In this regard, comparative studies of hydrogen-bonded complexes with indole and 3MI as solutes may shed light on the methyl substitution effect on the hydrogen-bond properties in such systems.

3MI lends itself as a suitable model molecule for investigating these problems in supersonic jet studies because of its chemical and physical properties:

- It is volatile enough to be seeded in a sufficient concentration in supersonic beams at a relatively mild heating ($\sim 90°C$);

- the molecule is small with a rigid skeletal structure and no long side chains. Therefore there exists only one conformer and the interpretation of ionization, absorption and fluorescence spectra is relatively uncomplicated and straightforward.

- The molecule is chemically stable even upon longer heating. Moreover it does not contain halogen atoms or other chemically active groups and is thus inert to reactions with other possibly present molecules in the jet or with the inlet system (O-rings, sample holders).

<div align="center">***</div>

Most of the experimental and theoretical research work on the spectroscopy of 3MI and its hydrogen-bonded complexes with various solvents as well as on the substitution effect in such systems has been focused on the neutral species in their S_0 and S_1 states [10-19]. Previous studies have reported that absorption [12] and emission [13] spectra of 3MI are very similar to those of tryptophan. It has been therefore proposed that the methyl group at C3 position has similar effect on the indole ring as the alanyl side chain in tryptophan and accordingly that 3MI serves as a better spectroscopic model than indole [14]. On the other hand, the effect of alkyl substitution in 3MI has been studied in the light of a more general research on indoles and indole hydrogen-bonded complexes. In particular, a large body of experimental and theoretical data [13-17] has been collected and interpreted with respect to studies of the relative energy difference of two electronically excited states that exist in indoles: ^1L_b (lower) and ^1L_a (upper) [15, 16]. These states lie close in energy and may in certain cases experience mixing through vibronic coupling. ^1L_a state is of great

interest in protein spectroscopy since it is considered to be responsible for the observed large red shifts in the fluorescence of tryptophan in polar solvents. However, despite the acknowledged role of the ^1L_a state as an indicator for tryptophan-environment interactions, finding evidence for ^1L_a absorption and emission in indoles has turned out to be a challenging task.

A widely exploited concept concerning the substitution effect in indole in previous studies is that the $^1L_a - {}^1L_b$ energy gap depends on the site of methylation. This has been explained with the different change in energy of the two electronically excited states upon substitution. ^1L_b has been shown to be localized mainly in the phenyl moiety while ^1L_a has been associated with the ethylene fragment (C2=C3) in the pyrrole ring [17]. Consequently, methylation in the phenyl ring causes greater lowering of the ^1L_b state and concomitant increase of the $^1L_a - {}^1L_b$ energy gap. In contrast to this effect, methyl group substitution in the pyrrole ring, particularly at C2 and C3 positions, lowers the ^1L_a state to a larger extent than the ^1L_b state and thus decreases the difference in the ^1L_a and ^1L_b energies. In this regard it has been suggested that 3MI has very closely lying ^1L_a and ^1L_b states [18], although the lowest excited state is still, as in indole, ^1L_b [14], [18], [19]. In other words, the $S_1 \leftarrow S_0$ origin corresponds to a $^1L_b \leftarrow {}^1A$, 0_0^0 transition. However, many features in the fluorescence and excitation spectra of 3MI below 1000 cm^{-1} above the origin have been described as having a ^1L_a character [18], [19] due to the aforementioned small $^1L_a - {}^1L_b$ energy difference.

Polar solvents are considered to decrease the $^1L_a - {}^1L_b$ energy gap as ^1L_a state is considered to possess a much larger dipole moment than ^1L_b and thus to be more strongly stabilized in polar environment. For substituted indoles and 3MI in particular, this may in certain cases lead to ^1L_a coming very close to ^1L_b and even below it, thus becoming the lowest excited electronic state in a polar solvent. Fluorescence experiments on hydrogen-bonded complexes of indoles with various solvents Y have led to the conclusion that the $^1L_a - {}^1L_b$ energy difference decreases as the proton affinity of the solvent molecule increases [20], [14]. According to these findings, for solvents with proton affinities less than 200 kcal/mol, ^1L_b of 3MI·Y hydrogen-bonded complexes can be still considered the lowest excited state (S_1) although near 200 kcal/mol the $^1L_a - {}^1L_b$ mixing is substantial and the $S_1 \leftarrow S_0$ origin may partially acquire a ^1L_a character.

It has been also shown that there is a correlation between *the ratio* of the hydrogen-bond strength in S_0 and S_1 states and the solvent proton affinity [20]. For hydrogen-bonded complexes of 3MI with solvents having proton affinities less/more than 200 kcal/mol, hydrogen bonding is considered to be stronger/weaker in the ground neutral state S_0 than

in S_1 [14], [20]. Such conclusion has been drawn on the basis of a linear dependence of the $S_1 \leftarrow S_0$, 0_0^0 complexation-induced red shift on the solvent proton affinity [20].

All these findings fit well with the model of hydrogen bonding at the N1–H1 site, i.e. between 3MI (or, generally speaking, indoles) as hydrogen-bond donors and solvents as hydrogen bond acceptors [20], [21]. Such type of bonding for 1:1 complexes of indole and 3MI has been deduced from the shift of the N–H stretching vibration measured with resonant ion-dip infrared spectroscopy [22], [23], as well as from the results of high-resolution R2PI experiments and rotational contour analysis [24], mass selective threshold ionization studies and *ab initio* calculations [25]. A different type of bonding in which indoles serve as hydrogen-bond acceptors in 1:1 complexes, has been experimentally suggested and theoretically predicted for 1-methylindole·H_2O system [22], [26].

<p align="center">***</p>

Despite the intense research on the ground and excited state of methylated indoles and their hydrogen-bonded complexes, there is relatively still little experimental spectroscopic information available on the ionized species of such systems [25-30]. Studies of the properties of hydrogen bonding and the substitution effect on these properties in the ground cationic state D_0 may be greatly alleviated with threshold ionization spectroscopy. As already pointed out (**Chapter VI**) pulsed field ionization techniques enable investigation on the vibrational (in MATI) and, in certain cases, the rotational (in ZEKE) structure of cations of molecules and molecular complexes. In addition, the ability of discriminating the threshold ions with respect to their masses renders MATI a suitable tool for studying the dissociation dynamics of weakly bound systems and therefore the *absolute* strength of the intermolecular bonding in D_0 and S_0 states as discussed in *Section VI.3.4.*

For indole and methylated indoles as well as for their noncovalently bonded complexes ionization techniques are particularly appropriate since the chromophore[1] is a rigid system. Therefore no prominent changes in the Franck-Condon factors for the $D_0 \leftarrow S_0$ transition due to large geometrical distortions or conformational changes upon ionization are likely to occur. This, on the one hand, is a prerequisite for the precise determination of the adiabatic ionization threshold with a high signal-to-noise ratio. On the other hand, it presumably allows for a sharp vibrational structure in the low excess energy region to be

---

[1]**The excitation and ionization of the complexes occur usually only in the indole (or methylated indole) moiety. The solvent molecules have in most cases (water, methanol, benzene...) ionization potentials much higher than these of indoles.**

obtained, in particular regarding peaks corresponding to the methyl group motion as well as bending and stretching modes of the hydrogen bond.

The goal of the present chapter is to demonstrate the application of Mass Analyzed Threshold Ionization as a suitable spectroscopic tool for the study of 3MI and two model hydrogen-bonded complexes: $3MI \cdot H_2O$ and $3MI \cdot C_6H_6$. The experimental results on the adiabatic ionization energies and the vibrational spectroscopy of the ionized species as well as on the properties of hydrogen bonding in the studied systems are supported and complemented by quantum mechanical calculations. Optimized molecular geometries, vibrational frequencies, ionization energies and binding energies in the S_0 and D_0 states are determined at the second order Møller-Plesset theory and DFT level employing the B3LYP functional. The agreement of the computational results with the experiment for both methods as well as discrepancies arising from the implementation of different basis sets are discussed.

DFT B3LYP calculations have been applied for the studies of hydrogen-bonded complexes [27, 28] and van der Waals complexes [29]. In particular, several works have demonstrated the successful implementation of DFT with the B3LYP functional for the studies of indole and substituted indoles as well as of their hydrogen-bonded complexes with water [20, 28-31].

The suitable application of the DFT B3LYP method in the aforementioned studies suggested the use of the same level of theory in the present theoretical treatment of 3MI and its hydrogen-bonded complexes with water and benzene. In addition, the MP2/cc-pVDZ calculations were carried out in order to compare the performance of two conceptually different approaches: DFT (dealing with electron density) and *ab initio* calculations (based on the concept of the wavefunction).

VIII.2. Experimental conditions

3MI was continuously heated to 95 – 100 °C in a small container built in the nozzle and located at about 3 cm behind the nozzle orifice in order to achieve sufficient vapor pressure. The buffer gas (Ar; at 2 – 2.5 Bar) was introduced in the nozzle through a system of thin tubes from the gas bottle. The mixture of 3MI vapors and Ar was left to homogenize 10 to 15 minutes prior to the measurement. In the case of studies of hydrogen-bonded complexes, water or benzene vapors were introduced in the inlet system prior to the filling of the nozzle body with Ar. A direct insertion of a drop of water or benzene in the 3MI container did not lead to an increase of the cluster signal but often reduced the signal intensity instead.

The output pulse energy of the excimer laser was ensured to be at least 160 mJ so that the dye lasers be efficiently pumped as well as the second harmonic generation in the BBO crystals be possible. The LPD dye laser (*Section VII.1.2*) was used as an excitation light source and the FL laser was used as an ionizing or a second-step excitation light source. The FL dye laser was almost exclusively operated with some degree of attenuation in order to avoid ionization saturation and a consequent peak broadening. This necessity was particularly important for reducing the direct ion signal in the threshold ionization measurements. In the case when UV dye (especially RDC Neu) was used, a filter was often needed for additional attenuation of the light intensity prior to its entrance in the vacuum chamber.

Both dye lasers were calibrated with a wavelength-meter (WaveMaster, "Coherent") which operates in a wavelength range from 380 to 1095 nm with an accuracy of 0.005 nm and a resolution of 0.001 nm.

The MCPs (*Section VII.2.1*) were set, depending on the experimental conditions, at − 1.65 to − 1.85 kV for measurements of the total ion current (R2PI) and at about − 1.90 kV for detection of threshold ions in the case of bare 3MI. In the study of hydrogen-bonded complexes the voltage at the MCPs was increased up to − 2.10 kV because of the lower ion yield in this case. The threshold ion signal in all studies was electrically amplified in order to achieve sufficient intensity and an optimal signal-to-noise ratio.

The experiments were carried out in two main steps:

- optimizing the experimental parameters in order to achieve strong intensity of the signal and high mass resolution under lowest possible laser intensities and applied voltages (high-voltage, separation voltage, voltage at the MCPs).

- measurements by performing multiple scans (up to 5) over a wide spectral region over long times, while keeping the experimental conditions as constant as possible. The latter were checked after every complete scan. The recorded signal was processed under LabView in such a way that each experimental point of the spectrum was an average of 40 to 50 single measurement cycles (Section VII.4). The scanning program featured a backup-subroutine that saved the obtained spectrum after each recorded experimental point. In this way an output file containing the spectrum with the latest scanned point (wavelength, signal) was generated in real time. This procedure prevented data loss in cases of a hardware or software malfunction or abrupt changes in the experimental conditions. On the other hand, it allowed for processing the available data in the backup file in other programs (Origin, Excell) before the end of the scanning.

The experimental conditions were optimized prior to every measurement by monitoring the signal at the mass channel(s) on the digital oscilloscope. The width of the signal at the mass channel(s) was controlled and optimized by:

- adjusting the ion optics of the linear ReTOF mass spectrometer

- adjusting the voltages at the reflectron

- tuning the delay time of the delay generator

In the case of threshold ion measurements it was additionally necessary to find

- an appropriate delay time for applying the high voltage on the second plate of the ion optics in the ReTOF mass spectrometer;

- the best trade-off between the separation voltage applied at the first plate of the ion optics in the ReTOF mass spectrometer and the voltage at the MCPs. Higher

separation voltages resulted primarily in stronger reduction of the direct ion signal than in decrease of the threshold ion signal (the latter being a consequence of losses of Rydberg molecules due to field ionization induced by the separation voltage, Section VI.2.). This allowed a relatively low voltage at the MCPs to be applied without deteriorating the signal-to-noise ratio due to direct ion background. However, for considerably weak peaks in the threshold ion current spectrum a weaker separation voltage was needed as well as a higher voltage at the MCPs. The settings were adjusted accordingly to the overall performance of the ion signal (both direct and threshold) that differed slightly from day to day but remained constant within 4 or 5 full scans.

When the adiabatic ionization energy AIE of the bare 3MI or a complex was found, the experimental conditions were often optimized at that wavelength, i.e., primarily further minimizing the direct ion signal and optimizing the separation voltage amplitude. A still finer optimization was achieved at threshold ion peaks of considerably smaller intensity although this often involved an additional adjustment of the ion optics position with the micrometric screws as well as the position of the nozzle.

VIII.3. 3-methylindole

VIII.3.1. 3-methylindole R2PI

The R2PI two-color spectrum of 3MI is shown in **Fig.VIII.2**. The $^1L_b \leftarrow {}^1A$ origin is located at 34 875.1 cm^{-1}. Within the error of the present experiment[2], this value agrees with the values for the $S_1 \leftarrow S_0, 0_0^0$ rotationless transition taken from high-resolution experiments in our group, 34 874.7 cm^{-1} [30] and also with the value reported by Remmers et al. [31]. The bands at 420 and 608 cm^{-1} marked with A and B, respectively, are used as intermediate states for the MATI spectra of the monomer. Lin et al. [32] have assigned these bands as out-of-plane N–H bending and in-plane C–C–C bending, respectively. The origin and the peaks at 420 (A) and 608 (B) cm^{-1} exhibit a split profile. The value for the splitting of the first two bands is 6 cm^{-1}, while for band B it is 9 cm^{-1}. The reason for this splitting may be an internal rotation of the methyl group. The peak X at 467 cm^{-1} has been assigned by Lin et al. [32] to a "skeleton rock" vibration, while other authors assign this peak as well as the ones at 737 (peak a1), and 757 cm^{-1} (peak a2) to transitions with ^1L_a character [33]. The 3MI spectrum also features the 26_0^1 breathing mode at 713 cm^{-1} above the origin and a hot band at 22 cm^{-1} below the origin.

VIII.3.2. 3-methylindole MATI

The threshold ionization spectra of 3MI via the S_1, 0^0 (lower trace), S_1, A (middle trace), and S_1, B (upper trace) are presented in **Fig.VIII.3**. The frequencies of the observed vibrational bands are listed in **Table VIII.1**. The lowest-in-energy strong peak at 60 711 $\pm$ 5 cm^{-1} is assigned to the adiabatic ionization energy, AIE. The uncertainty of 5 cm^{-1} is given mainly by the distance of the field-ionized high Rydberg states from the respective ionization energy and by the shift of the individual ionization thresholds in the presence of the electric field [34]. In the region above 100 cm^{-1} from the 0^0 band each spectrum features several vibrational modes of the indole ring: 42^1, 41^1, 29^1, 28^1, 27^1, and the ring breathing vibration 26^1 [35]. However, as evident from **Fig.VIII.3** the excitation via the A and B intermediate states leads to a denser vibrational structure in the ion spectrum than the excitation via the origin of S_1, 0^0.

---

[2] **The uncertainty of locating the R2PI peaks is 0.8 cm^{-1} and is mainly determined by the fluctuations of the values displayed on the wavemeter.**
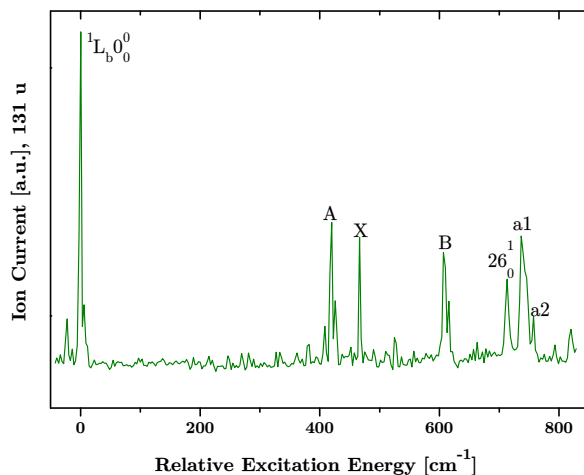
Fig.VIII.2. Two-color R2PI spectrum of 3MI, corrected for intensity fluctuations of the scanning laser and plotted on an excitation energy scale relative to the $^1L_b \leftarrow {}^1A$ origin at 34 875.1 cm^{-1} .
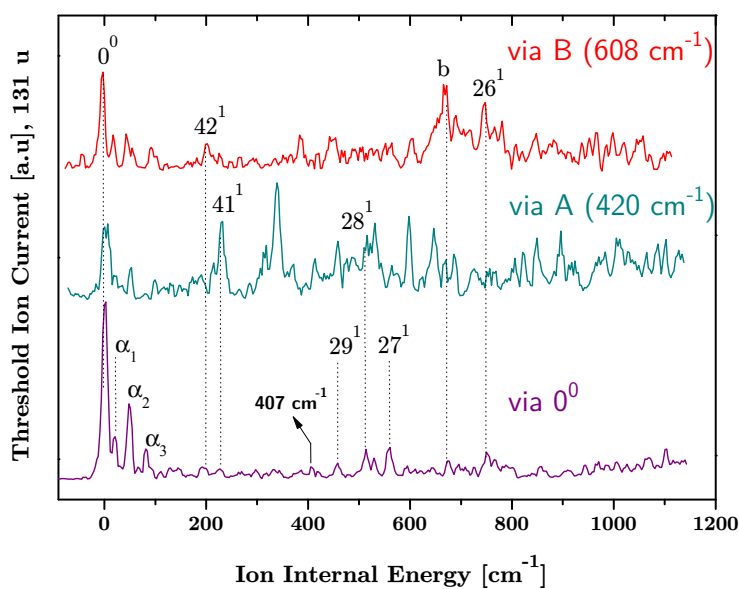

Fig.VIII.3. MATI spectra of 3MI$^+$ via the $S_1 \leftarrow S_0$ origin (lower trace), S_1, A band (middle trace) and S_1, B band (upper trace), recorded under common experimental conditions and represented on a common signal intensity scale. The peak 0^0 corresponds to the AIE of 3MI at 60 711 cm^{-1}.

It can be also seen that the change of the intermediate state affects the intensity of the observed peaks in the respective threshold ionization spectrum. These findings can be explained by different Franck-Condon factors for the second (ionization) step in the three spectra. For example, the strongest peak in the lower trace (excitation via the $S_1 \leftarrow S_0$ origin) is the band that corresponds to the AIE of 3MI. On the other hand, the peak at 673 cm^{-1} is very weak when the origin of S_1 is used as an intermediate state (lower trace). However, its intensity is considerably higher and comparable to that of 0^0 when the $D_0 \leftarrow S_0$ transition occurs via the B band (upper trace) at 608 cm^{-1}. Therefore it is quite plausible to assume that peak "b" at 673 cm^{-1} corresponds to the same vibration as the peak B in the R2PI spectrum, namely an in-plane bending of the indole ring as reported previously [32].

assignment	α_1	α_2	α_3	42^1	41^1	29^1	28^1	27^1	b	26^1
frequency, cm^{-1}	23	50	83	194	232	458*	516	563	673	751

Table VIII.1. Vibrational bands positions observed in the MATI spectrum of 3MI$^+$ in D_0 state. The assignment for the ring vibrational modes is given by comparison with the results from [35] except for the band "b" at 673 cm^{-1}. *The position of the 29^1 mode as well as the origin of the peak at 407 cm^{-1} in Fig. VIII.3 are discussed in *Section VIII.3.3c.*

The bands in the low-energy region (below 100 cm^{-1}) α_1, α_2, α_3 lie at 23, 50, and 83 cm^{-1}, respectively, and are very close to the ones for the *p*-fluorotoluene cation [36, 37]. The first two of these bands are present in the three traces in **Fig. VIII.3** and their relative intensities compared to that of the 0^0 peak are almost independent of the intermediate state used in the excitation process. The α_1, α_2, α_3 peaks are assigned to levels, resulting from the torsional motion of the CH$_3$ group.

VIII.3.3. *Quantum-chemical calculations on 3-methylindole*

a) Geometry of 3MI in the S_0 state

The geometry of 3MI in the ground neutral state S_0 and ground cationic state D_0 was optimized at the MP2/cc-pVDZ, B3LYP/6-31+G(d) and B3LYP/cc-pVDZ levels of theory.

Bond lengths

Table VIII.2 gives a comparison of the calculated bond lengths in the indole ring of 3MI in the ground neutral state and the experimental findings reported previously by Chadwick [38]. The calculations yield internuclear distances that are larger than the experimental values. However, it can be seen that all employed levels of theory show very good agreement with the experiment. In particular, the largest deviation for B3LYP is only $\approx 1\%$, while MP2 generally tends to overestimate somewhat more strongly the bond lengths, particularly for the C2–C3 and C6–C7 bonds ($\approx 2\%$ in both cases).

bond	exp.*	MP2/ cc-pVDZ	B3LYP/ cc-pVDZ	B3LYP/ 6-31+G(d)
N1–C2	1.380	1.384	1.385	1.387
C2–C3	1.358	1.389	1.376	1.373
C3–C9	1.436	1.441	1.444	1.444
C9–C4	1.398	1.416	1.408	1.407
C4–C5	1.381	1.398	1.391	1.391
C5–C6	1.396	1.421	1.413	1.412
C6–C7	1.372	1.399	1.392	1.392
C7–C8	1.395	1.409	1.401	1.400
C8–C9	1.410	1.432	1.426	1.424
C8–N1	1.374	1.379	1.379	1.380

Table VIII.2. Ground state experimental and calculated bond lengths in the indole ring of 3MI. All lengths are given in Å. *Experimental results obtained from averaging the geometries of 34 3-substituted indoles from the Cambridge Crystallographic Database [38].

Also, as evident from the data in **Table VIII.2**, the basis set has small effect on the calculations in the case of DFT B3LYP method.

Planarity:

The hydrogen at N1 does not lie precisely in the plane of the indole ring thus depriving 3MI of rigorous C_S symmetry as already discussed in the literature [39] . The calculations suggest, however, that this deviation is rather small (less than 1.2%) and the indole ring can be therefore considered as almost perfectly planar.

CH₃ group orientation and geometry

The methyl group in 3MI is oriented such that one of the C–H bonds lies in the plane of the indole ring, while the other two C–H bonds are placed symmetrically under and above this plane (**Fig.VIII.4** and **Fig.VIII.5**). The length of the C3–C10 bond is about 1.500 Å, thus it is shorter by $\approx$ 0.011 Å than that in toluene [40]. The C10–H bond lengths are larger than the C–H bonds in the indole ring which is expected from the different hybridization in the methyl group (sp^3) and the aromatic ring (sp^2). Furthermore, the C10–H$_b$ bond is shorter compared to the other C10–H bonds, which is in line with the observations made for other methylated aromatic rings [40]. The effect of the methyl group on the lengths of the neighboring C–C bonds in the indole ring in 3MI is discussed in *Section VIII.7.3a*.

b) Geometry changes in 3MI upon ionization

Table VIII.3 summarizes the bond lengths and the internuclear angles obtained for 3MI and 3MI$^+$ at the MP2/cc-pVDZ, B3LYP/6-31+G(d) and B3LYP/cc-pVDZ levels of theory. The following observations and conclusions can be made on the basis of the geometry optimization for the neutral and the ionized 3MI.

1. B3LYP predicts that the pyrrole ring experiences noticeable changes upon ionization. In particular, the N1–C2 bond length decreases by $\approx$ 3.5% and the C2–C3 bond lengthens by $\approx$ 4%. Somewhat smaller is the change in the length of the N1–C8 bond: it increases by $\approx$ 2%. By examining the data in **Table VIII.3** it can be seen that the calculated bond length changes are very weakly dependent on the employed basis set. The results from the MP2/cc-pVDZ level show similar trends in the deformation of the pyrrole ring except for the C3–C9 and N1–C8 bond lengths: the former *increases* by $\approx$ 2% and the

latter remains nearly *constant* upon ionization. The DFT calculations predict *decrease* by $\approx 1\%$ and *increase* by $\approx 2\%$ for the above bonds, respectively.
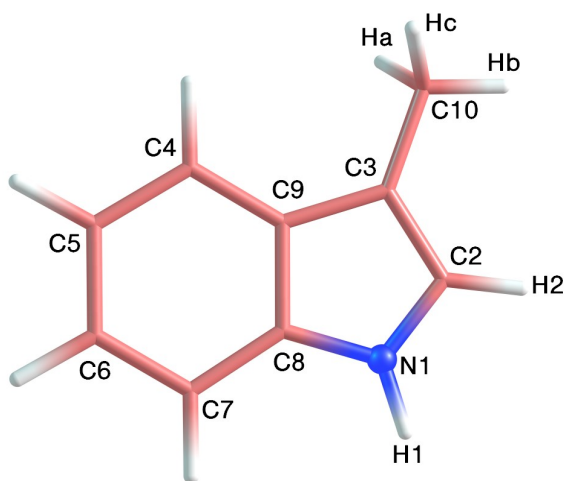
Fig.VIII.4. Geometry of 3MI in the ground, S_0, electronic state, optimized at all employed levels of theory (MP2/cc-pVDZ, DFT B3LYP/cc-pVDZ, and DFT B3LYP/6-31+G(d)). Only the numbering of the carbon and nitrogen nuclei is given as well as of the hydrogens at N1 and C2. The hydrogens in the methyl group are indexed arbitrarily for the purposes of the discussion (see text).
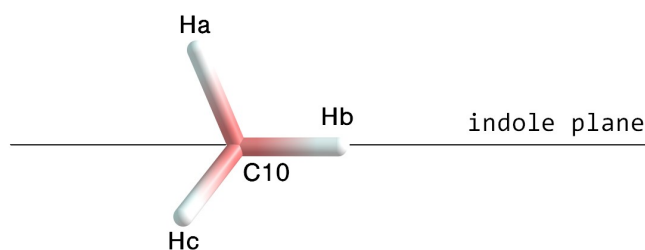
Fig.VIII.5. Orientation of the methyl group in 3MI in the S_0 state with respect to the indole ring, predicted at all employed levels of theory (MP2/cc-pVDZ, DFT B3LYP/cc-pVDZ, and DFT B3LYP/6-31+G(d)). The same geometry is valid also for the ground cationic state, D_0.

Geometrical parameter	MP2/ cc-pVDZ		B3LYP/ cc-pVDZ		B3LYP/ 6-31+G(d)	
N1–H1	1.013 (1.021)	0.008	1.010 (1.017)	0.007	1.008 (1.015)	0.007
N1–C2	1.384 (1.355)	-0.029	1.385 (1.336)	-0.049	1.387 (1.336)	-0.051
C2–C3	1.389 (1.415)	0.026	1.376 (1.433)	0.057	1.373 (1.431)	0.058
C3–C9	1.441 (1.468)	0.027	1.444 (1.427)	-0.017	1.444 (1.425)	-0.019
C9–C8	1.432 (1.418)	-0.014	1.426 (1.422)	-0.004	1.424 (1.421)	-0.003
N1–C8	1.379 (1.378)	-0.001	1.379 (1.409)	0.030	1.380 (1.410)	0.030
C8–N1–H1	125.4 (124.5)	-0.9	125.5 (125.3)	-0.2	125.6 (125.2)	-0.4
C8–N1–C2	109.4 (112.0)	2.6	109.2 (109.9)	0.7	109.1 (109.9)	0.8
N1–C2–H2	120.6 (122.1)	1.5	120.5 (121.8)	1.3	120.4 (121.8)	1.4
N1–C2–C3	110.0 (108.5)	-1.5	110.2 (109.8)	-0.4	110.2 (109.8)	-0.4
C4–C9	1.416 (1.387)	-0.029	1.408 (1.412)	0.004	1.407 (1.412)	0.005
C4–C5	1.398 (1.422)	0.024	1.391 (1.401)	0.010	1.391 (1.400)	0.009
C5–C6	1.421 (1.413)	-0.008	1.413 (1.399)	-0.014	1.412 (1.398)	-0.014
C6–C7	1.399 (1.404)	0.005	1.392 (1.419)	0.027	1.392 (1.419)	0.027
C7–C8	1.409 (1.419)	0.010	1.401 (1.379)	-0.022	1.400 (1.378)	-0.022
C4–C5–C6	121.2 (120.9)	-0.3	121.1 (120.8)	-0.3	121.0 (120.8)	-0.2
C3–C10	1.501 (1.482)	-0.019	1.499 (1.485)	-0.014	1.500 (1.488)	-0.012
C2–C3–C10	127.2 (127.2)	0.0	127.1 (125.7)	-1.4	127.1 (125.6)	-1,5
C2–C3–C9	106.0 (105.5)	-0.5	106.1 (105.6)	-0.5	106.2 (105.7)	-0.5
C3–C9–C4	133.6 (132.4)	-1.2	133.8 (133.1)	-0.7	133.7 (133.0)	-0.7
N1–C8–C7	130.6 (130.8)	0.2	130.7 (130.1)	-0.6	130.6 (130.1)	-0.5

Table VIII.3. Calculated bond lengths [Å] and bond plane angles [deg] in the S_0 state and D_0 state (in brackets) of 3MI. The shaded columns represent the change of the corresponding geometrical parameter upon ionization.

Jensen et al. [41] report similar findings with respect to the difference in the MP2 and B3LYP calculations on the geometry changes in the pyrrole ring of 3MI. On the other hand, a comparison of the results in **Table VIII.3** with the data in the aforementioned work shows that MP2 yields similar bond length changes when employing the cc-pVDZ and 6-31G(d,p) basis sets.

2. The estimated changes in the phenyl ring at both B3LYP/cc-pVDZ and B3LYP/6-31+G(d) levels are smaller than in the pyrrole moiety and are most prominent for the C6–C7 and C7–C8 bonds: the former increases in length by ≈ 1.9 %, while the latter shortens by $\approx 1.6\%$. MP2/cc-pVDZ predicts smaller changes for these bond lengths but larger changes for the C4–C5 and C4–C9 bond lengths (by $\approx 2\%$) than B3LYP (less than 1%).

3. The N1–H1 bond length increases weakly upon ionization as predicted by both MP2 and DFT B3LYP theories.

4. The ionization of 3MI to the D_0 state does not affect noticeably the relative orientation of the phenyl and pyrrole ring: $\sphericalangle$(C3–C9–C4) and $\sphericalangle$(N1–C8–C7) angles experience changes of around 1% as predicted by both MP2 and DFT B3LYP calculations.

5. The position of the CH_3 group relative to the indole ring experiences a small change upon ionization. This is manifested through: *i)* shortening of the C3–C10 bond by $\approx 1.0\%$, which is somewhat smaller than in the case of fluorotoluenes ($\approx 1.3\% - 2\%$ [42]) as shown by both MP2 and B3LYP models; *ii)* decrease of the angle $\sphericalangle$(C2–C3–C9) by $\approx 1.0\%$. The shortening of the C3–C10 bond when the molecule is ionized stems most probably from the larger hyperconjugation in the cation than in the neutral. On the other hand, the methyl group does not change its orientation with respect to the indole ring: the C10–Ha, C10–Hb, and C10–Hc bonds are rotated as in the case of the neutral molecule (**Fig.VIII.5**).

c) Vibrational structure of 3MI in the D_0 state

Table VIII.4 lists the calculated frequencies at the MP2/cc-pVDZ, B3LYP/cc-pVDZ and B3LYP/6-31+G(d) levels of theory without scaling and with scaling with appropri-

ate factors in order to account for anharmonicity, basis set incomplete-ness or poor inclusion of the electron correlation.

assign-ment	exp.	MP2/ cc-pVDZ		B3LYP/ cc-pVDZ			B3LYP/ 6-31+G(d)	
		unsc.	x 0.9538[b]	unsc.	x 0.9717[b]	x 0.9807[c]	unsc.	x 0.9636[b]
42^1	194	193.3	(184.4)	214.7	(208.6)	(210.6)	214.1	(206.3)
41^1	232	226.3	(215.8)	231.9	(225.3)	(227.4)	232.7	(224.2)
29^1	458	454.0	(433.0)	463.6	(450.5)	(454.6)	464.2	(447.3)
28^1	516	542.5	(517.4)	522.1	(507.3)	(512.0)	522.0	(503.0)
27^1	563	578.4	(551.7)	565.5	(549.5)	(554.6)	566.3	(545.7)
b	673	728.8	(695.1)	684.5	(665.1)	(671.3)	684.1	(659.2)
26^1	751	745.3	(710.9)	766.9	(745.2)	(752.1)	766.7	(738.8)

Table VIII.4. Experimental and calculated frequencies [cm^{-1}] of the D_0 state of ionized 3MI and the assignment of the corresponding vibrational bands. The shaded columns list the unscaled frequencies obtained at each of the employed quantum-chemical methods.
(b) Scaling factors taken from [43]. (c) Scaling factors taken from [44].

Comparison of the calculated vibrational frequencies with the experiment

The 29^1 band
In a recent work [4] the 29^1 vibration in 3MI was associated with the peak in the MATI spectrum at 407 cm^{-1} by comparison with the results from ZEKE spectroscopy on indole [35]. However, both MP2 and DFT calculations show that the 29^1 vibration in 3MI should be associated with the experimental peak at 458 cm^{-1}.
The intensities of both peaks at 407 and 458 cm^{-1} in the MATI spectrum (**Fig.VIII.3**) are, similarly to the indole case, very weak, which renders the unambiguous experimental assignment of either peak difficult. On the other hand, both MP2 and B3LYP calculations can be considered reliable with regard to the frequency of the 29^1 mode. This conclusion is supported on the one hand by the very similar results obtained with all employed methods, exhibiting differences within only 10 cm^{-1}. On the other hand, geometry optimizations of the indole cation performed at the same levels of theory (MP2/cc-pVDZ, B3LYP/6-31+G(d), and B3LYP/cc-pVDZ) as in the case of 3MI show that the theoreti-

cally estimated frequencies for the 29^1 in-plane ring vibration in indole are very close to the experimental value reported previously [35, 45].

The unscaled vibrational frequencies obtained at the MP2/cc-pVDZ level of theory show very small deviations $\delta\overline{v}$ (about 5 cm^{-1}) from the experimental values for the 42^1, 41^1, 29^1, and 26^1 modes. On the other hand, the deviations for the frequencies of the 28^1 and 27^1 modes as well as for the band at 673 cm^{-1} are noticeably larger (**Table VIII.4**).

When a scale factor of 0.9538 is used [43], the calculated frequencies for 42^1, 27^1 and particularly the 28^1 band are in quite reasonable agreement with the experiment. However, the other values exhibit larger deviations with the experimental findings compared to the unscaled frequencies. Obviously the MP2/cc-pVDZ level fails to give an accurate overall description of the intramolecular vibrational modes in the case of 3MI cation.

The next columns in **Table VIII.4** summarize the computational results on the vibrational structure of 3MI cation obtained at the DFT level employing the B3LYP functional in combination with the cc-pVDZ and 6-31+G(d) basis sets. It can be seen that both basis sets give similar unscaled intramolecular vibrational frequencies at the DFT B3LYP level that agree well with the experiment for the 41^1, 29^1, 28^1, and 27^1 bands. The largest deviation is observed for the frequency of the out-of-plane ring mode 42^1 (about 20 cm^{-1}).

It is worth noting that except for the 42^1 band, the B3LYP/cc-pVDZ frequencies are very close to the experimental ones when a scale factor 0.9807 [44] is used. A scale factor of 0.9717 recommended by Merrick et al. [43] for the same level of theory leads to somewhat lower values for the calculated frequencies and, respectively, greater $\delta\overline{v}$ from the experimental findings. However, the results suggest that for B3LYP the cc-pVDZ basis set generally yields scaled values closer to the experimental ones than those obtained with the 6-31+G(d) basis set (using a scale factor of 0.9636 [43]).

d) Adiabatic Ionization Energy

The AIE of 3MI was calculated at the MP2/cc-pVDZ, B3LYP/6-31+G(d), and B3LYP/cc-pVDZ levels of theory. In addition, CCSD/cc-pVDZ single point calculation was performed with the structure of 3MI optimized at the MP2/cc-pVDZ level. The results are listed in **Table VIII.5**.

MP2/cc-pVDZ	CCSD/cc-pVDZ SP	B3LYP/cc-pVDZ	B3LYP/6-31+G(d)
62 174 (+1463)	59 700 (−1011)	57 765 (−2946)	58 572 (−2139)

Table VIII.5. Calculated (ZPVE corrected) adiabatic ionization energy [cm^{-1}] of 3MI. The deviation of the computational results at each level of theory from the experimental value (60 711 cm^{-1}) is given in brackets.

The values in **Table VIII.5** show that MP2 overestimates the adiabatic ionization energy of 3MI, while the other levels of theory underestimate it. The smallest deviation from the experimental value (60 711 cm^{-1}) is obtained at the CCSD single point level with the optimized MP2 geometry but the MP2 AIE also shows fairly good agreement. On the other hand, B3LYP exhibits large deviations from the experimental value of AIE, although the values obtained with the 6-31+G(d) basis set show better agreement with the experiment than those obtained with the cc-pVDZ basis set.

VIII.4. 3-methylindole·water complex

VIII.4.1. 3MI·H$_2$O R2PI

The two-color R2PI spectra of the 3MI·H$_2$O complex and 3MI (for comparison) are shown in **Fig.VIII.6**. The origin of the S$_1$ ← S$_0$, 0_0^0 transition of 3MI·H$_2$O lies at 34 641.7 cm^{-1}, which agrees with the value of 34 641.1 cm^{-1} taken from high-resolution experiments in our group [30]. Therefore, the origin in the R2PI spectrum of the 3MI·H$_2$O complex is red shifted from the respective origin of the monomer by $\approx$ 233 cm^{-1}.

It has been shown that the 3MI·H$_2$O complex is formed by hydrogen bonding at the N1–H1 site (σ-type bonding) [22]. According to the findings from fluorescence lifetime measurements reported by Demmer et al. [20] the S$_1$ ← S$_0$, 0_0^0 transition of 3MI·H$_2$O can be considered as having ^{1}L$_b$ character since water has proton affinity less than 200 kcal/mol [46] . However, the ^{1}L$_a$ state is expected to lie sufficiently close to ^{1}L$_b$ to induce changes in the excitation spectrum in comparison to 3MI or indole·H$_2$O.
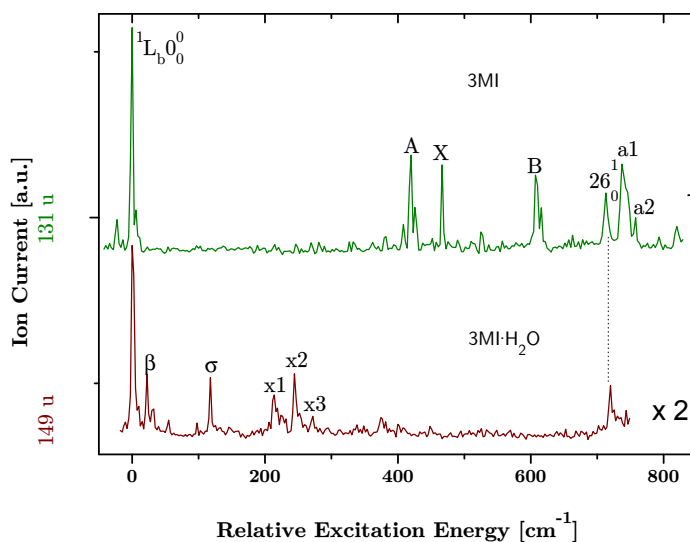
Fig.VIII.6. Two-color R2PI spectra of 3MI·H₂O complex (lower trace) recorded at the 149 u mass channel and 3MI (upper trace) recorded at the 131 u mass channel and plotted on a common excitation energy scale. The excitation energy is relative to the respective ^1L_b $S_1 \leftarrow S_0$ origin. The signal intensity in the excitation spectrum of the complex is increased by a factor of 2 for better visualization.

The spectra shown in **Fig.VIII.6** exhibit several interesting features. First, the relative excitation energy region below 100 cm^{-1} features peaks corresponding to bending (β) and stretching (σ) modes of the hydrogen bond at 23 and 118 cm^{-1}, respectively. These values agree well with the two-color R2PI frequencies reported by Huang and Sulkes [33]. The frequency of the peak right next to β at 33 cm^{-1} is also in good agreement with the one given in the aforementioned work and apparently is present in the one-color spectrum of 3MI·H₂O reported by Carney and Zwier [22]. The nature of this peak has not been rigorously ascertained, although it probably originates from a coupling of the methyl group motion and the bending mode of the hydrogen bond. Such a suggestion is plausible since there is no evidence for a similar band in the indole·H₂O R2PI spectrum [22, 33, 45]. On the other hand, the appearance of the peak under consideration may be due to a ^1L_a – ^1L_b mixing as suggested by Carney and Zwier [22]. The peaks at x1, x2, and x3 at 214, 244, and 272 cm^{-1}, respectively also lie close to the ones reported in ref. [33] and have been recognized as a progression-like envelope.

Second, many bands predominant in the monomer spectrum between 400 and 600 cm^{-1} are not present in the spectrum of the complex. One reason for this finding could be that the Franck–Condon factors for excitation are changed because of the water attachment. Another explanation might be, as suggested in *Section VIII.3.1*, that these bands originate from ^1L_a transitions in 3MI. Their absence in the R2PI spectrum of 3MI·H_2O would be therefore due to the larger $^1L_a - {^1L_b}$ shifts induced by water attachment for these bands than for the $S_1 \leftarrow S_0$ origin.

VIII.4.2. 3MI·H₂O MATI

The threshold ionization spectra of the 3MI·H_2O complex and 3MI (for comparison) via the $S_1 \leftarrow S_0$ origin are given in **Fig.VIII.7**. The AIE of 3MI·H_2O was found to be 57 614 $\pm$ 5 cm^{-1}, thus it is red shifted by 3097 cm^{-1} from the AIE of 3MI. The two spectra in **Fig.VIII.7** differ in some important aspects that merit a closer inspection.

First, it can be clearly seen that the spectrum of the complex exhibits a much denser structure in the region 0 – 400 cm^{-1} than the spectrum of the bare molecule due to additional vibrational activity in the former case. A comparison with the threshold ionization spectrum of (indole·H_2O)$^+$ [34] shows that the most prominent features in the vibrational structure of (3MI·H_2O)$^+$ are the bending (β) and particularly the stretching (σ) modes of the hydrogen bond at 36 and 180 cm^{-1}, respectively, as well as their overtones. The similar intermolecular vibrational pattern in the MATI spectra of (3MI·H_2O)$^+$ and (indole·H_2O)$^+$ apparently supports the concept of the same type of hydrogen bonding in both complexes, namely at the N1–H1 site in the pyrrole moiety.

Furthermore, the low-frequency bending modes contribute to the peak density in the region below 100 cm^{-1}, where modes due to the CH_3 motion are also present. However, except for β^2 and α_3 which appear to be superimposed, the β^1 intermolecular mode is well separated from the methyl group rotations α_1 and α_2. Thus these three peaks are clearly recognized as different bands.

The origin of the strong peaks at 267 and 298 cm^{-1} (red circle in **Fig.VIII.7**) is not clear. However, since such bands are absent in the threshold ionization spectrum of 3MI it is plausible to relate their appearance in the case of 3MI·H_2O to intermolecular vibrations of the hydrogen bond coupled with indole ring vibrations.
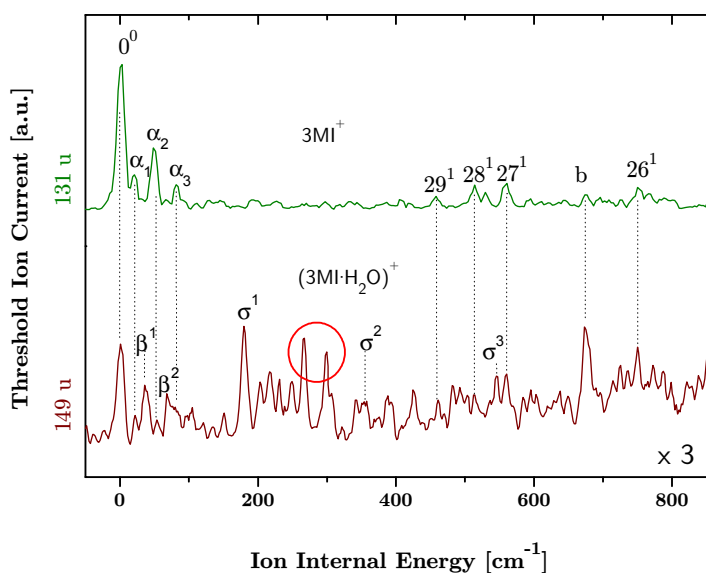
Fig.VIII.7. Mass analyzed threshold ionization spectra of the 3MI·H₂O complex (lower trace) recorded at the 149 u mass channel and 3MI (upper trace) recorded at the 131 u mass channel. The threshold ion current signal of the complex is increased by a factor of 3 for better visualization.

The positions of these peaks approximately match the frequencies of the combination modes $41^1\beta^1$ and $41^1\beta^2$. Such an interpretation seems plausible since there are apparently peaks (however much smaller) in the MATI spectrum of indole·H₂O complex [45], which lie around 270 cm^{-1} and near 300 cm^{-1} above the AIE. Therefore, although these bands have not been discussed and assigned, they roughly match also in frequency the $41^1\beta^1$ and $41^1\beta^2$ modes.

In the region above 400 cm^{-1} in the threshold ionization spectrum of $(3MI\cdot H_2O)^+$ the weak-in-intensity in-plane ring vibrational modes 29^1, 28^1, 27^1, and 26^1 cannot be clearly recognized due to the dense spectral structure arising apparently from intermolecular vibrational activity. Interestingly, the peak "b" at 673 cm^{-1} is a notable exception as its intensity increases substantially in the spectrum of the complex probably due to favorable Franck-Condon factors.

VIII.4.3. Dissociation of the (3MI·H₂O)⁺ complex

Fig.VIII.8 shows the MATI spectra of $(3MI \cdot H_2O)^+$ via S_1, 0^0 from 0 to 855 cm⁻¹ and from 4440 to 4824 cm⁻¹ above the AIE recorded simultaneously at the parent (149 u, lower trace) and the fragment $3MI^+$ (131 u, upper trace) mass channel. It is clearly seen that when increasing the second photon energy and thus the internal energy of the ionized complex above 4669 cm⁻¹ the signal breaks down at the parent mass channel and simultaneously there is an onset of the signal at the fragment mass channel. The overlap of about 25 cm⁻¹ of the breakdown and the onset regions stems from the field dependence of the appearance energy (*Section VI.3.4*). The value of 4669 ± 20 cm⁻¹ is taken as the dissociation threshold (energy) E_0 of the $(3MI \cdot H_2O)^+$ complex (marked by a vertical dashed line in **Fig.VIII.8**). The binding energy D_0 of the neutral $3MI \cdot H_2O$ in the ground state can be estimated according to **Eq.VI.4** on page 77. With the measured value of AIE for 3MI as well as the AIE and E_0 for $3MI \cdot H_2O$ the binding energy in the ground neutral state S_0 of $3MI \cdot H_2O$ is calculated to be $D_0 = 1572 \pm 20$ cm⁻¹.

The increased hydrogen-bond strength upon ionization of the $3MI \cdot H_2O$ complex stems from the additional charge-dipole interaction between the positively charged 3MI moiety and the water molecule. Weiner et al. [47] point out that the stronger hydrogen bonding *in vacuo* in cationic complexes compared to neutral complexes is due to the more negative enthalpy in the former case.
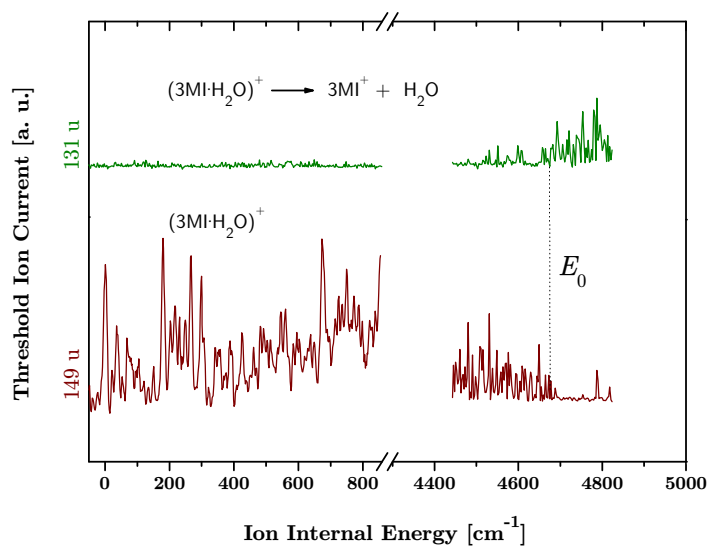
Fig.VIII.8. Mass analyzed threshold ionization spectrum of the 3MI·H₂O complex recorded at the parent (lower trace, 149 u) and fragment (upper trace, 131 u) mass channel in the low (0 – 855 cm⁻¹) and high (4440 – 4824 cm⁻¹) internal energy region. The first laser was fixed at the S₁ ← S₀ origin. The parent threshold ion signal breaks down at 4669 cm⁻¹, where there is an onset of the fragment threshold ion signal at the same energy. The dissociation threshold E_0 is marked by a vertical line.

VIII.4.4. Quantum-chemical calculations on the 3MI·H₂O complex

a) Hydrogen-bond geometry of 3MI·H₂O in the ground neutral state S₀

The σ-type N1–H1···O1 hydrogen bond in the 3MI·H₂O complex is characterized by the following geometrical parameters (**Fig.VIII.9**):

N1-O1 distance

O1–H1 bond length

∢(N1–H1···O1) angle

angle β between the N1-O1 axis and the water molecule plane.
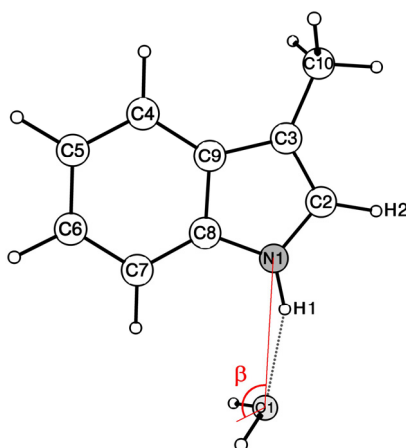
Fig.VIII.9. Numbering in the 3MI·H₂O complex and definition of the angle ß between the H₂O plane and the N1-O1 axis.

The optimized structures of the ground state of 3MI·H₂O obtained at MP2/cc-pVDZ, B3LYP/cc-pVDZ, and B3LYP/6-31+G(d) are shown in **Fig.VIII.10**. The geometrical parameters describing the hydrogen-bond geometry are given in **Table VIII.6**. All methods employed for geometry optimization of the 3MI·H₂O complex predict that the hydrogens of the water molecule are oriented symmetrically with respect to the plane of the indole ring.
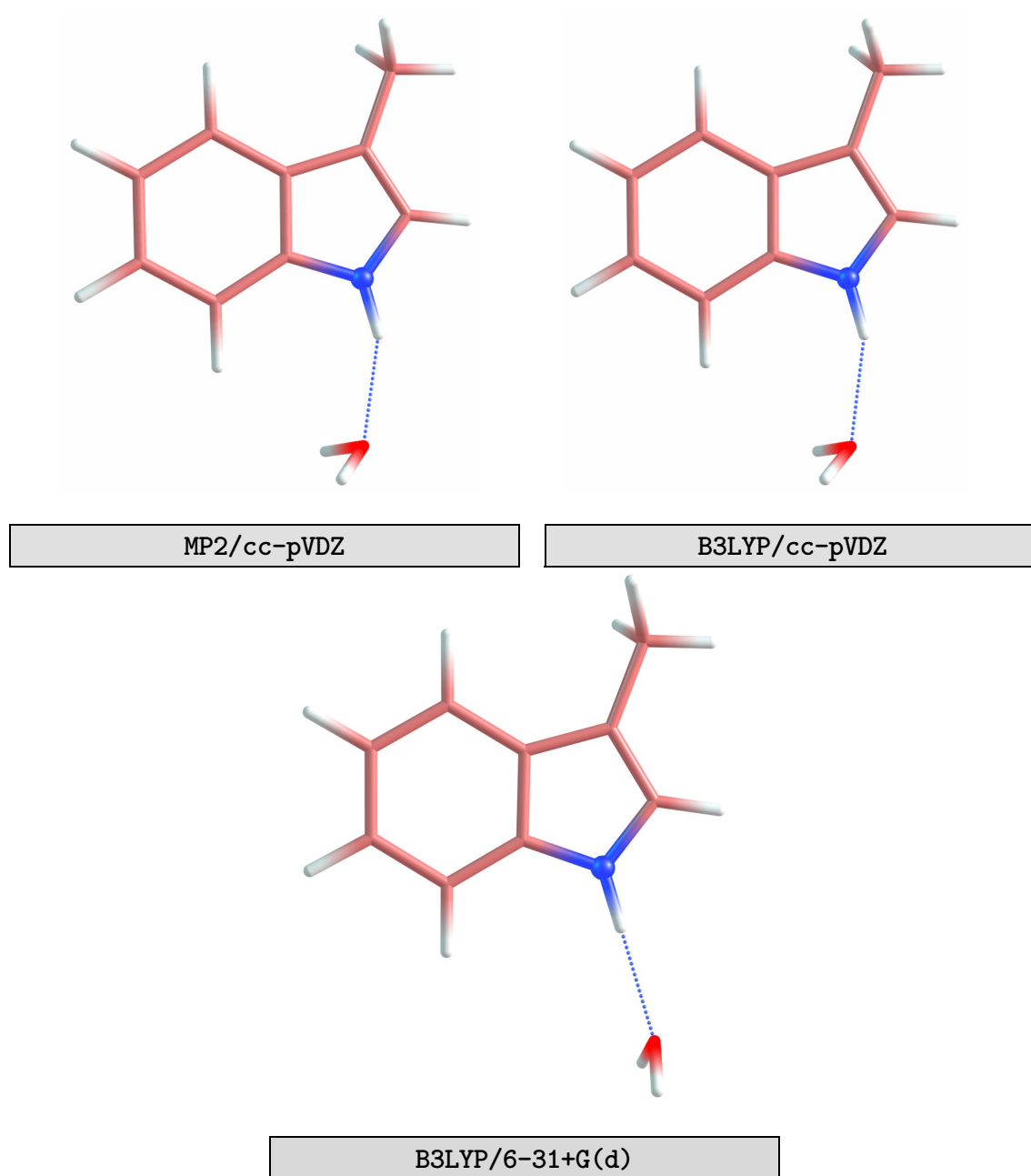
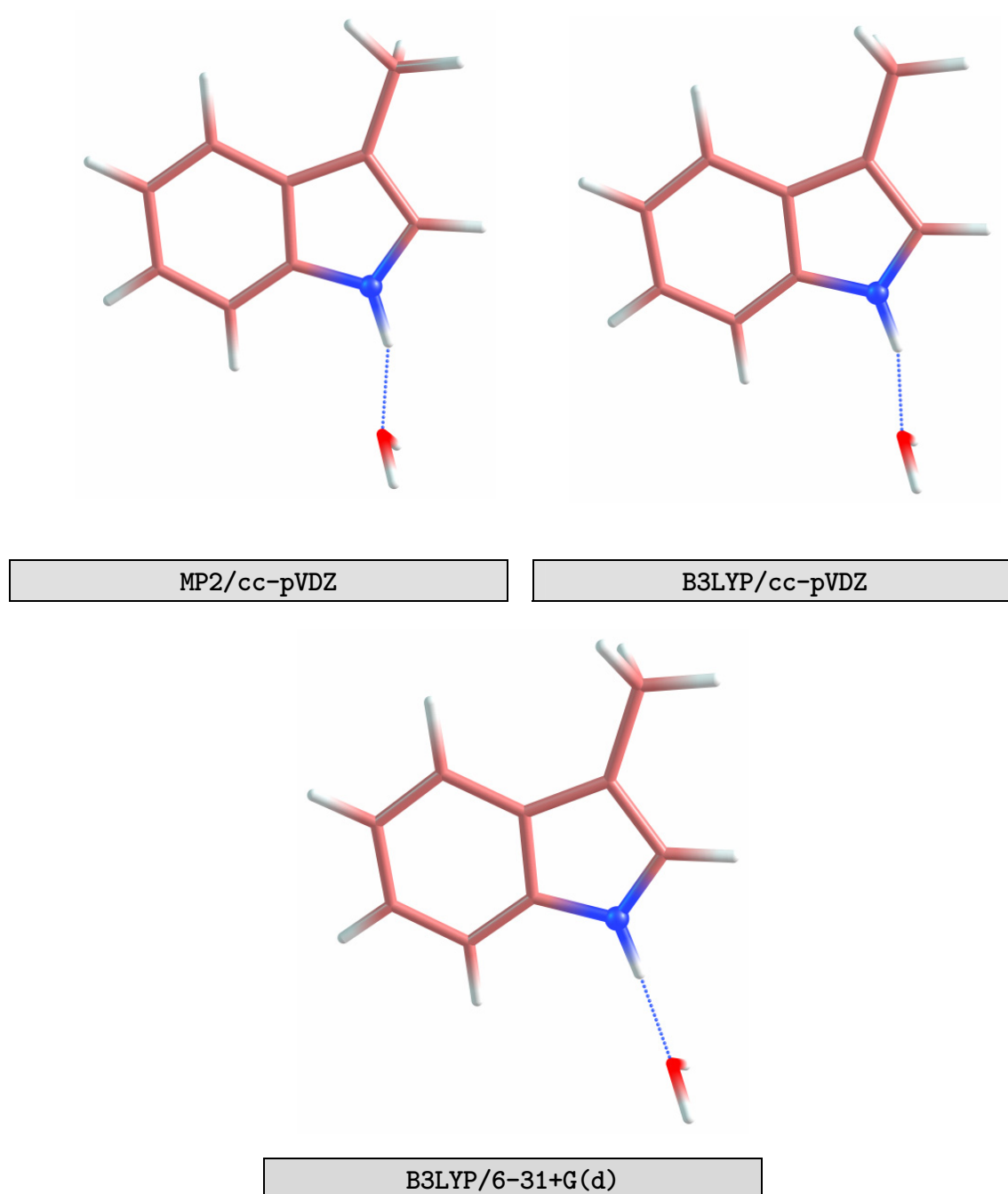**Fig.VIII.10.** Optimized structures of the 3MI·H₂O complex in S₀ state at all employed levels of theory. The dotted line indicates the σ-type hydrogen bond (N1–H1···O1) between 3MI and the water molecule. The calculations in all three cases used an identical initial geometry as a starting point. See text for more details on the orientation of the water molecule predicted in each case.

Moreover, MP2/cc-pVDZ and B3LYP/cc-pVDZ levels yield similar structures of the 3MI·H_2O complex, in particular concerning the orientation of the water molecule as both methods predict an N1–H1···O1 hydrogen bond tilted towards the phenyl ring with the water molecule rotated in the same direction. The angles ∢(N1–H1···O1) and β as well as the N1-O1 and H1···O1 distances are very similar in both cases.

On the other hand, B3LYP/6-31+G(d) yields quasi-linear N1–H1···O1 σ hydrogen bond with an ∢(N1–H1···O1) angle close to 180°. The water molecule is tilted only slightly towards the phenyl ring: the angle between the N1-O1 axis and the water molecule plane is 155.1°. As seen from **Table VIII.6** the N1-O1 and H1-O1 distances estimated at the B3LYP/6-31+G(d) level are larger than those predicted by the other two methods.

Geometrical parameter	MP2/ cc-pVDZ	B3LYP/ cc-pVDZ	B3LYP/ 6-31+G(d)
N1–O1	2.911	2.915	2.991
H1···O1	1.950	1.950	1.976
O1–H	0.967	0.970	0.969
ß	−126.7	−126.6	−155.1
N1–H1···O1	155.7	157.0	179.9

Table VIII.6. Calculated internuclear distances [Å] and bond angles [deg] characterizing the hydrogen-bond geometry in the ground electronic state S_0 of the 3MI·H_2O complex at the respective level of theory.

b) Geometrical changes in 3MI (S_0) upon 1:1 complexation with water

A comparison of the results in **Table VIII.7** shows that the formation of a hydrogen-bonded complex with one water molecule at the N1–H1 site in 3MI does not affect the orientation of the methyl group and does not induce prominent changes in the structure of the indole ring, including the plane angles at the site of hydrogen bonding, ∢(C8–N1–H1) and ∢(C8–N1–C2). The N1–H1 bond exhibits elongation by approximately 0.01 Å (1%), which can be associated with the formation of proper hydrogen bond at N1–H1. The changes in the lengths of the other bonds in the pyrrole ring are smaller as, for example, the N1–C2 and C3–C9 bond lengths slightly decrease by less than 0.005 Å and

≈ 0.001 Å, respectively, while the C2–C3 bond weakly elongates by ≈ 0.003 Å (MP2) and ≈ 0.002 Å (B3LYP).

Geom. parameter		MP2/cc-pVDZ			B3LYP/cc-pVDZ			B3LYP/6-31+G(d)	
		3MI	3MI·H₂O		3MI	3MI·H₂O		3MI	3MI·H₂O
N1–H1		1.013	1.021		1.010	1.019		1.008	1.016
N1–C2		1.384	1.380		1.385	1.382		1.387	1.383
C2–C3		1.389	1.392		1.376	1.378		1.373	1.375
C3–C9		1.441	1.440		1.444	1.443		1.444	1.442
C9–C8		1.432	1.433		1.426	1.426		1.424	1.425
N1–C8		1.379	1.376		1.379	1.375		1.380	1.378
C8–N1–H1		125.4	123.4		125.5	123.6		125.6	125.8
C8–N1–C2		109.4	109.0		109.2	108.8		109.1	108.8
N1–C2–H2		120.6	120.6		120.5	120.4		120.4	120.2
N1–C2–C3		110.0	110.3		110.2	110.5		110.2	110.5
C3–C10		1.501	1.501		1.499	1.499		1.500	1.500
C2–C3–C10		127.2	127.3		127.1	127.2		127.1	127.2
C2–C3–C9		106.0	106.0		106.1	106.0		106.2	106.0
C3–C9–C4		133.6	134.0		133.8	134.2		133.7	133.8
N1–C8–C7		130.6	130.2		130.7	130.2		130.6	130.5

Table VIII.7. Calculated internuclear distances [Å] and bond angles [deg] in the pyrrole ring for the ground electronic state S_0 of the 3MI monomer and the 3MI·H₂O complex.

As a whole, the deformations in the pyrrole and phenyl rings are less than 0.01 Å for the internuclear distances and about 1° for the bond angles, except for ∢(C8–N1-H1). Both MP2/cc-pVDZ and B3LYP/cc-pVDZ predict decrease of about 2° in the latter case upon hydrogen-bond formation. The respective change estimated at the B3LYP/6-31+G(d) level is much smaller, 0.2°.

c) Geometrical changes in 3MI·H_2O upon ionization

The results from the geometry optimization of the 3MI·H_2O complex in the ground cationic state D_0 are presented in **Fig.VIII.11** and in brackets in **Table VIII.8**.

Hydrogen-bond geometry

As in the case of S_0 state, MP2/cc-pVDZ and B3LYP/cc-pVDZ levels yield similar values for the N1-O1 and H1–O1 distances as well as for the ∡(N1–H1···O1) and β angles. In contrast to these methods, the results at the B3LYP/6-31+G(d) level differ noticeably, showing again larger values of the above geometrical parameters.

The results from the MP2/cc-pVDZ and particularly the B3LYP/cc-pVDZ calculations show that the ∡(N1–H1···O1) angle slightly increases (by ≈ 3° and ≈ 6°, respectively), i.e. the N1–H1···O1 bond manifests a minor tendency towards linearity upon ionization. The results from B3LYP/6-31+G(d) are somewhat contradictory in this regard as the corresponding angle slightly *decreases* by 3°. However, it is evident from **Fig.VIII.11** that, similarly to the results for the S_0 state, the 6-31+G(d) basis set predicts an essentially linear hydrogen bond for the ground cationic state of 3MI·H_2O, while for the other two methods the ∡(N1–H1···O1) noticeably differs from 180°.

The angle β describing the orientation of the water molecule plane with respect to the N1-O1 axis also changes when the complex is ionized, both in terms of magnitude and direction. As seen in **Fig.VIII.11** and **Table VIII.8** all implemented computational methods predict a flip of the water molecule to the side of the pyrrole ring, although to a different extent depending on the employed basis set. Upon ionization, the water molecule shifts in such a way that the bisector of the ∡(H–O1–H) angle in water strives to coincide with the O1-H1 axis. This tendency is most strongly expressed in the case of the B3LYP/6-31+G(d) basis set.

MP2/cc-pVDZ

B3LYP/cc-pVDZ

B3LYP/6-31+G(d)

Fig.VIII.11. Optimized structures of the $(3MI·H_2O)^+$ complex in D_0 state at all employed levels of theory. Similarly to the S_0 state, the dotted line indicates the σ-type hydrogen bond (N1–H1···O1) between 3MI and the water molecule. The calculations in all three cases used the respective optimized geometry in the S_0 state as a starting point. See text for more details on the orientation of the water molecule predicted for each of the cases.

Geometrical parameter	MP2/ cc-pVDZ		B3LYP/ cc-pVDZ		B3LYP/ 6-31+G(d)	
N1–O1	2.911 (2.726)	-0.185	2.915 (2.730)	-0.185	2.991 (2.816)	-0.175
H1···O1	1.950 (1.729)	-0.221	1.950 (1.718)	-0.232	1.976 (1.784)	-0.192
O1–H	0.967 (0.969)	0.002	0.970 (0.970)	0.000	0.969 (0.971)	0.002
ß	-126.7(153.3)		-126.6(159.2)		-155.1(170.6)	
N1–H1···O1	155.7 (159.3)	3.6	157.0 (162.9)	5.9	179.9 (177.3)	-2.6
N1–H1	1.021 (1.040)	0.019	1.019 (1.041)	0.022	1.016 (1.033)	0.017
N1–C2	1.380 (1.344)	-0.036	1.382 (1.331)	-0.051	1.383 (1.332)	-0.051
C2–C3	1.392 (1.434)	0.042	1.378 (1.436)	0.058	1.375 (1.433)	0.058
C3–C9	1.440 (1.412)	-0.028	1.443 (1.429)	-0.014	1.442 (1.427)	-0.015
C9–C8	1.433 (1.422)	-0.011	1.426 (1.421)	-0.005	1.425 (1.421)	-0.004
N1–C8	1.376 (1.402)	0.026	1.375 (1.407)	0.032	1.378 (1.409)	0.031
C8–N1–H1	123.4 (122.8)	-0.6	123.6 (123.0)	-0.6	125.8 (125.1)	-0.7
C8–N1–C2	109.0 (108.8)	-0.2	108.8 (109.4)	0.6	108.8 (109.4)	0.6
N1–C2–H2	120.6 (121.7)	1.1	120.4 (121.8)	1.4	120.2 (121.6)	1.4
N1–C2–C3	110.3 (110.0)	-0.3	110.5 (110.3)	-0.2	110.5 (110.2)	-0.3
C4–C9	1.417 (1.410)	-0.007	1.408 (1.410)	0.002	1.408 (1.410)	0.002
C4–C5	1.398 (1.370)	-0.028	1.392 (1.402)	0.010	1.391 (1.400)	0.009
C5–C6	1.422 (1.398)	-0.024	1.413 (1.399)	-0.014	1.413 (1.398)	-0.015
C6–C7	1.399 (1.402)	0.003	1.392 (1.418)	0.026	1.392 (1.418)	0.026
C7–C8	1.410 (1.357)	-0.053	1.402 (1.380)	-0.022	1.401 (1.378)	-0.023
C4–C5–C6	121.3 (120.1)	-1.2	121.1 (120.9)	-0.2	121.0 (120.8)	-0.2
C3–C10	1.501 (1.491)	-0.010	1.499 (1.486)	-0.013	1.500 (1.488)	-0.012
C2–C3–C10	127.3 (125.5)	-1.8	127.2 (123.9)	-3.3	127.2 (125.8)	-1,4
C2–C3–C9	106.0 (105.9)	-0.1	106.0 (105.5)	-0.5	106.0 (105.5)	-0.5
C3–C9–C4	134.0 (133.2)	-0.8	134.2 (133.6)	-0.6	133.8 (133.3)	-0.5
N1–C8–C7	130.2 (129.4)	-0.8	130.2 (129.3)	-0.9	130.5 (129.8)	-0.7

All levels predict shortening of the N1-O1 and the H1···O1 distances which along with the tendency for linearity may be interpreted as a manifestation of the increased hydrogen-bond strength upon ionization as already experimentally found in *Section VIII.4.3.* The largest changes of the above distances are estimated at MP2/cc-pVDZ and particularly B3LYP/cc-pVDZ, being more than 6% and about 11%–12% for N1–O1 and H1–O1, respectively, although the B3LYP/6-31+G(d) values are essentially close ($\approx 5.9\%$ and $\approx 10\%$).

Indole ring deformations and change of the methyl group geometry

Both the indole ring and the position of the methyl group experience geometrical changes when the 3MI·H₂O complex is ionized, which are as a whole, similar to the case of bare 3MI. The N1–C2 bond contracts by 0.051 Å ($\approx 4\%$) and the C2–C3 elongates by 0.058 Å ($\approx 4.2\%$). The N1–C8 bond length increases by 0.032 Å ($\approx 2.3\%$). As in the case of 3MI, in contrast to the DFT calculations MP2/cc-pVDZ underestimates the changes in the above bond lengths (although to a lesser extent for N1–C8) and overestimates as a whole the deformation of the phenyl ring. On the other hand MP2 predicts *shortening* of the C3–C9 bond by $\approx 2\%$ in case of 3MI·H₂O in contrast to the case of 3MI (*elongation* by 2%).

Compared to the monomer case, MP2/cc-pVDZ and B3LYP/cc-pVDZ slightly overestimate the decrease of the ∢(C2–C3–C10) angle upon ionization in 3MI·H₂O. The MP2 value remains constant when the monomer is ionized (**Table VIII.3**), while for the complex it decreases by 1.4° (**Table VIII.8**). B3LYP/cc-pVDZ predicts decrease of 1.4° and 3.3° in the former and the latter case, respectively. For comparison, B3LYP/6-31+G(d) yields similar values for the change of ∢(C2–C3–C10) angle in the $D_0 \leftarrow S_0$ transition for 3MI and 3MI·H₂O: -1.5° and -1.4°, respectively.

A noticeable exception in the similarities between the changes in 3MI and 3MI·H₂O complex upon ionization is observed for the N1–H1 bond. The estimated increase of the bond length is 2.2% for B3LYP/cc-pVDZ, 1.9% for MP2/cc-pVDZ, and 1.7% for B3LYP/6-31+G(d). Such elongation is larger than that due to ionization of the indole ring ($\approx 0.7\%$, **Table VIII.3**) and is therefore another manifestation of the increased hydrogen-bond strength in the cation discussed above.

← **Table VIII.8.** Calculated bond lengths [Å] and plane angles [deg] in the S_0 state and D_0 state (in brackets) of (3MI·H₂O)⁺. The shaded columns represent the change of the corresponding geometrical parameter upon ionization.

d) Vibrational structure of 3MI·H_2O in the D_0 state

The vibrational frequencies of the 3MI·H_2O complex in D_0 state were calculated at the B3LYP/6-31+G(d), B3LYP/cc-pVDZ, and MP2/cc-pVDZ levels of theory (**Table VIII.9**). Similarly to the case of bare 3MI, the latter method fails to give an overall accurate description of the vibrational modes of the ionized complex.

assign-ment	exp.	MP2/ cc-pVDZ		B3LYP/ cc-pVDZ			B3LYP/ 6-31+G(d)	
		unsc.	x0.9538[b]	unsc.	x 0.9717[b]	x 0.9807[c]	unsc.	x0.9636[b]
42^1	194	232.2	(221.5)	217.7	(211.5)	(213.5)	216.7	(208.8)
41^1	232	242.4	(231.2)	241.4	(234.6)	(236.7)	238.3	(229.6)
29^1	461	467.5	(446.0)	469.1	(455.8)	(460.0)	468.7	(451.6)
28^1	514	528.0	(503.6)	523.0	(508.2)	(513.0)	523.2	(504.2)
27^1	560	576.5	(550.0)	567.2	(551.1)	(556.2)	568.0	(547.3)
b	673	667.0	(636.2)	688.2	(668.7)	(675.0)	687.0	(662.0)
26^1	751	798.0	(761.1)	766.9	(745.2)	(752.1)	767.9	(739.9)
β	36	49.5	(47.2)	46.9	(45.6)	(46.0)	38.2	36.8
σ	180	203	(193.6)	208.7	(202.8)	(204.7)	187.7	180.9

Table VIII.9. Experimental and calculated frequencies [cm^{-1}] of the ground cationic state D_0 of (3MI·H_2O)$^+$ and the assignment of the corresponding vibrational bands. The shaded columns list the unscaled frequencies obtained at each of the employed quantum-chemical methods. (b) Scaling factors taken from [43]. (c) Scaling factors taken from [44].

The unscaled B3LYP intramolecular frequencies at both levels yield similar results and furthermore show quite acceptable agreement with the experiment (within 9 cm^{-1} in either case). The only exceptions are the 42^1 mode, the 26^1 mode and the b band, where the deviations are ≈ 23 cm^{-1}, ≈ 16 cm^{-1}, and ≈ 15 cm^{-1} for each frequency, respectively. Similarly to the case of 3MI (*Section VIII.3.3c*), when a scaling factor of 0.9807 [c] is used, the intramolecular B3LYP/cc-pVDZ frequencies are very close (within 5 cm^{-1}) to the experimental ones. The deviation for the frequencies scaled by a factor of 0.9717 is somewhat larger but not markedly different.

Larger disagreement (≈ 10 cm^{-1}) with the experiment is observed for the scaled frequencies calculated at the B3LYP/6-31+G(d) level, particularly for the 27^1 mode (≈ 13 cm^{-1}).

Unlike the case of the intramolecular modes, apparently there are noticeable discrepancies between the employed computational methods with respect to the predicted unscaled intermolecular vibrations of the hydrogen bond, β and σ. The results from the cc-pVDZ calculations exhibit large deviations from the experimental values, particularly for the intermolecular stretching vibration σ. This discrepancy is largest for the unscaled frequencies and somewhat smaller when scaling is applied. Interestingly, at the B3LYP/6-31+G(d) level, even the unscaled vibrational frequencies are already in very good agreement with the experiment. Applying a scaling factor of 0.9636 [43] brings the theoretical values even closer to the experimental frequencies (less than 1 cm^{-1})

e) Adiabatic Ionization Energy of 3MI·H₂O

The AIE of the 3MI·H₂O was estimated at the MP2/cc-pVDZ, B3LYP/cc-pVDZ and B3LYP/6-31+G(d) levels of theory. Similarly to the 3MI case (*Section VIII.3.3d*), CCSD/cc-pVDZ single point calculations were additionally performed for the optimized geometry at the MP2/cc-pVDZ level. The results are given in **Table VIII.10**.

MP2/cc-pVDZ	CCSD/cc-pVDZ SP	B3LYP/cc-pVDZ	B3LYP/6-31+G(d)
63 489 (+5875)	55 680 (−1934)	54 298 (−3316)	55 401 (−2213)

Table VIII.10. Calculated (ZPVE corrected) adiabatic ionization energy [cm^{-1}] of the 3MI·H₂O complex. The deviation of the computational results at each level of theory from the experimental value (57 614 cm^{-1}) is given in brackets.

Obviously, the best agreement with the experiment in regard to AIE of the 3MI·H₂O complex is achieved at the CCSD/cc-pVDZ single point level with the optimized MP2 geometry. As in the case of 3MI, MP2/cc-pVDZ overestimates the ionization energy, while the other levels underestimate it. However, unlike the calculated AIE of the monomer, the MP2 value obtained for the 3MI·H₂O complex shows prominent disagreement with the experiment ($\approx 10\%$). B3LYP yields, similarly to the case of the monomer, large

deviations from the experiment, although the value obtained with the 6-31+G(d) basis set is only by 279 cm^{-1} lower than that calculated at the CCSD single point level. Moreover, the B3LYP/6-31+G(d) underestimates the AIE of the 3MI·H_2O in a similar fashion as for the monomer ($\approx 4\%$).

f) Hydrogen-bond strength of 3MI·H_2O in the ground neutral (S_0) and ground cationic state (D_0).

The strength of the hydrogen bonding in the 3MI·H_2O complex was calculated at all levels of theory employed for geometry optimization in S_0 and D_0 state. Additionally, CCSD/cc-pVDZ single point calculation was performed with the optimized geometry for either state at the MP2/cc-pVDZ level. The results are summarized in **Table VIII.11**.

	Exp.	`MP2/cc-pVDZ`	`CCSD/cc-pVDZ SP`	`B3LYP/cc-pVDZ`	`B3LYP/6-31+G(d)`
D_0	1572	2785	2398	2760	1596
E_0	4669	1470	6418	6228	4768

Table VIII.11. Experimental and calculated (ZPVE corrected) binding energies D_0 and E_0 of the neutral (S_0) and the ionized (D_0) 3MI·H_2O complex, respectively. The obtained values are not BSSE corrected. Introducing BSSE correction by employing the counterpoise method led in the present calculations to poorer agreement with the experiment. This point is further discussed at the end of this chapter. All values are in cm^{-1}.

MP2/cc-pVDZ and B3LYP/cc-pVDZ levels yield fairly similar binding energies of the ground neutral state, with a difference of only 25 cm^{-1}. However, both methods apparently substantially overestimate the bond strength as the obtained values are more than 1.7 times larger than the experimental values. The CCSD/cc-pVDZ single point level only slightly improves the accuracy by decreasing the binding energy by 387 cm^{-1}. The overestimation in this case of 1.5 times is, however, still large. On the other hand, the B3LYP/6-31+G(d) level gives an excellent agreement with the experiment: the calculated binding energy D_0 in this case is higher than the experimental value by only 24 cm^{-1} (1.5%).

With respect to the dissociation energy E_0 in the ground cationic state, the MP2/cc-pVDZ and B3LYP/cc-pVDZ calculations again show large deviations from the experiment. B3LYP/cc-pVDZ overestimates E_0 by 1559 cm^{-1}, while MP2 strongly underestimates the hydrogen-bond strength in the ground state of the ionized 3MI·H₂O complex by 3199 cm^{-1}. CCSD SP yields larger disagreement with the experiment than the B3LYP with the same (cc-pVDZ) basis set. Again, as for the D_0 energy, the best agreement with the experimental finding for E_0 is achieved at the B3LYP level with employing the 6-31+G(d) basis set. Here the accuracy of the calculations is only slightly lower than in the case of the neutral as the theoretical value differs by $\approx$ 2%.

<p style="text-align:center">***</p>

Comparing the optimized structures of 3MI·H₂O obtained with the methods described in *Section VIII.4.4* it is interesting to note that the computational results on the geometry of the hydrogen bonding in 3MI·H₂O are more strongly dependent on the basis set than on the employed level. Two different methods (MP2 and B3LYP) implementing the same basis set (cc-pVDZ) show substantial similarity in predicting the geometry of the 3MI·H₂O, while going from cc-pVDZ to 6-31+G(d) basis set in the B3LYP calculations has a much more pronounced effect. Similar dependence of the mutual water/indole ring orientation on the basis set was previously reported for the indole·H₂O complex by Fang [48]. It was shown that adding diffuse functions to heavy and light atoms in the basis set leads to a tendency for linearity of the hydrogen bond in the computational results. The same effect of adding diffuse functions on heavy atoms on the predicted mutual orientation of the hydrogen-bond partners was elucidated by Jiang and Tsai [27] for DFT studies of the pyrrole·HF complex. Moreover, the authors report elongation of the N1-O1 distance when diffuse functions are used, similarly to the results in **Table VIII.8**.

The B3LYP/6-31+G(d) level yields intermolecular vibrational frequencies of 3MI·H₂O closer to the experimental values, although B3LYP/cc-pVDZ proves to be more reliable with respect to the intramolecular modes. B3LYP/6-31+G(d) surpasses the other two methods (MP2/cc-pVDZ and B3LYP/cc-pVDZ) with respect to the accuracy in estimating the adiabatic ionization energy of the monohydrated 3MI. Interestingly, the reliability of DFT calculations with a smaller basis set is comparable to that of the CCSD/cc-pVDZ single point level. Moreover, the implementation of the B3LYP functional in combination with the 6-31+G(d) basis set is apparently a proper choice for estimating the binding energies of the 3MI·H₂O complex as the computational results show excellent agreement with the experiment in this respect.

It is tempting to assume that B3LYP/6-31+G(d) describes more accurately the hydrogen bonding in the 3MI·H_2O than the more sophisticated B3LYP/cc-pVDZ and particularly MP2/cc-pVDZ. Such a supposition is justified since the method exhibits as a whole better agreement with the findings from the threshold ionization studies, namely the vibrational frequencies of the hydrogen bond, the adiabatic ionization energy, and the binding energies in the neutral and the cation. In contrast, the implementation of a larger basis set, cc-pVDZ, leads to overestimation of the hydrogen-bond strength (resulting in larger binding energies and larger red shift of the AIE). The orientation of the water molecule with respect to the indole ring predicted by the B3LYP/cc-pVDZ optimization suggests that the method probably accounts for an additional interaction between the water hydrogens and the π-electron system of the phenyl ring in the S_0 state. Oppositely, MP2 strongly underestimates the hydrogen bonding in the cation and overestimates it in the neutral state. Moreover, the energy E_0 in the cation is smaller than D_0 and accordingly the adiabatic ionization energy is larger than that of the monomer, which should not be the case as the water attachment has stabilizing effect on the cation state.

One important comment concerning the neglect of the basis set superposition error (BSSE) in estimation of the binding energy of 3MI·H_2O and (3MI·H_2O)$^+$ should be made at this point. Ignoring the BSSE in the present computational results seems unconventional and the good agreement of the B3LYP/6-31+G(d) with the experiment in regard to the binding energy may be attributed to fortuitous cancellation of errors between the basis set incompleteness and BSSE. However, Jiang and Tsai [27] showed that using diffuse functions on heavy atoms substantially decreases the BSSE, particularly in DFT calculations. Positive effect on the computational accuracy due to the neglect of BSSE has been reported for the case of covalent potential curves by Wright and Barclay [49] [49], for the theoretical determination of heats of formation by Oliphant et al. [50] and for quantum chemical calculations on the OH$^-$(H_2O) system by Weck at al. [51].

VIII.5. 3-methylindole·benzene complex

VIII.5.1. 3MI·C₆H₆ R2PI

The two-color R2PI spectrum of the $3MI \cdot C_6H_6$ complex is presented in **Fig.VIII.12** (lower trace) along with the spectrum of 3MI for comparison (upper trace).
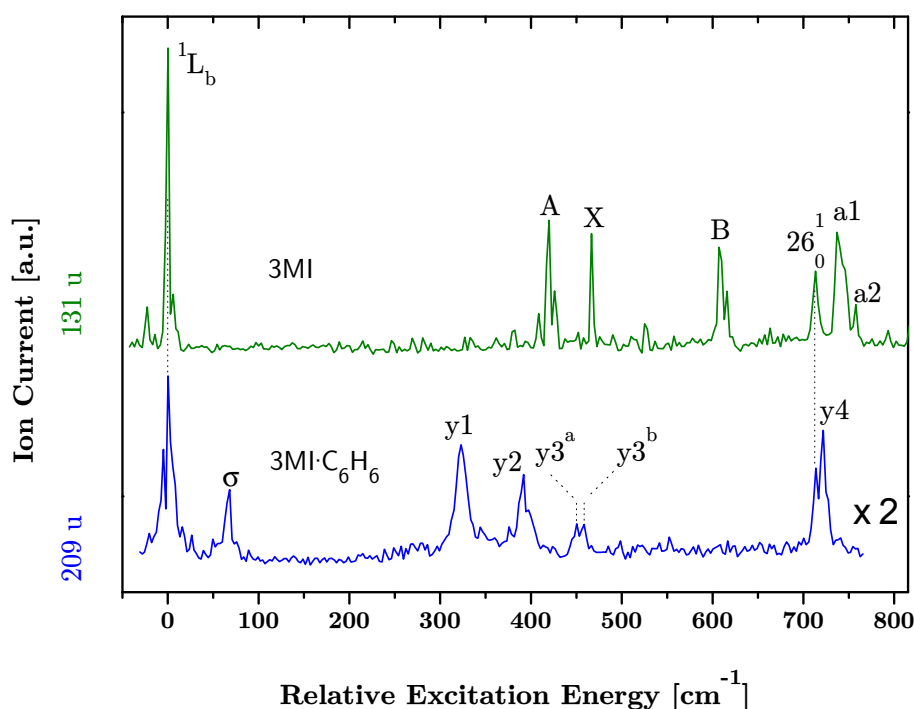
Fig.VIII.12. Two-color R2PI spectra of the $3MI \cdot C_6H_6$ complex (lower trace) recorded at the 209 u mass channel and 3MI (upper trace) recorded at the 131 u mass channel and plotted on a common excitation energy scale. The excitation energy is relative to the respective ^1L_b $S_1 \leftarrow S_0$ origin. The intensity in the excitation spectrum of the complex is increased by a factor of 2 for better visualization.

The height of the peaks was corrected for the fluctuations in the intensity of the scanning laser. The positions of the observed peaks are listed in **Table VIII.12**.

The origin of the excitation spectrum was searched in a frequency region $200 - 300$ cm^{-1} below the origin of the 3MI R2PI spectrum. Such a large scanning region was chosen sin-

ce the $S_1 \leftarrow S_0$ origin of 3MI·C_6H_6 is expected to be further red-shifted than that of 3MI·H_2O (233 cm^{-1}, *Section VIII.4.1*). This assumption implies *i*) hydrogen bonding as binding mechanism in 3MI·C_6H_6 *ii*) the effect of the larger proton affinity of benzene than that of water on the $S_1 \leftarrow S_0$ origin red shift upon complexation.

A π type hydrogen bonding was proposed previously for the indole·C_6H_6 complex [52, 53] in which the N1–H1 site of the indole system serves as hydrogen-bond donor and the π electron moiety in benzene serves as hydrogen-bond acceptor. It is plausible to suggest the same type of bonding in 3MI·C_6H_6 as the methyl group at C3 position lies remote from the complexation site, and consequently, is not expected to affect the bonding due to steric hindrance. The second condition stems from the results reported by Demmer et al. [20] on the induced red shifts in the $S_1 \leftarrow S_0$ origin upon hydrogen-bond formation in complexes of 3MI with various solvents.

In this regard the peak at 34 623.0 cm^{-1} was assigned to the $S_1 \leftarrow S_0$, 0_0^0 transition of the 3MI·C_6H_6 complex as no other peaks were observed when the laser was scanned 200 cm^{-1} further to lower frequencies. The obtained value is red shifted by 252 cm^{-1} from the respective transition of 3MI. The proton affinity of benzene is less than 200 kcal/mol ($\approx$ 177.5 kcal/mol [54]) which, similarly to the case of 3MI·H_2O, renders the $S_1 \leftarrow S_0$ origin of 3MI·C_6H_6 as ^1L_b type although the excitation spectrum is probably substantially affected by $^1L_a - {}^1L_b$ mixing [14, 20].

The band at 68 cm^{-1} can be identified as a stretching (σ) vibration of the hydrogen bond similarly to the case of the indole·C_6H_6 complex [53]. The origin of the peaks y1, y2, and y3 (which exhibits a split profile) in the region 300 – 500 cm^{-1} is not clear. These peaks appear to be nearly equidistant, which suggests that they form a progression-like envelope similarly to the x1, x2, and x3 bands in the case of 3MI·H_2O (**Fig. VIII.6**). A more speculative alternative is to explain the observed peaks as bands originating from $^1L_a \leftarrow {}^1A$ excitation. Such bands may be observable for 3MI·C_6H_6 in this frequency range because of the expected small $^1L_a-{}^1L_b$ energy difference as suggested from the results by Demmer et al. [20] as well as by Short and Callis [14]. Polarization fluorescence experiments [14, 19] or lifetime measurements [20] may shed light on this matter.

Furthermore, the y1, y2, and y3 peaks have FWHM which is about two times larger than that of the A, X, and B peaks in the excitation spectrum of 3MI. This most probably stems from the excitation of low-frequency vibrational modes in the complex, which are covered by the band envelope, as was suggested for indole·C_6H_6 system [53]. The peak at 722 cm^{-1} was assigned in an earlier work [55] as the 26^1 breathing mode of the indole ring

in 3MI·C_6H_6. However, it seems to be substantially shifted from the respective band in the excitation spectrum of 3MI (**Fig.VIII.12**, upper trace). The small peak at 714 cm^{-1} seems a more suitable candidate for the 26^1 mode, although it is probably buried in the peak y4 at 722 cm^{-1}. The latter, on the other hand, may be interpreted as having a ^1L_a character similarly to the peaks a1 and a2 in the excitation spectrum of 3MI (*Section VIII.3.1*).

assignment	σ	y1	y2	y3^a	y3^b	26^1 ?	y4
frequency, cm^{-1}	68	321	392	458	466	714	722

Table VIII.12. Observed peaks in the $S_1 \leftarrow S_0$ two-color R2PI spectrum of 3MI·C_6H_6 up to 750 cm^{-1} above the origin at 34 623 cm^{-1}.

VIII.5.2. 3MI·C_6H_6 MATI

Fig.VIII.13 shows the threshold ionization spectrum of the 3MI·C_6H_6 complex measured in the low-internal-energy region (-70 – 490 cm^{-1}) via the $S_1 \leftarrow S_0$, 0_0^0 transition. The first strong peak at 58 018 ± 5 cm^{-1} is taken as the adiabatic ionization energy, AIE. This value corresponds to a red shift of 2693 cm^{-1} from the AIE of 3MI. The spectrum in **Fig.VIII.13** is dominated by high intensity peaks in the region up to 200 cm^{-1}, which are assigned to an intermolecular bending mode (β) and intermolecular stretching (σ) mode, respectively (**Table VIII.13**), by comparison with the experimental data on the (indole·C_6H_6)$^+$ complex [34, 53]. Two of the bands corresponding to the methyl group motion, α_1 and α_3 which can be clearly recognized in the MATI spectrum of 3MI are superimposed by the bending and the stretching mode of the hydrogen bond. This is also evident from the frequencies of the observed peaks listed in **Table VIII.13**. Similarly, the third band α_2 is very weak unlike the case of 3MI and cannot be unambiguously determined.

assignment	β	σ	α_1	α_2	α_3
frequency, cm^{-1}	27	91	23	50	83

Table VIII.13. Low-frequency bands observed in the threshold ionization spectrum of (3MI·C_6H_6)$^+$ and their assignment.

Due to decreasing laser and signal intensity, the scan was performed only in the afore-mentioned ion internal energy range. Thus it was not possible to check whether intramolecular vibrations above 500 cm^{-1} would be observable unlike the case for 3MI and, to some extent, $(3MI \cdot H_2O)^+$.
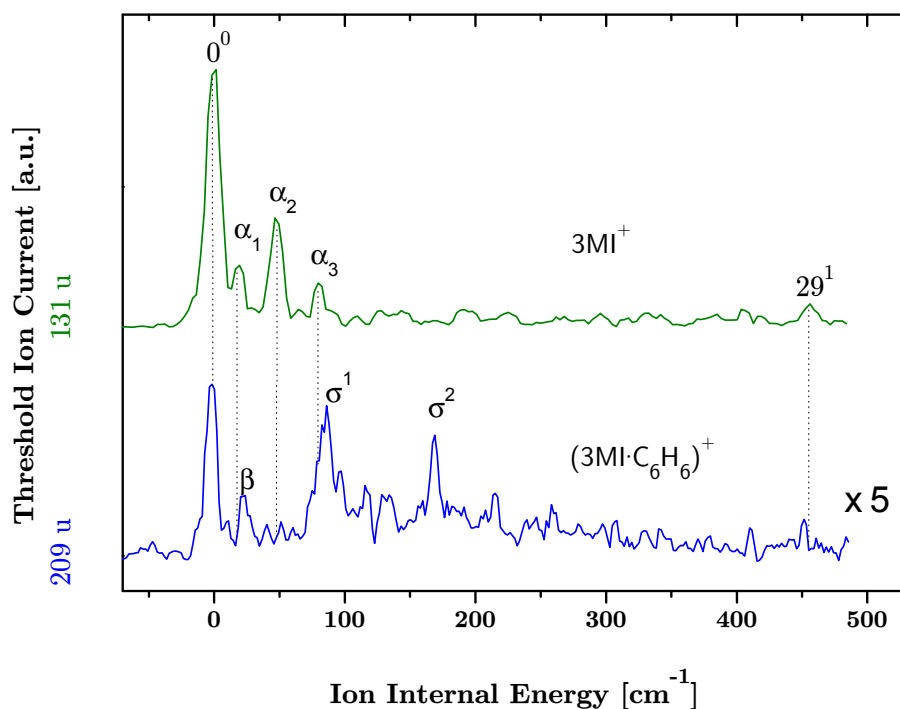
Fig.VIII.13. MATI spectra of the $(3MI \cdot C_6H_6)^+$ complex (lower trace, 209 u) and 3MI$^+$ (upper trace, 131 u). The threshold ion signal of the complex is increased by a factor of 5 for a better visualization.

VIII.5.3. Dissociation of the $(3MI \cdot C_6H_6)^+$ complex

The MATI spectrum of $(3MI \cdot C_6H_6)^+$ was measured in the excess energy region between 3970 and 4720 cm^{-1} above the AIE, where dissociation is expected from the results on $(indole \cdot C_6H_6)^+$ [53]. The scans were performed via two intermediate states: the origin of S_1 and the band at 321 cm^{-1} (peak y1 in **Fig.VIII.12**). The signal-to-noise ratio in the threshold ion current achieved via the S_1 origin was not sufficient for an unambiguous determination of the dissociation threshold of $(3MI \cdot C_6H_6)^+$. A much better result was obtained when measuring the MATI spectrum via the y1 band. The lack of resolved vibrational structure is quite reasonable for an excess energy above 4000 cm^{-1}.

The lower and the upper traces in **Fig.VIII.14** represent the threshold ion current at the complex (parent) mass channel and at the fragment (daughter) mass channel, respectively.
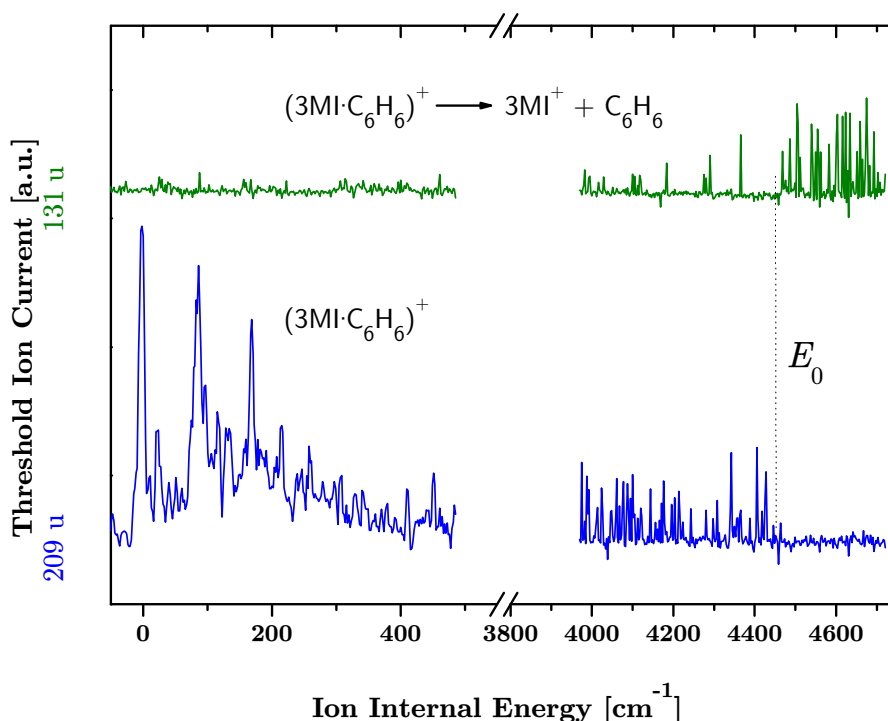
Fig.VIII.14. Mass analyzed threshold ionization spectrum of the $(3MI·C_6H_6)^+$ complex via the $S_1 \leftarrow S_0$, y1 band (321 cm^{-1}) recorded simultaneously at the parent (lower trace, 209 u) and fragment (upper trace, 131 u) mass channel. The scanning range comprises the low (up to 490 cm^{-1}) and high (3970 – 4720 cm^{-1}) ion internal energy region. The dissociation threshold E_0 at 4448 cm^{-1} is marked by a vertical line.

The frequency of the first (excitation) laser was fixed at the $S_1 \leftarrow S_0$, y1 transition (321 cm^{-1}) during the scan. The individual peaks in the 3970 – 4720 cm^{-1} range in the figure represent single ions. Similarly to the case of $(3MI·H_2O)^+$, there is no vibrational structure seen above 3970 cm^{-1}, which is expected for this energy range.

Although the signal-to-noise ratio is not very high, it is clear that there is no signal at the parent mass channel above $E_0 = 4448 \pm 20$ cm^{-1}, whereas at this energy there is an onset of the signal at the fragment mass channel. As in the case of $(3MI·H_2O)^+$ in **Fig.VIII.8** the dashed vertical line indicates the so-obtained dissociation threshold E_0.

The binding energy of 3MI·C_6H_6 (S_0) was calculated according to Eq. **VI.4** (p. 77) to be $D_0 = 1755 \pm 20$ cm^{-1}.

VIII.5.4. Indications of N1–H1···π hydrogen bonding in 3MI·C_6H_6

The red shift in the origin of the $S_1 \leftarrow S_0$ excitation spectrum of 3MI·C_6H_6 induced by complex formation is larger by approximately 20 cm^{-1} compared to that in the case of 3MI·H_2O. Since benzene has larger proton affinity than water, this finding is in agreement with the general trend found for hydrogen-bonded complexes in which 3MI serves as solute, namely that the $S_1 \leftarrow S_0$, 0_0^0 red shift upon complexation is proportional to the solvent proton affinity [20].

Furthermore, the appearance of an intermolecular stretching mode (σ) progression in the threshold ionization spectrum of (3MI·C_6H_6)$^+$ is similar to the case of (3MI·H_2O)$^+$ (*Section VIII.4.2*). On the other hand, the frequency of the σ stretching mode in the former case is half the respective frequency in the latter case. This is to be expected from the ratio of the reduced masses in both cases in a diatomic molecule approximation and points to a bonding at the same site in 3MI (i.e. N1–H1) as in 3MI·H_2O.

Finally, the binding energy of 3MI·C_6H_6 ($D_0 = 1755$ cm^{-1}) in the ground neutral state S_0 is higher by $\approx 67\%$ from that of toluene·C_6H_6 ($D_0 = 1049$ cm^{-1} [56]), although the dissociation thresholds in the ground cationic state are comparable ($E_0 = 4448$ cm^{-1} and 4270 cm^{-1}, respectively). The much smaller absolute value of the binding energy in the *neutral* toluene·C_6H_6 complex clearly demonstrates that the type of bonding is completely different from that in 3MI·C_6H_6. In the former case it has been shown theoretically that mainly dispersion and electrostatic quadrupole interaction are responsible for the bonding [57], while the 3MI·C_6H_6 complex is apparently formed by hydrogen bond at the pyrrolic N1–H1 site.

VIII.5.5. Quantum-chemical calculations on the 3MI·C_6H_6 complex

The structures of 3MI·C_6H_6 in the ground neutral (S_0) and ground cationic (D_0) state were optimized at the MP2/cc-pVDZ, B3LYP/cc-pVDZ, and B3LYP/6-31+G(d) levels of theory, similarly to the case of 3MI and 3MI·H_2O. Both stacked and T-shape geometries of the complex were used as starting points in the optimization procedure of the employed methods.

a) Geometry of 3MI·C₆H₆ in S₀ state

The only mutual orientation of 3MI and benzene found with the optimization procedure at the MP2/cc-pVDZ level is shown in **Fig. VIII.15**. As the results from the calculations suggest, MP2 fails to predict optimized hydrogen bonded N1–H1···π (T-shape) structure in the S_0 state. This finding is in line with the results reported by Braun et al. [25] who showed that MP2 combined with a large basis set (TZVPP) manifests preference for a stacked structure for indole·C₆H₆. Following this conclusion, a MP2/6-31+G(d) optimization procedure was performed. However, the mutual orientation of 3MI and benzene resulted again in a stacked one. Furthermore, unlike the results from Braun et al., no second optimized hydrogen-bonded structure was found, even when T-shape geometry was used as a starting configuration.

On the other hand, both DFT methods employing the B3LYP functional predict T-shape geometry of the complex with the N1–H1 axis pointing almost to the center of the benzene molecule, thus showing the formation of an N1–H1···π hydrogen bond. It is interesting to note that these results agree with the ones reported on indole·C₆H₆ with implementtation of a more sophisticated method, namely CCSD(T) with the 6-31G**(0.25, 0.15) basis set [25]. Furthermore, contrary to the MP2 calculations, a stacked optimized structure of the complex was not found with the B3LYP functional for 3MI·C₆H₆ with either basis set (cc-pVDZ and 6-31+G(d)).

b) Geometrical changes in 3MI (S_0) upon 1:1 complexation with benzene

The position of the methyl group as well as the internuclear distances and bond angles in the pyrrole ring of 3MI in the monomer and the complex are given in **Table VIII.14**. Here only the results from the DFT calculations are presented since MP2 fails to predict T-shape structure in the S_0 state, as discussed above. A comparison of the listed values in the table shows the following:

First, it can be seen that the position and orientation of the methyl group with respect to the indole ring are practically unaffected by complex formation. Second, the N1–H1 bond elongates weakly (by 0.002 Å) upon complex formation as expected for a proper (red shifting) bond. The other bond lengths and angles in the indole ring experience also minor changes or remain unaffected. The changes in the phenyl ring are of the same order and are not given in the table. All these findings apparently lead to the conclusion that the formation of the 3MI·C₆H₆ complex has little effect on the geometry of the indole ring in 3MI as well as on the orientation of the methyl group.
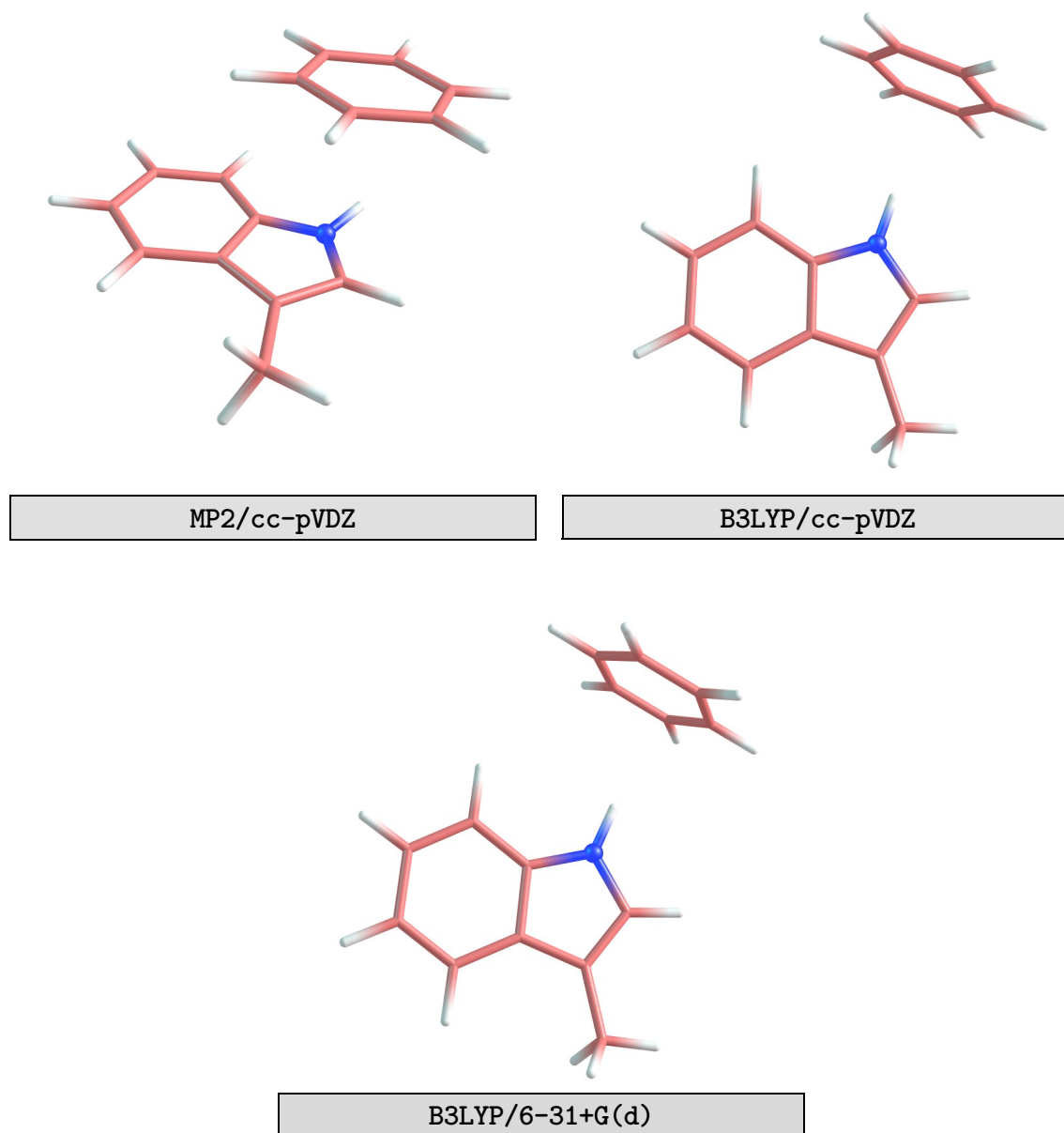
Fig.VIII.15. Optimized structures of the 3MI·C₆H₆ complex in the ground neutral (S₀) state at all employed levels of theory. These are the *only* geometries predicted with each method. See text for more details on the orientation of the benzene molecule in the three cases.

Geom.		B3LYP/cc-pVDZ			B3LYP/6-31+G(d)	
parameter		3MI	3MI·C₆H₆		3MI	3MI·C₆H₆
N1–H1		1.010	1.012		1.008	1.010
N1–C2		1.385	1.384		1.387	1.385
C2–C3		1.376	1.376		1.373	1.374
C3–C9		1.444	1.444		1.444	1.443
C9–C8		1.426	1.426		1.424	1.425
N1–C8		1.379	1.377		1.380	1.379
C8–N1–H1		125.5	125.8		125.6	125.9
C8–N1–C2		109.2	109.0		109.1	109.0
N1–C2–H2		120.5	120.3		120.4	120.2
N1–C2–C3		110.2	110.3		110.2	110.3
C3–C10		1.499	1.498		1.500	1.500
C2–C3–C10		127.1	127.2		127.1	127.2
C2–C3–C9		106.1	106.0		106.2	106.1
C3–C9–C4		133.8	133.8		133.7	133.7
N1–C8–C7		130.7	130.6		130.6	130.6

Table VIII.14. Calculated internuclear distances [Å] and bond angles [deg] in 3MI in the case of the monomer and the 3MI·C₆H₆ complex.

c) Geometrical changes in 3MI·C₆H₆ upon ionization

The optimized structures of 3MI·C₆H₆ in the D_0 cationic state are visualized in **Fig.VIII.16**. The most interesting result to notice is that MP2/cc-pVDZ predicts T-shape geometry of the complex in this case, thus pointing to the formation of a N1–H1···π hydrogen bond, unlike the case of S_0 state (**Fig.VIII.15**).
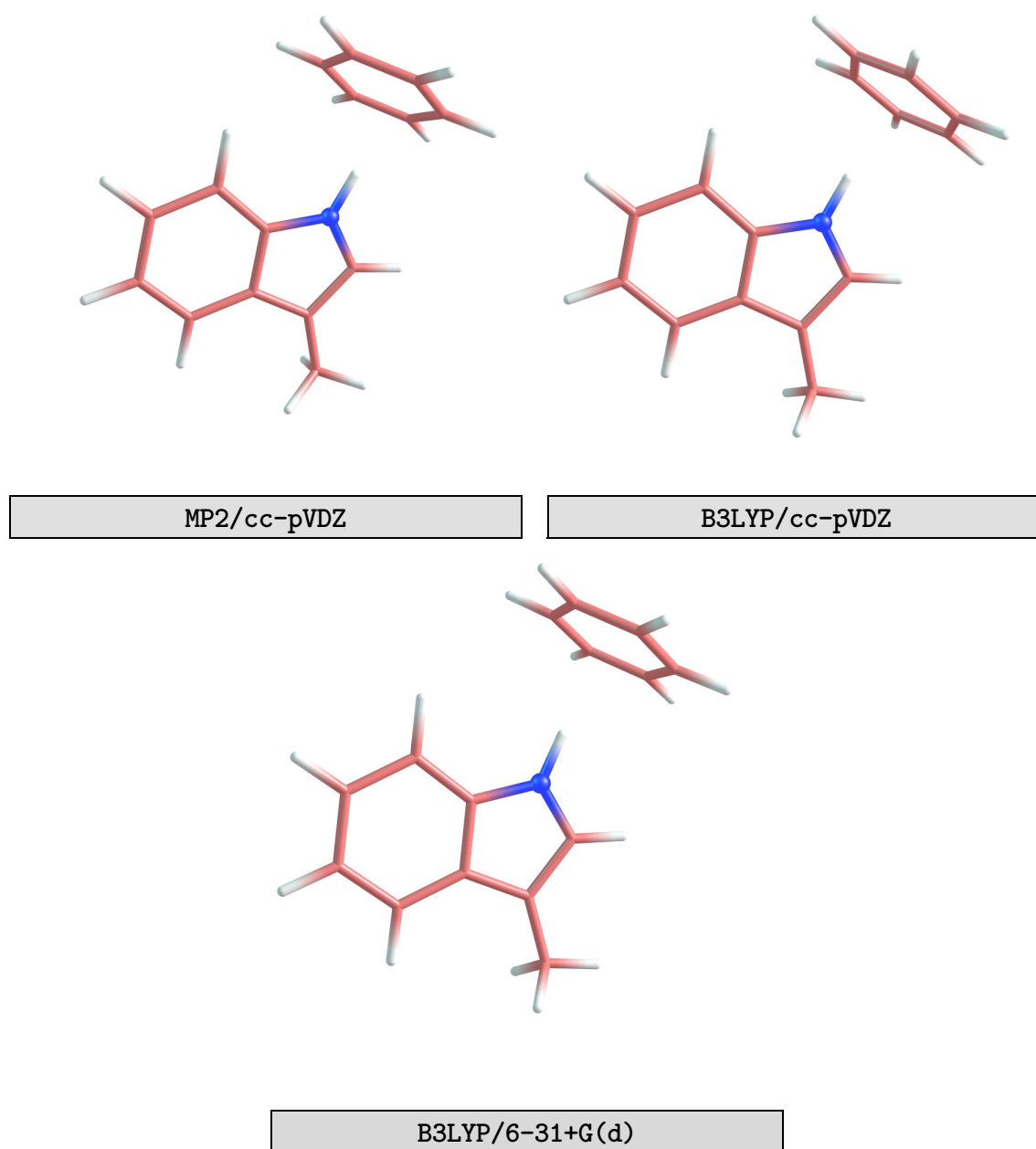
Fig.VIII.16. Optimized structures of the $(3MI \cdot C_6H_6)^+$ complex in the ground cationic D_0 state at all employed levels of theory. The calculations in all three cases were started from the optimized structures in the ground neutral S_0 state. See text for more details on the orientation of the benzene molecule predicted in each case.

Geom. parameter	MP2/ cc-pVDZ	Geom. parameter	B3LYP/ cc-pVDZ		B3LYP/ 6-31+G(d)	
N1–H1	1.028	N1–H1	1.012 (1.026)	0.014	1.010 (1.023)	0.013
N1–C2	1.345	N1–C2	1.384 (1.332)	-0.052	1.385 (1.332)	-0.053
C2–C3	1.433	C2–C3	1.376 (1.434)	0.058	1.374 (1.432)	0.058
C3–C9	1.418	C3–C9	1.444 (1.429)	-0.015	1.443 (1.427)	-0.016
C9–C8	1.423	C9–C8	1.426 (1.422)	-0.004	1.425 (1.421)	-0.004
N1–C8	1.400	N1–C8	1.377 (1.408)	0.031	1.379 (1.409)	0.030
C8–N1–H1	125.8	C8–N1–H1	125.8 (125.5)	-0.3	125.9 (125.5)	-0.4
C8–N1–C2	109.2	C8–N1–C2	109.0 (109.7)	0.7	109.0 (109.7)	0.7
N1–C2–H2	121.3	N1–C2–H2	120.3 (121.4)	1.1	120.2 (121.4)	1.2
N1–C2–C3	109.7	N1–C2–C3	110.3 (110.1)	-0.2	110.3 (110.0)	-0.3
C4–C9	1.410	C4–C9	1.408 (1.411)	0.003	1.407 (1.410)	0.003
C4–C5	1.370	C4–C5	1.392 (1.401)	0.009	1.391 (1.401)	0.010
C5–C6	1.398	C5–C6	1.413 (1.399)	-0.014	1.412 (1.398)	-0.014
C6–C7	1.402	C6–C7	1.393 (1.418)	0.025	1.392 (1.418)	0.026
C7–C8	1.357	C7–C8	1.402 (1.380)	-0.022	1.400 (1.378)	-0.022
C4–C5–C6	120.0	C4–C5–C6	121.0 (120.8)	-0.2	121.0 (120.7)	-0.3
C3–C10	1.490	C3–C10	1.498 (1.485)	-0.013	1.500 (1.488)	-0.012
C2–C3–C10	125.5	C2–C3–C10	127.2 (125.8)	-1.4	127.2 (125.7)	-1,5
C2–C3–C9	105.9	C2–C3–C9	106.0 (105.5)	-0.5	106.1 (105.6)	-0.5
C3–C9–C4	132.9	C3–C9–C4	133.8 (133.2)	-0.6	133.7 (133.2)	-0.5
N1–C8–C7	130.0	N1–C8–C7	130.6 (130.0)	-0.6	130.6 (130.0)	-0.6

a　　　　　　　　　　**b**

Table VIII.15. Calculated bond lengths [Å] and plane angles [deg] in 3MI·C₆H₆ **a)** in the cationic D₀ state at MP2/cc-pVDZ and **b)** in the neutral S₀ state and cationic D₀ state (in brackets) at DFT level. The shaded columns in **b** represent the change of the corresponding geometrical parameter upon ionization.

Performing DFT calculations employing the B3LYP functional with both cc-pVDZ and 6-31+G(d) basis sets yields, similarly to the case of the neutral complex, hydrogen bonding at the N1–H1 site.

The angle between the N1–H1 axis and the plane of the benzene molecule in the three cases in **Fig. VIII.16** is close to 90°.

As seen in **Table VIII.15** the MP2/cc-pVDZ values of the geometrical parameters of $(3MI \cdot C_6H_6)^+$ are close to the ones (given in brackets) from the DFT calculations. The only noticeably larger discrepancies are manifested for the C4–C5 and C7–C8 bond lengths. Both B3LYP/cc-pVDZ and B3LYP/6-31+G(d) calculations yield similar changes in the indole ring upon ionization for the $3MI \cdot C_6H_6$ complex as in the case of 3MI and $3MI \cdot H_2O$. The largest deformations occur in the pyrrole ring, particularly at the N1–C2 and C2–C3 bonds ($\approx 3.8\%$ and $\approx 4.2\%$, respectively). As in the case of $3MI \cdot H_2O$, the N1–H1 bond elongates to a larger extent when the complex is ionized in comparison with 3MI, which supports the experimental finding of the increased bonding strength in the cation (*Section VIII.5.3*).

d) Vibrational structure of 3MI·C₆H₆ in the D₀ state

The calculated intramolecular vibrational frequencies of $(3MI \cdot C_6H_6)^+$ in the ground state D_0 obtained at MP2/cc-pVDZ, B3LYP/cc-pVDZ, and B3LYP/6-31+G(d) levels of theory are given in **Table VIII.16**. The respective experimental frequencies of the bare molecule, 3MI are also listed in order to investigate the agreement of the computational results with the experimental findings. It should be noted that such a comparison is not completely rigorous unlike the case of 3MI and $(3MI \cdot H_2O)^+$. As pointed out in *Section VIII.5.2* the intramolecular vibrational frequencies in the MATI spectrum of $(3MI \cdot C_6H_6)^+$ are not available in the present study. However, comparing the calculated frequencies of D_0 $(3MI \cdot C_6H_6)^+$ with the experimental ones of $3MI^+$ is reasonable on account of the following consideration. It is plausible to assume that the hydrogen bonding in the $(3MI \cdot C_6H_6)^+$ complex does not exert large effect on the indole ring vibrations, as this was also the case for the $(3MI \cdot H_2O)^+$ complex. Therefore, even if a quantative comparison between theory and experiment for the ground state intramolecular vibrations of $(3MI \cdot C_6H_6)^+$ would not be completely rigorous, it is still possible to investigate the overall performance of the employed computational methods.

assign-ment	exp.	MP2/ cc–pVDZ		B3LYP/ cc–pVDZ			B3LYP/ 6–31+G(d)	
		unsc.	x 0.9538[b]	unsc.	x 0.9717[b]	x 0.9807[c]	unsc.	x0.9636[b]
42^1	194	231.2	(220.5)	217.0	(210.9)	(212.9)	215.8	(208.0)
41^1	232	236.4	(225.5)	232.2	(225.6)	(227.7)	232.8	(224.3)
29^1	458	464.2	(442.8)	463.4	(450.3)	(454.5)	464.5	(447.6)
28^1	516	525.4	(501.1)	522.8	(508.0)	(512.7)	522.8	(503.8)
27^1	563	575.5	(549.0)	566.8	(550.8)	(555.9)	567.5	(546.8)
b	673	661.9	(631.3)	684.7	(665.3)	(671.5)	684.5	(659.6)
26^1	751	798.6	(761.7)	767.8	(746.1)	(753.0)	767.5	(739.6)
β	27	23.2	(22.1)	29.6	(28.8)	(29.0)	(30.4)	(29.3)
σ	91	96.0	(91.6)	83.4	(81.0)	(81.9)	(79.8)	(76.9)

Table VIII.16. Experimental frequencies of 3MI⁺ and calculated frequencies of the (3MI·C₆H₆)⁺ complex [cm⁻¹] in the D₀ state. Also given is the assignment of the corresponding vibrational bands. The shaded columns represent the unscaled frequencies obtained at each of the employed quantum-chemical methods. (b) Scaling factors taken from [43]. (c) Scaling factors taken from [44].

The unscaled MP2/cc-pVDZ frequencies for the 41^1 29^1 28^1 vibrational modes exhibit small deviations $\delta\overline{v}$ from the experimental values (less than 10 cm⁻¹). The deviations for the 27^1 and b bands, respectively, are somewhat larger ($\delta\overline{v} \approx 12$ cm⁻¹ and ≈ 11 cm⁻¹, respectively). On the other hand, the MP2 values for the 42^1 and 26^1 bands are in poor agreement with the experiment ($\delta\overline{v} \approx 37$ cm⁻¹ and ≈ 48 cm⁻¹, respectively) unlike the case of 3MI⁺ (**Table VIII.4**). When scaling by a factor of 0.9538 [43] is applied, only the 42^1 and 26^1 frequency positions exhibit improved agreement with the experimental values, while the opposite is valid for the other frequencies.

Furthermore, similarly to the 3MI⁺ and (3MI·H₂O)⁺ case, DFT B3LYP method yields unscaled intramolecular frequencies that are almost independent of the basis set employed. In addition, the obtained values exhibit a reasonable agreement with the experiment (largest deviation of 7 cm⁻¹ for the 28^1 mode), except for the b, 26^1 bands and, particularly, for the 42^1 band. Scaling the B3LYP/cc-pVDZ frequencies by 0.9807 [44] brings as a whole the calculated values closer to the experimental ones than using a scaling factor of 0.9717 [43] (except for the 42^1 band), although the differences between the scaled frequencies in both cases are not large.

The vibrational frequencies at the B3LYP/6-31+G(d) level show somewhat poorer agreement with the experiment particularly for the 27^1 band (deviation ≈ 16 cm^{-1} as in the case of $(3MI \cdot H_2O)^+$ complex, **Table VIII.9**).

Comparing the last two rows in **Table VIII.16** it can be seen that generally all employed methods yield values for the vibrational frequency of the intermolecular bending mode, β, that are very close to the experimental finding. On the other hand, it is interesting to notice that the MP2/cc-pVDZ frequency for the stretching mode σ is closest to the experimental value, although B3LYP/cc-pVDZ exhibits also a reasonable agreement.

e) Adiabatic Ionization Energy of 3MI·C$_6$H$_6$

As the results in **Table VIII.17** show, the best agreement with the experimental value for the AIE of 3MI·C$_6$H$_6$ is attained at the B3LYP/6-31+G(d) level of theory: the adiabatic ionization energy is underestimated by only $\approx 2.8\%$. B3LYP/cc-pVDZ yields larger deviation ($\approx 4.1\%$) toward lower values, while the MP2/cc-pVDZ largely overestimates the AIE by approx. 11%.

MP2/cc-pVDZ	B3LYP/cc-pVDZ	B3LYP/6-31+G(d)
64 651 (+6633)	55 614 (−2404)	56 420 (−1598)

Table VIII.17. Calculated (ZPVE corrected) adiabatic ionization energy of the 3MI·C$_6$H$_6$ complex. The deviation of the computational results at each level of theory from the experimental value (58 018 cm^{-1}) is given in brackets. All values are in cm^{-1}.

f) Hydrogen-bond strength of 3MI·C$_6$H$_6$ in the ground neutral (S$_0$) and ground cationic state (D$_0$).

As evident from the results listed in **Table VIII.18**, B3LYP properly predicts the increase of the binding energy upon ionization in the 3MI·C$_6$H$_6$ complex for both basis sets. However, the employed DFT approach strongly underestimates the bonding strength in 3MI·C$_6$H$_6$ and $(3MI \cdot C_6H_6)^+$. The calculations performed with the cc-pVDZ basis set yield slightly larger energies than those employing the 6-31+G(d) basis set, but nevertheless

they are far smaller than the experimental values. Including BSSE corrections did not led to better agreement with the experiment. An overestimation of the experimental value of E_0 due to kinetic shift that would also contribute to the observed variance in **Table VIII.18** is unlikely to play an essential role due to the high detection sensitivity of the mass spectrometer [45].

The large deviation can be tentatively attributed to an inadequate description of all interactions involved. To account for the presumable dispersion interactions in this case, a recourse to specially developed for this purpose models, e.g. the M05 functional, might be helpful.

Furthermore, performing CCSD single point calculations with the optimized structure of $3MI·C_6H_6$ in the neutral and cation at the DFT level did not improve the estimation of the bonding strength. Braun et al. [25] reported a quite reasonable agreement of *ab initio* calculations with the experiment (0.1 kcal/mol $\approx$ 35 cm^{-1}) for the indole·C_6H_6 complex in S_0 state. However, the quantum-mechanical treatment in this case implied computations at the CCSD(T) level using the optimized structure of indole·C_6H_6 at the MP2 level in the ground neutral state. Such approach was not applicable in the current study on $3MI·C_6H_6$ since, as already discussed, MP2 completely failed to yield a hydrogen-bonded structure in this case for the S_0 state.

	Exp.	B3LYP/cc-pVDZ	B3LYP/6-31+G(d)
D_0	1755	731	577
E_0	4448	2883	2730

Table VIII.18. Experimental and calculated (ZPVE corrected) binding energies D_0 and E_0 of the neutral (S_0) and ionized (D_0) $3MI·C_6H_6$ complex. No BSSE correction applied. All values are in cm^{-1}.

VIII.6. Comparison of the hydrogen bonding in the $3MI \cdot H_2O$ and $3MI \cdot C_6H_6$ complexes

It is interesting to compare the hydrogen bonding in $3MI \cdot H_2O$ and $3MI \cdot C_6H_6$ complexes both in their ground neutral and ground cationic state as these two systems are examples of different bonding type, σ- and π-bonding. **Table VIII.19** summarizes the experimental findings for both complexes in the present work.

System	$S_1 \leftarrow S_0, 0_0^0$	Δ	AIE	δ		E_0	D_0
$3MI \cdot H_2O$	34 642	233	57 614	3097		4 669	1572
$3MI \cdot C_6H_6$	34 623	252	58 018	2693		4448	1755

Table VIII.19. Transition frequencies and binding energies of the neutral (D_0) and ionized (E_0) complexes studied in the present work. The red shifts of the $S_1 \leftarrow S_0, 0_0^0$ and AIE values for each complex from the ones for the monomer are designated with Δ and δ, respectively. All values are in cm^{-1}.

VIII.6.1 $S_1 \leftarrow S_0$, 0_0^0 red shift (Δ) upon complexation

As discussed in *Section VIII.5.1* the 1:1 complexation of 3MI with benzene induces larger red shift in the origin of the $S_1 \leftarrow S_0$ excitation spectrum than the 1:1 complex formation with water in accord with the general trend discussed by Demmer et al. [20].

VIII.6.2. Red shift in AIE (δ) upon complexation

As seen from **Table VIII.19**, the decrease in the adiabatic ionization energy upon complex formation is larger in the case of $3MI \cdot H_2O$ by approx. 400 cm^{-1} than for $3MI \cdot C_6H_6$. This finding points to a stronger stabilization of the ground cationic state, D_0, when 3MI forms a hydrogen bond with water than with benzene.

VIII.6.3. Hydrogen-bond strength in 3MI·H₂O and 3MI·C₆H₆

a) Experimental results

Fig.VIII.17 shows the threshold ionization spectra of $3MI·C_6H_6$ and $3MI·H_2O$ in the high ion internal energy region above 4000 cm^{-1} measured at the respective parent and fragment mass channels. They are plotted on a common ion internal energy scale, relative to the respective AIE in each case. As can be seen from the decrease in the parent signal and the onset of the fragment signal for each complex, both $(3MI·C_6H_6)^+$ and $(3MI·H_2O)^+$ dissociate in the internal energy region $4400 - 4800$ cm^{-1}. The dissociation thresholds of the two complexes are marked by the two vertical dashed lines in **Fig.VIII.17**. The dissociation energy E_0 of the $(3MI·H_2O)^+$ complex of 4669 ± 20 cm^{-1} is larger by 221 cm^{-1} than that of $(3MI·C_6H_6)^+$. However, the binding energy in the ground state of the neutral $3MI·C_6H_6$ is larger by 183 cm^{-1} than the one of the neutral $3MI·H_2O$, 1572 ± 20 cm^{-1}.

A comparison between E_0 and D_0 for the two complexes (**Table VIII.19**) shows therefore that the hydrogen bonding in the ground cationic state is *stronger* in $3MI·H_2O$ than in $3MI·C_6H_6$ by 221 cm^{-1} while in the ground neutral state it is *smaller* by 183 cm^{-1}. Previous studies have shown that there is a correlation between *the ratio* of the hydrogen-bond strength in S_0 and S_1 states and the solvent proton affinity [20]. In this regard it is plausible, however, only to assume that the hydrogen bonding in $3MI·H_2O$ and $3MI·C_6H_6$ complexes is stronger in their ground neutral state than in their excited neutral state as both water and benzene have proton affinities smaller than 200 kcal/mol.

On the other hand, the experimental results in the present work shed light on the absolute hydrogen-bond strength of $3MI·H_2O$ and $3MI·C_6H_6$ complexes. As the binding energy D_0 of the latter is larger and benzene has larger proton affinity than water, the aforementioned relation may be tentatively extended in the following manner: larger proton affinity of the solvent leads to stronger hydrogen bonding in the ground neutral state. However, for a more convincing conclusion in this regard to be made, the binding energies D_0 of other 3MI·Y (Y is a single solvent molecule) hydrogen-bonded complexes must be obtained. Such necessity is demanded since specifically in the case of $3MI·C_6H_6$ the larger binding energy compared to that of $3MI·H_2O$ may result from an additional contribution from dispersions interactions to the net interaction energy.
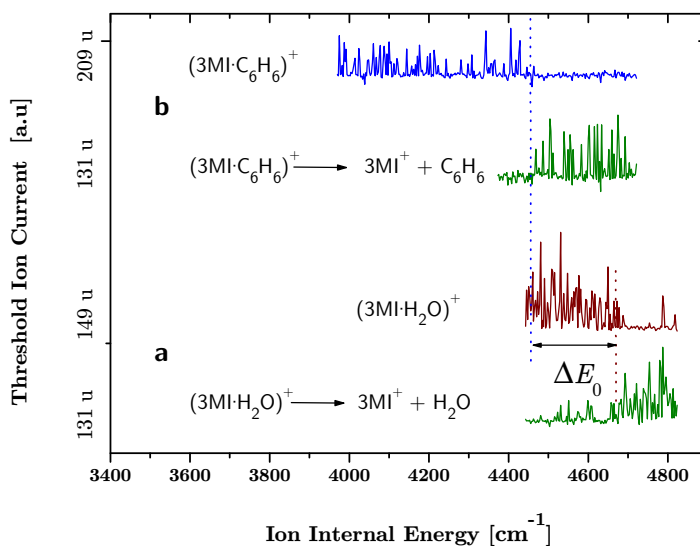
Fig.VIII.17. MATI spectra of the $(3MI \cdot H_2O)^+$ **(a)** and $(3MI \cdot C_6H_6)^+$ **(b)** complexes recorded in the 4000 – 4900 ion internal energy region at the respective parent and fragment (daughter) mass channels. The dissociation threshold of either complex is marked by a dashed line.

In the ionized complexes the situation is opposite: E_0 of $(3MI \cdot H_2O)^+$ is larger than that of $(3MI \cdot C_6H_6)^+$. Most probably this results from the stronger charge-induced interaction of $3MI^+$ with H_2O than with the more delocalized π electrons in benzene.

The stronger stabilization of the D_0 state in $3MI \cdot H_2O$ compared to that in $3MI \cdot C_6H_6$ as evident from the different induced red shifts in the AIEs upon complexation also supports this model. Even if the $3MI \cdot C_6H_6$ complex is additionally stabilized by dispersion interaction, its contribution in the cation is smaller than that of the charge-induced interaction.

b) Effect of hydrogen-bond formation on the N1–H1 stretching vibrational frequency and the N1–H1 bond length

It is interesting to investigate how the frequency of the N1–H1 stretching vibration, $\overline{v}$ (N1–H1), is affected by the hydrogen-bond formation in the ground neutral and ground cationic state. **Table VIII.20** lists the scaled frequencies of the N1–H1 stretching vibration in each of the studied systems calculated at the B3LYP/6-31+G(d) level of theory. For comparison, the experimental values reported by Carney at al. [22] for 3MI and 3MI·H₂O in S_0 state are also presented. The length of the pyrrolic N1–H1 bond in the S_0 and D_0 state for the three systems is given in **Table VIII.21**.

State	3MI	3MI · H₂O	3MI · C₆H₆
S_0	3536 (3526)	3428 (3442)	3512
D_0	3473	3164	3335

Table VIII.20. B3LYP/6-31+G(d) values of $\overline{v}$ (N1–H1) scaled by 0.9636 [43] in the case of 3MI, 3MI·H₂O, and 3MI·C₆H₆ as well as experimental findings (in brackets) from RIDIR[3] spectra [22]. All values are in cm⁻¹.

State	3MI	3MI · H₂O	3MI · C₆H₆
S_0	1.008	1.016	1.010
D_0	1.015	1.033	1.023

Table VIII.21. Calculated length of the N1–H1 bond at the B3LYP/6-31+G(d) level in the case of 3MI, 3MI·H₂O, and 3MI·C₆H₆. All values are in Å.

First, it can be seen that the employed level of calculations exhibits quite acceptable agreement with the experiment with respect to $\overline{v}$ (N1–H1). The deviations in the fre-

---

[3] **Resonant Ion-Dip InfraRed spectroscopy**

quency of the N1–H1 stretch from the values reported by Carney at al. is 10 cm^{-1} for the ground state 3MI and 14 cm^{-1} for the ground state 3MI·H_2O.

Second, the N1–H1 stretching frequency decreases upon hydrogen-bond formation at the N1–H1 site as expected for red shifting (proper) bonding. The estimated decrease in the case of 3MI·H_2O is 108 cm^{-1}, while that in the case of 3MI·C_6H_6 is only 24 cm^{-1}. The latter finding may be interpreted as an indicator for a weaker bonding in the case of complexation with benzene than with water. However, such a conclusion is potentially wrong since the red shift in the stretching vibration of the hydrogen donor X–H cannot be unambiguously related to the hydrogen-bond strength. Moreover, the employed computational methods underestimate the binding energy D_0 in the S_0 state of 3MI·C_6H_6 as discussed in *Section VIII.5.5f*. Considering in addition the inaccuracy of estimating the frequency of the N1–H1 stretch in the case of 3MI and 3MI·H_2O, it is therefore reasonable to conclude that the calculations only predict a $\bar{\nu}$ (N1–H1) red shift upon complexation in the S_0 state.

The $\bar{\nu}$ (N1–H1) red shift upon complex formation in the D_0 state is 309 and 138 cm^{-1} for (3MI·H_2O)$^+$ and (3MI·C_6H_6)$^+$, respectively. This result is on the one hand in accord, similarly to the case of S_0 state, with the concept of proper hydrogen bonding in the studied complexes. On the other hand, both values are larger than the ones for the neutral complexes, which agrees with the experimental findings that the hydrogen-bond strength increases upon ionization (*Sections VIII.4.3* and *VIII.5.3*). Furthermore, apparently the red shift of the N1–H1 stretching frequency is larger in the (3MI·H_2O)$^+$ complex than in (3MI·C_6H_6)$^+$. This finding *supports* the conclusion for a stronger bonding in the former case (*Section VIII.6.3a*), although for reasons discussed in the preceding paragraph it cannot serve as a rigorous indicator of the bond strength.

The results are supported by the estimated increase in the N1–H1 bond length in S_0 and D_0 states upon hydrogen-bond formation as can be seen from **Table VIII.21**.

Similar results were obtained also at the B3LYP/cc-pVDZ level of theory, which points to the ability of DFT B3LYP to describe (at least semi-quantatively) the effect of hydrogen-bond formation on the N1–H1 stretching frequency and N1–H1 bond length in the studied systems.

VIII.7. Methyl group substitution effect in 3MI, 3MI·H₂O, and 3MI·C₆H₆

The CH_3 group is a weak electron donating (activating) substituent, i.e., it is characterized by a small positive inductive effect, $+I$. By a comparative study of 3MI and indole in the following sections it is investigated how the structure and the spectroscopic properties of indole and its 1:1 hydrogen-bonded complexes with water and benzene are affected by methyl group substitution at the C3 site in the indole ring. Within the scope of the present work such a comparison comprises the experimentally elucidated substitution effect on the $S_1 \leftarrow S_0, 0_0^0$ energy gap, the AIE, and, additionally, the intermolecular bonding strength in the case of hydrogen-bonded complexes. Furthermore, the effect of methyl group substitution on the ring geometry is explored by employing quantum-chemical calculations.

VIII.7.1. 3-methylindole vs. indole

a) Substitution effect on the $S_1 \leftarrow S_0$ origin

The $S_1 \leftarrow S_0$ origin of the R2PI spectrum of 3MI is at 34 875 cm^{-1} (*Section VIII.3.1*). A comparison with the results on indole [53, 58, 59] shows that methyl group substitution at the C3 site in the indole ring causes a red shift of 356 cm^{-1} in the origin of the excitation spectrum of bare 3MI. On the other hand, the $S_1 \leftarrow S_0$ origin of the energetically most stable conformer of 3-ethylindole is 34 810 cm^{-1} [60], which indicates a red shift of 421 cm^{-1} compared to the case of indole. The decrease in the excitation energy in the alkylated indoles stems from the greater stabilization of the S_1 state compared to that of the S_0 state upon alkyl substitution. This effect is also present in benzene derivatives (e.g. toluene, ethylbenzene) and is typical for electron donating substituents (alkyl radicals, OH, NH_2,…).

The smaller red shift in 3MI compared to 3-ethylindole is expected from the weaker inductive effect of the substituent in the former case. However, it can be seen that extending the alkyl side chain does not reduce the $S_1 \leftarrow S_0 \ 0_0^0$ energy gap dramatically: substitution of the CH_3 group with the CH_2CH_3 alkyl residue shifts the origin by only 65 cm^{-1} to the red.

b) Substitution effect on the AIE

The adiabatic ionization energy of indole is 62 591 cm^{-1} [53, 58], i.e., according to the value obtained for 3MI, 60 711 cm^{-1} [*Section VIII.3.2*], the methyl group substitution at the C3 position lowers the AIE by 1880 cm^{-1}. The decrease of the adiabatic ionization energy stems from the stronger stabilization of the ground cationic state D_0 than that of the S_0 state upon methyl group substitution as expected for an electron activating substituent. The removal of an electron (leading to electron deficiency) decreases the stability of the molecule compared to the neutral. The methyl group reduces this instability (stabilizing the cation) by donating electron density to the aromatic ring.

A comparison with the AIE of 3-ethylindole measured in a ZEKE experiment [60] shows that substitution of the methyl group with a CH_2CH_3 alkyl side chain causes an additional decrease of the adiabatic ionization energy by 294 cm^{-1}. As in the case of the $S_1 \leftarrow S_0$, 0_0^0 red shift, the lower AIE in case of 3-ethylindole can be explained with the stronger positive inductive effect of the substituent. On the other hand, the decrease of the ionization threshold in 3MI is larger than that of other methylated indoles [32, 61], pointing to a relatively stronger stabilization of the ground cationic state D_0 when the methyl group substitution occurs at C3 position.

It is worth noticing that the methylation of the benzene molecule (resulting in toluene) causes a red shift of 3356 cm^{-1} in the AIE [62, 63], which is much larger than the corresponding red shift in 3MI and 1-methylindole from that in indole. This finding points to a stronger effect of the CH_3 group on the ionized electron in case of a single aromatic ring.

c) Methylation effect on the indole ring vibrations

A comparison of the results in **Table VIII.22** shows that methylation in 3MI induces a mode-specific effect on the indole intramolecular vibrations. Most of the modes observed in the MATI spectrum of 3MI have frequencies similar to those reported for indole [35, 45]. On the other hand, noticeable exceptions are the 27^1 and particularly the 29^1 mode. The frequency of the former exhibits a red shift of 24 cm^{-1}, while the frequency of the 29^1 mode increases by 68 cm^{-1} upon C3 methyl group substitution. Results from quantum-chemical calculations performed for 3MI$^+$ (*Section VIII.3.3*) and indole$^+$ at the MP2/cc-pVDZ, B3LYP/cc-pVDZ, and B3LYP/6-31+G(d) levels of theory support these experi-

mental findings and furthermore point to a similar substitution effect in the ground neutral state S_0.

assignment	α_1	α_2	α_3	42^1	41^1	29^1	28^1	27^1	b	26^1
3MI	23	50	83	194	232	458	516	563	673	751
indole				192	233	390	518	587		748

Table VIII.22. Observed intramolecular frequencies in the threshold ion spectra of 3MI and indole [45]. All values are in cm^{-1}.

As the calculations show, the large frequency shifts for the 27^1 and 29^1 vibrational modes stem from prominent changes in the reduced mass and particularly in the force constant in the case of 3MI. A possible explanation is the coupled motion between the respective in-plane ring mode and the CH_3 bending vibration.

The large substitution effect of the 27^1 and 29^1 mode frequencies is not unusual as can be deduced from the results reported for other substituted aromatic hydrocarbons by Wu et al. [64]. On the other hand, by comparing the present results with those in the aforementioned work, it is interesting to point out that the indole ring-breathing mode 26^1 is only weakly affected by methylation at least in the 3MI case in contrast to the findings for aniline$^+$ and N-methylaniline$^+$ [64].

VIII.7.2. 3MI·H_2O and 3MI·C_6H_6 vs. indole·H_2O and indole·C_6H_6

a) Substitution effect on the $S_1 \leftarrow S_0$, 0_0^0 red shift upon hydrogen-bond formation

Table VIII.23 summarizes the red shifts of the $S_1 \leftarrow S_0, 0_0^0$ transition upon complexation of indole [53] and 3MI with water and benzene, respectively. It can be seen that the formation of a hydrogen bond with water leads to different red shifts of the $S_1 \leftarrow S_0, 0_0^0$ origin in the cases of indole and 3MI. The same is also valid for the indole·C_6H_6 and 3MI·C_6H_6 complexes.

indole·H_2O	indole·C_6H_6
$x_1 = 132^*$	$x_2 = 164^*$
3MI·H_2O	**3MI·C_6H_6**
233 (x_1+101)	252 (x_2+88)

Table VIII.23. Red shifts in cm^{-1} upon hydrogen-bond formation in the $S_1 \leftarrow S_0$ origin of indole·Y and 3MI·Y complexes (Y = H_2O or C_6H_6). *Based on the results reported by Braun et al. [53].

A comparison with the results in *Section VIII.7.1a* shows that the C3 methylation in the indole ring exerts larger effect on the $S_1 \leftarrow S_0$, 0_0^0 energy gap (decrease by 356 cm^{-1}) than the 1:1 hydrogen-bond formation with water and benzene (decrease by $x_{1,2} < 200$ cm^{-1}, **Table VIII.23**). Furthermore, the increase of 101 cm^{-1} and 88 cm^{-1} in the red shift upon complex formation in case of 3MI·H_2O and 3MI·C_6H_6, respectively, compared to their not methylated analogues can be explained with the substitution effect of the methyl group.

b) Substitution effect on the hydrogen bonding induced red shift of AIE

As the results in **Table VIII.24** show, the complexation with water and benzene leads to slightly smaller red shifts in the ionization threshold in 3MI than in indole.

indole·H_2O	indole·C_6H_6
$X_1 = 3158^*$	$X_2 = 2758^*$
3MI·H_2O	**3MI·C_6H_6**
3097 ($X_1–61$)	2693 ($X_2–65$)

Table VIII.24. Decrease of the adiabatic ionization energy in cm^{-1} upon hydrogen-bond formation in indole·Y and 3MI·Y complexes (Y = H_2O or C_6H_6). *Based on the results reported by Braun et al.[53].

Unlike the case of $S_1 \leftarrow S_0$ origin (**Table VIII.23**), the red shift of AIE is apparently very weakly affected by methyl group substitution at the C3 site in indole (**Table VIII.24**). This is manifested by the very small difference of about 60 cm^{-1} ($\approx 2\%$) in the AIEs of the methylated and non-methylated complexes. Moreover, it should be mentioned that the ground cationic state, D_0, in indole is more strongly stabilized by hydrogen-bond formation (by 3158 cm^{-1} and 2758 cm^{-1} for indole·H$_2$O and indole·C$_6$H$_6$, respectively) than by methyl group substitution (by 1880 cm^{-1}). Apparently, the lowering of the adiabatic ionization threshold is mainly due to the stabilizing effect of hydrogen bonding in the cation (on account of charge-induced interaction). This might explain why contrary to $S_1 \leftarrow S_0, 0_0^0$, the $D_0 \leftarrow S_0$ energy gap *increases* in 3MI·Y compared to indole·Y, which is evident from the *smaller* red shift (i.e. smaller stabilization of the D_0 state) by ≈ 60 cm^{-1} of AIE upon complexation in the case of 3MI and indole. Since the hydrogen bonding induces much larger lowering of AIE than methylation at the C3 site, it is apparently the main factor that affects the $D_0 \leftarrow S_0$ energy gap.

c) Substitution effect on the hydrogen-bond strength

The smaller stabilization of the ground cationic state, D_0, in the complexes when hydrogen at the C3 site in the indole ring is substituted by a methyl group suggests a weaker bonding in 3MI·Y than in indole·Y (Y=H$_2$O, C$_6$H$_6$). To investigate further how the methyl group substitution at the C3 site affects the hydrogen-bond strength, this section presents a comparison of the binding energies E_0 of (indole·Y)$^+$ and (3MI·Y)$^+$ as well as the binding energies D_0 in the respective ground neutral states.

As shown in **Table VIII.25** there is a decrease in E_0 and D_0 upon C3 methylation by 121 and 60 cm^{-1}, respectively, for indole·H$_2$O, and by 133 and 68 cm^{-1}, respectively, for indole·C$_6$H$_6$. Since 3MI serves as a hydrogen-bond donor both in 3MI·H$_2$O and 3MI·C$_6$H$_6$ these results are in agreement with the studies of other hydrogen-bonded complexes and, in particular, with the general rule that electron donating substituents in the hydrogen-bond donor weaken the bonding strength [65, 66]. On the other hand, the small changes in E_0 and D_0 for the studied systems point to a weak substitution effect on the strength the hydrogen bonding, which is to be expected from the small electron donating ability of the methyl group.

Moreover, as pointed out in *Section VIII.6.3*, the hydrogen bonding in 3MI·H_2O is *stronger*/weaker in the ground *cationic*/neutral state than that in 3MI·C_6H_6. These findings are in line with the results reported for indole·C_6H_6 and indole·H_2O [34, 53] that manifest the same trend and show fairly similar differences in D_0 and E_0. Therefore methyl group substitution at C3 does not change the relative strength of the ground-state hydrogen bonding of indole with water and benzene in both neutral and ionized complexes.

system	E_0	D_0
indole·H_2O	4790[*]	1632[*]
3MI·H_2O	4669	1572
indole·C_6H_6	4581[*]	1823[*]
3MI·C_6H_6	4448	1755

Table VIII.25. Binding energies [cm^{-1}] of 3MI·H_2O and 3MI·C_6H_6 and their non-methylated counterparts in the S_0 state (D_0) and D_0 state (E_0). *Results reported by Braun et al.[53].

***

It is interesting to compare the methyl group substitution effect and the bonding in 3MI·C_6H_6 with respect to indole·C_6H_6 with those of benzene·C_6H_6 with respect to toluene·C_6H_6 [56]. The binding energies of benzene·C_6H_6 and toluene·C_6H_6 complexes are about 5320 and 4270 cm^{-1} in the respective cationic ground state and only 565 and 1049 cm^{-1} in the respective ground neutral state [56]. The extremely weak influence of the methylation in the position 3 on the binding energy of the *ionized* (3MI·C_6H_6)$^+$ complex (2.9%) compared to the (24.5%) reduction in case of (toluene·C_6H_6)$^+$ demonstrates the different character of the bonding in the ionized complex in addition to the conclusion in *Section VIII.5.4* though the absolute values are comparable: i.e. in (toluene·C_6H_6)$^+$ and (benzene·C_6H_6)$^+$ the main contribution is from charge resonance interaction [56, 67, 68], while in (indole·C_6H_6)$^+$ and (3MI·C_6H_6)$^+$ hydrogen bond is formed.

VIII.7.3. Theoretical studies of the C3 methyl substitution effect in indole

In addition to the 3MI and 3MI·H_2O cases, geometrical optimization at the B3LYP/6-31+G(d) level was also performed for indole and indole·H_2O systems.

a) Methylation effect on the internuclear distances

A comparison with the results reported by George et al. [40] shows that methyl group substitution in 3MI has similar effect on the adjacent C–C bond lengths as in the case of toluene: elongation of the C2–C3 and C3–C9 bonds by $\approx 0.15\%$ and $\approx 0.4\%$, respectively.

As the results in **Table VIII.26** reveal, C3 methylation of indole does not induce as a whole prominent geometrical changes. As expected, the largest effect occurs in the C3–H3 bond length, when H3 is substituted with the CH_3 group, which induces an elongation of 0.418 Å. The ∢(C2–C3–C10) angle experiences a weak increase by 1.2°, while the angle in the pyrrole ring at C3, ∢(C2–C3–C9) manifests even a smaller change, decreasing by 0.9° upon methyl group substitution.

The N1–C2 distance increases weakly upon methyl group substitution at C3 which can be explained with the slight destabilizing effect of the substituent on the N1–C2 bonding strength in the vicinity of the lone pair at N1. Also, the methyl group as an electron donating substituent increases the electron density at the N1 and C2 sites. This is opposite to the case of electron withdrawing substituents at C3 site in indole as can be seen from a comparison of the present results with the findings reported by Billes et al. [69] on formyl and acetyl groups substitution.

In the case of complexation with one water molecule at the N1–H1 site, the calculations show that the water oxygen draws electron density from the pyrrolic nitrogen, which slightly compensates for the aforementioned effect and leads to a slight decrease of the difference in the N1–C2 bond length in indole and 3MI from 0.003 Å to 0.002 Å. Apparently, the observed effects are very minor, which is to be expected for a weak substituent such as the CH_3 group and for more solid conclusions in this regard to be made, cases with stronger electron donating substituents should be studied.

Furthermore, as the results in **Table VIII.26** show, B3LYP/6-31+G(d) predicts no significant differences in the changes upon ionization of the respective geometrical parameters in indole and 3MI. A noticeable exception is, however, the C3–C9 bond length. The DFT calculations show for both basis sets (6-31+G(d) and cc-pVDZ) that the bond decreases in length much more substantially in indole (by 0.030 Å $\approx 2\%$) than in 3MI (by 0.019 Å $\approx 1.3\%$) when the molecule is ionized to the D_0 state.

Geom. parameter	indole			3MI		
N1–H1	1.009 (1.015)		0.006	1.008 (1.015)		0.007
N1–C2	1.384 (1.337)		-0.047	1.387 (1.336)		-0.051
C2–C3	1.372 (1.425)		0.053	1.373 (1.431)		0.058
C3–C9	1.438 (1.408)		-0.030	1.444 (1.425)		-0.019
C3–H3 or C3–C10	1.082 (1.082)		0.000	1.500 (1.488)		-0.012
C2–C3–C10	125.9 (125.0)		-0.9	127.1 (125.6)		-1,5
C2–C3–C9	107.1 (106.9)		-0.2	106.2 (105.7)		-0.5

Geom. parameter	indole·H_2O			3MI·H_2O		
N1–H1	1.016 (1.034)		0.018	1.016 (1.033)		0.017
N1–C2	1.381 (1.332)		-0.049	1.383 (1.332)		-0.051
C2–C3	1.374 (1.428)		0.054	1.375 (1.433)		0.058
C3–C9	1.437 (1.409)		-0.028	1.442 (1.427)		-0.015
C3–H3 or C3–C10	1.082 (1.082)		0.000	1.500 (1.488)		-0.012

Table VIII.26. Bond lengths [Å] in the pyrrole moiety of indole and 3MI as well as of indole·H_2O and 3MI·H_2O in the S_0 and D_0 (in brackets) states, respectively. The shaded columns represent the length change upon ionization for the case of the monomers and complexes. The employed level of theory is DFT B3LYP/6-31+G(d).

A comparison of the results on indole·H_2O and indole·C_6H_6 with their 3-methyl substituted analogues show the same trend in the change of the C3–C9 bond length upon ionization. On the other hand, MP2/cc-pVDZ calculations on indole show that the length of the C3–C9 bond in indole remains nearly constant changing from 1.438 Å to 1.437 Å in the $D_0 \leftarrow S_0$ transition. Similar discrepancy in the results on the C3–C9 bond length between DFT B3LYP and MP2 methods was observed for 3MI as discussed in *Section*

*VIII.3.3.*For indole, the present results obtained with B3LYP/6-31+G(d) and B3LYP/cc-pVDZ agree with the findings reported in a previous work by Unterberg et al. [70] from DFT B3LYP, CAS (10, 9) and CAS (9, 9) calculations performed with the 6-31G(d,p) basis set. Most probably MP2 underestimates the length change of the C3–C9 bond in indole and overestimates it in 3MI.

b) Methylation effect on the N1–H1 stretching frequency

The values for the S_0 $\overline{\nu}$(N1–H1) frequency in 3MI (*Section VIII.6.3b*) and indole exhibit quite reasonable agreement with the experimental findings reported by Carney at al. [22] with the deviation in both cases being ≈ 10 cm^{-1}. The discrepancy in the case of the complexes is somewhat larger (14 cm^{-1}) but still fairly acceptable.

As seen in **Table VIII.26**, for the case of the bare molecules methylation at the C3 site in the indole ring does not induce prominent changes in the pyrrolic N1–H1 bond length or the frequency of the N1–H1 stretching vibration, $\overline{\nu}$(N1–H1) (**Table VIII.27**). On the other hand, the stretching frequency experiences somewhat larger decrease upon hydrogen bond formation in the case of the non-methylated complex, particularly in the cation (15 cm^{-1}). The latter result as well as the slightly larger (by 0.001 Å) elongation of the N1–H1 bond length upon complexation in (indole·H$_2$O)$^+$ than in (3MI·H$_2$O)$^+$ could be attributed to the stronger *proper* hydrogen bonding in the non-methylated complex.

parameter	3MI	indole		3MI·H$_2$O	indole·H$_2$O
$\overline{\nu}$(N1–H1)	3536	3534		3428	3422
	(3473)	(3473)		(3164)	(3149)

Table VIII.27. Frequency of the N1–H1 stretch [cm^{-1}] in indole and 3MI in the respective S_0 and, in brackets, D_0 states, estimated at the DFT B3LYP/6-31+G(d) level of theory.

However, under the assumption made in *Section VIII.6.3b*, the discussed results have to be considered only as semi-quantative indications of the substitution effect on the hydrogen-bond strength. Moreover, as expected from the weak electron donating property of the methyl group, the induced changes upon substitution on the N1–H1 bond length and

$\overline{\nu}$ (N1–H1) frequency are apparently quite minor (and even smaller in the case of complexation with benzene).

VIII.7.4. Summary on the C3 methyl group substitution effect in the studied systems

Methyl group substitution at the C3 site in the monomer has stronger effect on the $S_1 \leftarrow S_0, 0_0^0$ energy gap and on the adiabatic ionization energy in comparison with other mono methylated indoles. However, the effect of hydrogen bonding exceeds that of C3 methyl substitution in regard with the AIE, as seen from the experimental results on $3MI \cdot H_2O$ and $3MI \cdot C_6H_6$. Methylation of indole at the C3 site also has small effect on the hydrogen-bond strength at N1–H1 site as has been demonstrated from the threshold ionization studies in the present work. This apparently strongly supports the local character of the hydrogen bonding in $3MI \cdot H_2O$ and $3MI \cdot C_6H_6$.

As the results from the quantum chemical calculations suggest, C3 methylation affects weakly the internuclear distances and bond angles in the indole ring. The changes upon substitution of these geometrical parameters are even smaller in the hydrogen-bonded complexes with water and benzene. This can be explained with the opposite effects of hydrogen bonding and methyl group substitution on the strength of covalent bonding in the pyrrole ring. The formation of a hydrogen bond at the N1–H1 site weakly stabilizes the N1–C2 bond by withdrawing electron density from N1 and C2, while the CH_3 group at C3 position slightly destabilizes it by increasing the electron density at nitrogen and C2.

The experimental and theoretical findings in the present work for the relatively small methylation effect in 3MI, $3MI \cdot H_2O$, and $3MI \cdot C_6H_6$ are in agreement with the fact that the methyl group is a weak electron donating substituent. Studies of indole derivatives substituted at the C3 site with stronger electron activating groups such as CH_2–CH_3, OH, and particularly NH_2 will presumably lead to more pronounced changes in the $S_1 \leftarrow S_0\ 0_0^0$ energy gap, AIE, as well as larger deformations in the pyrrole ring and thus may further shed light on the aforementioned effects.

VIII.8. Summary and perspectives

Overall performance of the employed computational methods in the study on 3MI, 3MI·H$_2$O and 3MI·C$_6$H$_6$ systems

All employed levels of theory (MP2/cc-pVDZ, DFT B3LYP/cc-pVDZ, and DFT B3LYP/6-31+G(d)) predict as a whole smaller changes upon ionization in the phenyl ring than in the pyrrole moiety of 3MI in all studied systems. This has been previously explained for indole by Walden and Wheeler [71, 72] with the nodal structure of the HOMO. The D$_0$ state of indole is formed by the removal of a π-electron similarly to other aromatic rings and the changes in the bond lengths are therefore related to the nodal structure of the π-orbital from which the electron is ejected. For the indole ring in particular, this concept also explains the differences in the deformations of the six- and five-membered ring [71, 72].

In addition all methods:

- correctly predict elongation of the C2–C3 and C3–C9 bond lengths upon methyl group substitution;

- correctly predict shortening of the C3–C10 bond length upon ionization;

- decrease of the N1–C2 distance upon complexation;

- support the experimental finding on hydrogen-bond strength decrease upon methylation and hydrogen-bond strength increase upon ionization.

There are, however, some important discrepancies between the theoretical predictions from the MP2 and DFT B3LYP levels. MP2/cc-pVDZ overestimates the AIE of all studied systems. However, while the method shows a satisfactory agreement with the experiment for the monomer, it yields large deviations for the adiabatic ionization energy of the 3MI·H$_2$O and 3MI·C$_6$H$_6$ complexes. Moreover, MP2 overestimates the AIE of 3MI·H$_2$O and 3MI·C$_6$H$_6$ in a similar fashion, namely by $\approx$ 10% and 11%, respectively (See **Table VIII.28**).

The MP2 values for the intramolecular vibrational modes exhibit large fluctuations when the results for the three systems are compared. The only modes for which the calculated frequencies show consistency with the experiment in all three systems are 41^1, 29^1 and 27^1. The unscaled frequency positions of the former two modes generally do not differ by more than ≈ 6 cm^{-1} from the experimental ones in the three cases. The unscaled frequencies of the 27^1 mode in 3MI$^+$, (3MI·H$_2$O)$^+$, and (3MI·C$_6$H$_6$)$^+$ exhibit a fairly good agreement within $12 - 15$ cm^{-1}. For comparison, the deviations of the calculated frequentcy (unscaled) for the 42^1 and 26^1 modes vary from 0.7 cm^{-1} and 5.7 cm^{-1}, respectively in 3MI$^+$ to nearly 40 cm^{-1} and 50 cm^{-1}, respectively, in the case of (3MI·H$_2$O)$^+$ and (3MI·C$_6$H$_6$)$^+$.

System	Exp.	MP2/ cc-pVDZ	B3LYP/ cc-pVDZ	B3LYP/ 6-31+G(d)
3MI	60 711	+2.4	−4.9	−3.5
3MI·H$_2$O	57 614	+10.2	−5.8	−3.8
3MI·C$_6$H$_6$	58 018	+11.4	−4.1	−2.8

Table VIII.28. Experimental adiabatic ionization energies [cm^{-1}] and the respective relative deviation [%] of the computationally estimated value at each of the employed levels of theory.

On the other hand, DFT B3LYP apparently underestimates the AIEs of all studied systems (**Table VIII.28**). However, in the case of the complexes, the deviations are much smaller than those at the MP2/cc-pVDZ level. It can be concluded therefore that the DFT B3LYP method estimates as a whole more accurately the adiabatic ionization energies of the studied complexes than MP2.

Furthermore, comparing the performance of the two DFT B3LYP methods it is worth noticing that:

i)   For all three systems the 6-31+G(d) basis set yields better agreement with the experiment with respect to the AIE than cc-pVDZ;

ii)   Both B3LYP/cc-pVDZ and B3LYP/6-31+G(d) results exhibit the smallest deviations from the experimental AIE in the case of the $3MI \cdot C_6H_6$ complex. This is an interesting results since the DFT B3LYP calculations with both basis sets fail to predict a rigorous T-shape structure in the ground cationic state, D_0.

DFT accurately estimates the intramolecular vibrations in the D_0 state of $3MI^+$, particularly in combination with the cc-pVDZ basis set. On the other hand , DFT B3LYP/6-31+G(d) accurately estimates *i)* the ground state frequency of the N1–H1 stretch[4] in the case of 3MI and $3MI \cdot H_2O$ as well as of indole and indole$\cdot H_2O$; *ii)* the internuclear distances and bond angles in 3MI.

Both MP2 and DFT B3LYP fail to describe properly the bonding strength in the ground state $3MI \cdot C_6H_6$ and $(3MI \cdot C_6H_6)^+$ at least with the employed basis sets. DFT B3LYP calculations generally are considered as not completely suitable for describing X–H$\cdots\pi$ hydrogen bonding, and, in particular, dispersion interactions [73-75]. However, DFT surpassses MP2 in the present study in terms of accuracy in predicting hydrogen-bonded structure in the ground neutral state of the $3MI \cdot C_6H_6$ complex. Also, both B3LYP/6-31+G(d) and B3LYP/cc-pVDZ correctly predict the trend of increasing the hydrogen bonding upon ionization. In addition, the former level best of all employed methods approximates the experimentally obtained adiabatic ionization energy of $3MI \cdot C_6H_6$.

It should be kept in mind that the examined performance of the employed quantum computational methods is restricted to three molecular systems, all involving 3MI, and to two relatively small (double zeta) basis sets (cc-pVDZ and 6-31+G(d)). The theoretical results in this work therefore do not aim at provoking general conclusions on the suitability of DFT or MP2 calculations. The aim of the presented quantum chemical studies is to demonstrate the applicability of the employed methods for the case of 3MI and 3MI hydrogen-bonded complexes. In the case of the $3MI \cdot C_6H_6$ complex, the results are to be considered semi-quantative and describing general trends found in the experiment, in particular when estimating the hydrogen-bond strength. Other, more sophisticated levels

---

[4] **It should be pointed out that the scaling factor of 0.9636 recommended by Merrick et al. [43] and used in the present work yields a better agreement between theory and experiment with respect to the N1–H1 stretching frequency (*Section VIII.6.3b* and *Section VIII.7.3b*) than the factor of 0.9775 used by Carney et al. [22].**

of theory, particularly in combination with larger basis sets may serve as a more rigorous approach to the investigation of the discussed systems.

<div align="center">***</div>

The R2PI and particularly mass analyzed threshold ionization studies in the present chapter shed light on the excitation transitions, adiabatic ionization energies, and vibrational structure in the ground cationic state of 3MI as well as of the $3MI \cdot H_2O$, and $3MI \cdot C_6H_6$ complexes. In addition, the binding energies in the S_0 and D_0 state of the latter two systems have been experimentally determined from the respective cation dissociation thresholds. The present results:

- support the concept of σ-type hydrogen bonding in $3MI \cdot H_2O$ and point to a π-type hydrogen bonding in $3MI \cdot C_6H_6$ at the N1–H1 site with the π electrons of benzene;
- support the experimental findings for the different hydrogen bonding strength of indole$\cdot H_2O$ and indole$\cdot C_6H_6$ as well as of the respective ionized complexes [45, 53];

The experimental results supported by quantum chemical calculations correctly predict the effect of a weak electron donating substituent such as the methyl group on the spectroscopic properties of indole: decrease of the AIE and the hydrogen-bond strength in the studied 1:1 complexes of 3MI with water and benzene.

It can be therefore concluded that mass analyzed threshold ionization spectroscopy is a suitable and reliable method for studying the ground cationic state of hydrogen-bonded complexes, for determining the bonding strength in the neutral and ionized species of such systems as well as for elucidating the role of substituents on the investigated properties. In addition, the methyl group substitution effect on the N–H stretching vibrational frequency in $3MI^+$ and $(3MI \cdot H_2O)^+$ can be experimentally investigated by IR/PIRI methods by a comparison with the results reported by Unterberg et al. on indole$^+$ and (indole$\cdot H_2O)^+$ [70]. In addition, such studies on the $(3MI \cdot H_2O)^+$ and $(3MI \cdot C_6H_6)^+$ complexes may further shed light on the effect of hydrogen bonding on the N–H stretching frequency complementing and confirming the theoretical findings in the present work. MATI Studies on hydrogen bonded complexes of 3MI with ammonia and alcohols may further elucidate the effect of hydrogen bonding on the AIE and the dependence of hydrogen bonding strength in the cation and neutral on the nature of the hydrogen bond acceptor.

CHAPTER IX

MATI spectroscopy and theoretical studies of the conformational structure of 2-phenylethanol

This chapter presents a detailed study of 2-phenylethanol with MATI spectroscopy and quantum chemical methods in particular in the ground cationic state D_0 [76]. Threshold ionization was performed via two intermediate states (at 48 and 58 cm^{-1} above the electronic *gauche* origin at 37 622.3 cm^{-1}). One of the main aspects in this study is unveiling the nature of the peak at 58 cm^{-1} in the $S_1 \leftarrow S_0$ excitation spectrum by comparing the threshold ionization profiles via 48 and 58 cm^{-1} bands. Vibrational activity in the cation, structure stabilizing factors and conformational isomerization upon ionization are discussed by comparison of the experimental results with DFT calculations, employing the new hybrid functional M05 as well as with computations at the MP2 level. In addition, the fluorination effect on the conformational variety, conformational structure and spectral characteristics of 2-phenylethanol is studied by comparison of the present experimental and theoretical results with those for 2-*para*fluorophenylethanol [77, 78] and 2-*ortho*-fluorophenylethanol [79, 80]. In particular, the role of fluorine substitution on the stabilizing OH···π bonding in the lowest-in-energy S_0 *gauche* structure has been elucidated.

IX.1. Introduction

2-phenylethanol, 2PE (**Fig. IX.1**) consists of a benzene ring and a flexible side chain with a terminate OH group. It is the hydroxyl analogue of the neurotransmitter 2-phenylethylamine. 2PE is biosynthesized from L-phenylalanine [81, 82] and is a scent compound in some flowers thus being extensively used in perfumery. Moreover, it has been found that 2-phenylethanol is a chemical with important biological functions: influence on growth and DNA synthesis in some mushrooms [83], as well as inhibition of biosynthesis of viral DNA [84].
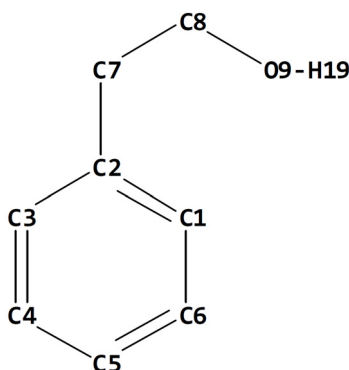
Fig. IX.1. Structure of 2-phenylethanol. Also shown is the numbering for the carbon nuclei as well as for the OH group.

The spectroscopic interest to 2-phenylethanol has been invoked by the presence of a side chain that is a prerequisite for conformational diversity as well as by the structural resemblance of 2PE to 2-phenylethylamine and other amines with neurochemical activity. Two main issues are of interest in the spectroscopic studies of 2PE:

 - its conformational variety and

 - the factors that determine the stability of the lowest-in-energy conformer.

The conformation of a biomolecule plays an important role in molecular recognition and affects the molecular biochemical functions, including the ability of a molecule to participate in forming noncovalent bonds, e.g. through hydrogen or dispersion interactions. In this regard it is important to find the most stable conformer, its relation to other conformers that lie close in energy, its spectroscopic and structural characteristics in the

neutral and cation state as well as to explore possible conformational changes upon excitation and ionization.

As a simple molecule with a flexible side chain 2PE is a suitable choice for experimental studies as well as computationally inexpensive theoretical treatment of the conformation problem with a comparatively straightforward interpretation of the obtained results. 2PE has been previously studied by a variety of spectroscopic techniques, focused mainly on the neutral species: UV and UV ion-dip spectroscopy [85], millimeter-wave spectroscopy [86], infrared-ultraviolet double resonance spectroscopy [87], dispersed fluorescence [88] as well as laser-induced fluorescence excitation and R2PI spectroscopy [89]. A study of the cation in the ground state was carried out by Weinkauf et al. who investigated structural changes upon ionization and their possible reasons with multiphoton ionization photoelectron (MPI-PE) spectroscopy and DFT calculations [90]. Recently a high-resolution R2PI study in our group has been carried out, yielding rotational structure of the vibronic bands in the $S_1 \leftarrow S_0$ UV spectrum [91].

Conformational variety of 2PE

Although *ab initio* [85, 86, 89, 91, 92] and DFT calculations [90] predict the existence of 5 conformers (3 *gauche* and 2 *anti* structures) for the neutral molecule in the S_0 and S_1 state, experimentally only one (the most stable) *gauche* and one *anti* conformer have been observed in cold molecular beams [85, 91, 93, 94]. By employing MP2/cc-pVDZ level of calculations it has been shown in our group that the appearance of two conformers in the supersonic jet is due to the following factors [91]:

- The energy barrier between the theoretically predicted three *gauche* conformers is sufficiently low, which favors relaxational intraconversion. Thus other *gauche* conformers relax to the most stable *gauche* conformer (**Fig. IX.2a**) during the process of adiabatic expansion. Similarly, only the most stable *anti* conformer (**Fig. IX.2b**) can be experimentally observed.

- The *gauche* and the *anti* conformers are separated by a high potential barrier which precludes the interconversion between them.

Non-classical intramolecular H···π hydrogen bonding in 2PE

The most stable *gauche* conformer, which is also the most stable of all 5 theoretically predicted structures, is the one where the hydroxyl H-atom is oriented towards the phenyl ring (**Fig. IX.2a**) [86, 90-92, 94].

a) *gauche* 2PE   **b)** *anti* 2PE
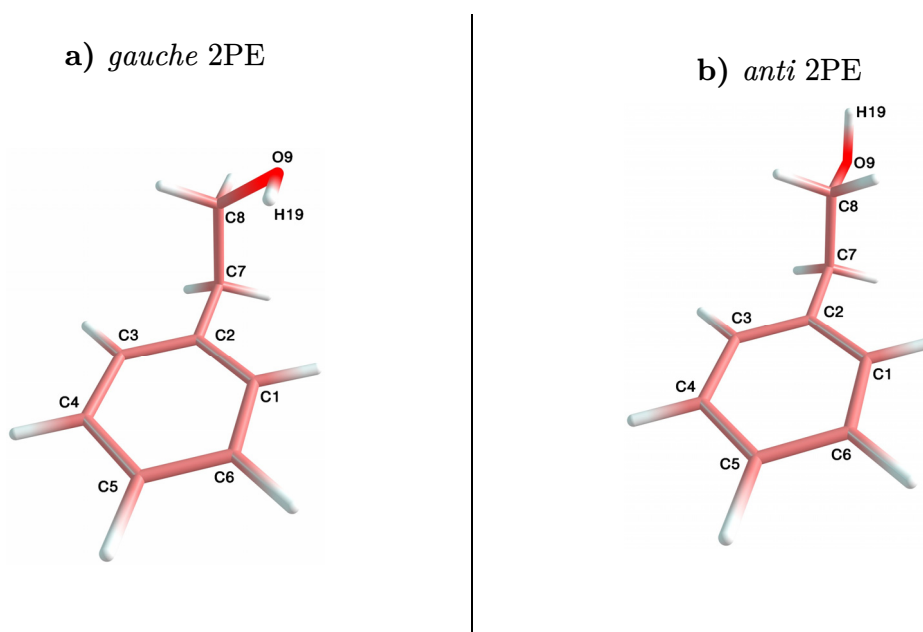
Fig.IX.2. The most stable *gauche* **(a)** and *anti* **(b)** conformer of 2-phenylethanol in the ground neutral electronic S_0 state predicted at the MP2/cc-pVDZ level of theory [91]. Experiments demonstrate only these structures in the supersonic jet. The *gauche* conformer, stabilized by a hydrogen bond between the OH terminal group and the π electron system of benzene is also the most stable of all 5 theoretically predicted structures. For further details, see text.

The structure is stabilized by a non-classical intramolecular H-bond between the hydroxyl hydrogen and the π-electrons of the aromatic ring [86, 92, 94]. Such bonding has been found to be the stabilizing factor for the lowest energy structures of 2-phenylethylamine [95] and histamine [96, 97]. For 2PE hydroxyl-aromatic interaction was suggested as early as the 1950s by Barnard et al. [98] and later studied experimentally [99]. There has been a debate to what extent the H···π bonding in 2PE does indeed stabilize the lowest-in-energy conformer. In contrast to a study by Spassov et al. [100], most works point out a substantial stabilization effect of the bonding [86, 92, 94, 99, 101, 102].

***

Most of the experimental and theoretical studies of 2PE are focused on the existence of different conformers in the S_0 and S_1 state. Following the work by Weinkauf et al. [90] on the ground cationic state of 2PE, here the threshold ionization spectroscopy, on the one hand and, DFT methods on the other hand, have been employed to shed light on the conformational variety of 2PE cationic structures observed experimentally in the free supersonic jet, the adiabatic ionization energies and vibrational activity of the observed conformers as well as to elucidate the effect of the ionization on the H⋯π bonding responsible for the stability of the lowest in energy *gauche* conformer in S_0 and S_1 states.

Experimental conditions:

The experimental conditions in the present study are similar to the ones for 3MI (Section VIII.2). In the case of 2PE, heating to a temperature of 105 °C was needed in order to obtain sufficient vapor concentration in the jet.

IX.2. Experimental studies of 2-phenylethanol

IX.2.1. R2PI spectrum of 2PE

The one-color R2PI spectrum of the first excited, S_1, electronic state of 2PE is shown in **Fig. IX.3**. The high-intensity peak at 37 622.3 cm^{-1} has been identified in a recent work [91] as the $S_1 \leftarrow S_0$ origin of the most stable *gauche* conformer 2 of 2PE. As pointed out in the Introduction, this structure is stabilized by an OH···π hydrogen bond between the terminate alcoholic group in the side chain and the π-moiety of the benzene ring.
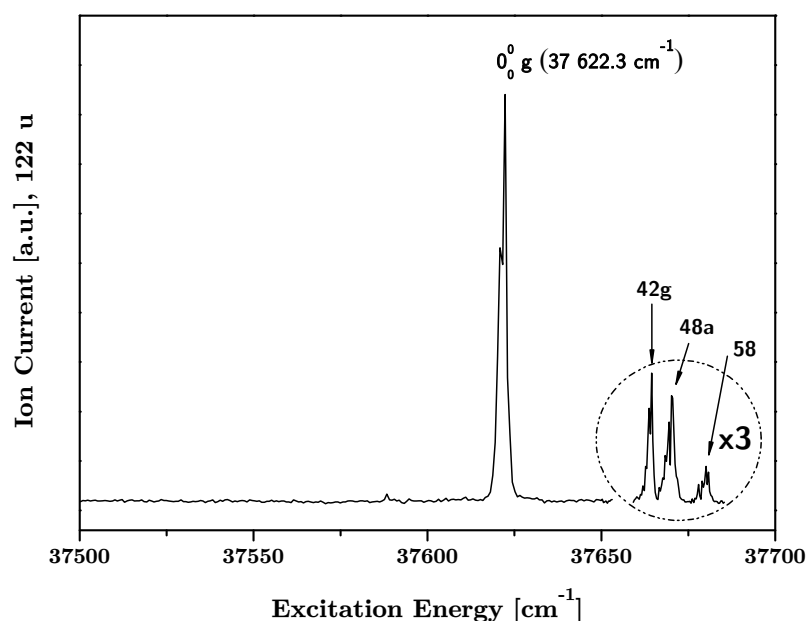
Fig.IX.3. One-color R2PI spectrum of 2PE, recorded at the 122 mass channel. The relative frequency position of each peak above the $S_1 \leftarrow S_0, 0_0^0$ *gauche* origin at 37 622.3 cm^{-1} is given in cm^{-1}. The letters "g" and "a" denote that the corresponding bands refer to excitation of the *gauche* and *anti* conformer (Fig. IX.2), respectively.

The peak at 37 670 cm^{-1} (+48 cm^{-1}) has been assigned to the $S_1 \leftarrow S_0$ origin of the most stable *anti* conformer 5 [91], while the nature of the peak at 37 680 cm^{-1} (+58 cm^{-1}) has not been unambiguously determined. However, on the basis of a similarity in the high-resolution $S_1 \leftarrow S_0$ spectra and the calculated inertial parameters for the bands at 48 and 58 cm^{-1}, the latter has been tentatively assigned to the same *anti* conformer as the 48 cm^{-1} band [91] .

IX.2.2. Total Ion Current Measurements of 2PE

Fig. IX.4 shows the total ion current (TIC) spectra measured via the *gauche* origin at 37 622.3 cm^{-1} **(a)** and the origin of the *anti* conformer at +48 cm^{-1} **(b)**. It can be seen that in the first case the signal increases monotonously. On the other hand, the TIC spectrum via the *anti* origin at 37 670 cm^{-1} features two well pronounced steps at around 71 422 cm^{-1} and 71 544 cm^{-1}, designating the approximate position of the AIE and a low-frequency vibration at $\approx$ 122 cm^{-1}, respectively.
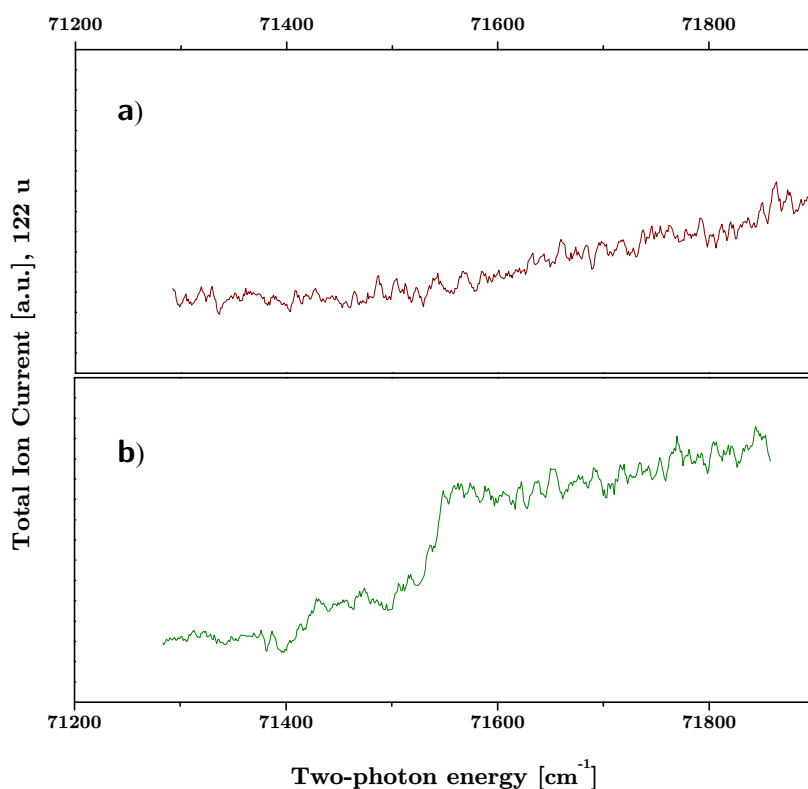
Fig.IX.4. Total ion current (TIC) spectrum of 2PE measured via the S$_1$ $\leftarrow$ S$_0$ origin of the *gauche* conformer at 37 622.3 cm^{-1} **(a)** and the *anti* conformer at 37 670 cm^{-1} **(b)**. Both scans have been performed under similar experimental conditions.

IX.2.3. MATI of 2PE

The MATI spectra of 2PE via three intermediate levels in the S_1 state, the *gauche* $S_1 \leftarrow S_0$ origin (a) and the bands at +48 (b) and +58 cm^{-1} (c), are presented in **Fig. IX.5**. Comparing the three traces in the figure the following observations can be made:

1. As expected (*Section VI.3.1*), in accord with the appearance of the TIC spectrum in **Fig. IX.5a** the threshold ionization spectrum of the *gauche* conformer displays neither a clear AIE threshold nor a well pronounced vibronic profile. This finding points to a prominent geometrical changes of the molecule upon ionization and consequently to small Franck-Condon factors for the $D_0 \leftarrow S_0$ transition. At higher two-photon energies, however, there are some indications for vibrational peaks, corresponding probably to high-frequency modes, which are not dependent on the structure of the side chain and thus may have favorable Franck-Condon factors. The widths of the observed peaks are about three times larger than those of the peaks in **Fig. IX.5b**. This broadening suggests short-lived states and most probably stems from intramolecular vibrational redistribution, which is encountered in flexible molecules [103].

2. In contrast, the MATI spectra via the 37 670 cm^{-1} (+48 cm^{-1}) and 37 680 cm^{-1} (+58 cm^{-1}) bands exhibit clearly resolved vibronic patterns. This finding points to large Franck-Condon factors for the observed transitions due to negligible geometrical changes upon ionization.

3. Both traces in **Fig. IX.5b** feature a lowest-energy peak at 71 422 $\pm$ 5 cm^{-1}, assigned to the *anti* AIE and a high-intensity band at 122 cm^{-1} above the adiabatic ionization energy. The found value for AIE is fairly close to the one of 8.865 $\pm$ 0.002 eV ($\approx$ 71 501 cm^{-1}) reported by Weinkauf et al. [90].

4. On the other hand, the spectra in **Fig. IX.5b** differ in two main aspects: i) the intensity ratio of the AIE peak and the band at 122 cm^{-1}; ii) the absence of the peak at 80 cm^{-1} above AIE in the MATI spectrum via the S_1, 58 cm^{-1} peak (lower trace). These dissimilarities can be due to different Franck-Condon factors in both cases.
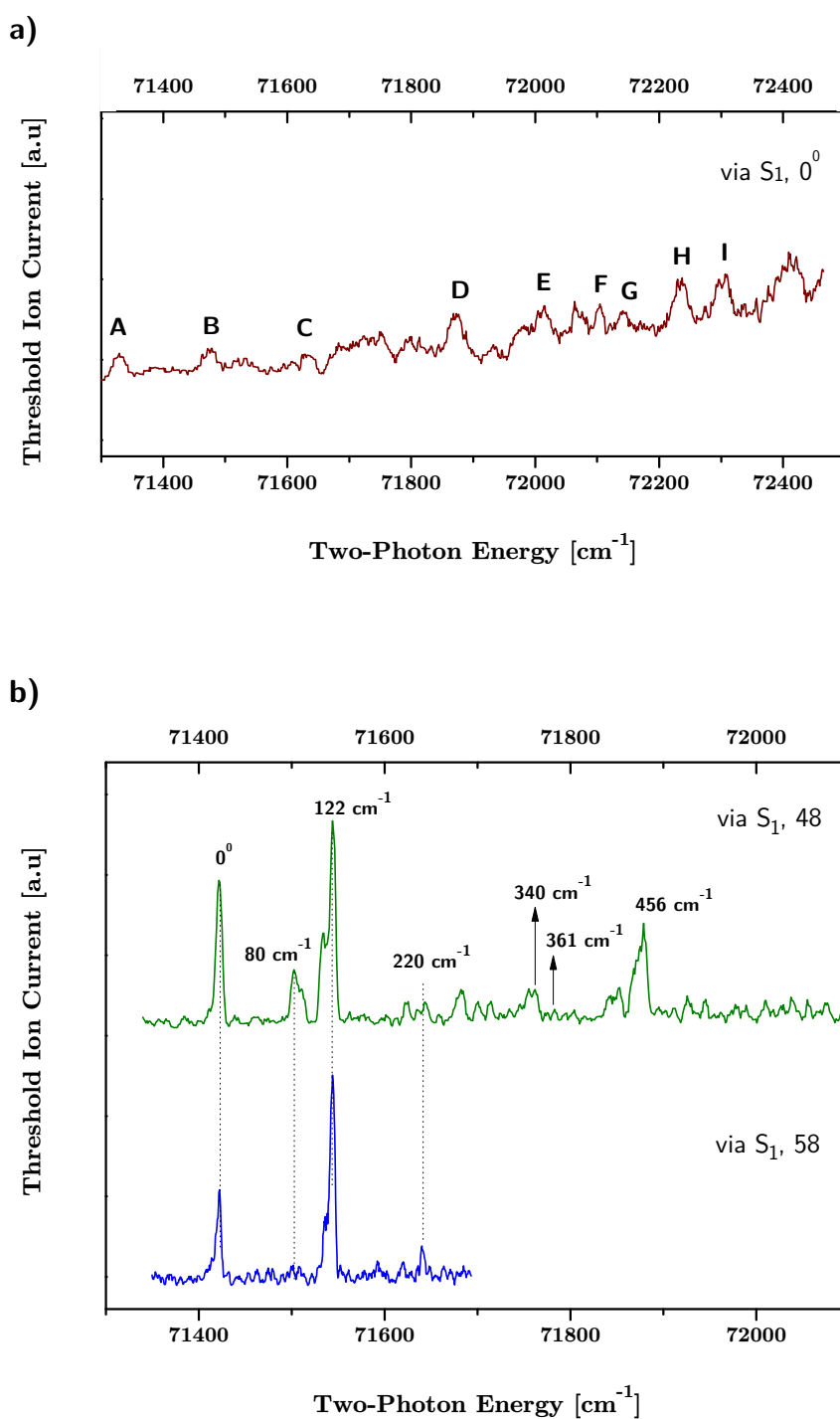
Fig.IX.5. MATI spectrum of 2PE recorded via the $S_1 \leftarrow S_0$ origin of the *gauche* conformer at 37 622.3 cm^{-1} **(a)**, the $S_1 \leftarrow S_0$ origin of the *anti* conformer at 37 670 cm^{-1}, S_1 48 **(b, upper trace)**, and the S_1 58 band **(b, lower trace)**. The three spectra have been recorded under similar experimental conditions.

Origin of the S_1, 48 cm^{-1} and S_1, 58 cm^{-1} bands

The identical AIE obtained when the threshold ionization is performed via the S_1, 48 cm^{-1} and S_1, 58 cm^{-1} band as well as the common spectral feature at 122 cm^{-1} in both cases (**Fig. IX.5b**) support the concept that the $S_1 \leftarrow S_0$ bands in question originate from the excitation of **one and the same** *anti* conformer [6, 12] shown in **Fig. IX.2b**. Moreover, it can be suggested that **only one** *anti* conformer exists in the cation, i.e. both traces present the threshold ionization spectra of the same *anti* cationic structure of 2PE. The validity of such a conclusion can be tested on the basis of theoretical geometry optimizations as will be shown in the following section.

Effect of the side chain on the AIE of the benzene chromophore

The obtained value of 71 422 cm^{-1} for the adiabatic ionization energy of 2PE can be compared with that of other benzene derivatives (**Table IX.1**).

	benzene (Bz)	*anti* 2PE	toluene	ethylBz	*anti* n-propylBz	phenol
AIE (ΔAIE)	74 555[a] (0)	71 422 (-3133)	71 199[b] (-3356)	70 762[c] (-3793)	70 266[d] (-4289)	68 628[e] (-5927)

Table.IX.1. Adiabatic ionization energy (AIE) in [cm^{-1}] of benzene, *anti* 2PE and other benzene derivatives. Also given is the decrease in the adiabatic ionization energy (ΔAIE) in [cm^{-1}] of the substituted benzene species with respect to benzene. Note: Values taken from [a] [104] [b] [105] [c] [106] [d] [90] [e] [107].

As expected for electron donating (activating) substituents, alkylation of benzene leads to a red shift in the AIE of the chromophore. Furthermore, this shift increases with extending the alkyl residue due to the increasing positive inductive effect $+I$ of the substituent. On the other hand, the AIE of the *anti* 2PE is larger than that for the other benzene derivatives listed in **Table IX.1**, although still smaller than the one for benzene itself. As will be shown in the following section, the AIE of the *anti* 2PE is obtained for a transition characterized by small geometrical changes in the molecule upon ionization. Weinkauf et al. [90] have shown that since the energy gap between the local ionization energies of the chromophore and the terminal hydroxyl group in 2PE is more than 1 eV, positive charge delocalization does not play a decisive role in stabilizing the ground ca-

tionic state D_0 of the molecule, i.e. in affecting remarkably the AIE. The ionization of 2PE can be therefore treated within the local charge concept [108], and the $D_0 \leftarrow S_0$ energy gap is therefore determined by the positive inductive effect of the side chain. As it is known from the general course in organic chemistry, the presence of the OH group in an alkyl side chain decreases the electron donating properties of the latter, which in the present case apparently leads to a smaller red shift of the AIE in comparison to the case of $CH_2CH_2CH_3$ substituted benzene (n-propylbenzene) [90]. The smaller decrease in the AIE of *anti* 2PE from benzene compared to the alkylated systems in **Table IX.1** is also substantially different from that in the case of phenol. This can be explained with the strong electron donating property of the OH group in this case, which leads to a large decrease of AIE upon OH substitution in the aromatic ring unlike the case of 2PE.

IX.3. Quantum-chemical calculations on 2-phenylethanol

Quantum-chemical calculations have been performed at the DFT M05/aug-cc-pVTZ level of theory for structural optimizations of $2PE^+$ in the D_0 state, its energetics, electron density distribution in the highest occupied molecular orbital (HOMO), and the normal-mode frequencies of the 2PE cationic conformers. The use of the M05 functional [109] in DFT calculations on 2PE systems is prompted by its ability for correctly describing molecules with a non-classical OH···π bond in which dispersion interactions should be considered [77] .

IX.3.1. Conformational structure in D_0 state

Fig. IX.6 shows the optimized structures of 2PE in the ground cationic state D_0 at the DFT M05/aug-cc-pVTZ level of theory as well as the predicted conformers in the S_0 and S_1 state. The optimization procedure in the cation started from the most stable conformational structures of 2PE in the S_0 state [91]. It is seen that the $S_1 \leftarrow S_0$ transition of 2PE is characterized by negligible structural changes of the stable conformers. Ionization, however, has a larger effect on the geometrical structures and furthermore reduces the number of predicted stable conformers from 5 to 3:
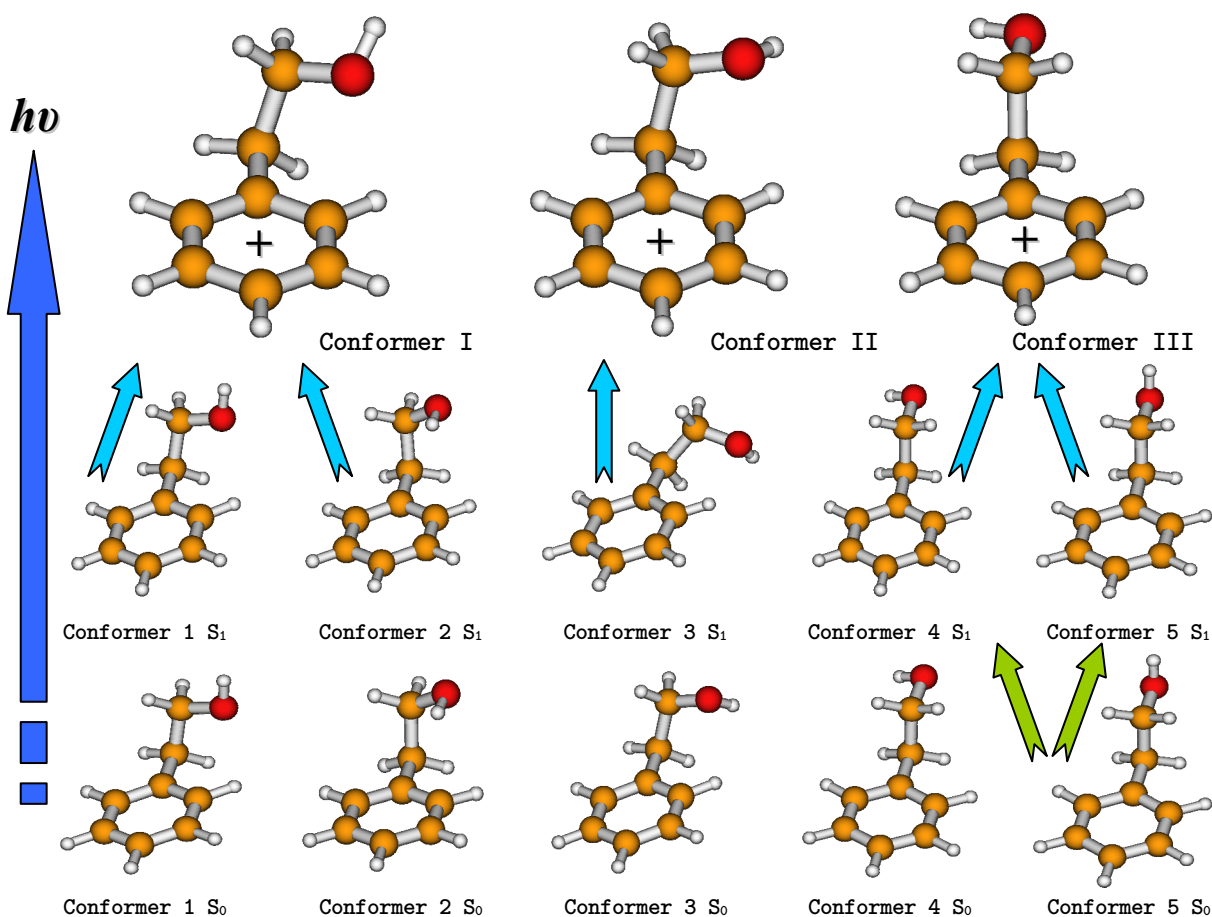
Fig.IX.6. Geometrical structures of 2PE in the S_0, S_1, and D_0 states, predicted at the MP2/cc-pVDZ [91], CIS/cc-pVDZ [91], and DFT M05/aug-cc-pVTZ levels of theory, respectively. The optimization procedures for the cationic structures employed the optimized structures of 2PE in S_0 as starting geometries.

	Conformer II	Conformer I	Conformer III
E	0	+31	+667

Table.IX.2. Relative electronic energies [cm^{-1}] of the theoretically predicted (DFT M05/aug-cc-pVTZ) conformers of 2PE$^+$ in the ground cationic D_0 state.
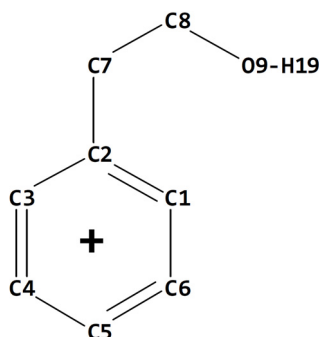
Geometrical parameter	Conformer I	Conformer II	Conformer III
C1–C2	1.440	1.429	1.429
C2–C3	1.423	1.430	1.427
C3–C4	1.362	1.364	1.365
C4–C5	1.424	1.413	1.412
C5–C6	1.404	1.412	1.410
C6–C1	1.366	1.364	1.365
C2–C7	1.471	1.459	1.454
C7–C8	1.551	1.594	1.613
C8–O9	1.398	1.380	1.370
O9–H19	0.958	0.959	0.960
C2–C7–C8	111.3	110.9	110.6
C7–C8–O9	108.1	112.4	109.7
C8–O9–H19	110.1	110.9	111.5
C3–C2–C7–C8	96.6	92.1	90.4
C2–C7–C8–O9	58.1	65.4	173.0
C7–C8–O9–H19	159.2	95.9	85.2

Table.IX.3. Bond lengths [Å], planar angles [deg] and dihedral angles [deg] predicted for the optimized structures of 2PE$^+$ in the ground cationic state D$_0$ at the DFT M05/aug-cc-pVTZ level of theory.

two *gauche* and one *anti* conformer. The relative electronic energies of the cationic conformers are given in **Table IX.2** (p. 184) and the geometrical parameters for each conformer are listed in **Table IX.3** (p. 185).

It is worth pointing out that none of the resulting two cationic *gauche* conformers is stabilized by an OH··· π hydrogen bond as is the case for the most stable *gauche* conformer in the S_0 state (number 2 in **Fig. XI.6**).

As seen in **Fig. IX.6** the *gauche* conformer 1 and the most stable of all 5 structures in S_0 state, *gauche* conformer 2, converge to one *gauche* conformer (labeled as I) in D_0 state. The ionization process for both conformers is accompanied by a geometrical change mainly in the C7–C8–O9–H19 dihedral angle. In particular, for the conformer 2 this leads to a break of the stabilizing OH··· π hydrogen bond. The structural change obviously leads to unfavorable Franck-Condon factors for the D_0 (I) $\leftarrow$ S_0 (1, 2) transition[5] as already manifested for conformer 2 in the TIC and MATI spectra in **Fig. IX.4 a** and **Fig. IX.5 a**, respectively. Conformer 3 converts to conformer II and similarly to the case of structure I, no resolved MATI signal is expected in the low-frequency range for conformer II due to the large geometrical change upon ionization.

The structural optimizations at the DFT M05/aug-cc-pVTZ level of theory show that conformer II is the most stable one in the ground cationic state D_0 of 2PE$^+$ (**Table IX.2**). It should be, however, pointed out, that employing other methods or basis sets may lead to an inversion of the energy order between conformers I and II due to the small energy gap (31 cm^{-1}) as it was demonstrated for 2-*para*fluorophenylethanol [77].

The two *anti* conformers 4 and 5 in the S_0 state converge to conformer III in the cation, which can be designated as D_0 (III) $\leftarrow$ S_0 (4, 5). This result supports the assumption made in *Section IX.2.3* on the basis of the single experimental value found for the *anti* AIE that only one *anti* conformer exists in the ground cationic state D_0 of 2PE.

IX.3.2. Geometrical changes upon ionization

Table IX.4 lists the geometrical parameters (bond lengths, bond planar and dihedral angles) for the ground state structures 2 and 5 as well as for the cationic structures I and

---

[5] **The number indicating the conformer in the respective electronic state is given in brackets for convenience.**

Geometrical parameter	Conf.2 (Conf.I)	Conf.5 (Conf.III)
C1–C2	1.394 (1.440)	1.394 (1.429)
C2–C3	1.395 (1.423)	1.394 (1.427)
C3–C4	1.386 (1.362)	1.387 (1.365)
C4–C5	1.389 (1.424)	1.388 (1.412)
C5–C6	1.387 (1.404)	1.388 (1.410)
C6–C1	1.389 (1.366)	1.387 (1.365)
C2–C7	1.502 (1.471)	1.502 (1.454)
C7–C8	1.527 (1.551)	1.518 (1.613)
C8–O9	1.407 (1.398)	1.412 (1.370)
O9–H19	0.958 (0.958)	0.956 (0.960)
C2–C7–C8	112.9 (111.3)	112.1 (110.6)
C7–C8–O9	113.7 (108.1)	108.3 (109.7)
C8–O9–H19	108.7 (110.1)	109.0 (111.5)
C3–C2–C7–C8	83.2 (96.6)	89.1 (90.4)
C2–C7–C8–O9	61.1 (58.1)	−180.0 (173.0)
C7–C8–O9–H19	−61.8 (159.2)	−180.0 (85.2)

Table.IX.4. Bond lengths [Å], planar angles [deg] and dihedral angles [deg] in the ground neutral state S_0 for the most stable *gauche* (2) and *anti* (5) conformer of 2-phenylethanol. The geometrical parameters in the ground cationic state D_0 for structures I and III are given in brackets. All parameters are obtained at the DFT M05/aug-cc-pVTZ level of theory.

III, yielded at the DFT M05/aug-cc-pVTZ level of theory[6]. As will be shown in *Section IX.3.4*, the observed MATI spectra in **Fig. IX.5 a** and **b** result from D_0 (I) ← S_0 (2) and D_0 (III) ← S_0 (5) transitions, respectively.

---

[6] **Both S_0 and D_0 DFT M05/aug-cc-pVTZ optimizations were performed for the optimized structures in the S_0 state at the MP2/cc-pVDZ level. For the S_0 state this led to changes in the geometrical parameters reported by Karaminkov et al. [91], but did not noticeably alter the geometries given in Fig. IX.6.**

Benzene ring

As seen in the **Table IX.4**, the benzene ring experiences deformations, showing similar trends upon ionization of the *gauche* conformer 2 and the *anti* conformer 5. In both cases the largest deformation in the benzene ring occurs for the C1–C2 bond, particularly when the *gauche* conformer 2 is ionized: the bond length increases by 0.046 A (3.3%) in this case. Also, most of the bonds elongate in both cases and only the C3–C4 and C6–C1 bonds decrease in length. Moreover, three of the bond lengths (C3–C4, C5–C6, and C6–C1) manifest similar changes in the case of the ionization of the *gauche* and *anti* structures (by ≈ 1.6% for C3–C4 and C5–C6 and by ≈ –1.6% for the C6–C1 bond length). On the other hand, the C1–C2 and C4–C5 bonds elongate to a lesser extent for conformer III (2.5% and 1.7%, respectively) than for conformer I (3.3% and 2.5%, respectively). On the contrary, the C2–C3 bond length increases to a larger extent in the case of the *anti* conformer (2.4%) than in the case of the *gauche* conformer (2%).

Side chain

The calculations at the DFT M05/aug-cc-pVTZ level predict that both the C2–C7 and the C8–O9 bonds decrease in length for the *gauche* and *anti* conformer, while the C7 – C8 bond elongates in either case upon ionization. However, it seems that the employed method overestimates the length changes for the *anti* conformer, particularly for the C7 – C8 bond (≈ 6%) and the C8–O9 bond (≈ 3%). For comparison, the respective bond length changes for the *gauche* conformer are ≈ 1.6% and ≈ 0.6%.

Both for conformers 2 and 5, the most prominent and evident changes occur in the orientation of the side chain and of the terminal OH group in particular. For conformer 2 the latter is manifested in the change of the dihedral angle C7–C8–O9–H19 from -61.8° to 159.2°. For conformer 5 the largest geometrical changes in the side chain are expressed in the changes of the C2–C7–C8–O9 and particularly the C7–C8–O9–H19 dihedral angles. The latter changes from –180.0 in the S_0 state to 85.2° in D_0, i.e. the O9 – H19 and C7 – C8 bonds are essentially not parallel in the ground state of the cation showing a tendency for perpendicularity.

As seen in **Fig. IX.6** the performed geometry optimizations predict small structural change for conformer 4 and a larger structural change for conformer 5 upon ionization. However, as evident from the step-like increase of the TIC signal in **Fig. IX.4b** and the clearly pronounced adiabatic ionization threshold in **Fig. IX.5b** the geometry change for the $D_0 \leftarrow S_0$ transition of the *anti* conformer 5 is sufficiently small to ensure favorable Franck-Condon factors.

IX.3.3. Adiabatic ionization energies of 2PE

The AIEs for the D_0 (I) ← S_0 (2) and D_0 (III) ← S_0 (5) transitions of 2PE have been calculated at the DFT M05/aug-cc-pVTZ and MP2/aug-cc-pVDZ levels of theory. The results are listed in **Table IX.5**.

	Experiment	M05/aug-cc-pVTZ	MP2/aug-cc-pVDZ
Conformer I	70 922[a], 69 614[b]	66 585	73 471
Conformer III	71 422	67 054 (−4 368)	75 379 (+3 957)

Table.IX.5. ***Measured*** (Conformer III) experimental and ***expected*** (Conformer I) experimental adiabatic ionization energy (AIE) of 2PE in [cm^{-1}]. Note: expectation is based on [a]DFT M05/aug-cc-pVTZ and [b]MP2/aug-cc-pVDZ levels of theory. Also given are the values directly obtained from quantum-chemical calculations at different levels of theory as well as their deviations from the experimental energies (in brackets). For further details, see text.

Similarly to the case of 3MI and its 1:1 hydrogen-bonded complexes with water and benzene (**Chapter VIII**), the DFT calculations underestimate the adiabatic ionization energy of the *anti* 2PE, while MP2 overestimates it. Although the deviations from the experimental value are larger for both computational methods than those found for the 3MI monomer at lower levels of theory (*Section VIII.3.3*), the manifested discrepancy of ≈ 6% is still acceptable. Moreover, the MP2/aug-cc-pVDZ method yields smaller deviation for the *anti* 2PE than MP2/cc-pVDZ employed for the estimation of the AIE of the 3MI·H_2O and 3MI·C_6H_6 hydrogen-bonded complexes (more than 10%, see **Table VIII.28**, p. 170).

The ratio between the experimental and theoretical value of AIE for the *anti* conformer is 1.065 at the DFT M05/aug-cc-pVTZ level and 0.947 at the MP2/aug-cc-pVDZ level. If it is assumed that the accuracy of the employed computational methods with respect to the estimation of the AIE is the same for the *gauche* and *anti* conformers, the above ratios lead to an expected experimental value for AIE of the *gauche* conformer of 70 922 cm^{-1} and 69 614 cm^{-1}, respectively. Both values do not differ essentially from the value of 8.870 eV (≈ 71 541 cm^{-1}) measured by Weinkauf et al. [90] with time-of-flight photoelectron spectroscopy.

IX.3.4. Vibrational analysis of 2PE in the ground cationic state D_0

a) Cationic *gauche* structure I

The peaks in the MATI spectrum measured via the $S_1 \leftarrow S_0, 0_0^0$ transition of gauche conformer 2 (**Fig. IX.5a**) exhibit two vibrational progression-like patterns: 1) for the bands E–F and G–H–I with spacing of about 90 cm^{-1} and 2) for the bands A–B–C and D–E with spacing of ≈ 140 cm^{-1}. The calculations at the DFT M05/aug-cc-pVTZ level of theory label the former periodical pattern as a progression of the C2–C7–C8 side-chain bending mode, while the latter may be referred to a progression of the side-chain torsional mode about the C7–C8 bond at 148 cm^{-1}. The established correspondence between the experimentally observed periodical patterns and the calculated progression frequencies shows that the spectral profile in **Fig.IX.5a** can be reconciled with the existence of the cationic *gauche* conformer I in the supersonic jet.

b) Cationic *anti* structure III

The calculated unscaled vibrational frequencies in the ground state of the cationic conformer III of 2PE$^+$ are listed in **Table IX.6**. In addition to the values yielded at the DFT M05/aug-cc-pVTZ level of theory, MP2/aug-cc-pVDZ frequencies are also given[7]. Furthermore, **Table IX.6** presents a comparison between the frequencies measured in the MATI spectrum via the $S_1 \leftarrow S_0$ origin of *anti* conformer 5 at 37 670 cm^{-1} (upper trace in **Fig. IX.5b**) and the theoretical vibrational frequencies calculated for conformer III of 2PE$^+$. The assignment of the corresponding modes is also given. Apparently, the MP2/aug-cc-pVDZ values are somewhat closer to the experimental ones, exhibiting discrepancies below 10 cm^{-1}.

Both employed levels of calculations predict a lowest vibrational frequency in the region between 50 and 70 cm^{-1}, referring to the fundamental torsional mode τ_1 around the C2–C7 bond. If the MP2/aug-cc-pVDZ value (52.7 cm^{-1}) is considered to lie closer to the experimental one as is the case for the other frequencies, then a peak near 50 cm^{-1} is expected to be seen in the MATI spectrum of the *anti* 2PE$^+$ (**Fig. IX.5b**). However, such

---

[7] **The calculation of the vibrational frequencies at the MP2/aug-cc-pVDZ level was performed with the DFT optimized geometries [76].**

band is not experimentally observed probably due to an unfavorable Franck-Condon factor.

assignment		exp.	MP05/ aug-cc-pVTZ	MP2/ aug-cc-pVDZ
τ_1	torsion about C2–C7	-	67.9	52.7
β_1	side chain bending	80	89.2	86.5
τ_2	torsion about C7–C8	-	107.0	102.0
	combination mode	122	–	–
β_2	out of plane ring bending	220	233.7	229.0
	combination mode	261	–	–
β_3	out of plane ring deformation	340	355.1	342.9
x	C2–C7 wagging	-	387.4	363.0
	combination mode	456	–	–

Table.IX.6. Experimental vibrational frequencies and theoretical vibrational frequencies of the cation *anti* conformer III (Fig. IX.6). All values are given in [cm^{-1}].

The vibration at 80 cm^{-1} in the threshold ionization spectrum refers to the fundamental side-chain bending mode with a frequency of 86 cm^{-1} (MP2/aug-cc-pVDZ). Interestingly, there is no theoretically predicted fundamental frequency for the most prominent experimental peak at 122 cm^{-1} above the AIE at both employed levels of theory. The nearest mode is the τ_2 torsional mode around the C7–C8 bond with a frequency of 102 cm^{-1} (MP2/aug-cc-pVDZ) and 107 cm^{-1} (M05/aug-cc-pVTZ). An explanation of the large frequency discrepancies of 20 cm^{-1} and 15 cm^{-1} from the experimental value on the basis of anharmonicity is not reasonable since the mode in question involves only the terminus of the side chain and thus is not expected to exhibit a significant anharmonicity.

On the other hand, calculations at the MP2 level predict that the τ_2 mode at 102 cm^{-1} almost overlaps with the first overtone of the mode τ_1. Since both modes involve torsions of the side chain, it is plausible to assume that these modes may be coupled, leading to a Fermi resonance-like splitting of the band at 102 cm^{-1} and intensity redistribution of this band over the two split components (arbitrarily designated as X and Y for example). The component Y pushed to higher frequencies thus may give rise to the high-intensity peak at 122 cm^{-1}. The second split component X, shifted to lower frequency is thus expected at

82 cm^{-1}, which is close to the position of the bending mode β_1 and in this way may lead to another coupling. In a recent work [76] it was proposed that a complex double resonance coupling of the first overtone of τ_1 with β_1 and τ_2 modes may lead to the appearance of a new vibrational pattern and intensity distribution in the threshold ionization spectrum. Such a model may explain the intensity gain of the blue shifted component Y at 122 cm^{-1} and the intensity depletion of the red shifted component X through interaction of the latter with the β_1 bending mode.

Continuing the assignment of the experimental peaks on the basis of the MP2/aug-cc-pVDZ frequencies, it may be suggested that the peak at 220 cm^{-1} above the AIE corresponds to the β_2 out-of-plane bending vibrational mode of the benzene ring. The peak at 261 cm^{-1} can be assigned to a combination mode of $122 + \beta_1 + \tau_1$. The weak-intensity band at 340 cm^{-1} corresponds to the fundamental bending mode β_3 with calculated frequency of 342.9 cm^{-1} and 355.1 cm^{-1} at the MP2/aug-cc-pVDZ and DFT M05/aug-cc-pVTZ levels of theory, respectively. The former method predicts a peak at 363 cm^{-1}, corresponding to a wagging fundamental mode (designated arbitrarily as x in **Table IX.6**). Such a band is, however, hardly recognizable in the spectrum due to its substantially low intensity. The peak at 456 cm^{-1} above AIE corresponds probably to the excitation of a combination mode of the vibration at 122 cm^{-1} and the β_3 band at 340 cm^{-1}.

The reasonable assignment of the observed vibrational bands in the MATI spectrum via the $S_1 \leftarrow S_0$ origin of *anti* conformer 5 at 37 670 cm^{-1} based on quantum-chemical calculations serves as an argument for the experimental existence of the *anti* cationic structure III.

IX.4. Fluorine substitution effect in 2-phenylethanol

Fluorine (F) is an example of a substituent that exerts two opposite effects on the aromatic ring. As an electronegative atom, fluorine withdraws electron density from benzene (negative inductive effect, −I), which renders it electron deactivating. On the other hand, however, F acts as an electron activating substituent by lone pair donation to the π electron system of the ring (positive mesomeric effect, +M).

The fluorine substitution (F-substitution) effect on the spectral properties and energy potentials in π-conjugated hydrocarbons has been studied in a number of publications. Red shifts upon fluorine substitution in the benzene ring on the $S_1 \leftarrow S_0, 0_0^0$ transition and the AIE have been observed by comparing *para*fluorotoluene and toluene. Medina et al. [110] report a fluorination effect on the excitation energies for a series of aromatic hydrocarbons and point out that fluorine substitution leads to red shifts or blue shifts depending on different positions of the F atom. A study on fluorinated polyphenylenevinylenes conveyed by Piacenza et al. [111] showed that the excitation energy gap depends on fluorine substitution in opposite ways in the cases of planar and nonplanar molecular geometries. In the first case, a red shift was observed, while an increased energy gap was reported in the second case. Fluorine substitution was shown to cause a three-fold barrier to the internal rotation of the methyl group in various singly-substituted fluorotoluenes [36, 112-115]. Moreover, the magnitude of this barrier also depends on the substitution position, being smallest for *para*fluorotoluene.

It is interesting to investigate the fluorination effect also in the case of 2PE. Such a study may shed light on the role of a halogen substituent with large electronegativity such as F on the conformational stability, conformational variety, and the spectroscopic properties of small biomolecules stabilized by nonconventional OH$\cdots\pi$ hydrogen bonding. For this purpose, the experimental and theoretical findings in the present work on the unsubstituted 2PE are compared with the results on 2-*para*fluorophenylethanol (2*p*FPE) and 2-*ortho*fluorophenylethanol (2*o*FPE) reported recently by Karaminkov et al. [77-80].

IX.4.1. Fluorine substitution effect on the structure of 2PE

Firstly, a comparison of the results in Section IX.3 with those for 2*p*FPE at DFT M05/aug-cc-pVTZ level of theory shows that the lowest-in-energy S_0 conformer in both

cases is a *gauche* structure with the side chain oriented in such a way that the terminal OH group forms a hydrogen bond with the π electronic system of the benzene ring (**Fig. IX.2a**). Such a similarity is also observed at the MP2 level of calculations [78, 91], at least on a qualitative comparative basis (with a variance in the exact values of the dihedral angles defining the geometry of the side chain). This justifies a comparison with the MP2/cc-pVDZ geometry of 2*o*FPE also to be made with the conclusion that the OH···π stabilized *gauche* structure is retained also upon *ortho* fluorosubstitution [32]. The latter is an interesting result as pointed out by the authors since one might expect that fluorine may disrupt the OH···π bonding due to the proximity of the electronegative F and the side chain in 2*o*FPE.

In contrast to the *gauche* case, fluorination changes the orientation of the OH group in the lowest-in-energy *anti* conformer in S_0 as shown for 2PE and 2*p*FPE in **Fig.IX.7**. In the case of *para* fluorinated 2PE, the dihedral angle C7–C8–O9–H19 is smaller than 90° as can be concluded from the M05/aug-cc-pVTZ calculations. As pointed out in *Section IX.3.2*, in the most stable *anti* 2PE conformer, the C7–C8–O9–H19 is –180 °, i.e. the side chain is completely extended away from the benzene ring.

The most stable *anti* conformer of 2*o*FPE represents a third case, in which the OH group points to the side of the fluorine atom [79]. An interesting result from the geometry optimization of the 2*o*FPE is that due to the reduced molecular symmetry, in contrast to 2PE and 2*p*FPE, where there are 5 stable conformers in S_0, the number of stable structures in the ground neutral state of *ortho* substituted 2PE is 9.

In the ground state of the cation D_0, the most stable *gauche* conformers of 2PE and 2*p*FPE show a similarity in the orientation of the side chain (**Fig.IX.8**), which is also the case for 2*o*FPE.The only D_0 *anti* structures existing in 2PE$^+$ and 2*p*FPE$^+$, however, differ again in the orientation of the OH group (**Fig.IX.9**). The values for the geometrical parameters in the *anti* conformers of 2PE and 2*p*FPE are given in **Table IX.7**. In case of 2*o*FPE$^+$, the most stable *anti* structure has a side chain geometry similar to that in *anti* 2PE$^+$ [80] .
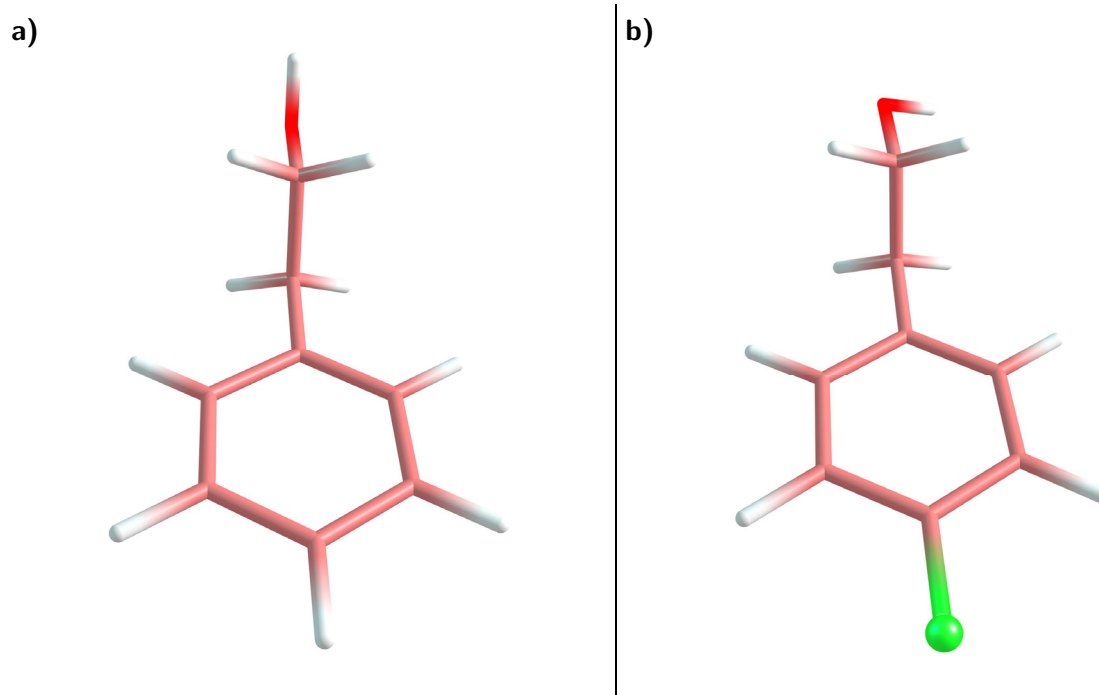
Fig.IX.7. Structure of the most stable *anti* conformers of 2PE **(a)** and 2pFPE **(b)** in the ground neutral state S_0 predicted at the DFT M05/aug-cc-pVTZ level of theory.
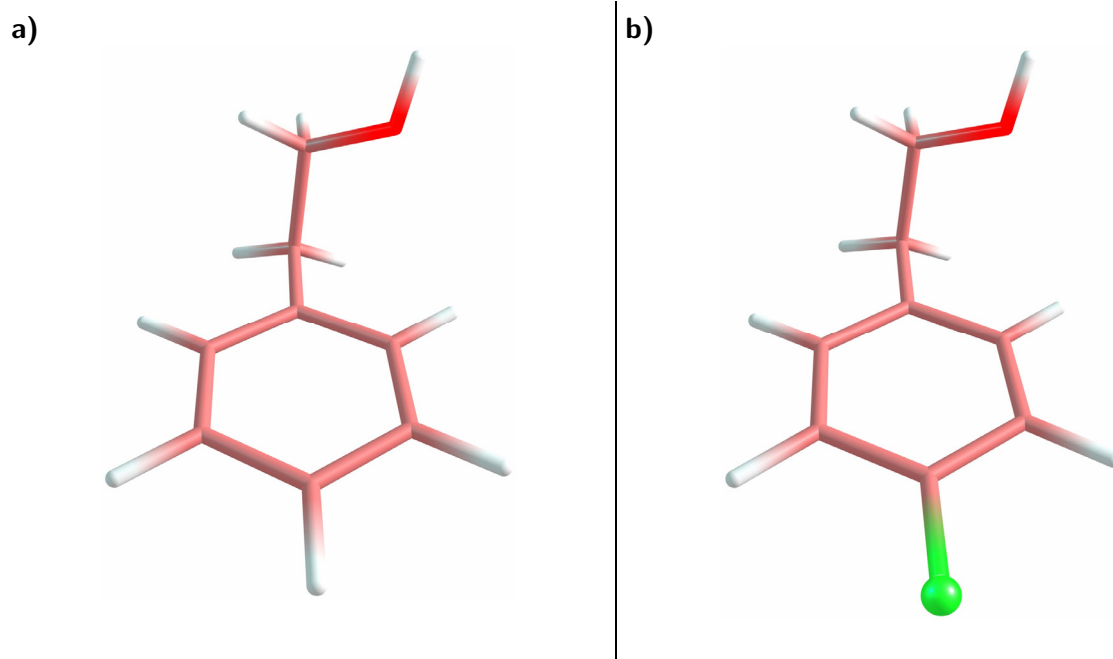
Fig.IX.8. Structure of the most stable *gauche* conformers of 2PE$^+$ **(a)** and 2pFPE$^+$ **(b)** in the ground cationic state D_0 predicted at the DFT M05/aug-cc-pVTZ level of theory.
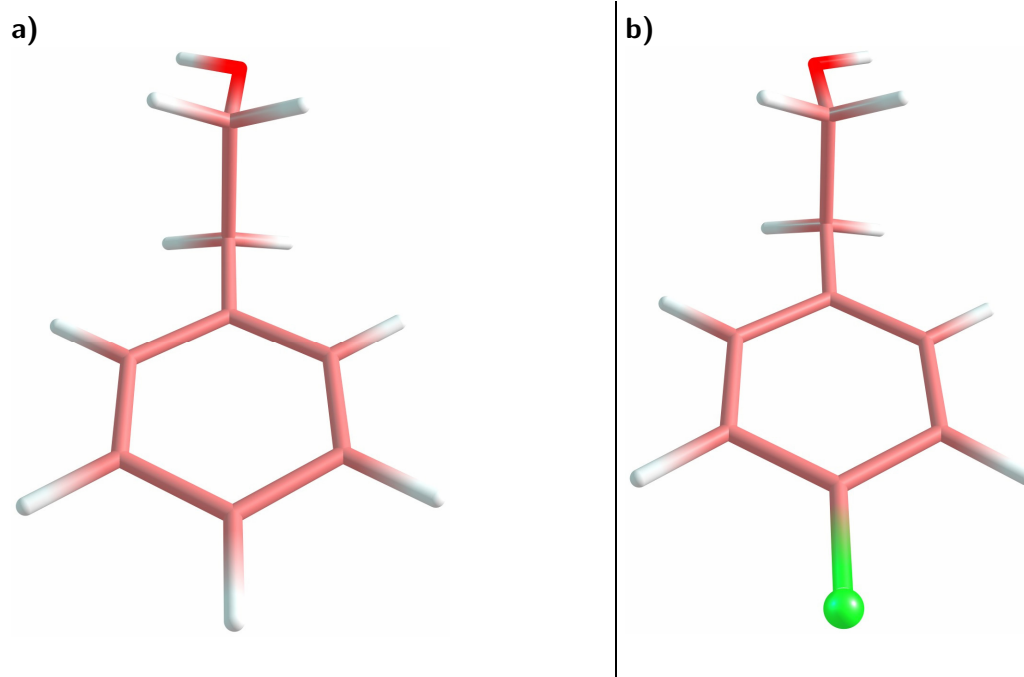
Fig.IX.9. Structure of the most stable *anti* conformers of 2PE$^+$ **(a)** and 2pFPE$^+$ **(b)** in the ground cationic state D$_0$ predicted at the DFT M05/aug-cc-pVTZ level of theory.

	gauche Conformer		*anti* Conformer	
	2PE	2*p*FPE	2PE	2*p*FPE
C1–C2	1.440	1.434	1.429	1.427
C2–C3	1.423	1.426	1.427	1.428
C3–C4	1.362	1.360	1.365	1.362
C4–C5	1.424	1.418	1.412	1.410
C5–C6	1.404	1.410	1.410	1.411
C6–C1	1.366	1.360	1.365	1.362
C2–C7	1.471	1.475	1.454	1.458
C7–C8	1.551	1.546	1.613	1.601
C8–O9	1.398	1.400	1.370	1.373
O9–H19	0.958	0.958	0.960	0.960
C2–C7–C8	111.3	111.4	110.6	111.1
C7–C8–O9	108.1	108.0	109.7	110.0
C8–O9–H19	110.1	110.1	111.5	111.5
C3–C2–C7–C8	96.6	97.4	90.4	87.4
C2–C7–C8–O9	58.1	57.9	173.0	−172.9
C7–C8–O9–H19	159.2	162.6	85.2	−85.4

Table.IX.7. Bond lengths [Å], planar angles [deg] and dihedral angles [deg] in the ground cationic state D_0 for the most stable *gauche* and *anti* conformer of 2PE and 2*p*FPE. All parameters yielded at the DFT M05/aug-cc-pVTZ level of theory.

IX.4.2. Fluorine substitution effect on the vibrational frequencies in D_0 of anti 2-phenylethanol

From the MATI spectra in **Fig. IX.10** and the values listed in **Table IX.8** it can be seen that fluorination of the benzene ring has a prominent effect on the frequencies of the vibrational modes in D_0 state of *anti* 2-phenylethanol as well as on the intensity of the corresponding peaks. The threshold ionization spectra of the respective *anti* conformers differ noticeably, particularly in the internal energy region below 200 cm^{-1}.
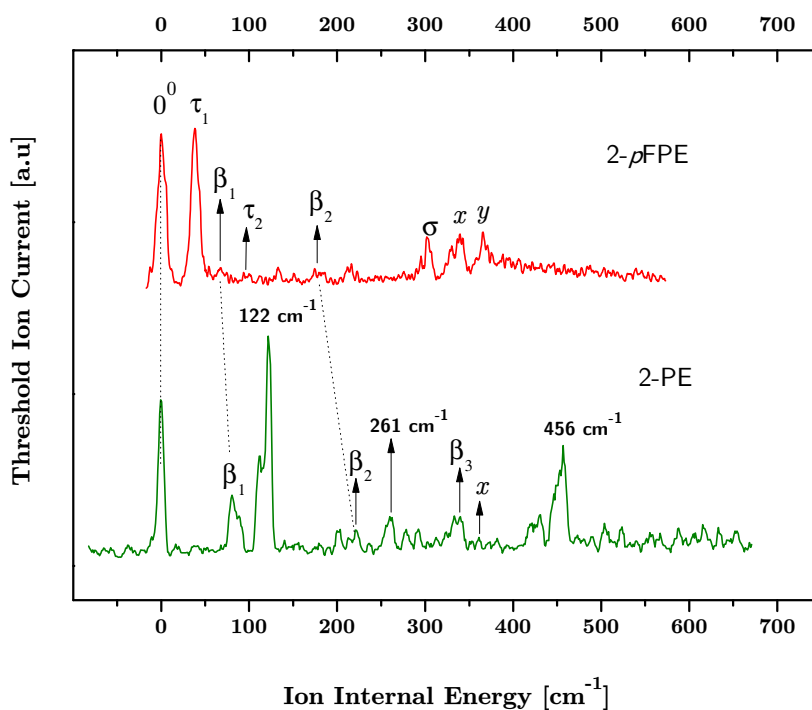
Fig.IX.10. MATI spectra of 2PE (lower trace) and 2*p*FPE (upper trace) [77] via the $S_1 \leftarrow S_0$ origins of the respective *anti* conformers: 37 670 cm^{-1} in 2PE and 37 147 cm^{-1} in 2*p*FPE. Both spectra are plotted on a common ion-internal-energy scale that refers to the respective AIE in each case.

assignment		2PE	2*p*FPE
τ_1	torsion about C2–C7	-	39
β_1	side chain bending	80	66
τ_2	torsion about C7–C8	-	85
	combination mode	122	-
β_2	out of plane ring bending	220	177
	combination mode	261	-
σ	stretching mode	-	302
β_3	out of plane ring deformation	340	-
x	C2–C7 wagging	-	337
y	OH torsion	-	365
	combination mode	456	-

Table.IX.8. Observed experimental vibrational frequencies in MATI spectra of *anti* 2PE and *anti* 2*p*FPE. In the latter case, the frequencies of the vibrational bands except for β_1 and β_2 was taken from the work of Karaminkov et al. [77]. The positions of β_1 and β_2 bands were directly determined from the MATI spectra in Fig.IX.10. All values are in cm^{-1}.

The most striking difference is the absence of the peak at 122 cm^{-1} and the presence of a peak corresponding to the mode τ_1 in the MATI spectrum of 2pFPE. In the region above 150 cm^{-1} the two traces in **Fig. IX.10** differ mostly in the frequency position and intensity of the β_2 and wagging mode x (the latter is hardly recognizable in the case of 2PE). Furthermore, a noticeable feature of the upper trace is the presence of a σ stretching band and OH torsional mode y, while peaks corresponding to the β_3 vibration and particularly to the 456 cm^{-1} band are clearly absent in the case of 2pFPE. The latter is actually expected since the peak at 456 cm^{-1} in the MATI spectrum of 2PE corresponds probably to a combination mode of β_3 and the band at 122 cm^{-1} as discussed in *Section IX.3.4.*

IX.4.3. Fluorine substitution effect on the $S_1 \leftarrow S_0, 0_0^0$ frequency and AIE

a) Effect on the $S_1 \leftarrow S_0$ origin

A comparison of the values listed in **Table IX.9** demonstrates that the $S_1 \leftarrow S_0$ origin of the most stable *gauche* conformer (stabilized by an OH$\cdots\pi$ hydrogen bond) is shifted to lower frequencies upon fluorine substitution. Furthermore, a comparison with the value of 37 589 cm^{-1} for the $S_1 \leftarrow S_0$ origin of *gauche* 2oFPE [79] shows that this red shift depends on the site of substitution. The largest decrease Δ of the $S_1 \leftarrow S_0$, 0_0^0 transition energy gap is observed in the case of 2pFPE (by 555 cm^{-1}), while the red shift in case of *ortho* substitution is only 33 cm^{-1}. Somewhat smaller is the bathochromic shift of the $S_1 \leftarrow S_0$ origin for the most stable *anti* conformer: 523 cm^{-1} for 2pFPE. In the case of *ortho* substituted 2PE there are no experimental indications of a $S_1 \leftarrow S_0$ origin for an *anti* structure in the spectrum [79] which precludes a comparison with the results on 2PE. It can be suggested however, that the trend observed in the *gauche* case is also valid in the *anti* case, i.e. *para* substitution induces larger $S_1 \leftarrow S_0, 0_0^0$ red shift than *ortho* substitution. It can be also supposed that the *anti* red shift is smaller than the *gauche* red shift also in 2oFPE.

b) Substitution effect on the AIE

Furthermore, the results in **Table IX.9** point to a fluorination effect on the AIE for the *anti* structures. *Para* fluorination of 2PE leads to a decrease in the AIE by 184 cm^{-1},

which is smaller by a factor of 2.8 than the $S_1 \leftarrow S_0, 0_0^0$ red shift (Δ=523 cm^{-1}). In addition, the estimated (by the method described in *Section IX.3.3*) values for the adiabatic ionization threshold of the unsubstituted and *para* fluorinated *gauche* structures suggest that, similarly to the $S_1 \leftarrow S_0, 0_0^0$ case, fluorination exerts larger effect ($\delta = 203$ cm^{-1}) in the case of the *gauche* conformer than in the case of the *anti* structure ($\delta = 184$ cm^{-1}). Moreover, similarly to the *anti* conformer, the AIE red shift upon *para* fluorination for the *gauche* conformer is presumably smaller than the decrease of the $S_1 \leftarrow S_0, 0_0^0$ transition energy (555 cm^{-1}).

It should be pointed out that a comparison at this point with the results on 2*o*FPE is not straightforward. There is no available experimental result for the AIE of the lowest-in-energy *gauche* conformer in this case, while on the other hand the resolved MATI spectrum most probably originates from a *gauche* rather than from an *anti* cationic conformer [80]. The adiabatic ionization threshold in the latter case is 72 159 cm^{-1}, which is higher by 737 cm^{-1} and 921 cm^{-1} than the AIE of the *anti* 2PE and 2*p*FPE, respectively.

Transition	2PE	2*p*FPE
gauche $S_1 \leftarrow S_0, 0_0^0$	37 622	37 067 (Δ=555)
gauche AIE[a]	70 922	70 719 (δ=203)
anti $S_1 \leftarrow S_0, 0_0^0$	37 670	37 147 (Δ=523)
Anti AIE	71 422	71 238 (δ=184)

Table.IX.9. Frequencies of the $S_1 \leftarrow S_0, 0_0^0$ transitions for the *gauche* and *anti* conformer of 2PE and 2*p*FPE as well as the corresponding adiabatic ionization energies, AIE. The symbols Δ and δ denote the lowering of the respective transition frequency upon *para* fluorine substitution in 2PE. All values are given in [cm^{-1}]. Note: [a] Value of AIE expected on the basis of DFT M05/aug-cc-pVTZ calculations (*Section IX.3.3*).

IX.4.4. Comparison with the fluorination effect in other para substituted benzene derivatives

From the results listed in **Table IX.10**. it can be seen that the *para* fluorine substitution in *anti* 2PE has a moderate effect on the $S_1 \leftarrow S_0, 0_0^0$ energy gap and the AIE in comparison to the case of the other benzene derivatives presented in **Table IX.10**. The same can be assumed also for the *gauche* 2*p*FPE conformer with the reservation that the

AIEs in this case are not directly obtained from the experiment as discussed in *Section IX.3.3.*
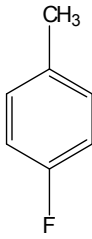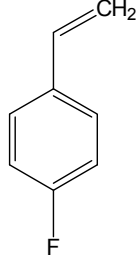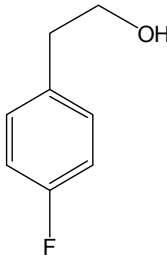
molecule			
	*p-fluoro*toluene[a]	*p-fluoro*styrene[b]	*anti* 2*p*FPE[c]
$S_1 \leftarrow S_0$, 0_0^0 shift	-615	-448	-523 (-555)
AIE shift	-264	-23	-184

Table.IX.10. Shifts in the frequencies of the $S_1 \leftarrow S_0$, 0_0^0 transition and AIE upon fluorine *para* substitution in benzene derivatives. [a] Values for *p-fluoro*toluene [116] compared with those for toluene [105]. [b] Values for *p-fluoro*styrene [37] compared with those of styrene [117] . [c] Values for 2*p*FPE [77] compared with those of 2PE (this work). All shifts are given in [cm^{-1}].

As discussed in the beginning of Section IX.4, fluorine substitution in the aromatic ring results in a subtle interplay between the electron withdrawing negative inductive effect $-I$ and the electron donating mesomeric effect $+M$ exerted by the fluorine atom. The observed red shifts in the $S_1 \leftarrow S_0, 0_0^0$ origin and the adiabatic ionization energy upon *para* fluorination in 2*p*FPE and other F-substituted aromatic hydrocarbons (**Table IX.10**) show that for these systems (*para* mono substituted) the latter effect ($+M$) is dominant. It can be therefore concluded that the net effect of fluorine *para* mono substitution renders fluorine as an electron **donating (activating)** substituent in this case. This leads to a greater stabilization of the S_1 and D_0 states than of the S_0 state, similarly to the case of methyl substitution in indole as discussed in Section VIII.7. *Ortho* substituted fluorine is also electron donating, at least as revealed by the induced $S_1 \leftarrow S_0, 0_0^0$ red shift of the most stable *gauche* conformer. The value of this red shift is, however, smaller for the *para* F-substituted *gauche* structure, i.e. *para* substitution exerts larger effect on the $S_1 \leftarrow S_0, 0_0^0$ energy gap than *ortho* substitution.

On the other hand, the larger red shift upon *para* fluorination in the origin of the $S_1 \leftarrow S_0$ spectrum of the *anti* conformer than in the AIE leads to the conclusion that *para* F-substitution distorts more strongly the electronic configuration of the S_1 state than of the cationic D_0 state of the chromophore. In the case of transitions to Rydberg states and/or to ionization thresholds, the mesomeric effect does not play a significant role and depending on the relative contributions of $-I$ and $+M$ the net effect may be again a red shift or a blue shift (as is the case for fluorine polysubstitution, where the $-I$ effect is substantial).

IX.5. Summary and conclusions

The experimental and theoretical results in the present work elucidate the effect of ionization on the conformational variety and conformational structure of 2-phenylethanol. Both MATI spectroscopy and quantum chemical calculations point to the existence of only two experimentally observable conformers in the cationic D_0 state: one *gauche* and one *anti* structure. The MATI spectrum via the S_1, 48 band features an unambiguously identifiable AIE and individual vibrational bands. The frequency positions of these bands are in agreement with the ones theoretically predicted for the *anti* structure III. On the other hand, the MATI spectrum via the $S_1 \leftarrow S_0$ *gauche* origin is a monotonously increasing threshold ion signal with a smooth onset. This finding is in accord with the theoretically predicted large geometrical changes upon ionization for the neutral *gauche* structure expressed in the breakage of the stabilizing OH$\cdots\pi$ hydrogen bond. Although a rigorous assignment of vibrational bands in the D_0 state in this case is not possible, the agreement between the frequency positions of the two observed progression-like patterns and the theoretical results characterize the MATI spectrum as originating from the cationic *gauche* conformer I. Moreover, the latter case represents an interesting and important finding. The mass analyzed threshold ionization generally sheds light on the adiabatic ionization energy and the vibrational frequencies in ground cationic state D_0 of a molecule when the ionization process is not accompanied by large geometrical changes. This in the present work is the case of *anti* 2PE as well as the 3MI and 3MI 1:1 hydrogen-bonded complexes with water and benzene studied in **Chapter VIII**. However, the observed progression-like vibrational pattern in the threshold ionization spectrum of the *gauche* 2PE conformer clearly demonstrates that MATI is capable of providing spec-

troscopic information even when prominent structural changes do occur. As demonstrated from the agreement with the DFT calculations for 2PE, such information may aid the identification of the quantum chemically predicted conformational structure in this case.

Furthermore, the similarities in the threshold ion spectra via the S_1, 48 and S_1, 58 bands, in particular the identical AIE, reveal that these peaks in the $S_1 \leftarrow S_0$ spectrum of 2PE result from the excitation of one, namely the most stable neutral *anti* conformer. This finding supports the results reported previously by Karaminkov et al. [91] and Mons et al. [85]. This apparently renders MATI as a suitable method for investigating the origin of debatable peaks in the $S_1 \leftarrow S_0$ spectra of molecules and in particular their hypothetical correspondence to various conformational structures.

The comparative experimental and theoretical study of 2PE, 2*p*FPE, and 2*o*FPE shows that fluorine substitution exerts a site-dependent effect on the spectral characteristics, the conformational structure and the conformational variety of 2PE. *Para* F-substitution in 2-phenylethanol does not change the number of stable conformers in the S_0 state, while *ortho* F-substitution leads to a greater number of stable conformers (9). However, it should be again emphasized that in all three cases the most stable conformer in the S_0 state is a *gauche* structure, stabilized by a hydrogen OH$\cdots\pi$ bond. This underlines the role of such bonding in biomolecules as well as its stability against fluorine substitution. On the other hand, the geometry of the lowest-in-energy S_0 *anti* conformer is noticeably affected by fluorine substitution and the site of substitution. In the cation, the effects of fluorine substitution and the site of this substitution on the geometry of the molecule, particularly regarding the side chain are again larger for the *anti* than for the *gauche* conformer.

Para fluorine substitution causes frequency shifts of the vibrational modes in the ground cationic state D_0 of the *anti* conformer. Also, *para* F-substitution causes a red shift in the $S_1 \leftarrow S_0$, 0_0^0 transition and the AIE for the lowest-in-energy *anti* 2PE, similarly to the case of other mono *para* substituted benzene derivatives. The same is also valid for the $S_1 \leftarrow S_0$ origin of the most stable *gauche* conformer, while for the AIE in this case such a conclusion is only suggested from estimating the experimental AIE of *gauche* 2PE (*Section IX.3.3*) and *gauche* 2*p*FPE [77] on the basis of DFT M05/aug-cc-pVTZ calculations.

In addition, the experimental results point to a conformation-dependent effect of *para* F-substition on the $S_1 \leftarrow S_0$, 0_0^0 transition frequency. The experimental findings unambigu-

ously show that *para* F-substitution causes a larger decrease of the $S_1 \leftarrow S_0$, 0_0^0 energy gap in the *gauche* conformer than in the *anti* conformer. The same conclusion is suggested for the AIE decrease upon *para* fluorination on the basis of the estimated experimental adiabatic ionization energies of *gauche* 2PE and *gauche* 2pFPE.

Threshold ionization studies and quantum chemical calculations on other 2PE substituted derivatives may further shed light on the substitution effect on the studied spectral and structural properties and in particular on the influence of other electron activating or deactivating substituents on the stabilizing OH⋯π hydrogen bond in 2PE and other similar biomolecules.

<div align="center">***</div>

The obtained results on the one hand and the satisfactory agreement between the experimental and theoretical findings in the present work, on the other hand, render the combination of MATI spectroscopy and quantum chemical calculations a powerful and reliable method in the ground cationic state study of small biomolecules such as 2-phenylethanol. In addition the employed methods shed light on the effect of halogen substituents such as fluorine on the molecular geometrical structure and spectroscopic properties.

Bibliography to Part III

1. H. Krause, Diplomarbeit, Fakultät für Chemie, Biologie und Geowissenschaften der Technischen Universität München, 1988.

2. R. Weinkauf, Zulassungsarbeit zur wissenschaftlichen Prüfung für das Lehramt an Gymnasien, München, 1982.

3. T.L. Grebner, Dissertation, Fakultät für Chemie, Biologie und Geowissenschaften der Technischen Universität München, 1996.

4. S. Georgiev and H.J. Neusser, Chem. Phys. Lett., 2004. **389**(1-3): p. 24.

5. S. Georgiev and H.J. Neusser, J. Electr. Spectrosc. Rel. Phenom., 2005. **142**: p. 207.

6. J.R. Rizzo, C.A. Alt, and T.Y. Zhang, Tetrahedron Letters, 2008. **49**(48): p. 6749.

7. T. Okauchi, M. Itonaga, T. Minami, T. Owa, K. Kitoh, and H. Yoshino, Organic Letters, 2000. **2**(10): p. 1485

8. V. Kozmík, B. Košata, J. Svoboda, and M. Kuchař, Collect. Czech. Chem. Commun., 2006. **71**: p. 679.

9. V.A. Budylin, L.G. Yudin, and A.N. Kost, Khimiya Geterotsiklicheskikh Soedinenii, 1980. **9**: p. 1181.

10. D.V. Gopal, B. Srinivas, V. Durgakumari, and M. Subrahmanyam, Applied catalysis. A: General 2002. **224**(1-2): p. 121.

11. P. Siwach, S. Singh, and R.K. Gupta, Catalysis Communications, 2009. **10**(12): p. 1577.

12. E.H. Strickland, J. Horwitz, and C. Billups, Biochem., 1970. **9**(25): p. 4914-4921.

13. M.R. Eftink, L.A. Selvidge, P.R. Callis, and A.A. Rehms, J. Phys. Chem., 1990. **94**: p. 3469.

14. K.W. Short and P.R. Callis, J. Chem. Phys., 2000. **113**: p. 5235.

15. J.R. Platt, J. Chem. Phys., 1949. **17**: p. 484.

16. J.R. Platt, J. Chem. Phys., 1951. **19**(1): p. 101.

17. H. Lami, J. Chem. Phys., 1977. **67**: p. 3274.

18. J.W. Hager, D.R. Demmer, and S.C. Wallace, J. Phys. Chem., 1987. **91**: p. 1375.

19. D.M. Sammeth, S.S. Siewert, L.H. Spangler, and P.R. Callis, Chem. Phys. Lett., 1992. **193**: p. 532.

20. D.R. Demmer, G.W. Leach, and S.C. Wallace, J. Phys. Chem., 1994. **98**: p. 12834.

21. J. Hager and S.C. Wallace, J. Phys. Chem., 1984. **88**: p. 5513.

22. J.R. Carney and T.S. Zwier, J. Phys. Chem. A, 1999. **103**: p. 9943.

23. J.R. Carney, F.C. Hagemeister, and T.S. Zwier, J. Chem. Phys., 1998. **108**: p. 3379.

24. R.M. Helm, M. Clara, T.L. Grebner, and H.J. Neusser, J. Phys. Chem. A, 1998. **102**: p. 3268.

25. J. Braun, H.J. Neusser, and P. Hobza, J. Phys. Chem. A, 2003. **107**(19): p. 3918.

26. M. Mons, I. Dimicoli, B. Tardivel, F. Piuzzi, V. Brenner, and P. Millié, J. Phys. Chem. A, 1999. **103**: p. 9958.

27. J.C. Jiang and M.H. Tsai, J. Phys. Chem. A, 1997. **101**: p. 1982.

28. S. Alavi and D.L. Thompson, J. Phys. Chem. A, 2004. **108**: p. 8801.

29. V.B. Delchev and H. Mikosch, Journal of Structural Chemistry, 2006. **47**(5): p. 979.

30. S. Chervenkov, P. Wang, and H.J. Neusser, unpublished results.

31. K. Remmers, E. Jalviste, I. Mistrik, G. Berden, and W.L. Meerts, J. Chem. Phys., 1998. **108**: p. 8436.

32. J.L. Lin, S. Zhang, and W.B. Tzeng, J. Chem. Phys., 2004. **120**(11): p. 5057.

33. Y. Huang and M. Sulkes, J. Phys. Chem., 1996. **100**: p. 16479.

34. J.E. Braun, T. Mehnert, and H.J. Neusser, Int. J. Mass. Spectrom., 2000. **203**: p. 1.

35. T. Vondrák, S. Sato, and K. Kimura, J. Phys. Chem. A, 1997. **101**: p. 2384.

36. K. Takazawa, M. Fujii, and M. Ito, J. Chem. Phys., 1993. **99**(5): p. 3205.

37. S. Georgiev, T. Chakraborty, and H.J. Neusser, J. Chem. Phys., 2004. **120**(17): p. 8015.

38. D.J. Chadwick, *Chapter 3.04*, in *Comprehensive Heterocyclic Chemistry: The Structure, Reactions, Synthesis, and Uses of Heterocyclic Compounds*, A.R. Katritzky and C.W. Rees, Editors. 1984, Pergammon: Oxford p. 155.

39. A. Combs, K. McCann, D. Autrey, J. Laane, S.A. Overman, and G.J. Thomas Jr., J. Mol. Struct., 2005. **735-736**: p. 271.

40. P. George, C.W. Bock, J.J. Stezowski, T. Hildenbrand, and J.P. Glusker, J. Phys. Chem., 1988. **92**: p. 5656.

41. G.M. Jensen, D.B. Goodin, and S.W. Bunte, J. Phys. Chem., 1996. **100**: p. 954.

42. Y. Sonoda and S. Iwata, Chem. Phys. Lett., 1995. **243**: p. 176.

43. J.P. Merrick, D. Moran, and L. Radom, J. Phys. Chem. A, 2007. **111**(45): p. 11683.

44. P. Sinha, S.E. Boesch, C. Gu, R.A. Wheeler, and A.K. Wilson, J. Phys. Chem. A, 2004. **108**(42): p. 9213.

45. J.E. Braun, Dissertation, Institut für Physikalische und Theoretische Chemie Lehrstuhl 1, Technische Universität München, 2001.

46. S.G. Lias, J.E. Bartmess, J.F. Liebman, J.L. Holmes, R.D. Levin, and W.G. Mallard, J. Phys. Chem. Ref. Data Suppl. 17, 1988. **17**: p. 1.

47. S.J. Weiner, P.A. Kollman, D.A. Case, U.C. Singh, C. Ghio, G. Alagona, S. Profeta, and P. Weiner, J. Am. Chem. Soc., 1984. **106**: p. 765.

48. W. Fang, J. Chem. Phys, 1999. **111**: p. 5361.

49. J.S. Wright and V.J. Barclay, J. Comp. Chem., 1991. **12**(6): p. 697.

50. N. Oliphant, M.E. Rosenkrantz, and D.D. Konowalow, Chem. Phys. Lett., 1994. **223**: p. 7.

51. G. Weck, A. Milet, R. Moszynski, and E. Kochanski, J. Phys. Chem. A, 2002. **106**: p. 12084.

52. J. Hager, M. Ivanco, M.A. Smith, and S.C. Wallace, Chem. Phys., 1986. **105**: p. 397.

53. J.E. Braun, T.L. Grebner, and H.J. Neusser, J. Phys. Chem. A, 1998. **102**: p. 3273.

54. S.-L. Chong and J.L. Franklin, J. Am. Chem. Soc., 1972. **94**(19): p. 6630.

55. S. Georgiev and H.J. Neusser, J. of Electron Spectrosc. and Relat. Phenom., 2005. **142**(3): p. 207.

56. H.J. Neusser and H. Krause, Chem. Rev., 1994. **94**: p. 1829.

57. V. Spirko, O. Engkvist, P. Soldan, H.L. Selzle, E.W. Schlag, and P. Hobza, J. Chem. Phys., 1999. **111**: p. 572.

58. J.E. Braun and H.J. Neusser, Mass Spectrom. Rev., 2002. **21**: p. 16.

59. J. Küpper, D.W. Pratt, W.L. Meerts, C. Brand, J. Tatchen, and M. Schmitt, Phys. Chem. Chem. Phys., 2010. **12**: p. 4980.

60. J.D. Pitts, S. Basu, and J.L. Knee, J. Chem. Phys., 2000. **113**(5): p. 1857.

61. J.L. Lin and W.B. Tzeng, Chem.Phys.Lett, 2003. **377**: p. 620.

62. H. Krause and H.J. Neusser, J. Chem. Phys., 1992. **97**(8): p. 5923.

63. W.D. Geppert, C.E.H. Dessent, M.C.R. Cockett, and K. Müller-Dethlefs, Chem. Phys. Lett., 1999. **303**: p. 194.

64. R.H. Wu, J.L. Lin, J. Lin, S.C. Yang, and W.B. Tzeng, J.Chem.Phys., 2003. **118**(11): p. 4929.

65. H.M. Lee, N.J. Singh, and K.S. Kim, *Weak to Strong Hydrogen Bonds* in *Hydrogen bonding - new insights (Challenges and Advances in Computational Chemistry and Physics) 1 edition*, S.J. Grabowsky, Editor. 2006, Springer.

66. M. Cheng, X. Pu, N.-B. Wong, M. LI, and A. Tian, New J. Chem., 2008. **32**: p. 1060.

67. H. Krause, B. Ernstberger, and H.J. Neusser, Chem. Phys. Lett., 1991. **184**: p. 411.

68. K. Ohashi and N. Nishi, J.Chem.Phys., 1998. **109**: p. 3971.

69. F. Billes, P.V. Podea, I. Mohammed-Ziegler, M. Tosa, H. Mikosch, and D.-F. Irimie, Spectrochimica Acta Part A, 2009. **74**: p. 1031.

70. C. Unterberg, A. Jansen, and M. Gerhards, J. Chem. Phys., 2000. **113**: p. 7945.

71. S.E. Walden and R.A. Wheeler, J. Chem. Soc., Perkin Trans. 2, 1996. **3**: p. 2663.

72. S.E. Walden and R.A. Wheeler, J. Phys. Chem., 1996. **100**: p. 1530.

73. Y. Zhao, O. Tishchenko, and D. Truhlar, J. Phys. Chem. B, 2005. **109**(41): p. 19046.

74. T. van Mourik, Chem. Phys., 2004. **304**: p. 317.

75. Y. Zhao and D.G. Truhlar, J. Phys. Chem. A, 2004. **108**: p. 6908.

76. S. Georgiev, R. Karaminkov, S. Chervenkov, V. Delchev, and H.J. Neusser, The Journal of Physical Chemistry A, 2009. **113**(44): p. 12328.

77. R. Karaminkov, S. Chervenkov, and H.J. Neusser, Phys. Chem. Chem. Phys., 2009. **11**: p. 2249.

78. R. Karaminkov, S. Chervenkov, and H.J. Neusser, Phys. Chem. Chem. Phys., 2008. **10**(19): p. 2852.

79. R. Karaminkov, S. Chervenkov, H.J. Neusser, V. Ramanathan, and T. Chakraborty, J.Chem.Phys., 2009. **130**: p. 034301.

80. R. Karaminkov, S. Chervenkov, and H.J. Neusser, J. Phys. Chem. A, 2010. **114**: p. 11263.

81. M. Sakai, H. Hirata, H. Sayama, K. Sekiguchi, H. Itano, T. Asai, H. Dohra, M. Hara, and N. Watanabe, Biosci Biotechnol Biochem., 2007 **71**(10): p. 2408.

82. Z. Yang, M. Sakai, H. Sayama, T. Shimeno, K. Yamaguchi, and N. Watanabe, Journal of Plant Physiology, 2009. **166**(8): p. 887

83. C.J. Bostock, Journal of Cell Science, 1970. **7**: p. 523.

84. W.E.G. Müller, D. Falke, B. Heicke, and R.K. Zahn, Archives of Virology, 1973. **40**(3-4): p. 205.

85. M. Mons, E.G. Robertson, L.C. Snoek, and J.P. Simons, Chem. Phys. Lett., 1999. **310**: p. 423.

86. P.D. Godfrey, R.N. Jorissen, and R.D. Brown, J. Phys. Chem. A, 1999. **103**(38): p. 7621.

87. N. Guchhait, T. Ebata, and N. Mikami, J. Am. Chem. Soc., 1999. **121**(24): p. 5705.

88. S.S. Panja and T. Chakraborty, J. Phys. Chem. A, 2003. **107**(50): p. 10984.

89. M. Hockridge and E.G. Robertson, J. Phys. Chem. A, 1999. **103**(19): p. 3618.

90. R. Weinkauf, F. Lehrer, E.W. Schlag, and A. Metsala, Faraday Discuss., 2000. **115**: p. 363.

91. R. Karaminkov, S. Chervenkov, and H.J. Neusser, J. Phys. Chem. A, 2008. **112**(5): p. 839.

92. J.A. Dickinson, M.R. Hockridge, R.T. Kroemer, E.G. Robertson, J.P. Simons, J. McCombie, and M. Walker, J. Am. Chem. Soc., 1998. **120**(11): p. 2622.

93. E.G. Robertson, L.C. Snoek, J.P. Simons, and M. Mons, Central Laser Facility Annual Report 1999/2000, 2001: p. 124.

94. S. Chervenkov, R. Karaminkov, J.E. Braun, H.J. Neusser, S.S. Panja, and T. Chakraborty, J. Chem. Phys., 2006. **124**: p. 234302.

95. P.D. Godfrey, R.D. Brown, and L.D. Hatherley, J. Am. Chem. Soc., 1995. **117**(31): p. 8204.

96. B. Vogelsanger, P.D. Godfrey, and R.D. Brown, J. Am. Chem. Soc., 1991. **113**: p. 7864.

97. P.D. Godfrey and R.D. Brown, J. Am. Chem. Soc., 1998. **120**: p. 10724.

98. D. Barnard, K.R. Hargrave, and G.M.C. Higgins, J. Chem. Soc., 1956: p. 2845.

99. H.H. Kirchner and W.Z. Richter, Phys. Chem. Neue Folge, 1972. **81**: p. 274.

100. S.L. Spassov, M.F. Simeonov, and E.W. Randall, Journal of Molecular Structure, 1981. **77**(3-4): p. 289.

101. J.L. Atwood, F. Hamada, K.D. Robinson, G.W. Orr, and R.L. Vincent, Nature, 1991. **349**: p. 683.

102. P.v.R. Schleyer, C. Wintner, D.S. Trifan, and R. Backsai, Tetrahedron Lett., 1959. **14**: p. 1.

103. C.S. Parmenter, Faraday Discuss. Chem. Soc., 1983. **75**: p. 7.

104. L.A. Chewter, M. Sander, K. Müller-Dethlefs, and E.W. Schlag, J. Chem. Phys., 1987. **86**: p. 4737.

105. K.T. Lu, G.C. Eiden, and J.C. Weisshaar, J. Phys. Chem., 1992. **96**: p. 9742.

106. S. Sato, T. Kojima, K. Byodo, H. Shinohara, S. Yanagihara, and K. Kimura, J. Electron Spectrosc. Relat. Phenom., 2000. **112**: p. 247.

107. O. Dopfer, Dissertation, Fachbereich für Chemie, Biologie und Geowissenschaften der Technischen Universität München, 1994.

108. F.W. McLafferty and F. Turecek, *Interpretation of Mass Spectra*. 1993: University Science Books, Mill Valley.

109. Y. Zhao, N.E. Schultz, and D.G. Truhlar, J. Chem. Phys., 2005. **123**: p. 161103.

110. B.M. Medina, D. Beljonne, H.-J. Egelhaaf, and J. Gierschner, J. Chem. Phys., 2007. **126**: p. 111101.

111. M. Piacenza, F. D. Sala, G. M. Farinola, a. C. Martinelli, and G. Gigli, J. Phys. Chem. B, 2008. **112**(10): p. 2996.

112. K. Okuyama, N. Mikami, and M. Ito, J. Phys. Chem., 1985. **89**: p. 5617.

113. K.T. Lu, F. Weinhold, and J.C. Weisshaar, J. Chem. Phys., 1995. **102**: p. 6787.

114. K. Okuyama, N. Mikami, and M. Ito, Laser Chem., 1987. **7**: p. 197.

115. R.A. Walker, E. Richard, K.T. Lu, E.L. SibetIii, and J.C. Weisshaar, J. Chem. Phys., 1995. **102**: p. 8718.

116. S. Georgiev, T. Chakraborty, and H.J. Neusser, J. Phys. Chem. A, 2004. **108**(16): p. 3304.

117. J.M. Dyke, H. Ozeki, M. Takahashi, M.C.R. Cockett, and K. Kimura, J. Chem. Phys., 1992. **97**(12): p. 8926.

118. M. J. Frisch, G. W. Trucks, H. B. Schlegel, G. E. Scuseria, M. A. Robb, J. R. Cheeseman, J. A. Montgomery Jr., T. Vreven, K. N. Kudin, J. C. Burant, J. M. Millam, S. S. Iyengar, J. Tomasi, V. Barone, B. Mennucci, M. Cossi, G. Scalmani, N. Rega, G. A. Petersson, H. Nakatsuji, M. Haga, M. Ehara, K. Toyota, R. Fukuda, J. Hasegawa, M. Ishida, T. Nakajima, Y. Honda, O. Kitao, H. Nakai, M. Klene, X. Li, J. E. Knox, H. P. Hratchian, J. B. Cross, C. Adamo, J. Jaramillo, R. Comperts, R. E. Stratmann, O. Yazyev, A. J. Austin, R. Cammi, C. Pomelli, J. W. Ochterski, P. Y. Ayala, K. Morokuma, J. A. Voth, P. Salvador, J. J. Dannenberg, V. G. Zakrzewski, S. Dapprich, A. D. Daniels, M. C. Strain, O. Farkas, D. K. Malick, A. D. Rabuck, K. Raghavachari, J. B. Foresman, J. V. Ortiz, Q. Cui, A. G. Baboul, S. Clifford, J. Cioslowski, B. B. Stefanov, G. Liu, A. Liashenko, P. Piskorz, I. Kamaromi, R. L. Maetin, D. J. Fox, T. Keith, M. A. Al-Laham, C. Y. Peng, A. Nanayakkara, M. Challacombe, P. M. W. Gill, B. Johnson, W. Chen, M. W. Wong, C. Gonzales, and J. A. Pople, Gaussian 03, Revision B.04, 2003.

Summary and Perspectives

Spectroscopy is a powerful tool for investigating various molecular properties that are the key to the chemical reactivity of molecules and their tendency to take part in weak molecular interactions. In particular, threshold ionization experiments shed light on a variety of aspects regarding the spectroscopic investigation of molecular ions. A key advantage of this approach that provoked its implementation also in the present experimental studies is the well defined internal energy of the so produced cationic species. In addition, the mass selectivity of the employed method, MATI, provides information on the dissociation dynamics and energetics of the cations. Quantum-chemical calculations can be implemented to support and complement the experimental findings. Theoretical methods such as those employed in the present work, DFT, MP2, and CCSD proved to be suitable and reliable in the studies of molecules, varying in size and structural complexity.

The choice of the studied systems in this work was prompted by several reasons. First of all, both 3-methylindole (3MI) and 2-phenylethanol (2PE) are of interest from a biochemical viewpoint. Furthermore, their chemical and physical properties render them amenable to spectroscopic studies both in their neutral and cationic forms, while their relatively small size and simple structure make them suitable for a fairly uncomplicated quantum-chemical treatment. The presented spectroscopic and theoretical investigation of 3MI and 2PE reveal their geometry and vibrational structure in the ground neutral and ground cationic state, as well as properties such as excitation energies, ionization energies and the nature of the studied transitions. The results are focused mainly on the ionization of the studied molecules and on their properties in the ground cationic state D_0. On the one hand, this research was dictated by the important role that ionized species of biomolecules play in the course of biochemical reactions, in particular regarding molecular systems for which 3MI and 2PE serve as models. On the other hand, the effects on the cation of different substituents and nonchemical interactions due to electrostatic, induction, or dispersion forces are different from those exerted on the neutral molecule. It is interesting to investigate how such interactions change their magnitude or even direction when the studied molecule is ionized. In addition, in the ionic species processes such as charge transfer may occur: an important phenomenon in biochemistry. The present studies on 3MI and 2PE in the present work illustrate a variety of effects that different factors (e.g. substitution of functional groups or nonchemical interacttions) exert on the structural properties and ion stability of more complex biomolecules,

particularly those with flexible side chains as in 2PE and thus exhibiting a tendency towards conformational changes.

One of the main tasks in the ion spectroscopy of biomolecules is to elucidate to what extent ionization alters their geometrical structure and therefore their chemical and biochemical activity. The MATI and theoretical studies on 2PE have shown that ionization leads to reorientation of the side chain and break of the stabilizing OH$\cdots\pi$ hydrogen bond between the hydroxyl group in the side chain and the π-moiety of the phenyl ring for the S_0 most stable gauche conformer. Furthermore, quantum-chemical calculations have shown that ionization reduces the number of stable conformers of 2PE. On the other hand, the number of the theoretically predicted conformers is larger than the experimentally observed ones both in the ground neutral S_0 and ground cationic D_0 state. This brings forward the concept of relaxational intraconversion within the two groups of conformers, *gauche* and *anti* in the neutral and the ionized molecule. The structural changes in 3MI upon ionization are less prominent as demonstrated from both the threshold ionization spectroscopy and quantum-chemical calculations in this work, which is expected for a rigid moiety such as the indole ring.

Another central topic in the discussion of the spectroscopic properties of cations is the stability of the cationic electronic states, in particular the ground state D_0. Charged species are rarely free from interactions with the surrounding media, especially in the myriad of biochemical reactions that occur in the living cell. Even within a molecule, e.g. a protein, various functional groups or atoms may exert effects on the charged chromophore thus modifying its interaction-free stability. Interactions that occur between a chromophore and other parts of the same molecule or other molecules may vary in their nature depending on the particular case. Functional groups or substituents in the molecule affect the stability of the ground cationic state D_0 of a chromophore by the means of their electron donating or electron withdrawing properties. Even if chemical reactions are not involved and the chemical nature of the interacting partners is therefore unaltered, the chromophore may still be a subject to nonchemical forces such as electrostatic, induction, or dispersion interactions.

In spectroscopy the effects on the stability of the ground cationic state D_0 of a chromophore are elucidated by exploring the $D_0 \leftarrow S_0$ energy gap and in particular the adiabatic ionization energy AIE as shown for 3MI and 2PE in the present work. Since electron donating substituents stabilize the D_0 state of an aromatic hydrocarbon, the AIE of the latter decreases in comparison to that of the unsubstituted system, while electron withdrawing substituents exert the opposite effect. Furthermore, if the local ionization

energies of a chromophore and a near functional group do not differ substantially, charge transfer (migration, delocalization) may occur: a situation quite common in biomolecules. The experimental and theoretical studies on the molecular systems in the present work explore a variety of effects that modify the stability of the ground cationic state of the chromophore and thus its AIE. 3-methylindole and 2-phenylethanol differ in one important aspect, i.e. the energy difference between the local ionization energies (IE) of the chromophore and the substituent. In 3MI the substituent (the methyl group) has a local IE of 9.95 eV[a] or $\approx$ 80 256 cm^{-1}, which is much higher (by more than 2 eV) than that of the indole moiety (62 591 cm^{-1}). This large energy difference renders the ionization of 3MI local (involving only the indole ring). On the other hand, the energy difference between the local IEs of the chromophore and the side chain in 2PE is lower, being $\approx$ 1.4 eV[b]. As discussed in Section IX.2, Weinkauf et al. have shown that in this case positive charge delocalization should be accounted for, since it is responsible for the structural changes upon ionization even when charge-dipole interaction is neglected. However, the energy barrier of 1.4 eV is still considered high enough to ensure an approximately local character of the ionization in 2PE similarly to the case of 3MI.

The influence of the hydrocarbon residue on the ionization energy of the chromophore (indole in 3MI or benzene in 2PE) can be therefore examined mainly in terms of effects stemming from the electron donating or electron withdrawing properties of the substituent, particularly in the case of 3MI. In Chapter VIII the decrease in the AIE of 3MI has been discussed completely in the light of the methyl group substitution at C3 site in the indole ring. With some reservations it is also reasonable to assert that the lower AIE of 2PE compared to that of benzene is to a large extent due to the substitution of an H nuclei by the CH_2–CH_2–OH residue, similarly to the case of other substituted benzenes (toluene, ethylbenzene, chlorobenzene, aniline, nitrobenzene,...).

In 3MI the substituent (the CH_3 group) is a weak electron *donor*, i.e. it lowers the cationic ground state D_0 in energy by stabilizing the positively charged (electron deficient) indole ion. Similarly, in case of 2PE, the CH_2CH_2OH group is electron-donating and its effect on the AIE of the benzene chromophore is similar to that of the CH_3 group.

The present work reaches beyond the spectroscopic studies of a single molecule by comprising the experimental and theoretical results on two molecular complexes, 3MI·H_2O

---

[a] **F.P. Lossing, K.U. Ingold, and I.H.S. Henderson, J. Chem. Phys. , 1954. 22: p. 621.**

[b] **R. Weinkauf, F. Lehrer, E.W. Schlag, and A. Metsala, Faraday Discuss., 2000. 115: p. 363-381.**

and $3MI \cdot C_6H_6$. The mass selectivity of the employed threshold ionization method, MATI, proved to be particularly suitable in these cases since it enabled the studies on the dissociation energetics of the two ionized complexes. The so obtained binding energies of the complexes in the ground cationic and, as demonstrated in **Chapter VIII**, the ground neutral states are much higher than those typical for van der Waals complexes. These findings as well as the observed red shifts in the excitation and ionization energies upon complexation demonstrate that $3MI \cdot H_2O$ and $3MI \cdot C_6H_6$ systems are formed by intermolecular *hydrogen* bonding. For the $3MI \cdot H_2O$ complex the findings on hydrogen bonding support the results from previous studies extending them to the cation case. On the other hand, for the $3MI \cdot C_6H_6$ complex such type of intermolecular interaction is reported for the first time.

The experimental results are consistent with the concept of proper hydrogen bonding at the NH site in the indole ring between 3MI as a solute and water or benzene as solvents. This bond topology is of particular interest in the case of the $3MI \cdot C_6H_6$ complex since it points to N–H$\cdots\pi$ hydrogen bonding. The latter belongs to a class of interactions known as π hydrogen bonds which play an indispensable role in biochemistry, e.g. in forming the shape of large proteins.

The experimental results on the hydrogen bonding type, hydrogen bonding strength, the effect of hydrogen bonding on the excitation energy and the AIE of the solute chromophore in $3MI \cdot H_2O$ and $3MI \cdot C_6H_6$ complexes are in agreement with the experimental findings from studies on indole$\cdot H_2O$ and indole$\cdot C_6H_6$ systems.

The quantum-chemical calculations performed on the studied systems are as a whole in agreement with the experimental findings. DFT showed better performance over MP2, coming close in terms of accuracy to the CCSD single point calculations in the case of 3MI. However, except for the case of the $3MI \cdot C_6H_6$ complex, MP2 manifested also satisfactory results. For all studied systems MP2 overestimated the AIE, while DFT underestimated it. The degree of underestimation in the latter case depended on the choice of the employed basis set. Calculations at the DFT level employing B3LYP functional and the cc-pVDZ and 6-31+G(d) basis sets were in a satisfactory agreement with the experimental findings on the AIEs of the $3MI \cdot H_2O$ and $3MI \cdot C_6H_6$ systems. The DFT B3LYP/6-31+G(d) theoretical studies on the complex geometry supported the concept of proper hydrogen bonding at the NH site in both complexes, predicting an elongation of the N–H bond length and a bathochromic shift of the NH stretching frequency. In addition, the calculations showed that the former parameter further increases, while the latter one further decreases upon ionization of the complexes as a result of the increased hydrogen

bonding strength. In the case of the 3MI·H_2O complex, B3LYP/6-31+G(d) correctly estimated the hydrogen bond energies both in the ground neutral and ground cationic state. The satisfactory agreement between the experimental results and theory is demonstrated also in the reasonable assignment of the vibrational bands in the studied systems: 3MI, 3MI·H_2O, 3MI·C_6H_6, and 2PE. In the latter case, this aided the identification of the experimentally observed cationic conformers, while for the 1:1 complexes of 3MI with water and benzene the identification of the intermolecular vibrational frequencies serves as additional indication for hydrogen bonding in these systems.

Furthermore, both MATI spectroscopy and quantum-chemical calculations correctly elucidate the effect of methyl group and fluorine substitution on the excitation energies, the adiabatic ionization energies, and the hydrogen bonding strength in the studied systems. The obtained experimental and theoretical results are in a reasonable agreement with the general concept of substitution effects stemming from the electron donating properties of the substituent. Furthermore, the magnitude of the substitution effect is adequate to the nature of the substituents under consideration. Particularly in the case of the 3MI·H_2O and 3MI·C_6H_6 complexes, hydrogen bonding was found to be weaker than in indole·H_2O and indole·C_6H_6. This is consistent with the electron donating property of the methyl group substituted in the indole ring which contains the hydrogen bond donor site, NH. On the other side, the substitution effect in this case is very small, which is to be expected as the CH_3 group is a weak electron releasing group. The presence of an additional alkyl group in 3MI compared to indole proved to be more essential and problematic regarding the accuracy of the quantum-chemical calculations on the structure and bonding energies of the hydrogen bonded complex between the indole ring and benzene.

In the case of 2PE, the comparison with its *para* fluorinated counterpart demonstrated a substitution effect consistent with that in other benzene derivatives.

<div align="center">***</div>

The present results render the combination of mass analyzed threshold ionization and the employed quantum-chemical calculations as a reliable and suitable approach in the study of conformational changes of biomolecules, identification and proper description of hydrogen bonding as well as a correct elucidation of substitution effects on the spectroscopic and energetic properties of the studied systems. Mass selective threshold ionization and quantum-chemical studies of other hydrogen-bonded complexes may further shed light on the role of substitution as well as on the hydrogen bonding in larger biomolecules such as proteins and amino acids. For example, in addition to the studies of 3MI and its 1:1 hyd-

rogen-bonded complexes with water and benzene, it would be interesting to investigate the substitution effects and the hydrogen bonding in complexes with solutes such as 5-hydroxyindole or 5-hydroxy-3-methyilindole as solutes, where there exist two possible hydrogen bond donor sites: the pyrrolic N–H site and the phenyl O–H site. The substitution effects on the AIE and the excitation energy can be examined in molecules such as 3-aminoindole and 3-nitroindole, where the substituent is a strong electron donating and strong electron withdrawing group, respectively. Studies on hydrogen bonded complexes where these molecules serve as solutes may further elucidate the influence of the substituent on the hydrogen bonding strength. Furthermore, the studies on 2PE in the present work may serve as a basis for the threshold ionization and theoretical investigation of the cations of larger biomolecules with flexible side chains.

The MATI studies of molecules and hydrogen-bonded complexes can be complemented by ADIR, IRPD or IR/PIRI spectroscopy (p. 81). These methods are based, similarly to MATI, on the excitation of high-lying Rydberg states but allow for the experimental observation of high-lying vibrational frequencies (e.g. the N–H stretch in indoles) in the ground cationic electronic state D_0. In particular, the latter technique is based on a depletion of the MATI signal attained through autoionization of the ion core by a third, IR, laser. An alternative to this method is to use a UV laser as an additional excitation source that would access vibrational levels in the first excited electronic state of the cation. Such studies may shed light on the vibrational spectroscopy of electronically excited threshold ions of biomolecules and their hydrogen-bonded complexes. In addition, these "three-laser experiments" may elucidate the role of hydrogen bonding and functional-group substitution in modifying the energy difference between the ground and the first excited cationic state.

The experimental research suggested in this section may, however, face a problem inherent to the supersonic-jet studies of molecules with low vapor pressure: the low concentration of the investigated species in the molecular beam. Such a drawback can be overcome by an increased heating or, alternatively, by laser desorption.

Suitable theoretical levels that may be applied to excited states of cations are for example the complete active space self-consistent field method (CASSCF) and the complete active space second-order perturbation theory method (CASPT2).

The final goal of such experimental and theoretical studies of the ground and excited electronic states of cations as well as of the respective vibrational structure is to achieve

an unified picture and a better understanding of the spectroscopic and structural properties of positively ionized larger biomolecules and hydrogen-bonded complexes as well as the dependence of such properties on a variety of factors such as substituents, neighboring molecules, or adjacent functional groups. This may aid the understanding of cationic interactions and therefore the chemical and noncovalent activity of positively charged molecular species, in particular cations of biomolecules.

List of Figures

List of Tables

List of Publications

S. Georgiev, R. Karaminkov, S. Chervenkov, V. Delchev, H. J. Neusser
Mass-analyzed threshold ionization spectroscopy of 2-phenylethanol:
Probing of Conformational Changes Caused by Ionization
J. Phys. Chem. A, 2009, vol. 113, issue 44, p.12328

S. Georgiev, H. J. Neusser
Mass analyzed threshold ionization of hydrogen bonded clusters of biological molecules:
the 3-methylindole·C_6H_6 complex
Journal of Electron Spectrosc. and Relat. Phenom., 2005, vol. 142, issue 3, p. 207

S. Chervenkov, P. Q. Wang, J. E. Braun, S. Georgiev, C. K. Nandi, T. Chakraborty, H. J. Neusser
High-resolution ultraviolet spectroscopy of p-fluorostyrene-water: Evidence for a sigma
hydrogen-bonded dimer
J. Chem. Phys., 2005, vol. 122, p. 244312

S. Georgiev, H. J. Neusser
Investigation of hydrogen bonding in 3-methylindole·H_2O cluster by mass analyzed
threshold ionization
 Chem. Phys. Lett., 2004, vol. 389, issue 1-3, p. 24

Georgiev, S. Georgiev, H. J. Neusser, T. Chakraborty
Mass-analyzed threshold ionization spectroscopy of p-fluorostyrene
J. Chem. Phys., 2004, vol. 120, issue 17, p. 8015

S. Georgiev, T. Chakraborty, H. J. Neusser
Binding energy and intermolecular vibrations of neutral and ionized p-fluorotoluene·Ar
cluster by Mass-analyzed threshold ionization
J. Phys. Chem. A, 2004, vol. 108, issue 16, p. 3304

Acknowledgments: